Rewinding a Supernova with Machine Learning

by

Eleonora Parrag

A Thesis submitted to Cardiff University
for the degree of Doctor of Philosophy

December 2023

Abstract

This thesis focuses on supernova (SN) spectra. It begins by examining SN 2019hcc, an unusual SN which displays a 'w'-shape in its early spectrum characteristic of a certain class of SN (the ultra-bright and exotic Type I superluminous supernovae, SLSNe I) but, by all other criteria, appears to be an ordinary core-collapse Type II. This work is expanded upon in a subsequent chapter by investigating this 'w'-shape via a quantitative analysis of these lines' properties for a sample of SLSNe I, and their correlation to other physical quantities. This analysis also includes spectral modelling of SN spectra for various elemental compositions, in order to better understand the contributions to the 'w'-shape by different ions. This work has significance in expanding our understanding of the mechanisms involved in producing the ultra-bright SLSNe. The study of SN spectra takes another angle in the final chapter on machine learning to predict SN spectra, which takes a large sample of publicly available core-collapse Type II SNe as the training sample for an algorithm to create synthetic spectra in order to augment and supplement existing datasets. This work allows us to make use of the massive volume of astronomical data available in augmenting our existing data and could allow for applications to population studies, spectral template libraries, and cosmology.

Publications

First Author Publications

E. Parrag, et al. 2021; *SN2019hcc: A Type II Supernova Displaying Early OII Lines*, Monthly Notices of the Royal Astronomical Society, Volume 506, Issue 4, pp.4819-4840

Acknowledgments

Funding Bodies and Affiliations

I would like to give my thanks to the STFC and the CDT for making this work possible.

Personal Thanks

I would like to thank my supervisor for his tireless help and contributions, and my friends and family for their support throughout my PhD.

Chapter 0

Contents

Chapter 1

Introduction

1.1 Background

Supernovae (SNe) are the explosions of dying stars. They are extremely energetic events, with kinetic energies typically on the order of 10^{51} ergs, and can outshine entire galaxies, with some historic galactic supernovae visible even in daylight (Stephenson & Green, 2002). SNe fade rapidly over hundreds of days, and leave behind a compact object such as a neutron star or black hole, or are completely destroyed.

SNe are transient objects, similar to, for example, Novae, Tidal Disruption Events (TDEs), or Gamma Ray Bursts (GRBs). A SN is identified from observations of electromagnetic spectra and broadband imaging, mainly in the optical regime, and can often be associated with a host galaxy. SNe can originate from a wide variety of progenitor stars and host environments and can therefore produce very different observational signatures. Explosion types can range from thermonuclear explosions of white dwarfs to the collapse of massive stars, to exotic transients which are much more fast or luminous than can be explained by classical mechanisms.

To date, thousands of SNe have been discovered, with the rate of discovery greatly accelerating as new surveys and greater observing power are developed. On the Transient Name Server (TNS)*, the official International Astronomical Union (IAU) mechanism for reporting new transients, approximately 120,000 transients have been reported since 1976, with approximately 12,000 spectroscopically classified SNe. SN spectra are usually classified based on their chemical composition and whether signatures of elements such as Hydrogen are present - see Section 1.4 for more details. Upcoming sky surveys could result in an unprecedented number of SNe candidates, beyond resources to classify them and our capacity to process them, requiring the aid of machine learning or other large-scale data analysis tools. The upcoming Legacy Survey for Space and Time (LSST) at the Vera C. Rubin

*https://www.wis-tns.org/

Observatory is forecast to discover three to four million more SNe during its ten-year survey[†]. Most SNe in our own Galaxy occur in the dusty disk (where most stars are), where severe extinction due to dust means only a small fraction of these SNe are detected (Branch & Wheeler, 2017). No new SN has been detected in the Milky Way for more than 400 years.

SNe have a significant impact on many areas of astrophysics. For example, SNe influence the birth of stars via compression of the Interstellar Medium by the shocks they produce, and they play an important role in the production of dust in the Universe. They are also major contributors to the chemical enrichment of the Universe, producing most of its Iron and other elements near to Iron in the periodic table. Additionally, SNe can also act as probes of stellar evolution, as they can provide information about their progenitor stars or star formation history. Increased knowledge of the physics involved in a SN explosion links back to the areas of research they are related to, and for example allows for more accurate cosmic distance measurements or reveals a better understanding of mechanisms or progenitors, or allows us to track stellar populations over cosmic time.

1.2 Observations of Supernovae: Light Curves and Spectra

1.2.1 Light Curves

As a SN evolves, its luminosity changes over time, typically on the order of hundreds of days. A light curve, or photometry, is the measure of this changing luminosity. SN light curves fundamentally depend on the timescales for photons to diffuse out of the ejecta and the time for the SN to expand. They are predominantly powered by internal energy deposited by the shock from the explosion and by complete or partial trapping of the products of the ^{56}Ni decay chain.

Early in expansion, the ejecta is optically thick, and little light can diffuse out, and at very late times as the SN cools and the ejecta becomes optically thin, heat is lost and the luminosity is low, therefore the typical morphology of a light curve is an increase to a maximum followed by a decline. The declining luminosity often follows the rate of radioactive decay of elements synthesised in the explosion, primarily the decay chain of ^{56}Ni to ^{56}Co to stable ^{56}Fe, and this would be the primary contributor of luminosity during this late decline after maximum. This radioactive decay is a delayed release that heats the ejecta and leads by thermal emission to higher luminosity. Various energy sources and radiation mechanisms determine the exact shape of light curves, and therefore they can provide information on the properties of a SN through the many factors that can influence the duration and peak magnitude (Branch & Wheeler, 2017).

[†]https://www.lsst.org/science/transient-optical-sky/supernovae

1.2.2 Spectra

SN spectra provide a wealth of information on the chemical composition and geometry of the explosion. Different elements produce absorption and emission at different wavelengths, and the nature of these lines is also dependent on the excitation and ionisation state of the gas. Characteristic of SNe is the presence of both absorption and emission in the profile of the same spectral line, which is known as a P-Cygni profile, and is due to spectral line formation occurring in optically thick, rapidly expanding ejecta. It indicates the existence of a gaseous envelope expanding away from the star. The material moving towards the observer causes blue-shifted absorption lines, whereas photons scattered perpendicular to the line of sight produce emission lines that are not red-shifted but at rest wavelength (once corrected for the overall redshift of the SN). At the centre the SN is an occluded region that cannot be seen whilst the centre of the ejecta is opaque.

The expected rest wavelengths can be calculated from atomic transitions and therefore a measured shift from this expected wavelength combined with the Doppler effect can reveal the redshift of the host (from galaxy emission lines). The velocity of the ejecta at the depth of the line formation can be estimated through the wavelength difference of the blue-shifted absorption from the rest wavelength (Jeffery & Branch, 1990a). The broadness of lines can give an indication of atomic density, and the presence of narrow lines in the spectrum gives an indication of interaction with an unshocked circumstellar medium (CSM). Generally, spectral lines are well described by Gaussian profiles, however the wings of these narrow lines are better fit by a Lorentzian profile which suggests electron scattering rather than Doppler broadening, and hence an additional mechanism from this shock collision with the CSM.

The entire composition of a SN is slowly revealed as the ejecta expands. During the first few months after the explosion a SN is optically thick and the spectrum forms outside a 'photosphere' (where optical depth is 1), however over time deeper and deeper layers are revealed. During this photospheric phase the spectrum is a product of photon emissions, absorption and scatterings, and an approximation of Local Thermodynamic Equilibrium (LTE) can be assumed. At this stage, the excitation and ionisation states of the gas are determined by local electron temperature and density. Line features are usually blended due to Doppler broadening, hence often synthetic model spectra are necessary for interpretation to identify the contributing elements (Branch & Wheeler, 2017).

During the photospheric phase, the optically thick photosphere of the SN is the deepest we can see into the ejecta. The photosphere can be approximated as a blackbody, which would be approximately followed by the continuum of SN spectra (the background shape of the spectrum without the absorption and emission lines), therefore allowing an estimate of the temperature and radius of the photosphere from a blackbody fit to the continuum, which can help track the evolution of the SN. The temperature can also be measured from the light curve by comparing the relative amounts of flux in different wavelength ranges (this is called spectral energy distribution (SED),

i.e. the broadband flux), which is often a more accurate way to measure temperature when flux calibration of the spectrum is less reliable. When the expanding ejecta becomes optically thin to continuum photons, it can be considered to have reached the nebular phase, where radiative transfer effects are absent as photons can escape. As a result, emission lines dominate, and LTE no longer applies, nor does the blackbody approximation.

In the case of an expanding ejecta composed of Hydrogen-rich material, as the material cools ionised hydrogen recombines to neutral hydrogen and becomes transparent. As a result, the photosphere recedes as the SN expands and cools, allowing us to see deeper into the SN. The combination of the ejecta expanding and cooling can result in a stage where the photosphere remains at the same temperature for a short period of time, which can cause a plateau in the light curve, as seen in some core-collapse SNe.

1.3 Spectral Modelling and TARDIS

Spectral modelling codes are very useful for line identification and inferring the composition, mass and explosion energy of an event, as spectra are complex and features are often blended, noisy, and not uniquely identifiable. A variety of codes exist for this purpose, from computationally inexpensive and one-dimensional codes purely for line identification such as SYN++ (Thomas et al., 2011), to more physically complex codes (see Kerzendorf & Sim, 2014 and references therein), though these come at a significantly greater computational cost. TARDIS approaches modelling with the goals of being as physical accurate as possible whilst minimising computational time. Creating these codes requires implementing a range of physical assumptions and approximations to model the state of the SN ejecta at every stage, and as such, though more and more sophisticated codes result in higher and higher quality spectra, spectral modelling is always an approximation and not 100 percent physically accurate and cannot exactly match all the conditions of the spectra we are trying to replicate.

Kerzendorf & Sim (2014) presented TARDIS, an open-source modular radiative transfer code for the rapid spectral modelling of SNe. The code uses Monte-Carlo methods to obtain a self-consistent description of the plasma state and compute a synthetic spectrum. TARDIS assumes that the ejecta is in a symmetric and homologous expansion, and as such there is a direct correlation between time since explosion and temperature. TARDIS operates by seeding a set of Monte-Carlo (MC) quanta representing photon bundles and following their propagation through a model for the SN ejecta, and the emerging photon packets are evaluated in frequency-space to create a synthetic spectrum.

The stages of the TARDIS creation of model spectra are as follows: the TARDIS simulation is set up from a TARDIS configuration, involving the creation of the SN model and the initial conditions of the SN's plasma, as well as initializing the Monte Carlo transport. The code takes a one-dimensional model for the SN ejecta, including density, abundance, luminosity, and time since explosion. TARDIS

neglects multi-dimensionality in favour of more rapid modelling and lower computational costs. The computational domain is defined by inner and outer radial boundaries, discretised by multiple spherical shells. Models with stratified abundances and complex density profiles can be created, however simple models with uniform abundances and standard density profiles are created directly by the code.

Next is the Monte Carlo Iteration where the packets of light are sent through the supernova and tracked as they interact with matter. TARDIS uses information from the Monte Carlo iteration to update properties of the plasma, such as temperature and dilution factor, to eventually find the correct plasma state. This process of doing a Monte Carlo iteration and then updating the plasma is repeated for a specified number of times or until certain aspects of the plasma state converge. After that, data generated in the Monte Carlo simulation is used to synthesize the output spectrum of the supernova. Synthetic spectra can be obtained directly from the MC radiative transfer calculations by binning the quanta emerging from the outer boundary in frequency-space. For TARDIS, the algorithm is slightly more sophisticated, and involves creating test packets (or 'virtual packets') which have the same properties of the emerging quanta, except they have a propagation direction and energy assigned based on a probability distribution associated with the creation of the original packets, which can improve the quality of the synthetic spectra.

1.4 Supernova Classification

Spectra and light curves are also used to classify SNe into different categories with similar properties. SNe are historically classified according to specific observational characteristics. The modern classification scheme was developed by Minkowski (1941). SNe can be broadly classified into two main types - those which show Hydrogen lines (Type II) and those which do not (Type I). Core-collapse of a massive star with a retained Hydrogen envelope produces the Hydrogen-rich Type II SNe, whereas if such envelope has been stripped, stripped-envelope SNe (SESNe) are observed, which fall into the Hydrogen-poor Type I. Thermonuclear SNe also fall into the Type I class. Figure 1.1 shows a summary of the current classification scheme (but is not an exhaustive guide, as there are many SNe that do not fall into it).

1.4.1 Type I

SNe Ia

SNe I are SNe without signatures of Hydrogen and can include both CC-SNe stripped of their Hydrogen envelope (SNe Ib/c), and Thermonuclear SNe. SNe Ia are Thermonuclear SNe produced by white dwarfs, typically thought to be produced when material is accreted onto them from a

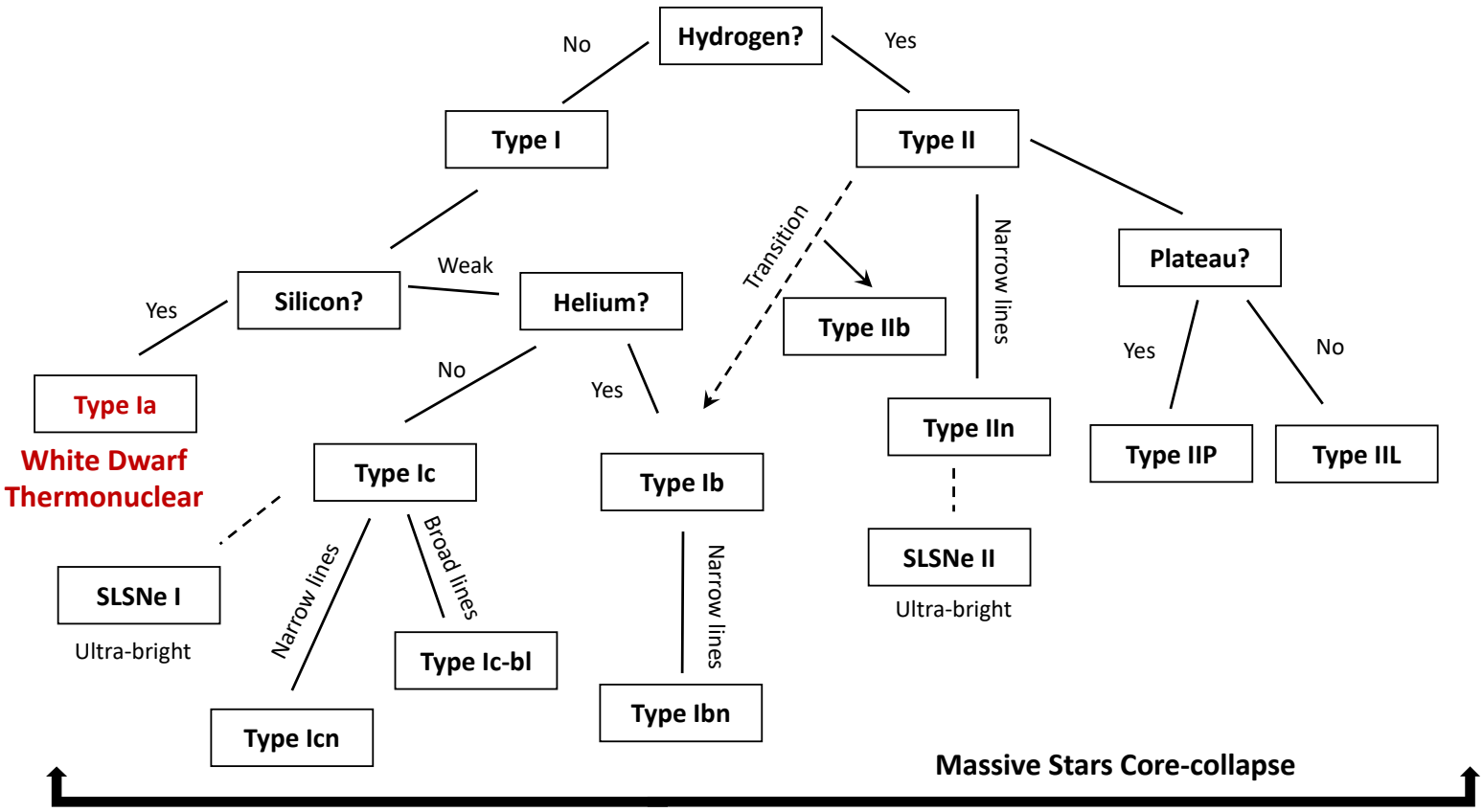

Figure 1.1. A summary of the classification scheme for SNe. Dotted lines for SLSNe suggest possible links or similarities in properties or progenitors, and Type IIb is a subclass for SNe whose spectra evolve from Type II at early times to Type Ib. This flow chart is based largely on optical spectra however the plateau divider for Type IIP/IIL is based on the light curves.

companion star in a binary system, and push them past the Chandrasekhar limit of maximum mass. However the exact mechanism is still under debate, and a 'double degenerate' scenario has also been proposed, which is the merging of two white dwarfs (Shen et al., 2018). Spectroscopically, they are characterised by a deep absorption trough around 6150Å, produced by blue-shifted Si II. In SN Ib and Ic this Si II line is weaker. Late time (approx. 4 months) optical spectra of SNe Ia display blends of dozens of Iron emission lines mixed with some Cobalt (Filippenko, 1997).

The light curves of SNe Ia have a high degree of homogeneity, and the light curve of a SN Ia consists of an initial rise of about 17-18 days and fall over 40 days followed by a slowly fading linear tail, and are powered by the ^{56}Ni decay chain. In the near-IR, SNe Ia show a secondary peak in their light curves. SN Ia light curves within hours to days after explosion can be used to search for potential shock interaction between SN ejecta and a companion star - early time 'bumps' have been seen but these are not uniquely interpretable as interaction events. Observations have shown greater variety in SN Ia light curves at early times compared to near or after maximum light (Jha et al., 2019).

Despite not being truly standard candles, luminosity strongly correlates with the shape of a SN Ia light curve, and given enough high-quality observations the luminosity of each object can be calibrated (Filippenko, 1997). Therefore they are standardisable candles whose distance can be observationally inferred, meaning they are essential for precise measurements of cosmic parameters (Jha et al., 2019). In cosmology, SNe are among the best tools for distance indicators, and SNe Ia are most suitable for this purpose as their distance can be calibrated most consistently (e.g. Branch & Tammann, 1992; Riess et al., 1998; Perlmutter et al., 1999). The standardization of SN Ia involves correcting for duration and peak magnitude of the light curve, as well as a correction for the host galaxy properties (Jha et al., 2019).

SN Ia, as cosmological distance indicators, have played a big role in the discovery of the accelerating expansion of the Universe and in measurements of the current expansion rate. A fundamental understanding of dark energy and the energy component causing cosmic acceleration is still missing, and imposing more restrictive constraints over cosmological parameters has the potential to lead to the properties of dark energy.

SNe Ib/c

SNe Ib and SNe Ic are SESNe, produced by the core-collapse mechanism but with the outer envelope of Hydrogen, or both Hydrogen and Helium, stripped prior to the explosion. SNe Ib show strong helium lines, whilst SNe Ic are characterised by a lack of both hydrogen and helium in the optical spectra, and of (strong) Silicon lines. Evidence of He I lines have been identified in the spectra of SNe Ic in their near-IR spectra, however the smaller amount of He compared to SNe Ib implies a significant difference in progenitor evolution. Both have relatively unblended emission lines of

intermediate-mass elements such as O and Ca (Filippenko, 1997). See Figure 1.2 for typical spectra of SNe Ib/c alongside SNe II.

SNe Ib/c have much more heterogeneous light curves than SNe Ia and can be roughly put in three categories of slow, intermediate, and rapid decline (see Figure 1.3) (Clocchiatti & Wheeler, 1997). The immediate decline from maximum tends to be slower than the rise time, with a late decline significantly faster than ^{56}Co decay (though there are exceptions to this typical behaviour). SESNe do not show the secondary peak in near-IR which characterises SNe Ia.

Further splitting of SNe Ib/c can be made: SNe Ic-bl (broad line SNe Ic) are a subclass that has been connected with long-duration GRBs and superluminous SNe (SLSNe), which require high photospheric velocities (Valenti et al., 2008). SNe Ibn contain narrow lines of Helium and no Hydrogen which suggests the presence of a Hydrogen-poor but Helium-rich CSM around exploding star (Modjaz et al., 2019). Gal-Yam et al. (2021) also identified SNe Icn, SNe Ic showing prominent narrow emission lines of Carbon and/or Oxygen, whilst lacking lines of Hydrogen and Helium, as typical of SNe Ic.

SNe Ib and Ic could represent the extremes of a continuum in a range of outer Helium abundance, therefore it is common to refer to Ib/c to capture this ambiguity, however some evidence suggests SNe Ic are distinct (e.g. Wheeler et al., 1994). Even if trace abundances of Hydrogen are present in Type Ib and of Helium in Type Ic the spectral differences still imply a distinctly different evolution for the progenitors of Type Ib from Type Ic. SN Ib/c are thought to result from short-lived massive stars, as they are associated with regions of recent star formation. Their progenitors are a matter of debate with some evidence suggesting intermediate mass (less than 20 M$\odot$) stars in binary systems, or in other cases linking them to single massive Wolf-Rayet stars (an unusual class of massive stars that have lost their outer H/He envelope) (e.g. Gal-Yam et al., 2014). Taddia et al. (2018) studied the light curves of a sample of SESNe and through modelling inferred a range of ejecta masses compatible with intermediate mass ($M_{ZAMS} \leq 20$ M$\odot$) progenitor stars in binary systems for the majority of SESNe

1.4.2 Type II

SNe II show Hydrogen lines in their spectra and are a result of core-collapse SNe which retained their Hydrogen envelope (Minkowski, 1941). SNe II have a large spectral and photometric diversity observed in contemporary samples (e.g. Gutiérrez et al., 2017a). SNe II were historically split into two categories based on their photometric evolution, SNe IIL showing a linear decline in the light curve and SNe IIP showing a plateau for up to 3 months after peak. The original description of a standard SN IIP as described by Barbon et al. (1979) is a rapid decline occurring in the first 30-35 days following maximum, where the SN drops about 1.2 mag, then a plateau up to about 80 days past maximum where the luminosity is roughly constant, then a second rapid decline up to 120-130

days past maximum where the SN loses 2.5 mag, then the final linear radioactive tail. Figure 1.3 shows a sample of SNe II in grey in the left panel. SNe IIL have been observed in less detail, however for this subclass the plateau phase would not remain at constant luminosity and instead have a similar rate of decline to the initial drop past peak. Arcavi (2017) suggested that the difference in Type IIL, a typically more luminous subclass of Type II SNe, could be due to the presence of a magnetar. However, Anderson et al. (2014b) suggested that the diversity observed in SN II light curves and their spectra is due to the mass and density profile of the retained Hydrogen envelopes. For years, it has been a matter of dispute whether IIL and IIP are a continuous population or have distinctly different physics and progenitors but, recently, increasing evidence has suggested that they are coming from a continuous population e.g. Anderson et al. (2014b); Sanders et al. (2015); Galbany et al. (2016); Valenti et al. (2016); de Jaeger et al. (2018). Anderson et al. (2014b) also noted that very few SNe II actually fit the classical description of SNe IIL as most show a plateau of some form. However, there have been contradicting studies, such as Davis et al. (2019), who performed a spectroscopic analysis in the near-infrared (NIR) which found distinct populations corresponding to fast (SN IIL) and slow (SN IIP) decliners, though they suggested this could alternatively be accounted for by a gap in the data set. Overall, it is generally accepted that there is a continuous population of SNe II displaying varying lengths of a plateau, though the SNe IIP and SNe IIL descriptors can still be useful in describing SNe II.

The progenitors of SNe IIP are Red Supergiants (RSGs), which are expected to be produced by stars with a Zero Age Main Sequence (ZAMS) mass of 10-30 $M_\odot$ when their cores collapse. Pre-explosion images of SN IIP suggested a lack of SN IIP progenitors above 16 $M_\odot$, which is known as the RSG problem. However, high mass progenitors such as a 17-25 $M_\odot$ RSG progenitor for SN 2015bs (Anderson et al., 2018a) have been found, and current and future surveys will continue to broaden the SN II parameter space and hopefully shed further light on the range of progenitor masses for SNe II. The progenitors of SNe IIL are generally believed to have relatively low-mass hydrogen envelopes otherwise they would exhibit distinct plateaus as do SNe IIP (Filippenko, 1997).

Further splittings of SNe II are based on spectroscopic features, again refer to Figure 1.2. SNe IIb are transitional events between Hydrogen-rich SNe II and Hydrogen-poor SNe Ib e.g. Filippenko et al. (1993). This transition arises as SNe IIb are nearly completely stripped of their hydrogen envelope so the photosphere rapidly retreats through the small mass of Hydrogen into underlying Helium-rich layers, at which point they resemble SNe Ib. SNe IIn display narrow emission lines attributed to interaction with dense circumstellar material e.g. Schlegel (1990).

The left panel of Figure 1.2 shows typical spectra of the different classes of core-collapse SNe, both Type II and SESNe. The lines used for identification - Helium, Silicon, and the Balmer lines - have been marked on the spectra. The narrow emission lines with Lorentzian wings can be noted in SN IIn and SN Ibn, and the broad lines in SN Ic-bl. Figure 1.3 displays a range of light curves for core-collapse SNe, showing the diversity in SNe II and SESNe.

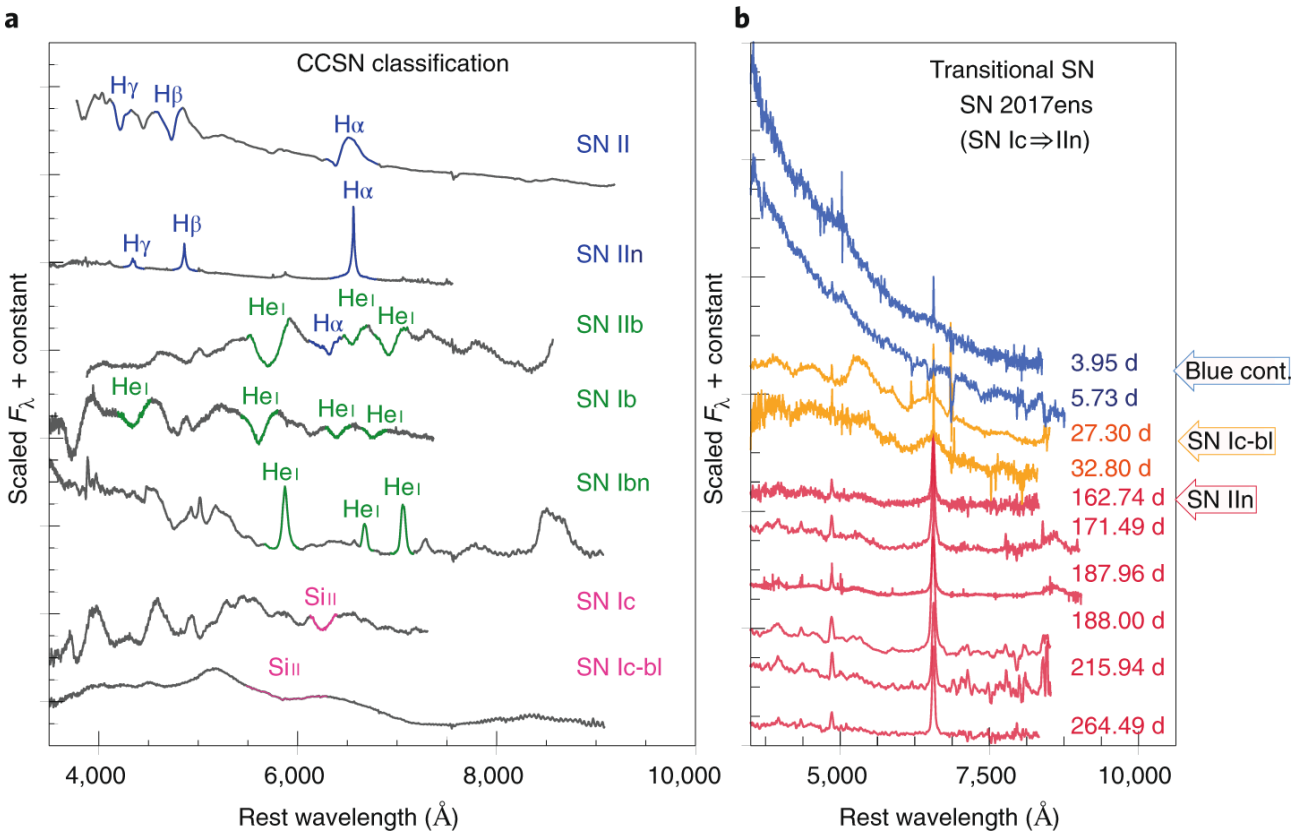

Figure 1.2. Panel a): Example spectra of core-collapse SNe, including both Type II and SESNe. Characteristic lines used for classification are highlighted: Hydrogen, Helium, and Silicon. Panel b): an example of a transitional event, SN 2017ens, evolving from a SN Ic to a SN IIn. Figure reproduced from Modjaz et al. (2019).

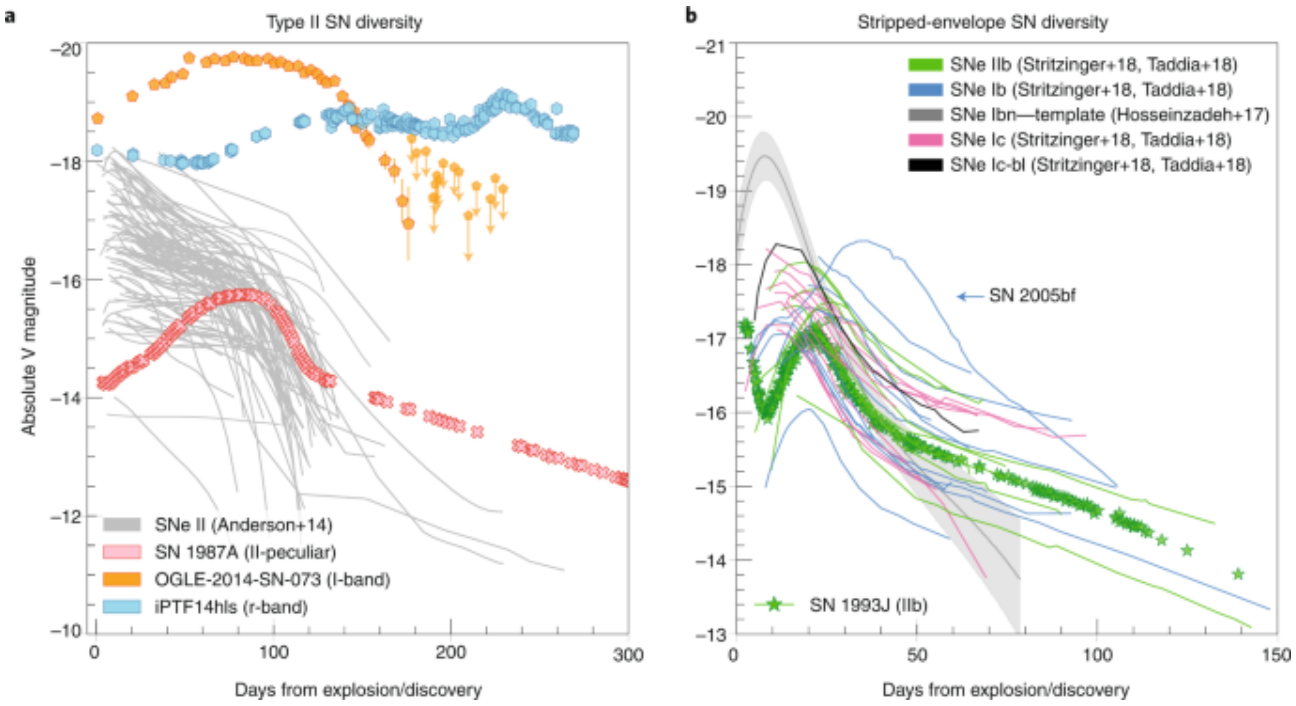

Figure 1.3. Light curves of core-collapse SNe, demonstrating a large diversity in luminosity and light curve shape, reproduced from Modjaz et al. (2019). Panel a): light curves of SESNe: SNe Ib/c, as well as interacting SNe Ibn, broad line SNe Ic-bl, and the transitional SNe IIb subclass. Panel b): A sample of typical Type II SNe, alongside long-lived outliers OGLE-2014-SN-073, iPTF14hls, and SN 1987A, which shows signatures of Hydrogen in their spectra but produce unusual light curves that differ from standard SNe II.

1.4.3 SN 1987A

SN 1987A is a link between SNe II and SNe Ib/c. The early spectra resemble a SN II, with broad Hα lines. At late times many months after maximum the broad Hα that dominates the late time spectra of SNe II had no signatures in SN 1987A, and rather had broad emission lines of [O I] and [Ca II] dominate the spectrum, typical of the late spectra of SNe Ib. This supported the physical continuity between progenitors and explosion mechanisms of SNe II and at least some SNe Ib/c **?**.

1987A-like SNe II are an unusual subclass of SNe II which follow the prototype of SN 1987A, which spectroscopically resemble SNe II but have an unusually long rise to peak (on the order of 100 days) (Menzies et al., 1987). These SNe have been linked to the explosion of a Blue Supergiant rather than a Red Supergiant as for the majority of Type II (see e.g. Pumo et al., 2023, and references therein). The progenitor of SN 1987A has also been directly observed (Gilmozzi et al., 1987). The left panel on Figure 1.3 shows the light curve of SN 1987A compared to a sample of more typical SNe II, and the unusually long rise to peak luminosity.

1.4.4 Transitional Events

SN classification can be time-dependent, as some objects have been observed to dramatically change their observables over time, ranging on timescales from weeks to years. In recent years, wide-field surveys have revealed a large diversity of unusual transients that include extreme transitional objects (Modjaz et al., 2019). One such example is SN 2017ens (Chen et al., 2018), a transition between a luminous broadline SN Ic and a SN IIn. The right panel in Figure 1.2 demonstrates the spectral evolution of SN 2017ens and how it transitions from one class to another over the course of hundreds of days.

SN 2017ivv is another, sharing properties with fast-declining SN II and SN IIb (Gutiérrez et al., 2020), or SN 2014C, which underwent a change from a SN Ib to SN IIn due to interaction with a Hydrogen-rich CSM (Milisavljevic et al., 2015). Objects such as these can support physical continuity between progenitors and explosion mechanisms of different types (Filippenko, 1988).

1.5 SNe II as Standard Candles

Distances to cosmological objects are key in estimating the expansion rate and age of the Universe. SNe Ia are often used for cosmology as standard candles and measures of cosmic distance (e.g. Branch & Tammann, 1992; Riess et al., 1998; Perlmutter et al., 1999) as they are ideal for this purpose due to their homogeneity and relatively bright luminosities. However, core-collapse SNe, specifically the plateauing SNe IIP, have also been considered as standard candles to measure cosmic

distance (e.g. Hamuy & Pinto, 2002; Nugent et al., 2006; Kasen & Woosley, 2009). The benefit of using SNe II is that, though they are less luminous, they have the potential to be discovered in greater numbers in the local Universe. For example, Perley et al. (2020) suggested a rate of 2.35×10^4 Gpc^{-3}yr^{-1} and 1.01×10^5 Gpc^{-3}yr^{-1} for SNe Ia and Core-Collapse SNe respectively. This was based on the ZTF Bright Transient Survey (BTS), which aims to provide a large and purely magnitude-limited (m < 19 mag for discovery and m < 18.5 mag for classification) sample of extragalactic transients in the northern sky. For CCSNe the redshifts of the sample were $z < 0.05$, and for SNe Ia $z < 0.1$. Alternatively, Graur et al. (2017) considered a sample of 180 SNe and SN impostors, complete for SNe Ia out to 80 Mpc and core-collapse SNe out to 60 Mpc. They presented different rates for different Galaxy Stellar Mass cuts, however for a cut of $M_* \leq 10^{10} M_\odot$, SNe Ia had a fraction of $0.20^{+0.07}_{-0.06}$ and SNe II $0.61^{+0.12}_{-0.12}$, three times as much for all SNe out to 60 Mpc, similar to the ratio found by Perley et al. (2020). Hence SNe IIP have the potential to be observed in greater numbers in the local Universe.

Hamuy & Pinto (2002) approached calibrating distance for SNe IIP via a correlation between the absolute brightness of the plateau, and the Fe II λ5169 velocities observed during the plateau phases, known as the Standard Candle Method (SCM). Note that Fe II λ5169 is merely an estimate of the photospheric velocities (e.g. Takáts & Vinkó, 2012). More detailed spectroscopy in these phases could help to further constrain these relationships for different SNe II, as direct measurement of the plateau velocities is possible only in the case of precise timing of the spectroscopic observation, which is rarely achievable for all SNe. They also suggested Hβ could be a substitute for Iron in early spectra when the latter is not visible due to the high temperature. Recent works use an updated version of the SCM, with amendments such as incorporating colour, for example de Jaeger et al. (2020).

An alternative means of calibrating distance, the Expanding Photosphere Method (EPM, Kirshner & Kwan, 1974), compares the angular size of the expanding SN ejecta with the ratio between its observed and theoretical flux. The input quantities are fluxes, temperatures and velocities observed at several epochs during the photospheric phase. Thus, EPM requires both photometric and spectroscopic monitoring of SNe throughout the plateau phase. The EPM has undergone significant improvement since the original formalism (e.g. Takáts & Vinkó, 2012; Gall et al., 2018). Gall et al. (2018) compared EPM and SCM and found good agreement between them.

Kasen & Woosley (2009) found, through the use of models, a tight relationship between luminosity and expansion velocity, similar to what Hamuy & Pinto (2002) employed empirically to make SNe IIP standardized candles. This relationship can be explained by hydrogen recombination in the SN ejecta, but systematic errors could originate from a sensitivity related to progenitor metallicity and mass. They suggested from their modelling that SNe IIP could be used to obtain distances accurate to $\sim$20 percent using only photometric data. Additionally, Dessart et al. (2013) found through modelling that variations in parameters like rotation, metallicity, and overshooting in the SN progenitor alter global quantities e.g. progenitor radius which significantly influence synthetic light curves even though

the same main sequence mass and explosion energy characterise these models, which confirms the difficult in associating a SN IIP explosion with a main-sequence progenitor.

Another means of distance calibration, which uses detailed spectral fitting, is the Spectral Expanding Atmosphere Method (Mitchell et al., 2002, SEAM), which attempts to establish the physical conditions in the SN. In this case, the emergent flux is determined through detailed model fitting for each spectral epoch. This method requires excellent spectral data, and has so far been applied only to the brightest and nearest SNe (SNe 1987A and SN 1999em).

1.6 Thermonuclear Supernovae

Thermonuclear SNe are objects where the energy released in the explosion is primarily the result of thermonuclear fusion. The progenitors of this category of SNe are white dwarf stars in a close binary system, where the accretion of matter from a companion star triggers the explosion, or alternatively from the merging of two white dwarfs in a binary system. These are classified as Type Ia SNe (SN Ia), as discussed above.

There are a plethora of Type Ia subclasses, generally named after a prototype SN Ia which is used to define the subclass. Slow-declining, hot, luminous events are known as 91T-like or 99aa-like objects. Fast-declining, cool, subluminous events are 91bg-like, and are sometimes claimed to be a separate population. SNe Ia with low ejecta velocities are Type Iax, however Iax differ from all other SN in never becoming fully nebular in their spectra. Possibly related to Iax are 02es-like events, which also have low luminosity and ejecta velocity, but have cooler spectra than Iax. Calcium-rich SNe are spectroscopically similar to SNe Ib with strong [Ca II] emission dominating their nebular spectra. Multiple progenitor scenarios have been proposed, one of which is the delayed thermonuclear explosion of a white dwarf in a binary system which was dynamically ejected from its host (Foley, 2015). SNe Ia-CSM are otherwise spectroscopically standard SN Ia which show Hα emission, taken as a sign of interaction with hydrogen-rich material (e.g. Silverman et al., 2013).

Super-Chandrasekhar SN Ia are over-luminous SNe Ia (e.g. Howell et al., 2006; Scalzo et al., 2010). As the luminosity of SNe Ia is powered by Ni^{56} decay, these luminosities would require a mass of Ni^{56} in the ejecta which is not consistent with the Chandrasekhar mass limit. It has been suggested rapid rotation may support such a massive white dwarf (Yoon & Langer, 2005), or that the merger of two massive white dwarfs could also produce a super-Chandrasekhar product (Tutukov & Yungelson, 1994; Howell, 2001).

The thermonuclear zoo also contains many unusual objects that have not yet been easily grouped into classes. Figure 1.4 demonstrates this zoo of SNe Ia with the parameter space of light curve properties of peak absolute magnitude and decline rate, compared to a sample of normal SNe Ia.

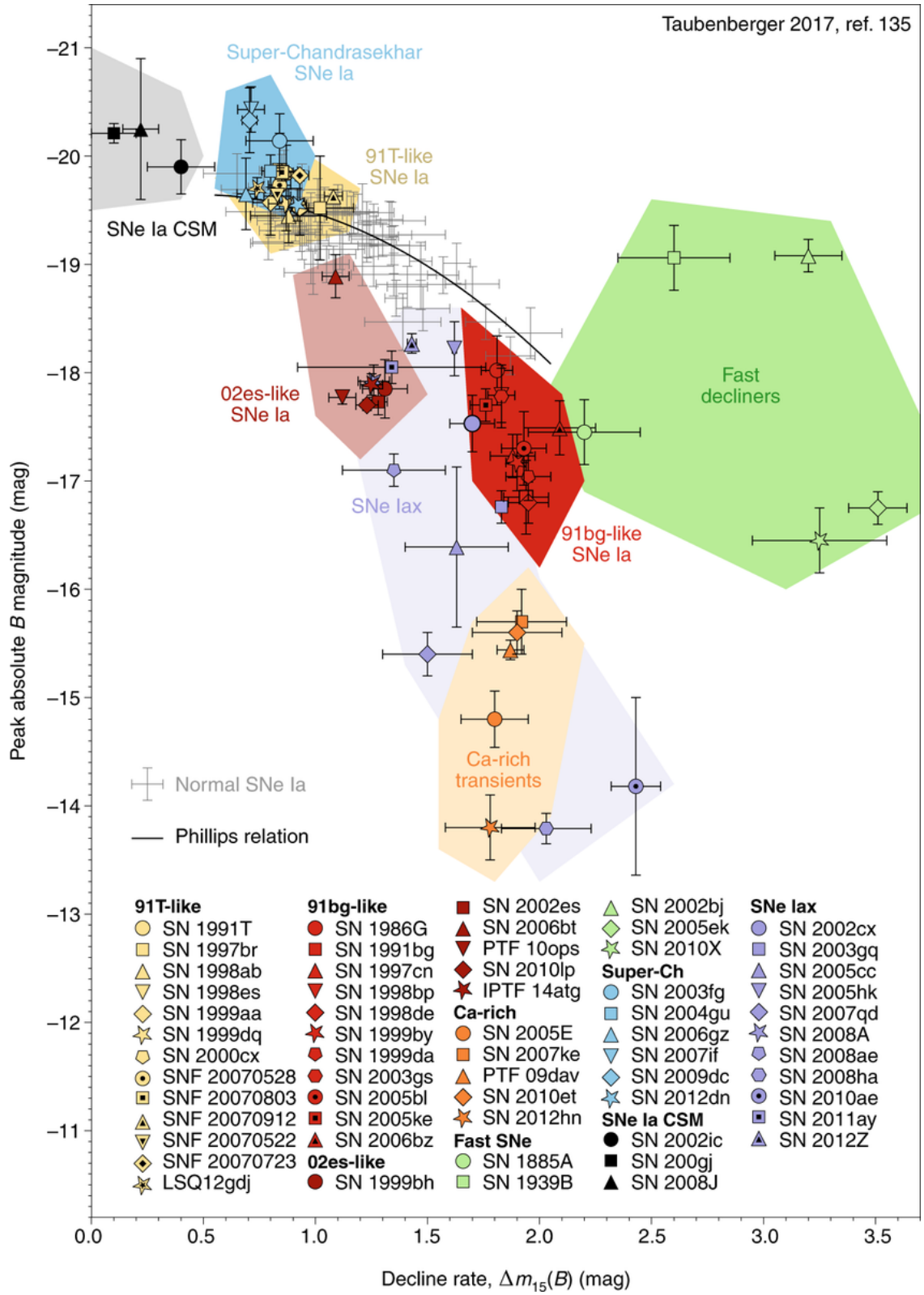

Figure 1.4. The parameter space of peak absolute magnitude and decline rate for SNe Ia, showing both 'standard' SNe Ia and the range of SNe Ia subclasses. Reproduced from Jha et al. (2019) and Taubenberger (2017).

1.6.1 Explosion Mechanisms

The exact mechanisms for the explosions of white dwarfs are still under debate. Whilst there is strong indirect evidence, the direct evidence for thermonuclear SNe explosions of white dwarfs is limited (Jha et al., 2019). Current areas of research involve looking for signatures of the companion star - this is thought to be either another degenerate white dwarf, or a non-degenerate star e.g. main sequence. Kerzendorf et al. (2018) searched for a surviving companion star, and concluded their findings were consistent with either a completely destroyed companion (such as in a merger) or a very dim surviving companion white dwarf. Open questions about the explosion mechanism include how the explosion begins and proceeds, the kind of material accreted, at what mass the primary white dwarf explodes, and whether it is completely disrupted (Jha et al., 2019).

1.7 Core Collapse Supernovae

1.7.1 Explosion Mechanisms

Core collapse of a massive star is an alternative route toward a SN explosion. By the end of a massive star's life, the star consists of concentric shells of previous burning phase elements. The production of Iron in the core begins the end of hydrostatic burning. This is a result of the synthesis of elements heavier than Iron not releasing energy, but instead using energy, decreasing the pressure of the core. Below the Chandrasekhar mass limit, the Iron core can support itself by electron degeneracy, however, beyond this it is not sufficient to counter gravity and the core collapses. Nuclear matter has a much lower compressibility, so when the infalling core reaches nuclear densities the collapse is decelerated and bounces in response to increased nuclear matter pressure. This drives a shock wave into the outer core, which has continued to fall inwards at supersonic speed (Janka et al., 2007).

The bounce-shock mechanism suggests that the shock wave produced by this core bounce is sufficient to trigger the SN event and ejection of stellar material (Janka, 2012). However this requires the shock wave to be strong enough to stop collapse and explode outer layers - and models show there is not sufficient energy to trigger a SN explosion via this mechanism (Janka et al., 2007).

Following the core bounce, the shock wave loses significant energy by dissociation of heavy nuclei in the outer core. A great number of neutrinos are created in this process, a large fraction of which escape the star in the neutrino burst at shock breakout, carrying away energy. Thus the shock is weakened and stalls. The core bounce with the formation of the shock wave is therefore only the starting point of the sequence of events that trigger the SN explosion, however the exact mechanism is still controversial.

After core bounce, a compact remnant begins to form at the centre of the collapsing star, rapidly growing via the accretion of infalling stellar material - this is the proto-neutron star (PNS), which will

evolve into a neutron star or may collapse to a black hole. This PNS still contains a large number of degenerate electrons and neutrinos. As neutrinos escape, they are scattered and convert their energy to thermal energy. The 'delayed neutrino heating mechanism' suggests the stalled shock wave can be revived by these streaming neutrinos. These neutrinos carry most of the energy set free in the gravitational collapse of the stellar core, and deposit their energy behind the shock front, increasing the pressure and driving the shock outwards again, eventually leading to the SN explosion (Janka et al., 2007).

Other mechanisms have been suggested. After the results of 2D hydrodynamic simulations, which did not yield explosions by the neutrino-heating mechanism, the acoustic mechanism was proposed. This was based on the idea that PNS vibrations are damped by sending strong sound waves into the surrounding medium, and the dissipation of these helps heat the post-shock region (Burrows et al., 2006). Magnetohydrodynamic mechanisms are thought to be relevant for the explosion of very rapidly spinning stars and possibly linked to long GRBs and Hypernovae (Ostriker & Gunn, 1971). The Phase-transition mechanism involves a first-order hadron-to-quark matter phase transition that occurs at sufficiently low density. This can have dynamical consequences during the post-bounce accretion phase of the collapsing stellar core (Fischer et al., 2011). An additional exotic route to collapse could be a Pair Instability SN, where gravitational instability occurs due to the formation of electron-positron pairs from high-energy photons (Janka, 2012).

There are still a number of open questions related to CC-SNe beyond the explosion mechanism itself. These include but are not limited to: the link between the properties of SNe and their progenitor stars, the fraction of stellar collapses that do not yield explosions, or what the characteristics of the neutrino burst from a SN are and what they tell us about neutrino properties and extreme conditions in a newly formed neutron star (Janka, 2012).

1.8 Extreme Supernovae

Extreme SNe are unusually luminous and fast transients, whose luminosity and time evolution cannot be explained purely by the classical mechanisms discussed above, the thermonuclear and core-collapse models. Below are discussed superluminous SNe, fast blue optical transients, and kilonovae. Figure 1.5 demonstrates this through the transient parameter space with peak luminosity as a function of the rise time for extreme SNe, considering also the physical limits of both thermonuclear and core-collapse SNe.

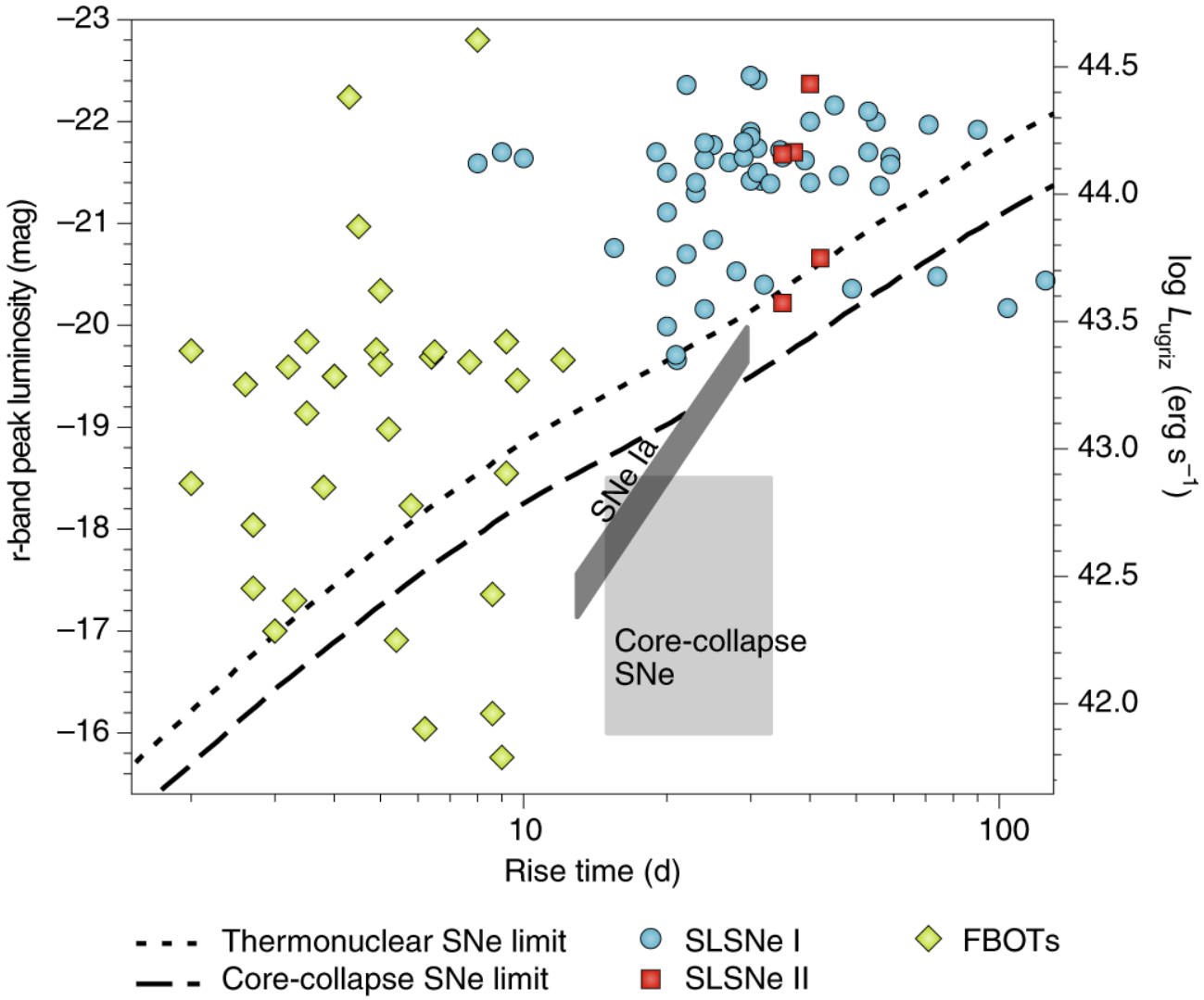

Figure 1.5. Reproduced from Inserra (2019). Peak magnitude against rise time for a sample of extreme transients, alongside the region of parameter space typically occupied by SNe Ia and CC-SNe. As can be seen, these extreme events display magnitudes that cannot be explained by these classical mechanisms, and by the physical limits of both mechanisms marked by the dashed lines. Such limits are determined using the standard diffusion formalism, the maximum ratio of Ni^{56} mass with respect to that of the ejecta as derived from theory, and average values from observational studies Inserra (2019)

1.8.1 SLSNe

A finding of the wide-field survey has been the discovery of a population of 'superluminous' SNe (Quimby et al., 2011). SLSNe are intrinsically rare with respect to common core-collapse SNe (Quimby et al., 2013; McCrum et al., 2015; Inserra, 2019), with a recent measurement by Frohmaier et al. (2021) reporting a local ratio of SLSNe I to all types of CCSNe of $\sim 1/3500^{+2800}_{-720}$. SLSNe are characterised by absolute luminosities at maximum light of approximately -21 mag (Gal-Yam, 2012; Inserra, 2019), though recent evidence suggests that SLSNe in fact occupy a wider range of luminosities, with peak luminosities reportedly as faint as -20 mag e.g. Angus et al. (2019). They are typically found in dwarf, metal-poor, and star-forming galaxies, suggesting that SLSNe are more effectively formed in low metallicity environments e.g. Lunnan et al. (2014); Leloudas et al. (2015a); Chen et al. (2017d); Schulze et al. (2018).

There have been many attempts to explain the luminosities of superluminous SNe. Kasen & Bildsten (2010) suggested that magnetar birth is likely to impact a few percent of all core-collapse SN, and may naturally explain some of the most luminous events seen. They showed that the energy deposited into an expanding SN remnant by a highly magnetic spinning neutron star can substantially increase the magnitude of the curve. Other suggestions have been pulsational pair-instability, consisting of a series of pair-instability explosion events (Woosley et al., 2007), or interaction of the SN shock with a sufficiently opaque circumstellar medium (Chevalier & Irwin, 2011).

SLSNe can be split into subclasses based on whether they contain signatures of hydrogen (SLSN II), or if they are absent (SLSN I) (Gal-Yam, 2017; Inserra, 2019)

SLSNe I

Type I Superluminous SNe (SLSNe I) are now usually identified by a lack of H or He features, and in their early, usually up to peak, spectra by broad absorption features forming a characteristic 'w'-shape around 4200 Å and 4400 Å. These are usually associated with O II, and consist of a complex blend of many individual lines (Quimby et al., 2011; Gal-Yam, 2019a). The presence of O II lines in this region has been attributed to non-thermal excitation requiring a power source in the CO cores of massive stars (Mazzali et al., 2016). This is in contrast with other Oxygen lines, which appear when Oxygen is ionised by sufficiently high temperatures. Therefore, the lack of observed O II features in normal luminosity SNe Ic may be the product of rapid cooling or lack of non-thermal sources of excitation (Quimby et al., 2018), which is also thought to be the case for SN 2020wnt (Gutiérrez et al., 2022), a SLSNe I without O II lines.

There is debate on the source of the non-thermal excitation required to produce these lines. Maeda et al. (2007) proposed non-thermal excitation in the form of strong X-ray flux from a magnetar, such as the injection of X-rays from interaction with a magnetar wind. Non-thermal excitation could also be due to high energy electrons produced by γ-rays from the radioactive decay of ^{56}Ni

(Li et al., 2012), however this would more likely be relevant for later times, and the radioactive decay of ^{56}Ni plays a small, or even non-existent, role to the luminosity of SLSNe I (Inserra et al., 2013b). Interaction between the ejecta and an Oxygen-rich circumstellar medium (CSM - e.g. Nymark et al., 2006; Chatzopoulos & Wheeler, 2012) has also been suggested as a mechanism to produce the associated spectral features. Nicholl et al. (2015a) found the range of shapes of SLSN light curves can be reproduced by both magnetar engines and CSM interaction. Recently, several signs of interaction have been observed in the spectra of SLSNe I (e.g. Inserra et al., 2017; Lunnan et al., 2018a; Gutiérrez et al., 2021; Pursiainen et al., 2022). Other models such as a Pair Instability SN have also been suggested (e.g. Heger & Woosley, 2002; Kozyreva & Blinnikov, 2015).

Pastorello et al. (2010) observed SLSN-I SN2010gx to develop SNe Ic features, and detailed follow-up suggested transients of this type are linked to SNe Ic. However, the slow spectral evolution of SLSNe I is quite different from SNe Ic timescales, which raises questions on the progenitor stars, and the origin of the luminosity, which does not appear to be powered by ^{56}Ni. An object which appears to connect SNe Ic and SLSNe I, suggesting a link between their progenitors, is SN 2020wnt (Gutiérrez et al., 2022), which resembles the SN Ic SN 2007gr spectroscopically, yet photometrically shows properties similar to SLSNe I such as a long rise and high luminosities, with a typical metal-poor, star-forming host.

SLSNe I can observationally be split into further Fast and Slow subclasses, based on the speed of the rise and decline of the light curves. Fast SLSNe I have an average rise time of 28 days, and Slow 52 days (Inserra, 2019). Inserra et al. (2017) considered extensive observational data for four of the 'Slow' SLSN I subclass and found features that are quite distinct from the faster evolving SLSNe. It was also suggested that there is at least some interaction between the expanding ejecta of the SN, and the surrounding material. Gaia16apd (or SN2016eay, Yan et al., 2017a) has been proposed to be an intermediate event which fits into a possible continuum between fast- and slowly declining events, as photometrically it exhibits an intermediate evolution, with an early evolution closer to the fast-declining events. Despite the early photometric differences, the spectra at late times are similar to slowly-declining SLSNe I, suggesting that both Fast and Slow subclasses originate from similar progenitors (Kangas et al., 2017).

SLSNe II

SLSNe II exhibit signatures of hydrogen in their optical spectra. Some SLSNe II display signatures of interaction similar to classical SNe IIn, and can be further divided into a subclass of SLSNe II dominated by interaction: SLSN IIn. Such an example of a CSM-interaction powered high luminosity object is SN 2006gy (e.g. Smith et al., 2007; Ofek et al., 2007; Agnoletto et al., 2009) which characteristically displays multi-component hydrogen and narrow emission lines. SLSNe II are generally featureless around peak epoch with a broad, very shallow H-alpha profile (Inserra, 2019).

The massive luminosities of SLSN IIn are suggested to be powered by CSM interaction, given their observed spectral signatures such as narrow spectral features and multi-component profiles which suggest interaction with an unshocked CSM. However, SLSNe II without obvious spectral signatures of interaction could be powered by multiple sources, such as a magnetar central engine providing the bulk of the luminosity, with some additional energy output from interaction between the magnetar-powered ejecta and CSM shells of varying density (Inserra et al., 2018).

1.8.2 FBOTs

Fast Blue Optical Transients (FBOTs) show timescales and spectroscopic evolution inconsistent with any standard scenario and resemble events powered by interaction or recombination rather than radioactive decay. They are characterised by a rapid light curve rise to peak (<10 days) and an exponential decline in 30 days after peak. They are generally quite blue and are hot, featureless blackbodies (10,000-30,000 K) at peak. A wide range of possibilities have been suggested to explain their behaviour, one of which is an optically thick low-mass circumstellar wind surrounding a core-collapse SN. The spectra are consistent with being powered by shock-breakout or recombination in this extended envelope. Other explanations could be the formation of a magnetar in a binary neutron star merger, or a TDE (Inserra, 2019).

1.8.3 Kilonovae

Another type of extreme transient is the kilonova. Mergers of black holes or neutron stars are predicted to eject material rich in heavy radioactive isotopes that can power an electromagnetic signal. The first detected kilonova coincided with gravitational wave source GW170817, due to a binary neutron star merger. A rapidly fading electromagnetic transient spatially coincident with GW170817 and a weak short GRB was observed (Smartt et al., 2017). This was a fast fading transient with a light curve and spectra consistent with a source powered by r-process decay timescales. The spectra are suggested by modelling to show features of the heavy elements Caesium and possibly Tellurium (Smartt et al., 2017). The r-process is a certain branch of nucleosynthesis - in the presence of a high density of free neutrons at high temperatures, neutrons are captured into Iron-group seed nuclei on a rapid timescale of milliseconds. After the rapid neutron captures there is a return to stability by beta decay. The classical r-process produces about half of nuclides beyond the Iron group (Seeger et al., 1965). However there is a question of where this r-process occurs, and this first detected kilonova provides some evidence in its spectra for the presence of r-process products, and therefore of the r-process occurring in this neutron star merger which provides the hot neutron-rich environment (Branch & Wheeler, 2017).

1.9 Machine Learning Applied to SNe Research

Advanced data analysis tools offer a means of processing the large volumes of astronomical data from current and upcoming surveys. Machine learning is one such tool, which consists of producing algorithms that allow the computer to learn from data. The machine learning approach promises to be an excellent method for processing such a large quantity of data which could otherwise provide a daunting challenge. Machine learning can be split into two broad types: supervised and unsupervised learning. Supervised learning is where data has been labelled for the algorithm to learn from (e.g. classified into categories), whereas unsupervised learning looks more generally for patterns in unlabelled data. Examples of supervised learning include decision trees, regression, and Neural Networks (NN) - though some NN can also be unsupervised or semi-supervised. Examples of unsupervised learning include clustering or dimensionality reduction.

A great variety of work has been done in applying machine learning to astrophysics, and specifically SNe. Some approaches have focused on spectroscopic analysis. Existing tools for spectral analysis such as radiative transfer simulations have a high computational cost, and the aim is to create a more efficient way to infer underlying physical properties than the existing time-consuming solutions. Vogl et al. (2020) approached this by obtaining compact representations of spectra as parameters (using Principle Component Analysis, Tipping & Bishop, 1999), and performing regression analysis to reconstruct a spectrum from predicted parameters. Kerzendorf et al. (2021) considered a deep learning emulator for TARDIS, a Monte-Carlo radiative transfer code for modelling SN spectra, which involved using machine learning to minimise as much of the modelling process as possible when creating model spectra as this process is slow and time/resource intensive. Lu et al. (2023) created spectral templates of SNe Ia using similar techniques of principle component analysis (PCA) and Gaussian Process Regression, as well as exploring autoencoders for the same purpose of dimensionality reduction. Similar preprocessing techniques for creating SNe II templates were used by Vincenzi et al. (2019), and for SNe II spectral classification by de Souza et al. (2023).

Another application is to classification of SN spectra (e.g. Muthukrishna et al., 2019; Burhanudin et al., 2021) or anomaly detection (e.g. Villar et al., 2021; Ishida et al., 2021), to quickly identify which SNe require follow-up. However, the current existing SN dataset is heavily unbalanced in both photometry and spectroscopy towards SN Ia, which presents a problem as this would introduce bias into the machine learning models unless it is accounted for. Boone (2019) considered classifying SN light curves, and overcame the problem of an imbalanced dataset by augmenting their data with Gaussian Processes to generate new light curves. However, the most common solutions to balancing a dataset is to undersample (take less of the more common category) or oversample (make duplicates of less common categories) - both of which come with their advantages and drawbacks - undersampling discards a lot of usable data, and oversampling can lead to overfitting as data is duplicated. Additionally, many works were produced as a result of the Photometric LSST

Astronomical Time Series Classification Challenge (PLAsTiCC), an open data challenge to classify simulated astronomical time-series data in preparation for observations from LSST (Kessler et al., 2019).

Additional techniques which can help overcome issues with data available for training could be active learning, or transfer learning (e.g. Ishida et al., 2019; Vilalta, 2018; Vilalta et al., 2019). Active learning aims to minimise labelling costs by identifying a few chosen objects which have the highest potential to improve classifier predictions. Ishida et al. (2019) considered applying active learning to target the objects available for spectroscopy which would maximally improve the model if adding to the training set. Vilalta (2018) and Vilalta et al. (2019) considered applications of transfer learning to astronomy, where an algorithm is trained on one dataset and applied to another. Vilalta et al. (2019) discussed domain transformation - an example is to build a predictive model on spectroscopic data to identify Type Ia supernovae (SNe Ia), while subsequently trying to adapt such a model to photometric data.They assume a strong similarity in model complexity across domains, and use active learning to mitigate the dependence on source examples.

Deep learning is an alternative to feature-based learning (where features are manually identified), where features are learned from the data - deep learning has been found to be good at discovering intricate patterns in high dimensional data - for example with convolutional neural networks (Lecun et al., 2015). Hu et al. (2022) applied deep learning in the form of an LSTM NN (Long Short-Term Memory, a type of Gated Recurrent NN) to predicting Type Ia SNe. They used up to two spectra to make predictions and found good results in predicting a full evolution of various Ia subclasses from just one spectrum at peak.

1.10 Motivation and Thesis Outline

There are two main areas which will be explored in this thesis. The first concerns SLSNe: these ultra-luminous events cannot be explained by classical core-collapse mechanisms, and as of yet there is still much to discover about these extreme SNe. The questions considered here centre around: what powers SLSNe and is responsible for their extreme luminosity? Can these mechanisms occur in normal luminosity SNe? What can this tell us about stellar evolution? These will be explored through a close look at O II lines in SLSNe I, as these lines are characteristic of this extreme SN type, and therefore further investigation could reveal what makes these events unique and shed light on the mechanisms that produce these lines almost exclusively in SLSNe I. The chapters concerning SN 2019hc and investigating O II lines in SLSNe I look at the 'w'-shaped feature characteristic of SLSNe I, and analyse this feature which is so ubiquitous in this class. Investigating SN 2019hcc, an apparently ordinary SNe II that appears to show these lines, leads to an exploration of the possibility of a magnetar in ordinary-luminosity SNe.

The second area of focus is linked to an open question related to observations. How can we overcome limitations in resources for spectroscopy, and process the extremely large amount of data expected in the era of LSST at the Vera C. Rubin Observatory? The final science chapter concerns using machine learning to predict the spectra of SNe II. This work focuses on expanding the data we already have by using existing information to create artificial spectra for epochs where we do not have observations. This could be useful in a range of areas, such as in creating spectral templates, calibrating cosmic distances, and shortcutting computationally exhaustive tasks such as modelling via radiative transfer codes. In particular, the SCM as discussed in Section 1.5 could benefit from machine learning and accurate predictions of spectra and hence velocity at custom epochs, and this could allow SNe II to be more widely used as standard candles alongside SNe Ia, providing more data with which to achieve more precise and accurate measurements of the expansion of the Universe.

Chapter 2

Data Techniques

2.1 Photometry

2.1.1 Photometric Observations and Telescopes

Photometry is used to obtain the light curve for a SN, which measures its magnitude over time. The devices used for photometric imaging and spectrographs are Charged-Couple Devices (CCDs), which are used for light detection - the output is split into pixels where each pixel measures how many photons were detected in the exposure period, and records this as a 'count'. For fainter objects greater exposure times are required for enough photons to be detected to make the object distinguishable. Thermal noise and cosmic rays may alter the pixels in the CCD array, as can illumination variations, dark current (additional background from long exposures), and other systematic defects such as dead pixels, hot pixels, etc. in the CCD. Therefore, data reduction techniques must be used to clean and prepare this data for analysis.

CCD detectors can cover different wavelength ranges (bands), and the 'colour' is found from the difference between brightness in different bands. For example, the colour could be taken as the difference in magnitude measured in the B (445 nm central wavelength) and V (551 nm) bands, denoted as $B - V$. However, colour can be measured in a variety of ways using different bands, such as $u - g$, $g - r$, etc. This colour is useful as it can be related to, for example, temperature or reddening.

Data Reduction

Data reduction is the process of converting raw CCD data to usable images. Data reduction involves removing unwanted signatures produced by the detector and instrument. The following are the steps involved in data reduction:

- Bias Subtraction: The bias level is an electronic offset added to the signal from the CCD to make sure that the Analogue-to-Digital Converter (ADC) always receives a positive value. It is common practice to create a master bias image from the median of several (>10) bias images to reduce the readout noise and remove cosmic rays. A bias frame is an image taken with the shutter closed, with no light falling on the CCD.

- Overscan correction: In principle the bias level is constant, but it can slightly change during the night because of external factors (like temperature variations). To monitor this effect, the bias level of each image is measured in the "overscan" region (a stripe of a few columns/rows at the edge of the CCDs, which is not exposed to the light) and removed from the whole frame, before the bias images combination. After use, the overscan region can be cut off trimming the images.

- Flat fielding: Due to a variety of factors such as construction faults, variation of transmissivity in the CCD coating, and dust contamination, the CCD response to the incident light is not uniform. This means it can show variation on different scales from that of the whole frame to pixel-to-pixel. A solution is to divide the data by a flat-field, which is essentially a sensitivity map created from calibration exposures. A flat-field is usually obtained by imaging a uniformly illuminated screen inside the telescope dome (dome-flats) or the sky at twilight/dawn (sky-flat). To reduce the Poisson statistics and remove cosmic rays, several flats can be averaged to also obtain a master-flat. For spectroscopic master-flats, another process has to be added, i.e. their normalization along the dispersion axis.

Sometimes for deeper exposure images, multiple images are taken which are 'dithered' (where the telescope is pointed varies slightly) - these images need to be combined to get the final image. Dithering is also useful for the removal of detector blemishes such as hot pixels or cosmic rays.

Zero Point

There can be a difference in how counts are measured due to a host of factors - these include the camera itself, the CCD and the CCD quantum efficiency, as well as factors from the night sky such as weather (clear/cloudy) and the airmass (i.e. altitude) to which the telescope is pointing. Therefore to calibrate a system to a standard magnitude system the zero point is used. The zero point in a photometric system is defined as the magnitude of an object that produces 1 count per second on the detector. Traditionally, Vega was used as the calibration star for the zero point magnitude in specific pass bands (U, B, and V), however now usually photometric standard stars are used, or an average of multiple stars for higher accuracy. Nowadays, as a result of surveys gathering more detailed information on stars, such as SDSS or Gaia (Gaia Collaboration et al., 2016), zero points can be produced with a 'local star sequence' which is created by an average from multiple stars

always in the field of view in the SN images, with their calibrated magnitudes found in catalogues such as Pan-STARSS (Chambers et al., 2016).

2.1.2 Photometry Pipeline

Many separate pipelines exist for converting raw photometry data to a calibrated light curve, often linked to specific telescopes, however, the below code was custom-written for Parrag et al. (2021), as presented in Chapter 3. Objects in a photometry image are dispersed in a manner that can be described by a Point Spread Function (PSF), which describes the response of a focused optical imaging system to a point source or point object. A PSF can be acceptably approximated as a 3D Gaussian (the three dimensions being x, y, and counts), which is generally found to produce a good fit. Therefore the total flux of an object can be calculated by integrating under this fitted function.

In this pipeline, the total flux is calculated from the pre-reduced data (bias and flat field subtracted) fitted with the Iteratively Subtracted PSF Photometry from PhotUtils (Bradley et al., 2020). The PSF fitting is confined to a 50-pixel-width square around the central SN coordinates. With an average Full Width at Half Maximum (FWHM) below 10 pixels, this size is assumed to safely include all the associated flux. Alternatives to the Gaussian PSF were also considered. Of the two main methods tested, one was an ePSF (effective PSF), which uses a custom PSF constructed from a selection of reference stars in the image. The other was aperture photometry, where two 2D Gaussians are fitted to the point source across x and y to determine the FWHM and therefore the extent of the object, and then all flux data in this radius is counted as belonging to the object, minus flux counted in a nearby empty patch of sky. Aperture photometry however is a simplification compared to PSF photometry which can be more precise, as aperture photometry assumes the object is perfectly symmetric in x and y. A Gaussian PSF was found to be the method where the scatter between adjacent points was minimized. The magnitude Mag is calculated as below (where ZP is the zero-point, $Counts$ the integrated flux, and $Exposure$ the exposure time of the image) (Smartt et al., 2015):

$$Mag = ZP - 2.5\,log(Counts/Exposure) \tag{2.1}$$

An additional added correction, the colour term ($Colour(Mag) \times Colourterm$), can increase the accuracy of this equation by considering the difference between the magnitude in different bands, depending on which band the image was taken with. Valid PSF fits are filtered by setting a threshold of 3σ variation from background flux and requiring no close stars which would suggest an unreliable fit. These constraints are optimized through variation and inspection of residuals. The uncertainty is obtained by combining in quadrature the uncertainty in the fit given by the PSF and the uncertainty in the image. The uncertainty in the image (based on Smartt et al. (2015) and Brennan & Fraser (2022)) is given by :

$$Error = \sqrt{\frac{Counts + Sky}{Gain} + Npix \times (Readnoise + Sky)} \tag{2.2}$$

Where Sky is the sky counts measured from an empty patch of sky over an area the size of the SN, calculated by finding the sigma-clipped mean in the environment surrounding the SN and multiplying by the number of pixels, $Npix$ in the above. $Gain$ and $Readnoise$ come from the header of each fits file and are related again to the specifics of the instrument. The equation below shows how this uncertainty in counts is converted to magnitude.

$$Error = \frac{2.5}{ln(10)} \sqrt{\frac{Error(Count)}{Count(Total)}} \tag{2.3}$$

This uncertainty is then combined in quadrature with the extinction and the colour uncertainties, which are taken as 0.03 and 0.011 respectively. These values are taken from Valenti et al. (2016) for one telescope and are carried over as an approximation for the others. Such an assumption might appear unreasonable, but it is indeed acceptable as these terms are a small contribution to the uncertainty budget, and these values are roughly representative (ranges are 0.02-0.09 for extinction, and 0.011-0.036 for the colour). The mean contribution to the total error from the extinction and colour uncertainties are measured for a sample of 84 images for SN 2019hcc to be 17.1$\pm$0.4%. Cosmic ray artifacts are removed using lacosmic (van Dokkum et al., 2012).

Images are taken in various wavelength bands and the colour term is a telescope-specific correction when calculating the zero-point. The reference stars are chosen based on a recorded magnitude in a star catalogue. To calculate the zero point, the magnitude of the reference stars in the specific band is checked in a catalogue, then the flux of the reference stars is also measured with a PSF fit, and the difference is used to calculate the zero point. The below equation is used, rearranged from 2.1:

$$ZP = Mag_{Stars} + 2.5\, log(Counts/Exposure) - Colour(Mag) \times Colourterm \tag{2.4}$$

The Zero Point calculation is achieved in the code by accessing the Pan-STARRS (Chambers et al., 2016) catalogue using Vizier (Ochsenbein et al., 2000) and selecting all available stars in a 5 arcmin radius around the SN coordinates (see Figure 3.1).

To improve the quality of the PSF fit, multiple images taken on the same night (when available) were (and can be in a general workflow) aligned and stacked using the SNOoPY (SuperNOva PhotometrY) package *.

Template subtraction is another stage to improve the quality of the magnitude calculation. This is where a galaxy reference image is taken after the SN has completely faded and is removed from

*SNOoPy is a package for SN photometry using PSF fitting and/or template subtraction developed by E. Cappellaro. A package description can be found at http://sngroup.oapd.inaf.it/ecsnoopy.html.

all images to subtract the galaxy contribution and allow the measured flux to be from the SN alone. Template subtraction for this code is as follows: host images (which could be combined using SNOoPY, excluding poorer images) and the flux of both the host image and each SN image are found using the PSF fitting method described above. Equation 2.4 is used to convert the host flux to what it would be if it had the same ZP and exposure of the SN image, then the fluxes are subtracted, and the uncertainties propagated.

Figure 2.1 displays the PSF fitting for a few example images. The first column displays the image data, whilst the second and third show the residual (PSF subtracted from the image) and PSF fit, respectively. As can be seen, the Gaussian PSF fit can produce relatively clean residual images, and recognises multiple sources.

2.2 Spectroscopy

2.2.1 Data Collection and Telescopes

A spectrograph is an instrument that separates light by its wavelengths and records this data. The addition of a grism (grating prism) to a CCD camera means only light of a chosen central wavelength passes through, and creates a dispersed spectrum centered on the object's location. Optical spectra in this work have been reduced where required using standard IRAF tasks and the PESSTO pipeline. After the preliminary removal of detector signatures which includes bias, overscan (only for the optical spectra), and flat field correction (as mentioned in Section 2.1.1), a 2D to 1D flux extraction is done by summing the data within the extraction aperture, along the dispersion axis. Below are the data reduction steps for spectra once this has been done:

- Wavelength Calibration: One-dimensional spectra are extracted from the CCD output across the dispersion axis, and the host galaxy contribution is subtracted using a polynomial fit. The wavelength is calibrated using the position of background sky-lines in the spectra, which are compared to lamp spectra (usually He-Ne, He-Ar, Hg-Cd lamps) obtained using the same instrumental configuration. From this, a relation between pixels and known lines of those lamps is made so that a conversion array can be created. The accuracy of the wavelength calibration is verified against the position of the background sky-lines in the spectra, and if the position is not correct the spectrum is manually adjusted with a rigid shift which is usually below 20 Å. This method allows the wavelength calibration with errors on the order of <2Å. Spectra can be taken with different wavelength coverages depending on the grism used, and for a full wavelength coverage in the optical region, these spectra can be combined using standard IRAF tasks.

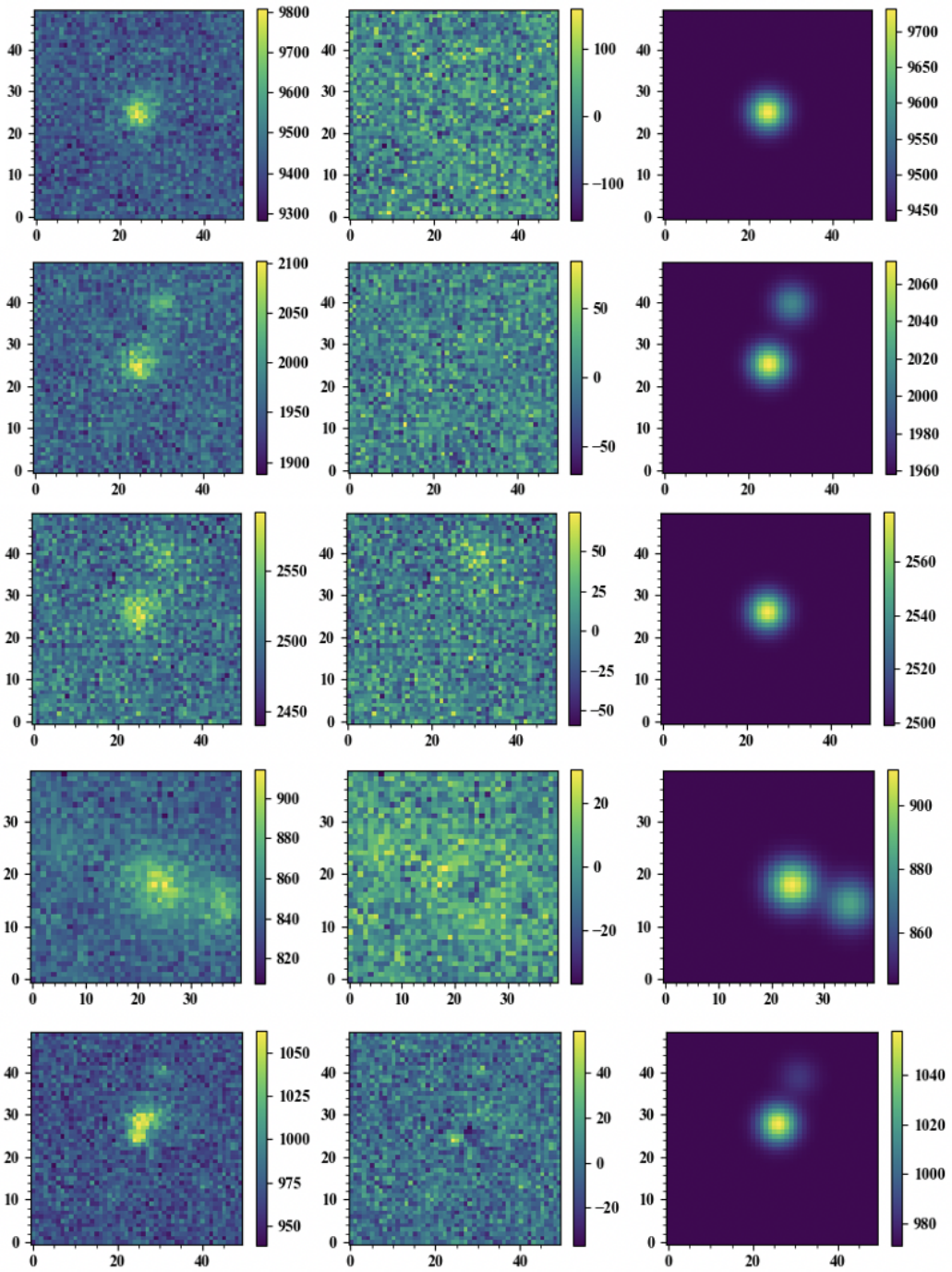

Figure 2.1. Demonstration of PSF fitting for sample image data from a single object, SN 2019hcc, at various stages of its evolution. Column 1: Image Data. Column 2: Residual, Column 3: PSF fit. Row 1: $i-$band, Row 2: $z-$band, Row 3: $z-$band, Row 4: Host galaxy image in $i-$band, Row 5: $r-$band. All images above were taken by the Liverpool Telescope (Steele et al., 2004). The images display the 50-by-50 pixel width square centred on the coordinates of SN 2019hcc, and the colourbar displays the counts as represented by the intensity.

- Flux calibration: Flux calibration of the spectra is done using standard stars, where the response curve of the instrumental configuration is obtained and compared to the tabulated flux for the star. Spectroscopic standard stars are taken from the lists of Oke (1990) and Hamuy et al. (1992, 1994). This flux calibration is typically accurate within 20%, with errors arising from poor photometric conditions, or an object not centered in the slit. The flux calibration from the spectra can also be checked against the photometry for the same target SN.

- Atmospheric Corrections: There are corrections that need to be made to the spectra due to Earth's atmosphere. The average extinction curves available for each site are used for atmospheric extinction correction. Broad telluric absorptions can sometimes contaminate spectra. Once again a standard star spectrum taken with the same instrumental configuration can be used, where the telluric lines are identified and removed, and can be correspondingly removed from the object spectrum. This is done by dividing the standard star spectrum by the same spectrum with the telluric removed, resulting in a spectrum that is one everywhere but the tellurics, and this can then be multiplied by the object spectrum to remove the telluric lines in the correct wavelength and the correct amount of contribution to flux.

  The same process can also be done with a telluric model such as that of Patat et al. (2011), where a radiative transfer model creates an atmospheric spectrum for H_2O and O_2, and this model spectrum is scaled so the intensities of the absorption matches those observed in a standard star (with an observation time which best matches the SN), which is then used to correct the SN spectra.

  The telluric correction is done automatically within the package iraf, which is how spectra were reduced throughout this thesis where required.

- Additional Corrections: Additional corrections when analysing spectra are to correct for the redshift of the host galaxy. This is generally founded by identifying the spectral lines of the host and estimating the expansion velocities. Other means of identifying the redshift could include SN identification software such as SNID (Blondin & Tonry, 2007), which matches a spectrum to a template library to provide an estimate of the redshift, and is used for fast automated classification. Correction is also necessary for interstellar extinction, and usually used here is the Cardelli extinction law Cardelli et al. (1989). We use this law for both Milky Way extinction and host galaxy extinction (when it is observed). When host galaxy extinction is not observed only the Milky Way extinction is used.

  Interstellar dust can produce three main effects: extinction, reddening, and attenuation. Dust grains scatter and absorb light, resulting in reddening (due to blue light/short wavelengths being preferentially scattered) and extinction (light lost through absorption along line of sight) - these effects can be described by the Cardelli extinction law. Attenuation also considers the

effects of the distribution of stars and dust in galaxies, and may include e.g. varying column densities/optical depths (e.g Cardelli et al., 1989; Calzetti, 2001; Salim & Narayanan, 2020).

Chapter 3

SN2019hcc: A Type II Supernova Displaying Early O II Lines

3.1 Introduction

Here I present the data and analysis of SN 2019hcc, which appears to show typical features of both SLSNe I and SN II at different stages in its evolution. This chapter is a reorganisation of a work which has been presented in Parrag et al. (2021) for which I was the main author.

The first spectrum appeared to contain a 'w' shape associated with O II lines near maximum, typical of SLSNe I (e.g. Quimby et al., 2011; Inserra, 2019). However, subsequent spectra identify SN 2019hcc as a moderately bright Type II supernova, similar to those discussed in Inserra et al. (2013a), due to the presence of Balmer lines. This is the first such object (to our knowledge) to be identified in the literature. Studying this object could allow further insight into open questions of transitional events as this object initially appears to be a SLSNe I, however its evolution and later spectra appear typical of SNe II. This chapter will demonstrate the typical analysis of a SN, consider the properties of both SLSNe I and SNe II, and examine potential mechanisms for this behaviour through comparisons of both the light curves and the spectra.

3.2 Observations and Data Reduction

SN 2019hcc was discovered by the *Gaia* satellite (Gaia Collaboration et al., 2016) as Gaia19cdu on MJD 58640 (Delgado et al., 2019), and subsequently by the Asteroid Terrestrial-impact Last Alert System (ATLAS; Tonry et al., 2018a; Smith et al., 2020) on MJD 58643 as ATLAS19mgw (Frohmaier et al., 2019). The first spectrum was taken on MJD 58643, 3 days after discovery and 7 days after the photometric maximum, see Section 3.5. It was then classified on MJD 58643 as a

SLSN I (Swann et al., 2019) as a consequence of the 'w'-shaped absorption feature around 4000 Å. The redshift was found to be z = 0.044 based on the Doppler shift from rest wavelength of the host galaxy emission lines as visible from the second spectrum (identified as strong narrow lines), and then confirmed by the host galaxy spectrum taken at the end of the SN campaign. We assume a flat ΛCDM universe with a Hubble constant of H_0 = 70 km s^{-1}Mpc^{-1} and Ω_m = 0.3 and hence a luminosity distance of 194.8 Mpc.

However, the second spectrum taken on MJD 58655 showed a prominent Hα profile implying the target was not a SLSN I, but rather a bright Type II. It had equatorial coordinates of RA: 21:00:20.930, DEC: -21:20:36.06, with the most likely host J210020.73-212037.2 in the WISEA catalogue at M_r = 19.3 mag (Cutri et al., 2013), since the redshift of this host and that of SN 2019hcc are matched. The Milky Way extinction was taken from the all-sky Galactic dust-extinction survey (Schlafly & Finkbeiner, 2011) as Av = 0.19. Taking Rv = 3.1 (relative visibility), this gives an E(B-V) of 0.06 (measure of excess colour, or reddening). The width of Na I D absorption lines in the host have been correlated with reddening (Poznanski et al., 2012). However, since there are no Na I D absorption lines related to the host, and the SN luminosity and colour evolution appear to be as expected in a SN II (see Section 3.5), the host galaxy reddening has been assumed negligible.

Figure 3.1 shows the finder chart which identifies SN 2019hcc and its local environment.

3.3 Photometry

3.3.1 Data Reduction

Five optical spectra were taken for SN 2019hcc over a range of 5 months with the NTT+EFOSC2 at the La Silla Observatory, Chile. This was under the advanced Public ESO Spectroscopic Survey of Transient Objects programme (ePESSTO+; Smartt et al., 2015). This was alongside a host galaxy spectrum taken over a year after explosion when SN 2019hcc was no longer visible. The spectra were reduced using the PESSTO NTT pipeline*. There was also one spectrum taken by the Goodman High Throughput Spectrograph at the Southern Astrophysical Research telescope (SOAR) (Clemens et al., 2004), reduced using the dedicated pipeline (Sánchez-Sáez et al., 2019).

3.3.2 Photometry for SN 2019hcc

Photometric data was obtained by the Las Cumbres Observatory (LCO; Brown et al., 2011) with the camera Sinistro built for the 1m-class LCO telescopes, and by the Liverpool Telescope (LT;

*https://github.com/svalenti/pessto

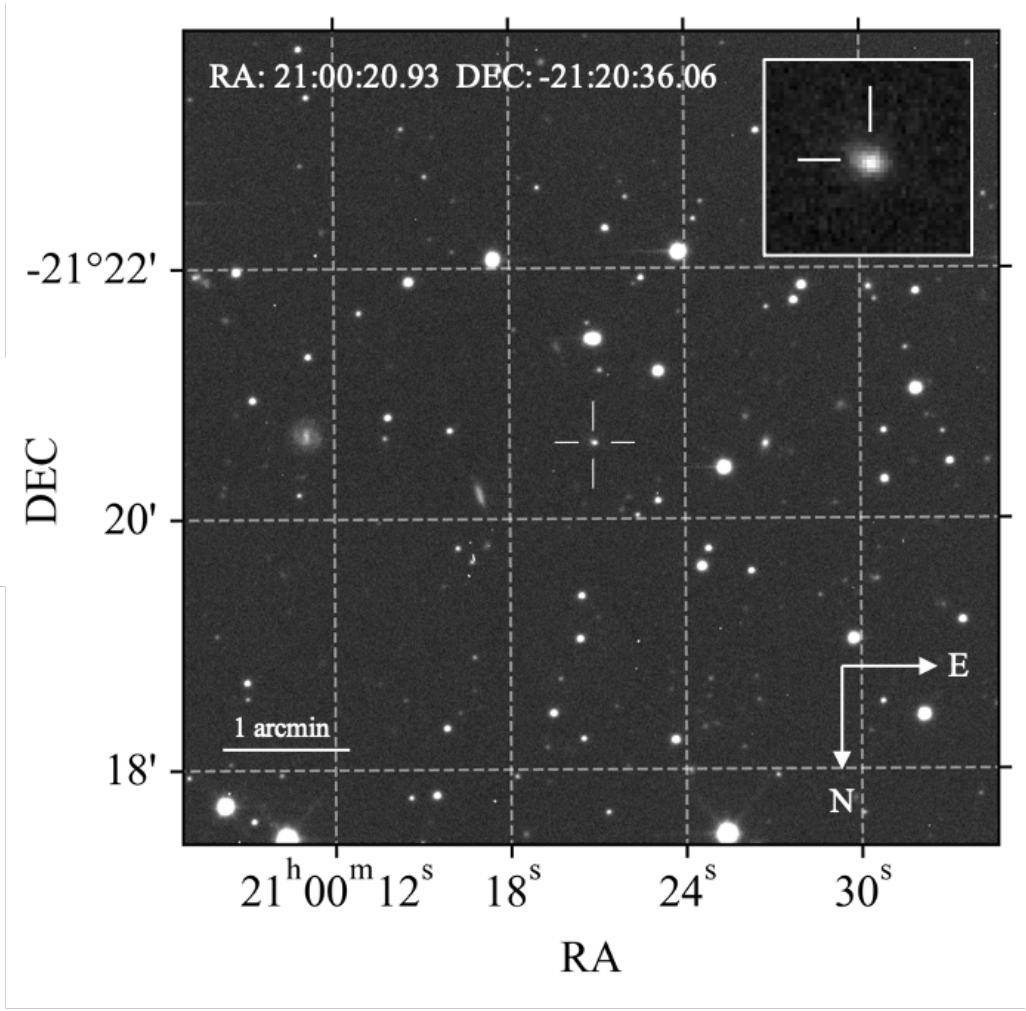

Figure 3.1. The finder chart for SN 2019hcc displaying the local environment, taken in $r-$band at MJD = 58660 by LCO. The host is a low luminosity galaxy. SN 2019hcc is marked by the white crosshairs, and in the blow-up image in the top-right corner.

Steele et al., 2004) on the Canary Islands. Dithered images were combined using SNOoPY [†] and the magnitudes were retrieved using PSF photometry, with the zero-point calibration completed using reference stars accessed from the Panoramic Survey Telescope and Rapid Response System (Pan-STARRS; Chambers et al., 2016) and the Vizier catalogues (Ochsenbein et al., 2000). This was performed using the code described in detail in Chapter 2. Additional photometry was also taken by ATLAS, *Swift* + Ultraviolet/Optical Telescope (UVOT; Roming et al., 2005) and the Gamma-Ray Burst Optical and Near-Infrared Detector (GROND; Greiner et al., 2008). GROND is an imaging instrument to investigate Gamma-Ray Burst Afterglows and other transients simultaneously in seven bands $grizJHK$ mounted at the 2.2 m MPG telescope at the ESO La Silla Observatory (Chile). The GROND images of SN 2019hcc were taken under the GREAT survey (Chen et al., 2018). GROND (Krühler et al., 2008), ATLAS and *Swift* data were reduced using their own pipelines. The photometry and spectroscopy logs, including dates, configurations, and magnitudes are reported in the Appendix. As *Swift* observes simultaneously with UVOT and the X-ray Telescope (XRT), we report that the corresponding upper limit on the unabsorbed 0.3-10 keV flux is 2.6x10^{-14} cgs (assuming a power law with photon index 2 and the Galactic column density of 4.9x10^{20} cm^{-2}) resulting in an upper limit on luminosity of $\sim$10^{41} erg/s at SN 2019hcc distance. The closest non-detections were taken by ATLAS from 34 days to 22 days before discovery, with a confidence of 3σ. Non-detections are taken in regular surveying of the sky and help to constraint the explosion date as they provide a lower limit on when the SN was not yet present.

3.4 Host Galaxy

Examining the host galaxy can provide insight into the environment of SN 2019hcc, and can be compared to the typical environments of both SNe II and SLSNe I. The host galaxy spectrum for SN 2019hcc was taken with NTT+EFOSC2 (Buzzoni et al., 1984) at the La Silla Observatory, Chile, on MJD 59149, when the SN was no longer visible, as part of the ePESSTO+ programme (Smartt et al., 2015). The line fluxes were measured using the splot function in iraf (Tody, 1986) by taking a number of measurements and averaging to account for the uncertainty in the location of the continuum.

Useful analysis of the host galaxy would be to consider, among other things, mass, age, and metallicity. Metallicity is the abundance of elements present in an object that are heavier than hydrogen and helium. These properties are useful as they can be compared to the typical hosts for different SN types - as different types of SNe have shown preferences for different environments. The host galaxy spectrum was analysed for metallicity using pyMCZ. This is an open-source Python code

[†]SNOoPy is a package for SN photometry using PSF fitting and/or template subtraction developed by E. Cappellaro. A package description can be found at http://sngroup.oapd.inaf.it/snoopy.html

which determines a metallicity indicator, Oxygen abundance (ratio of the abundance of Oxygen to Hydrogen), given as 12 + log(O/H), through Monte Carlo sampling, and gives a statistical confidence region (Bianco et al., 2016). The input of this code is the line flux and associated uncertainties for lines such as [O II] and Hα from the host galaxy spectrum. Kewley & Ellison (2008) found that the choice of metallicity calibration has a significant effect on the shape and y-intercept (12+log(O/H)) of the mass-metallicity relation, therefore multiple markers are used to measure the metallicity in an effort to give a representative range.

Figure 3.2 shows the input (upper panel) and output (lower panel) for pyMCZ (see Bianco et al., 2016). The metallicity estimators are those of Zaritsky et al. (1994) [Z94], McGaugh (1991) [M91], Maiolino et al. (2008) [M08], and Kewley & Ellison (2008) [KK04]. These metallicity markers are all based on R_{23}, see Bianco et al. (2016) for a summary and further details:

$$R_{23} = \frac{[\text{O II}]\lambda 3727 + [\text{O III}]\lambda\lambda 4959, 5007}{H\beta} \tag{3.1}$$

[N II] λ6584 is not visible in this spectrum, and at this resolution it would be very difficult to resolve as it is so close to Hα. A lack of [N II] is an indicator of low metallicity, therefore the lower branches of the metallicity indicators were used in the code, apart from Z94, where only the upper branch is available in pyMCZ. The metallicity markers used are those available given the line fluxes which were input into pyMCZ, which are labelled in the top panel of Figure 3.2. Averaging them we obtain a host galaxy metallicity of 12 + log(O/H) $= 8.08 \pm 0.05$, which is below solar abundance. Z94 is most likely incorrect as the upper branch value is output from pyMCZ, and therefore is excluded from this average. It is nevertheless included in Figure 3.2 to indicate an upper limit.

We also note that the Hα/Hβ flux ratio in the host spectrum is measured to be 2.2 $\pm$ 0.1, less than the intrinsic ratio 2.85 for case B recombination at T = 10^4 K and $n_e \sim 10^2 - 10^4$ cm^{-3} (Osterbrock, 1989). A ratio of less than 2.85 can result from an intrinsically low reddening combined with errors in the stellar absorption correction and/or errors in the line flux calibration and measurement (Kewley & Ellison, 2008).

Models by Dessart et al. (2014) hint to a lack of SNe II below 0.4 $Z_\odot$, where $Z_\odot$ is the solar mass fraction of all elements heavier than Hydrogen and Helium. However, this may be biased as higher luminosity hosts were used which tend to have higher metallicity.

The mass fraction of heavy elements Z can to be converted to the oxygen abundance 12+log(O/H) in a simplified way (Chruslinska & Nelemans, 2019): log($Z/Z_\odot$) = $Z_{O/H}$ - $Z_{O/H\odot}$. Assuming a solar abundance of 8.69 (Asplund et al., 2009), the value $Z/Z_\odot$ = 0.4 would approximately correspond to 12+log(O/H)= 8.29. This is higher than all the metallicity markers except Z94 for SN 2019hcc.

On the other hand, SLSNe I are predominantly found in dwarf galaxies, indicating that their progenitors have a low metallicity. A 0.5 $Z_\odot$ threshold has been suggested for the formation of SLSNe I (Chen et al., 2017d). Lunnan et al. (2014) found a median 12+log(O/H) metallicity of

8.35 = 0.45 $Z_\odot$ for a sample of 31 SLSNe I, which is higher than the mean metallicity measured for SN 2019hcc. Therefore it can be concluded that SN 2019hcc has a low metallicity host.

The measured metallicity was compared to both Type II and SLSN I hosts. Table 3.1 contains the mean metallicity excluding Z94 (as Z94 is likely incorrect as it is the upper branch) from Figure 3.2, compared to averages for SLSNe I and SNe II. Schulze et al. (2021) performed a comprehensive analysis of SN hosts based on a sample of 888 SNe of 12 distinct classes, and found a median metallicity 12 + log(O/H) $= 8.26^{+0.26}_{-0.30}$ for a sample of 37 SLSNe I. Galbany et al. (2018) presented a compilation of 232 SN host galaxies, of which 95 were Type II hosts with an average metallicity (12 + log(O/H)) of 8.54 $\pm$ 0.04. The mean metallicity for SN 2019hcc is within the range of the SLSN I host metallicity found by Schulze et al. (2021), and is low compared to the average metallicity of Type II hosts.

The host galaxy absolute magnitude was measured to be -15.8 ± 0.3 in $r-$band and -15.8 ± 0.2 in $B-$band. Gutiérrez et al. (2018) defined a faint host as having $M_r \gtrsim -18.5$ mag, and analysed the hosts of a sample of low-luminosity SNe II, finding a mean host luminosity of -16.42 ± 0.39 mag. Anderson et al. (2016) examined a sample of SNe II in a variety of host types and found a mean host luminosity M_r of -20.26 ± 0.14 mag. For SLSNe I, Lunnan et al. (2014) found a low average magnitude ($M_B \approx -17.3$ mag). Table 3.1 also contains the average M_B magnitudes for both SLSNe I and SNe II from Schulze et al. (2021). SN 2019hcc has a lower luminosity and metallicity host with respect to the average value for SNe II and SLSNe I reported in the literature (see Table 3.1).

We retrieved further SN 2019hcc host galaxy properties by modelling the spectral energy distribution (SED) over wavelength using the software package Prospector version 0.3 (Leja et al., 2017; Johnson et al., 2019). An underlying physical model is generated using the Flexible Stellar Population Synthesis (FSPS) code (Conroy et al., 2009). A Chabrier initial mass function (Chabrier, 2003) is assumed and the star formation history (SFH) is approximated by a linearly increasing SFH at early times followed by an exponential decline at late times (functional form $t \times \exp(-t/\tau)$). The model was attenuated with the Calzetti et al. (2000) mode, and a dynamic nested sampling package density (Speagle, 2020) was used to sample the posterior probability function. To interface with FSPS in python, python-fsps (Foreman-Mackey et al., 2014) was used. Note that the Calzetti dust law assumes a universal dust model which leads to biases in derived galaxy properties, as well as generally providing a poorer fit to the UV (Kriek & Conroy, 2013). Additionally, variations in dust/star geometry can introduce a large scatter, and intermediate redshift galaxies ($z \sim 1-3$) appear to be more heavily attenuated by dust meaning a larger fraction of the star formation is obscured, also leading to imprecise derived galaxy properties (Battisti et al., 2016) - though this should not affect SN 2019hcc as it only has a redshift of 0.044.

The photometry images were sourced from the Panoramic Survey Telescope and Rapid Response System (Pan-STARRS, PS1) Data Release 1 (Chambers et al., 2016), the *Galaxy Evolution Explorer* (GALEX) general release 6/7 (Martin et al., 2005), the ESO VISTA Hemisphere Survey (McMahon

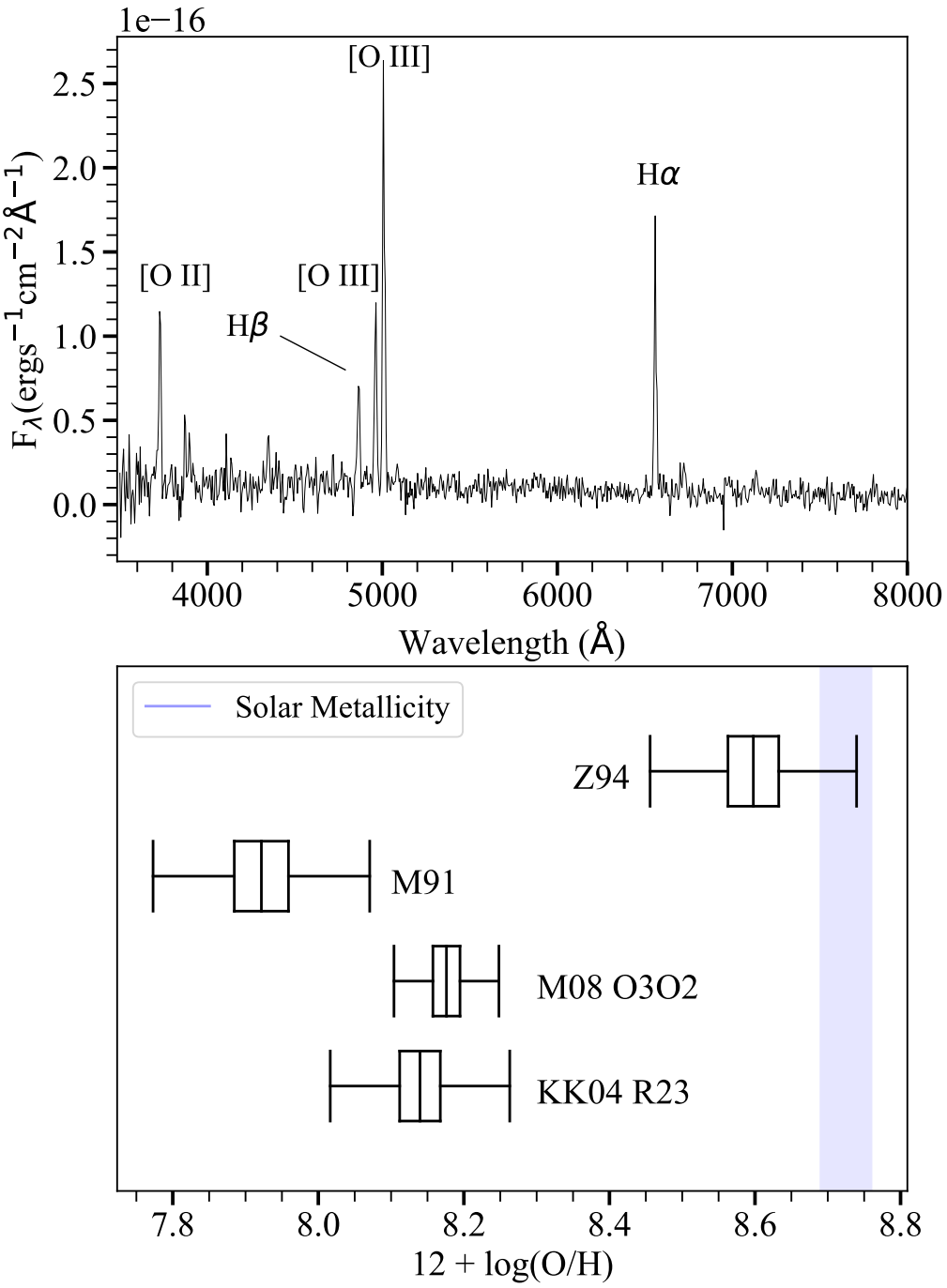

Figure 3.2. Top panel: NTT galaxy spectrum used as input for pyMCZ, with the relevant lines labelled. The Hα/Hβ ratio is 2.2 ± 0.1. The wavelength is in the rest frame. Bottom panel: Reproduced output of pyMCZ, the metallicity measured via several markers is displayed as box plots. The central value is the median (or 50$^{\text{th}}$ percentile). The inner box represents the inter-quartile range (IQR) - 50$^{\text{th}}$ to 16$^{\text{th}}$ percentile and 84$^{\text{th}}$ to 50$^{\text{th}}$ percentile (the 16% is an analogy to the Gaussian 1σ interval), whilst the outer bars represent the minimum and maximum data values, excluding outliers. The outliers are those values further than 1.5xIQR from the edges of the IQR. The blue band is a range of solar metallicity values found in literature - from 8.69 in Asplund et al. (2009) to 8.76 in Caffau et al. (2011).

Property	SN 2019hcc	SLSN I	SN II
log(M/M$_\odot$)	$7.95^{+0.10}_{-0.33}$	$8.15^{+0.23}_{-0.24}$	9.65±0.05
SFR (M$_\odot$yr^{-1})	$0.07^{+0.04}_{-0.01}$	$0.59^{+0.22}_{-0.20}$	0.58±0.05
log(sSFR) (yr^{-1})	$-9.10^{+1.42}_{-1.78}$	$-8.34^{+0.30}_{-0.32}$	−9.86±0.02
Age (Myr)	2971^{+2079}_{-2131}	427^{+119}_{-124}	4074±188
E(B-V)	$0.04^{+0.06}_{-0.03}$	$0.31^{+0.05}_{-0.04}$	0.14±0.01
12+log(O/H)	8.08±0.05	$8.26^{+0.26}_{-0.30}$	8.54±0.04
M_B (mag)	-15.80 ± 0.20	$-17.51^{+0.30}_{-0.28}$	-19.15 ± 0.09

Table 3.1. Galaxy properties from Prospector for SN 2019hcc, and median values from Schulze et al. (2021) for SLSNe I and SNe II, excluding 12+log(O/H) for Type II which is from Galbany et al. (2018).

et al., 2013), and preprocessed WISE images (Wright et al., 2010) from the unWISE archive (Lang, 2014)[‡]. The unWISE images are based on the public WISE data and include images from the ongoing NEOWISE-Reactivation mission R3 (Mainzer et al., 2014; Meisner et al., 2017). The host brightness was measured using LAMBDAR[§] (Lambda Adaptive Multi-Band Deblending Algorithm in R; Wright et al., 2016) and the methods described in Schulze et al. (2021).

Figure 3.3 shows the best fit SED to the SN 2019hcc photometry for filters GALEX FUV (20.69±0.30 mag) and NUV (20.48±0.14 mag), PS1 $GIRYZ$ (19.86±0.03 mag, 19.76±0.04 mag, 19.76±0.04 mag, 19.74±0.17 mag, 20.02±0.14 mag), VHS JK (20.08±0.08 mag, 19.99±0.16 mag) and WISE $W1$ (20.58±0.42 mag) and $W2$ (21.05±0.40 mag). The magnitudes are in the AB system and corrected for Milky Way extinction. Table 3.1 shows the galaxies properties inferred from the best-fit SED to the host galaxy photometry. The E(B-V) inferred for SN 2019hcc matches well with the E(B-V) based on the Milky Way extinction. The mass of the host best matches the median SLSN I host mass, whilst the Star Formation Rate (SFR) is low for both SLNSe I and SNe II. The age of the SN 2019hcc host has a large uncertainty that covers the range of both classes, and the magnitude is low for both classes. The SFR is significantly lower for SN 2019hcc. However, the mass of the host is lower than the median for both SLSNe I and SNe II, and therefore the specific SFR (sSFR) falls between the two.

3.5 Photometry Analysis

3.5.1 Rise time and Explosion Epoch

Rise time is useful to consider as this is strongly dependant on the properties of the progenitor. To measure the rise time the explosion epoch needs to be determined, which can be difficult as the

[‡]http://unwise.me

[§]https://github.com/AngusWright/LAMBDAR

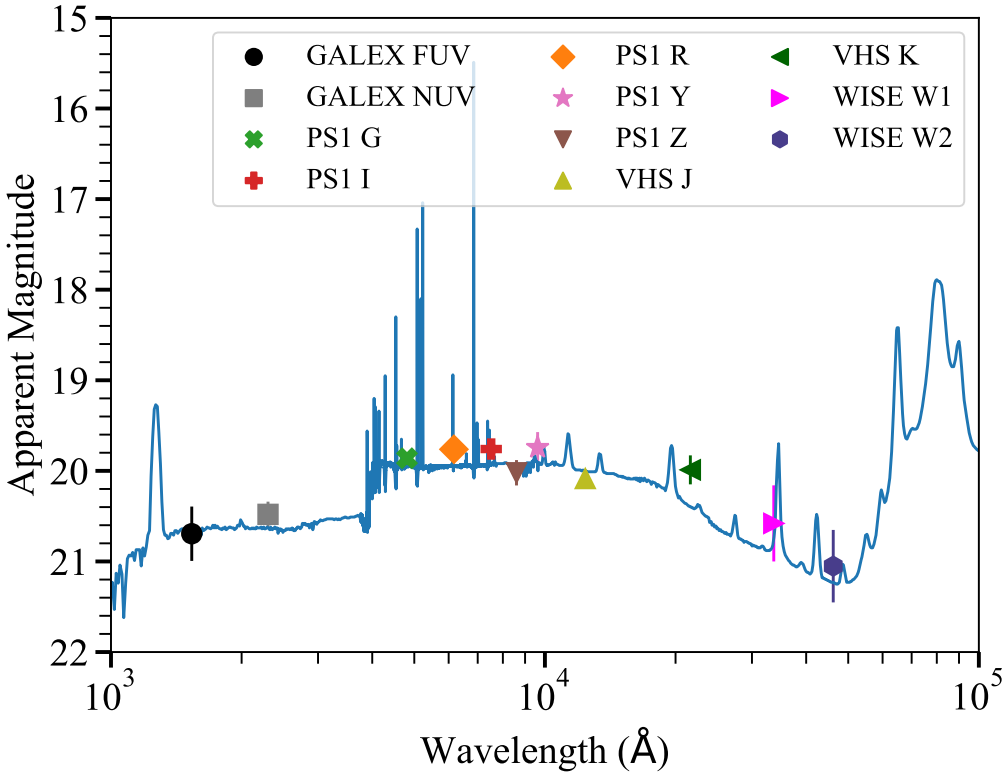

Figure 3.3. Galaxy photometry of SN 2019hcc from GALEX, PS1, VHS and WISE, with the best fit SED from Prospector, The median χ^2 divided by the number of filters (n.o.f.) is 10.65/11 and includes emission lines from H II regions in the fitting.

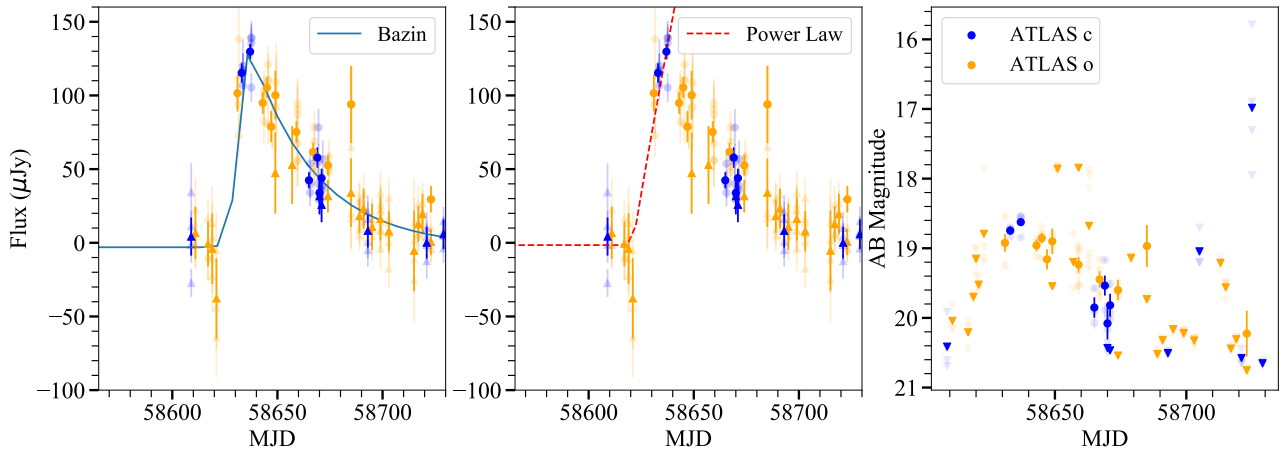

Figure 3.4. Left panel: fit to the ATLAS forced photometry weighted mean flux (Bazin et al., 2009), in order to determine the peak epoch. This finds the maximum epoch to be MJD 58636.2 ± 2.2. Points with errors $> 30\mu$Jy have been removed for clarity. Middle panel: a power law fit to the pre-peak flux data (including the upper limits) - this finds an explosion epoch of MJD 58621.0 ± 7.2. Upper limits are marked as triangles. Where multiple points from the same epoch were taken, these were averaged - the original points are marked with a lighter hue. Right panel: ATLAS forced photometry weighted mean flux converted to AB magnitude, for orange and cyan filters. Images with flux significance $< 3\sigma$ were converted to upper limits.

exact moment of explosion is rarely captured. However, non-detection measurements combined with the start of the light curve can be fitted to try and infer this date.

We determined the rise time and explosion epoch following the methodology presented in González-Gaitán et al. (2015). We applied this approach to the ATLAS data only, both orange and cyan bands, as it is the only photometry available which covers the pre-peak light curve albeit with many upper limits. Upper limits provide an upper limit on the flux rather than an exact measurement. It is not ideal to combine different bands however as there are few points it is an unavoidable uncertainty. We then measure the explosion epoch using a power law fit (Equation 3.2) to the start of the light curve ranging from the earliest pre-peak upper limit to maximum luminosity, with all the pre-peak upper limits/non-detections included in the fit to better constrain the beginning of the rise. The equation for the power law fit is as below:

$$\begin{aligned} f(t) = a(t - t_{\rm exp})^n \text{ if } t > t_{\rm exp} \\ f(t) = 0 \text{ if } t < t_{\rm exp}\,. \end{aligned} \tag{3.2}$$

Here a is a constant and n is the power index, both of which are free parameters, and $t_{\rm exp}$ is the explosion date in days. This fit was done using a least squares fit as implemented by scipy.curve_fit in Python to the pre-maximum light curve in flux, and the explosion epoch was measured to be

MJD 58621.0 ± 7.2. An alternative method of measuring the explosion epoch is to take the midpoint between the first non-detection and the first detection - this would be between MJD 58609 and MJD 58631, giving an estimate of the explosion epoch of MJD 58620, which is within the errors and consistent with the previous measurement.

For the epoch of maximum light, we used the phenomenological equation for light curves from Bazin et al. (2009). This form, as shown in Equation 3.3, has no physical motivation but rather is flexible enough to fit the shape of the majority of supernova light curves.

$$f(t) = A\frac{e^{-(t-t_0)/t_{\rm fall}}}{1+e^{(t-t_0)/t_{\rm rise}}} + B\,. \tag{3.3}$$

Here t_0, $t_{\rm rise}$, $t_{\rm fall}$, A and B are free parameters. The derivative, as seen in Equation 3.4, was used to get the maximum epoch ($t_{\rm max}$), and the uncertainties from the fit were propagated through the below equation (González-Gaitán et al., 2015):

$$t_{\rm max} = t_0 + t_{\rm rise} \times log(\frac{-t_{\rm rise}}{t_{\rm rise}+t_{\rm fall}})\,. \tag{3.4}$$

The maximum epoch was found from the Bazin fit to be MJD 58636.2 ± 2.2 - this was done by fitting to the flux data, see the right panel on Figure 3.4. This will be the maximum hereafter referred to in the paper, and can be approximated as the peak in ATLAS $o-$band, as this is the band the majority of these points are in. Points with an error greater than 30 μJy have been removed for clarity. Combining this result with the explosion epoch gives a rise time of 15.2 ± 7.5 days.

ATLAS $o-$band is close to $R-$band. The average $R-$band rise from the 'gold' samples (consisting of 48 and 38 SNe each from different surveys) of SNe II from González-Gaitán et al. (2015) was $14.0^{+19.4}_{-9.8}$ days. Pessi et al. (2019) reported an average $r-$band rise time for a sample of 73 SNe II of 16.0 ± 3.6 days. Both results are consistent with our measured value - therefore it seems the rise of SN 2019hcc is typical for a SN II. In contrast, SLSNe I light-curves have longer timescales with an average rise of 28 and 52 days for SLSNe I Fast and Slow respectively (Nicholl et al., 2015a; Inserra, 2019). Despite the average longer rise of SLSNe I to SNe II, it should be noted that the fastest riser SLSNe I can have some overlap within the errors of the slowest SNe II values from González-Gaitán et al. (2015).

3.5.2 Multi-band light curve

The majority of photometric data were taken by LCO in bands $BVgri$, and by LT in bands $griz$. The light curve produced from this data was created using a code written using Python packages AstroPy and PhotUtils (see Chapter 2 for further detail). This was complemented by ATLAS data in the orange and cyan bands, UV data from *Swift*, optical ($griz$) and NIR (JHK) data from GROND. Figure 3.5 shows the photometric evolution of SN 2019hcc in all available bands. The UV data

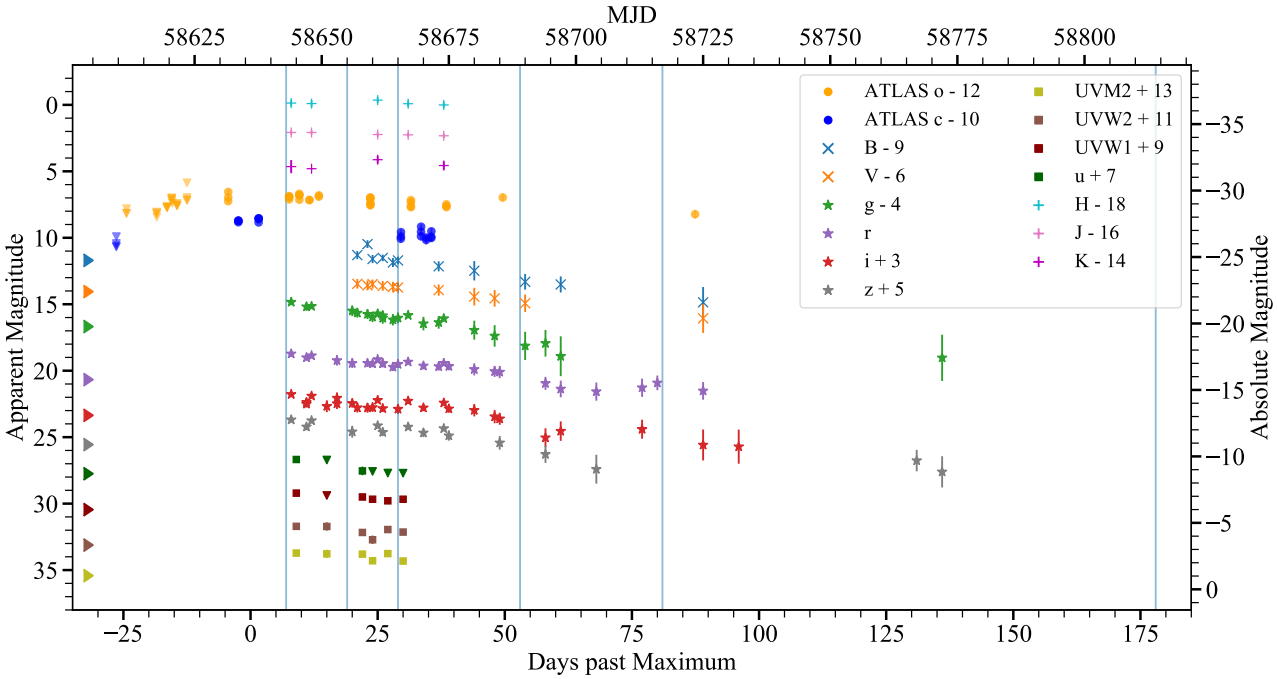

Figure 3.5. Photometry for SN 2019hcc - the light curves from various sources: $BVgri$, bands were taken by LCO, and $griz$ bands were also taken by LT. Alongside this, there is ATLAS data including the pre-peak limits, *Swift* UV data, and GROND NIR data. The vertical lines mark the epochs when the spectra were taken. The markers on the left y-axis signify the galaxy magnitude in the respective bands.

covers 21 days, and appears to follow a linear decline. The NIR data covers a similar period of 30 days, and are roughly constant in magnitude. There is a linear decline of ∼50 days from peak in all optical bands, with a magnitude change of ∼1.5 mag in $r-$band, followed by a steeper drop of ∼2 mag from 50 to 70 days. The decline rate is similar in the other bands with the exception of $g-$band which declines faster, at a rate of ∼2 mag in the first ∼50 day after maximum light, and subsequently ∼3 mag in the steeper decline. The $BV-$bands data for *Swift* were excluded as they were contaminated by host galaxy light. Such a contamination is far less in u, $uvw1$, $uvm2$ and $uvw2$. The *Swift* detections were at level of 3-4 σ. GROND $griz$ magnitudes were not template subtracted as there were no templates available. However, the data were taken soon after maximum light, where the difference between the host galaxy magnitude and that of SN 2019hcc is at its maximum, and therefore should not add significant uncertainty. LT and LCO magnitudes were template subtracted as part of the photometry code described in Chapter 2.

Figure 3.6 shows the evolution of the blackbody temperature fit to the photometric data together with the $B-V$ colour evolution, both for SN 2019hcc and a selection of SNe II. As mentioned in Chapter 1, when the SN is in the photospheric phase it can be approximated by a blackbody and the continuum of the spectrum can be fit with a blackbody curve. However, the flux across wavelength can also be measured from the photometry when sufficient bands are taken - the magnitude in each band can be converted to flux using $Flux = Ref \times 10^{-0.4 \times Mag}$(where Ref is the reference flux, a value specific to each band), and plotted against the central wavelength of each band, and this can also be fitted with a blackbody curve. Measuring the temperature evolution of the SN can be a useful metric to compare to both SNe II and SLSNe I to see which SN type better matches the behaviour seen. The colour evolution is another such measure which can be used for comparison. Here $B-V$ is shown.

The SNe II used for comparison are: SN 2013ej (Valenti et al., 2014), SN 2014G (Terreran et al., 2016), SN 2008fq (Taddia et al., 2013), SN 1998S (Fassia et al., 2000, 2001), SN 2009dd and SN 2010aj (Inserra et al., 2013a) together with a sample of 34 SNe II from Faran et al. (2014). SNe 1998S and 2014G - a Type IIn and IIL, respectively - were chosen for their spectroscopic similarity to SN 2019hcc near peak. SN 2013ej, SN 2010aj, and SN 2008fq provide a small sample of well observed SNe II displaying a similar peak magnitude of SN 2019hcc, which fall in the category of relatively bright Type II (Inserra et al., 2013a). The $griz$ bands for SN 2019hcc were individually interpolated to 10 evenly spaced points across the date range, and the temperature was found by fitting to these bands at each point. The interpolation was done using gaussian processes from sklearn, and the errors from the photometric points were interpolated using interp1d from scipy. For the colour the points were chosen where both B and V were available. The fits for temperature are expected to become worse as the photospheric phase passes and the blackbody approximation is less appropriate. The temperature and colour evolution for the Type II supernovae were taken from the above papers. The temperature and colour evolution of the SNe II sample (Faran et al.,

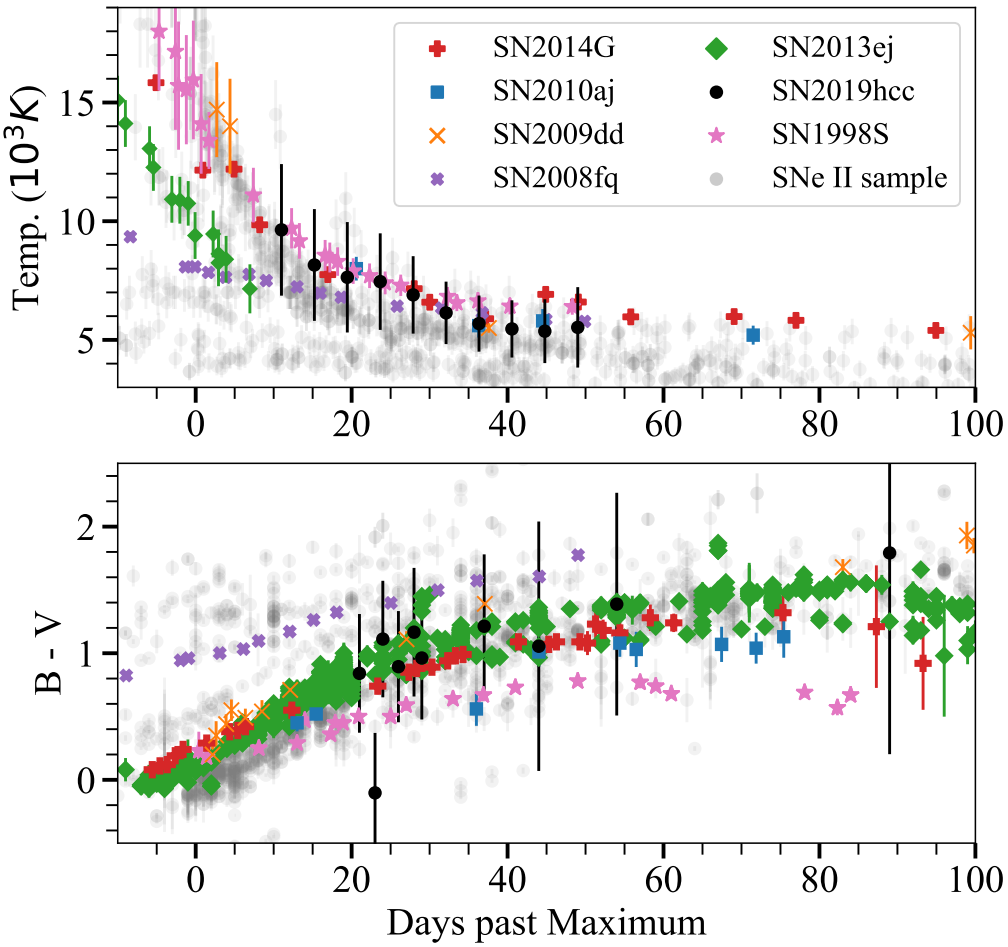

Figure 3.6. Top panel: the blackbody temperature evolution - for SN 2019hcc this is from the fit to the photometric data, whilst for the other SNe it is from the literature. The uncertainties for SN 2019hcc are from the curve fit. There were no uncertainties reported in the literature for the temperatures of SN 2014G and SN 2008fq. Bottom panel: colour evolution $B - V$ compared with the same SNe of the upper panel.The temperature and colour evolution from the sample of SNe II from Faran et al. (2014) is shown in grey.

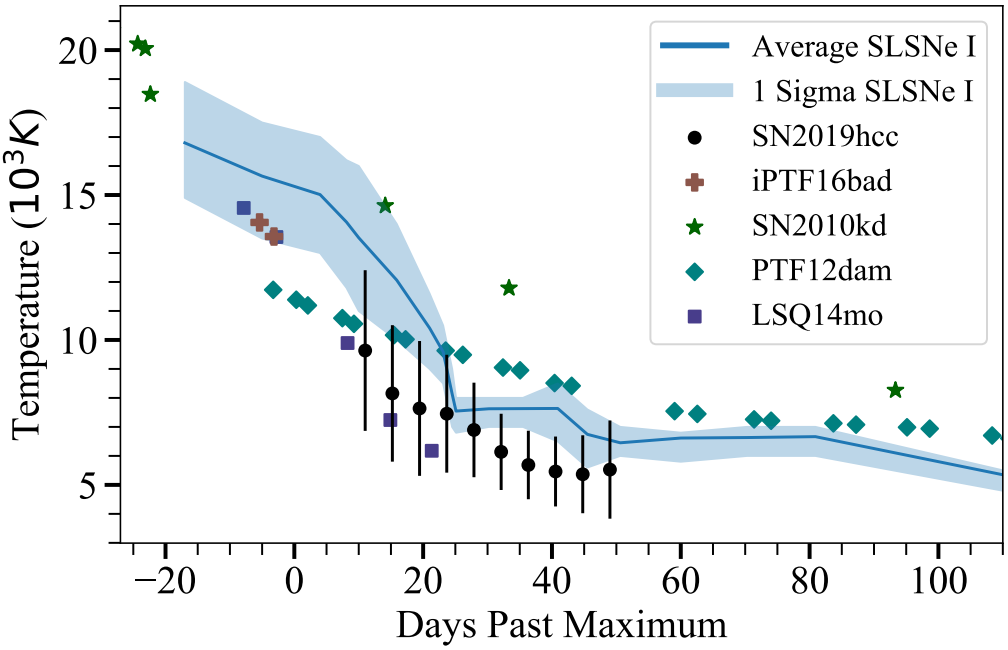

Figure 3.7. Temperature comparison of SN 2019hcc with a small sample of SLSNe I. The closest SLSN I in temperature to SN 2019hcc at the epoch of +7 days is LSQ14mo. The SLSN temperatures are taken from the literature (see text). The average temperature for SLSNe I is taken from Inserra et al. (2017) and reference therein.

2014) were calculated from the data available on the Open Supernova Catalogue (Guillochon et al., 2017). These SNe have a large range within which the temperature evolution falls, and appears to have multiple branches, which spans the range of temperature and colour evolution of the SNe II selected for a direct comparison. From Figure 3.6, it appears the colour and temperature evolution of SN 2019hcc is not unusual with respect to the SNe chosen for a direct comparison or that of Faran et al. (2014). Overall, SN 2019hcc colour and temperature evolution appears to closely resemble those of SN 2014G and SN 2009dd. The colour evolution appears to have two regimes, a steeper slope until ∼30-40 days followed by a less steep rise. The first slope is 2.8 mag per 100 days which is very similar to the average 2.81 mag per 100 days obtained by de Jaeger et al. (2018) for $B - V$. They also found a transition between the two regimes at 37.7 days which is roughly consistent with what is seen in the colour evolution.

In Figure 3.7 the temperature evolution of SN 2019hcc is also compared with a sample of SLSNe I: iPTF16bad (Yan et al., 2017b), SN 2010kd (Kumar et al., 2020), PTF12dam (Nicholl et al., 2013), and LSQ14mo (Chen et al., 2017b; Leloudas et al., 2015b). We selected this small subset of SLSNe I mainly due to the spectral similarity, see Section 3.7 for further information. We also compare to an average temperature evolution for SLSNe I (Inserra et al., 2017, and reference therein), similarly to what was previously done with SNe II. LSQ14mo is the only SLSNe I with a similar temperature evolution to SN 2019hcc.

3.5.3 Bolometric light curve

A bolometric light curve displays the total luminosity of a SN, in order to more fundamentally relate to the physics of the explosion, and hence would require an integration over all wavelengths. However in practice a 'pseudo-bolometric' curve is measured, which uses only near-UV, optical and near-infrared (UVOIR), a region which covers the peak of a blackbody at temperatures on the order of what is observed in most SNe Branch & Wheeler (2017).

We created a pseudo-bolometric light curve from an SED fit to the available photometry, which was interpolated according to the chosen reference band. We used the SDSS $r-$band and the ATLAS $o-$band as reference, as these bands should approximately cover a similar region of the electromagnetic spectrum, to cover as many epochs as possible. Each band was integrated using the trapezium rule. The redshift, distance, and reddening used were reported in Section 3.2.

The light curve evolution of SNe II was considered quantitatively by Anderson et al. (2014b) and Valenti et al. (2016). The decline of the initial steeper slope of a light curve and the second shallower slope can be described as S1 and S2 respectively - in SNe IIL (a subtype of SNe II characterised by the lack of a plateau) these are very similar or the same (Anderson et al., 2014b). See Figure 3.8 which displays the typical morphology of a Type II, the key physical phases, and S1/S2. S1 and S2 were originally described for $V-$band, however Valenti et al. (2016) also performs this analysis for pseudo-bolometric light curves and the key parameters are very similar - and in fact the transition between the early fast slope S1 and the shallow late slope S2 is more evident in pseudo-bolometric curves (Valenti et al., 2016). S2 is followed by the plateau-tail phase (Utrobin, 2007), also known as the post-recombination plateau (Branch & Wheeler, 2017), which drops into the ^{56}Co tail. The formalism reported in Valenti et al. (2016) can be described by the following equation:

$$f(t) = \frac{-A_0}{1 + e^{(t-t_{\rm pt})/w_0}} + (t \times p_0) + m_0 \tag{3.5}$$

Here the variables A_0, w_0, m_0 are free parameters describing the shape of the drop, p_0 describes the decline of the tail, and $t_{\rm pt}$ describes the length of the plateau, measured from the explosion to the midpoint between the end of the plateau phase and start of the radioactive tail.

The top panel on Figure 3.9 shows the pseudo-bolometric light curve, however there is no distinguishable change in the slope leading to a clear distinction of S1 and S2, and after approximately 60 days past maximum the light curve transits into a 'plateau-tail phase' and then drops into a radioactive tail. As there are not multiple slopes in the initial decline, S1 and S2 will hereafter be collectively referred to as S2 for SN 2019hcc, leading to a Type IIL sub-classification for the supernova. Refer back to Chapter 1 on SNe II for further detail on subtypes. The S2 decline was found to be 1.51 ± 0.09 mag per 50 days. The best-fit $t_{\rm pt}$ was 66.0 ± 1.1 days, and p_0 was measured via a linear fit and found to be 1.38 ± 0.49 mag per 100 days. Valenti et al. (2016) found a mean length of the plateau in SNe II of $t_{\rm pt} = 100$, which is up to the midway in the plateau-tail phase.

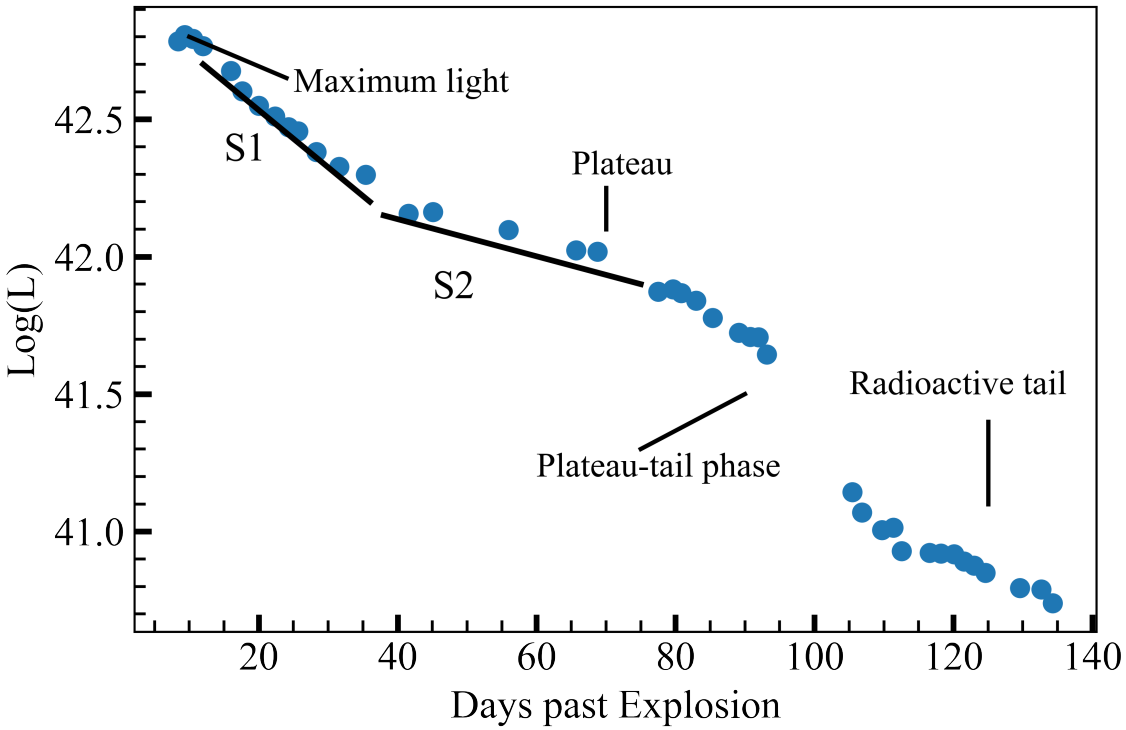

Figure 3.8. Bolometric light curve for SN 2013ej, a typical Type IIP Valenti et al. (2014). Maximum light is the stage powered by ^{56}Ni decay and shock deposition. The plateau is where hydrogen recombination begins, and the plateau tail phase is where all hydrogen has been recombined. The radioactive tail is powered by the decay of ^{56}Co. S1 and S2 mark two distinct slopes before the plateau-tail phase.

Considering this average, SN 2019hcc has a relatively short plateau duration, which could suggest a lower ejecta mass, but could also be due to a smaller progenitor radius or a higher explosion energy (Popov, 1993). This fitting was performed for the pseudo-bolometric light curve rather than $V-$band due to the sparsity of photometric data in this band, particularly for the tail of the light curve.

The middle panel of Figure 3.9 shows the full bolometric light curve - this was found by fitting a blackbody to the photometry and integrating between 200 Å and 25000 Å. The bolometric light curve required interpolation and extrapolation of additional points for epochs where some bands were not observed. This was done by taking a constant colour from the nearest points in the other bands - however this is an assumption that increases the uncertainty in the resultant curve. The tail luminosity $L_{\rm tail}$ is marked, and a ^{56}Co tail has been plotted using Equation 3.6, as from Jerkstrand et al. (2012), which gives the bolometric luminosity for the theoretical case of a fully-trapped ^{56}Co decay.

If full trapping of gamma-ray photons from the decay of ^{56}Co is assumed, the expected decline rate is 0.98 mag per 100 days in $V-$band (Woosley et al., 1989; Anderson et al., 2014b). The tail of SN 2019hcc clearly declines faster than the ^{56}Co tail as shown in the middle panel of Figure 3.9. If this is indeed the radioactive tail, it seems that SN 2019hcc displays incomplete trapping. This is not entirely unexpected as Gutiérrez et al. (2017b) showed that most fast-declining SNe show a tail decline faster than expected from ^{56}Co decay. Terreran et al. (2016) found incomplete trapping for SN 2014G, one of the SNe in our comparison sample. They suggested a few possibilities for incomplete trapping such as a low ejecta mass, high kinetic energy, or peculiar density profiles. However, dust formation could also result in a fast-declining tail, and additional effects such as different radioactivities could affect the decline (Branch & Wheeler, 2017), as well as CSM-ejecta interaction, which can contribute to the luminosity at late times (e.g. Andrews et al., 2019).

The lower panel of Figure 3.9 shows a comparison of the bolometric light curve of SN 2019hcc with Type II SNe 2013ej and 2014G, and with the Type IIn SN 1998S. These were chosen for comparison as they present a similar photometric evolution to SN 2019hcc (see Section 3.3). The bolometric light curves from the sample of SNe II from Faran et al. (2014) are also included, and two distinct branches can be seen which would correspond to the historic SN IIL and SN IIP sub-classifications. However, note the small sample size of this study compared with other sample analyses. All light curves have been normalised by the peak luminosity for comparison. This panel supports that the sample of SNe II discussed would all be considered SNe IIL, or fast decliners.

A SN IIL has been defined as where the $V-$band light curve declines by more than 0.5 mag from peak brightness during the first 50 days after explosion (e.g. Faran et al., 2014). The initial decline of SN 2019hcc was also measured in $V-$band and is displayed, along with other properties, in Table 3.2 together with the comparison SNe and the average values for SN IIP and SN IIL. Looking at Figure 3.9, the S2 slope of SN 2019hcc appears steeper, and the plateau shorter, than the comparison SNe II SN 2014G and SN 2013ej. However, SN 1998S has a faster intial decline, and appears to

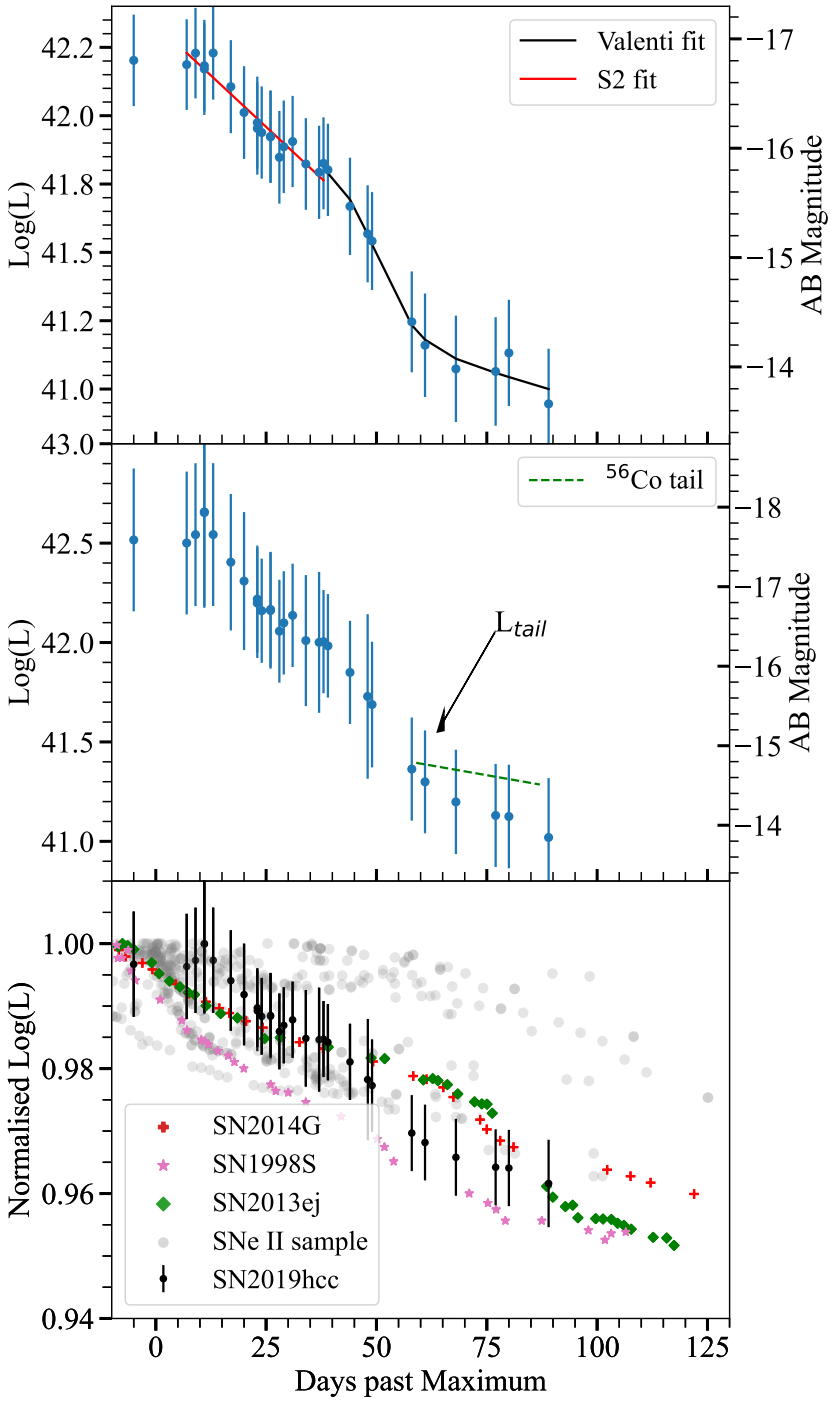

Figure 3.9. Top panel: the pseudo-bolometric light curve of SN 2019hcc, with $r-$band as the reference. Middle panel: the bolometric light curve of SN 2019hcc. The tail magnitude and comparison to ^{56}Co decay rate is marked. The S2 fit is measuring the slope of the plateau. Bottom panel: the bolometric light curve of SN 2019hcc, compared to those of SNe II SN 2014G (Terreran et al., 2016), SN 2013ej (Huang et al., 2015), and SN 1998S (Fassia et al., 2000, 2001). The bolometric light curves of the sample of SNe II from Faran et al. (2014) is shown in grey - two distinct branches can be seen which could be described with the SN IIL and SN IIP subcategories. The light curves have been normalised with respect to the maximum.

SN	V_{50}	Rise (days)	Peak (Absolute Mag)
SN 2019hcc	1.52±0.03	15.3±7.4	-17.7
SN 2014G	1.58±0.06	14.4±0.4	-18.1
SN 2013ej	1.24±0.02	16.9±1	-17.64
SN 1998S	1.87± 0.07	$\sim$18	~ -18.1
SNe II	1.43±0.21 (IIL) 0.31±0.11 (IIP)	16.0±3.6	-16.96±1.03

Table 3.2. Here V_{50} is the $V-$band mag decline in the first 50 days (roughly equivalent to S2), measured directly from the light curves with a linear fit. Rise times and peak absolute magnitude are in $R-$band for SN 2014G (Terreran et al., 2016) and SN 2013ej (Richmond, 2014; Huang et al., 2015), or ATLAS $o-$band for SN 2019hc. Rise time and peak values for SN 1998S are also in the $R-$band, however they are estimated from the light curve rather than taken from literature. Also shown are the average values for a sample of 10 SN IIL and 18 SN IIP from Faran et al. (2014). Though these populations have been previously discussed as continuous, the distinction is still useful to give context to the measured values. Anderson et al. (2014b) found a mean S2 of 0.64 for a sample of 116 SNe II, roughly the average of the IIL and IIP sub-classes in the above. The rise time for SNe II is taken from Pessi et al. (2019). The average absolute peak magnitude in $R-$band from SNe II comes from Galbany et al. (2016).

transition to the tail at a comparable epoch. SN 2013ej has the most distinct S1 and S2. The radioactive tail of SN 2019hcc shows a similar decline rate to all comparison SNe which also seem to display incomplete trapping, or at the very least a radioactive tail decay faster than ^{56}Co decay. The SN 2019hcc light curve evolution drops out of the photospheric phase sooner than SN 2013ej and SN 2014G - implying a lower ejecta mass. It could therefore be suggested that the ejecta mass of SN 2019hcc is lower than the that of these other SNe, however other factors such as explosion energy could also play a role (Popov, 1993).

3.5.4 ^{56}Ni Production

^{56}Ni is produced in the SN explosion and the decay of ^{56}Ni to ^{56}Fe is a significant contributor to the luminosity of the light curve. However, the luminosity of SLSNe I is much higher than what could be produced by a mass of ^{56}Ni which is sensible w.r.t the estimated mass of the ejecta, and therefore the luminosity is thought to be powered by alternative means, such as a magnetar. In examining SN 2019hcc, it is useful to examine the estimated ejecta and ^{56}Ni mass to see if this is sensible and in line with other SNe II.

Jerkstrand et al. (2012) presented a method to retrieve the ^{56}Ni mass produced by comparing the estimated bolometric luminosity in the early tail-phase with the theoretical value of fully trapped ^{56}Co deposition, which is given by:

$$L(t) = 9.92 \times 10^{41} \times \frac{M_{^{56}\mathrm{Ni}}}{0.07 M_{\odot}} \times (e^{-t/111.4d} - e^{-t/8.8d}) \tag{3.6}$$

Where t is the time since explosion, $L(t)$ is the luminosity in ergs^{-1} at that time, 8.8 days is the e-folding time of ^{56}Ni and 111.14 days is the e-folding time of ^{56}Co decay. It is also assumed that the deposited energy is instantaneously re-emitted and that no other energy source has any influence. To calculate the mass of ^{56}Ni, the tail luminosity and the time at which the tail begins should be used in Equation 3.6.

A visible transition can be seen in Figure 3.9 into the tail of SN 2019hcc at 61 days past maximum, therefore we selected the tail luminosity as the magnitude at the point of transition.The uncertainty was calculated as 0.1 dex, as a measure of the distance to the adjacent points, as the exact location of the tail start is uncertain. This is combined with the errors in luminosity, which for the bolometric light curve in Middle Panel are the errors in integration of the blackbody, the blackbody fitting to the photometry, and the errors associated with the distance used to convert flux to luminosity.

When considering the errors from the blackbody fitting to the photometry, as only bands B,V,g,r,i and z were used, and bands u, J, H, and K were not as there was not sufficient data - an additional 20% error is assumed (5% per missing band). Additionally, the uncertainty in distance is largely from the error in the Hubble Constant and redshift. The redshift was measured from the host galaxy spectrum, and therefore there is an associated error due to the 18Å resolution of the spectrum. The Hubble Constant and associated error for calculating the bolometric light curve was taken as 73$\pm$6 from Freedman & Madore (2010) (though many different measurements exist). These errors in the distance measurement have been propagated through the conversion from flux to luminosity, and the mass of ^{56}Ni is measured to be 0.035 ± 0.023 M$_{\odot}$, with the biggest systematic error the uncertainty in the distance. More precise measurements of the Hubble Constant would decrease this error.

This is also only a lower limit due to likely incomplete trapping. Anderson et al. (2014b) performed this analysis on a large set of SNe II, and found a range of ^{56}Ni masses from 0.007 to 0.079 M$_{\odot}$, with a mean value of 0.033 M$_{\odot}$ (σ= 0.024). A survey of literature values led to a mean mass ^{56}Ni = 0.044 M$_{\odot}$ for a sample of 115 SNe II (Anderson, 2019). Therefore we conclude that the value retrieved for SN 2019hcc is within the expected range for a SN II.

3.6 Spectroscopy

Figure 3.10 shows the spectral evolution of SN 2019hcc, labelled with the phase with respect to maximum light (MJD 58636). The spectra have been flux-calibrated according to the broadband photometry. This is done by once again converting the magnitude in different bands to flux, and this flux is then plotted against the central wavelength of each band. The spectrum continuum is then 'mangled' in order to flux-calibrate to what is expected from the photometry. The last epoch was

Table 3.3. Spectroscopy Data as displayed in Figure 3.10 in Chapter 3. The resolutions of the spectra are found from measuring the skylines using iraf, excluding the SOAR spectrum resolution which was was taken from http://www.ctio.noao.edu/soar/content/goodman-spectrograph-gratings.

Epoch	Phase from maximum (days)	Instrument	Grisms	Range (Å)	Resolution (Å)
58643	7	EFOSC2	Gr 11	3380-7520	13.7
58655	19	SOAR	400mm	3200-8500	6.0
58665	29	EFOSC2	Gr 13	3685-9315	25.7
58689	53	EFOSC2	Gr 13	3685-9315	17.4
58717	81	EFOSC2	Gr 13	3685-9315	17.1
58814	178	EFOSC2	Gr 13	3685-9315	17.3
59149	Host Spectrum	EFOSC2	Gr 13	3685-9315	16.0

not calibrated according to the photometry as none was available. At +81 days, the SED no longer follows a blackbody assumption as the ejecta is now optically thin and the photospheric phase is over, however the blackbody fit to the photosphere is a valid approximation for the earlier spectra. The light curve analysis from Section 3.5 suggests the end of the plateau/photospheric phase, $t_{\rm pt}$, at approximately +66 days from explosion. Emission lines from the host galaxy can be seen, particularly from +53 days. The resolution of the spectra can be found in Table 3.3.

The spectra were also corrected for redshift and de-reddened according to the Cardelli Extinction law using Av = 0.19 mag and Rv = 3.1 (Cardelli et al., 1989). They have been offset for clarity on an arbitrary y-axis. The flux has been converted to log(F_ν) where $F(\nu) = F(\lambda)\lambda^2/3e18$ to highlight the absorption features.

As can be seen, the first spectrum at +7 days after peak displays a 'w'-shaped profile at the rest-wavelengths typical of O II lines with absorption minima at approximately 4420 Å and 4220 Å, which originally motivated the classification as a SLSN I. However, these signatures disappear in subsequent spectra with the Hα emission becoming the dominant spectral feature. Aside from the w-shape, the first spectrum is relatively featureless. A well developed Hα profile can be seen from +19 days, as well as Hβ and Hγ, though less developed Balmer lines can also be seen at +7 days. Fe II and He I lines can also be seen from the +7 days spectrum and become well-developed by +19 days. The typical core-collapse SN forbidden lines of [O I] at $\lambda\lambda$6300, 6363 and [Ca II] at $\lambda\lambda$7291, 7323 are not seen despite SN 2019hcc appearing to reach the nebular phase, which roughly starts at 100-200 days (Fransson & Chevalier, 1989). Forbidden lines are transitions which are forbidden by normal selection rules and occur at low rates only at extremely low densities. There could be a few possibilities for their absence. The first is that the nebular phase has not been reached. Alternatively, as the strength of [O I] increases with the Zero Age Main Sequence (ZAMS) mass (e.g. Dessart & Hillier, 2020), it would imply a ZAMS mass of the SN 2019hcc progenitor sufficiently low that the [O I] are not visible. Another possibility is that SN 2019hcc is too faint with respect to the host and

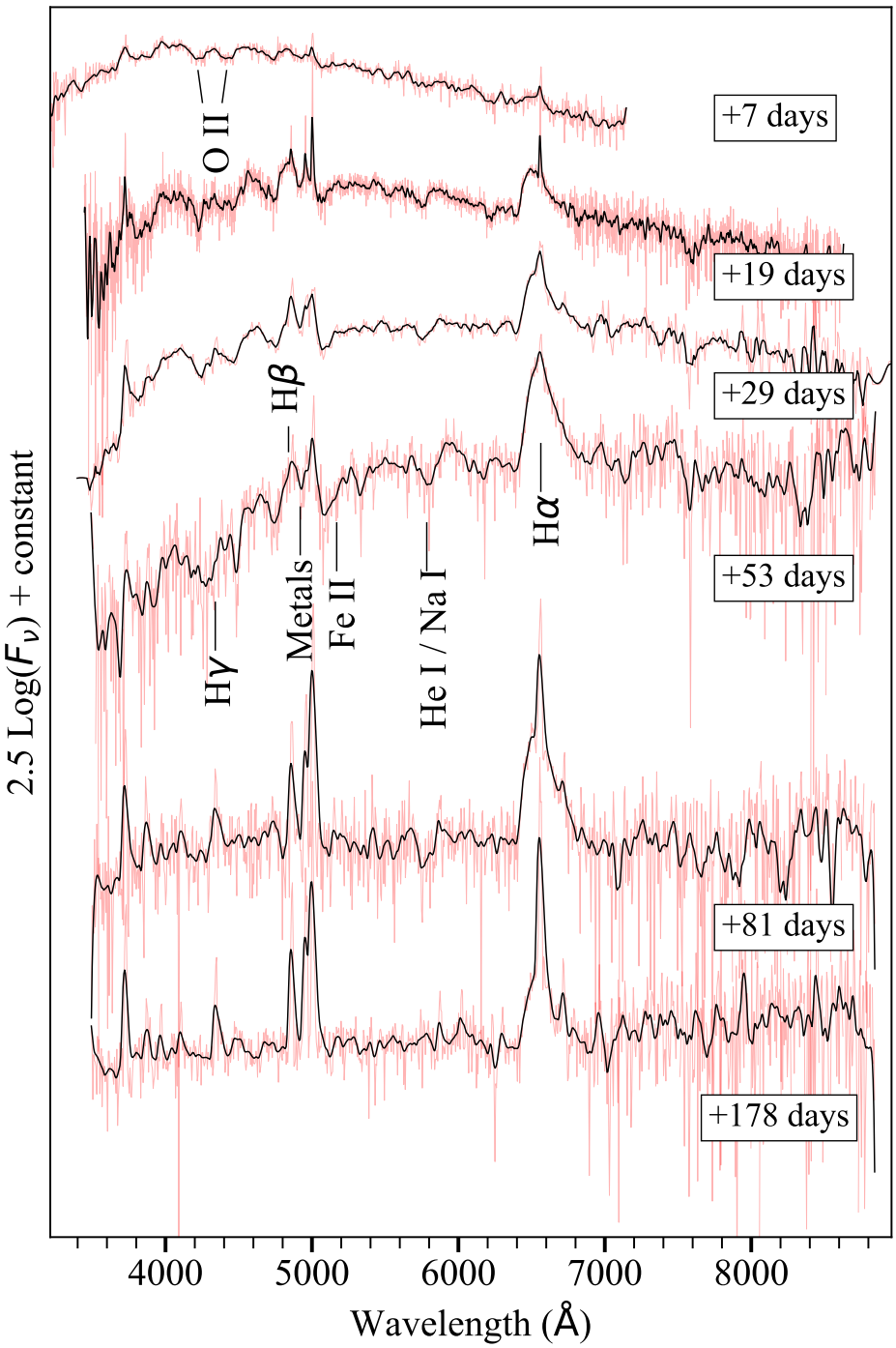

Figure 3.10. The spectra for SN 2019hcc and their phase with respect to maximum light (MJD 58636). The wavelength is in the rest frame. The spectra have been corrected according to the photometry (excluding the last epoch which had no photometry available), de-reddened and redshift-corrected. They have also been smoothed using a moving average - this recalculates each point as the average of those on either side, in this case for five iterations - (black) with the original overlaid (red). The flux has been converted to log(F_ν) to emphasize absorption features. The most prominent elements have been labelled - here 'Metals' refers to a combination of Ba II, Sc II and Fe II.

the lines have not yet developed.

In SN 2014G, after ∼80 days the emission feature of [Ca II] at $\lambda\lambda$7291, 7323 starts to become visible, approximately coincident with the sudden drop in the light curve (Terreran et al., 2016). SN 2013ej also shows [Ca II] and [O I] forbidden lines from 109 days, when the SN entered the nebular phase (Bose et al., 2015), suggesting SN 2019hcc is unusual in this respect. However, Branch & Wheeler (2017) noted the spectra of some SN IIL (e.g. SN 1986E, SN 1990K) do not contain the standard emission lines of core-collapse supernovae, and the forbidden lines arising in the ejecta may be suppressed by high densities or obscured by the circumstellar medium (CSM) that produces the extended Hydrogen emission.

The flux of Hα in the +178 days spectrum (excluding the narrow host contribution component) is ∼5 times that of Hβ. For case B recombination in the temperature regime 2500 $\leq$ T(K) $\leq$ 10000 and electron density $10^2 \leq n_e \leq 10^6$, the Hα line should be 3 times stronger than Hβ (Osterbrock & Ferland, 2006). However, the case B recombination is not observed in SNe II before a couple of years. Kozma & Fransson (1998) suggested at 200 days past explosion in SN 1987A this ratio should have been around 5, based on the total calculated line flux and using a full Hydrogen atom with all nl-states up to $n = 20$ included. The ratio of SN 2019hcc appears similar to SN 1987A and other SNe II at the onset of the nebular phase. Despite the Hα/Hβ ratio being higher than the case B recombination, it is still sufficiently low that we can conclude that any additional flux to Hα should be insignificant. Excess flux in Hα could be a clue that Hα is also collisionally excited, suggesting interaction (Branch et al., 1981). As the Hα profile evolves it appears to become asymmetrical, suggesting a multi-component fit in the late spectra. The simplest explanation for this is that a mostly spherical ejecta is interacting with a highly asymmetric, Hydrogen-rich CSM (Benetti et al., 2016). This is in contrast with the quick decay of the tail, suggesting that such asymmetry might be intrinsic of the ejecta or the result of other lines that are not resolved, for example [N II] λ6584. An asymmetric line profile, with suppression of the blue side of a spectral line, can also be interpreted as evidence for dust formation in the ejecta (e.g. Smith et al., 2008). This is caused by dust more effectively blocking the light coming from the more distant receding side of the SN, as there is more dust to pass through. Other signs of dust formation could be e.g. far-IR excess in the bolometric light curve, which could be interpreted as thermal emission by grains in the ejecta (e.g. Lucy et al., 1989). However there is not sufficient far-IR photometry available for SN 2019hcc to investigate this scenario.

3.6.1 Spectral Comparison

Comparison of SN 2019hcc with the moderately luminous SNe II (Inserra et al., 2013a) reported in Section 3.5 and Figure 3.6, together with SLSN I iPTF16bad, is shown in Figure 3.11 ¶.

iPTF16bad at late times displays Hα emission due to the collision with a H-shell ejected approximately 30 years prior, thought to be due to pair instability pulsations (Yan et al., 2015, 2017b), and merits comparison as it is a SLSN I displaying a w-shaped profile at early times and Hα at late times. SN 2019hcc has a good match with some features, e.g. Balmer lines, however there are some discrepancies in the comparison, such as the lack of a P-Cygni profile for Hα in iPTF16bad. The Fe II lines at approximately 5000 Å are also not observable in the spectrum of the SLSN I. If the Hα in SN 2019hcc was a consequence of interaction similar to iPTF16bad, we would expect other signs of interaction. These could be undulations or a second peak in the light curve (e.g. Nicholl et al., 2016; Inserra et al., 2017), but the SN 2019hcc light curve appears to be that of a typical SN IIL (see Section 3.5). Additionally, the relatively earlier appearance of the Hα emission in SN 2019hcc would require a much closer H-shell than for iPTF16bad.

Figure 3.11 also displays a comparison to moderately luminous SNe II SN 2013ej, SN 2014G, and SN 1998S. SN 1998S did not have a spectrum available at the +29 days epoch, so is shown at the nearest later epoch, with SN 2019hcc at +53 days for comparison. The spectra do not significantly evolve in this time frame. There are strong similarities between spectral features at the epoch of comparison, with good matches of Hα and Fe II features. The comparison would strengthen that SN 2019hcc is a Type II.

Figure 3.12 shows a closer look at the Hα profiles for the previous spectra, and additionally SN 2018bsz, a SLSN I. In SLSNe I, carbon lines produced in the Hα region could be mistaken for Hydrogen, such as in the case of SN 2018bsz, which displays C II λ6580 line in the Hα region (Anderson et al., 2018b). SN 2018bsz does also show Hydrogen but it is not observed at the phase being considered here. However, if C II is present in a spectrum, we should observe it at λ7234 and λ5890 (Anderson et al., 2018b), lines which are not seen in SN 2019hcc, while Hβ can be seen at λ4861. This strengthens the idea that is indeed Hα observed in SN 2019hcc as opposed to C II.

SN 2019hcc spectra show an emission redward of Hα at approximately 6720 Å visible at +29 days. Figure 3.12 shows that SN 2018bsz also contains the redward emission at approximately 6720 Å. Singh et al. (2019) identifies this as [S II] lines at 6717 Å and 6731 Å from the parent H II region.

¶These spectra were taken from the Weizmann Interactive Supernova Data Repository (WISeREP) (Yaron & Gal-Yam, 2012)

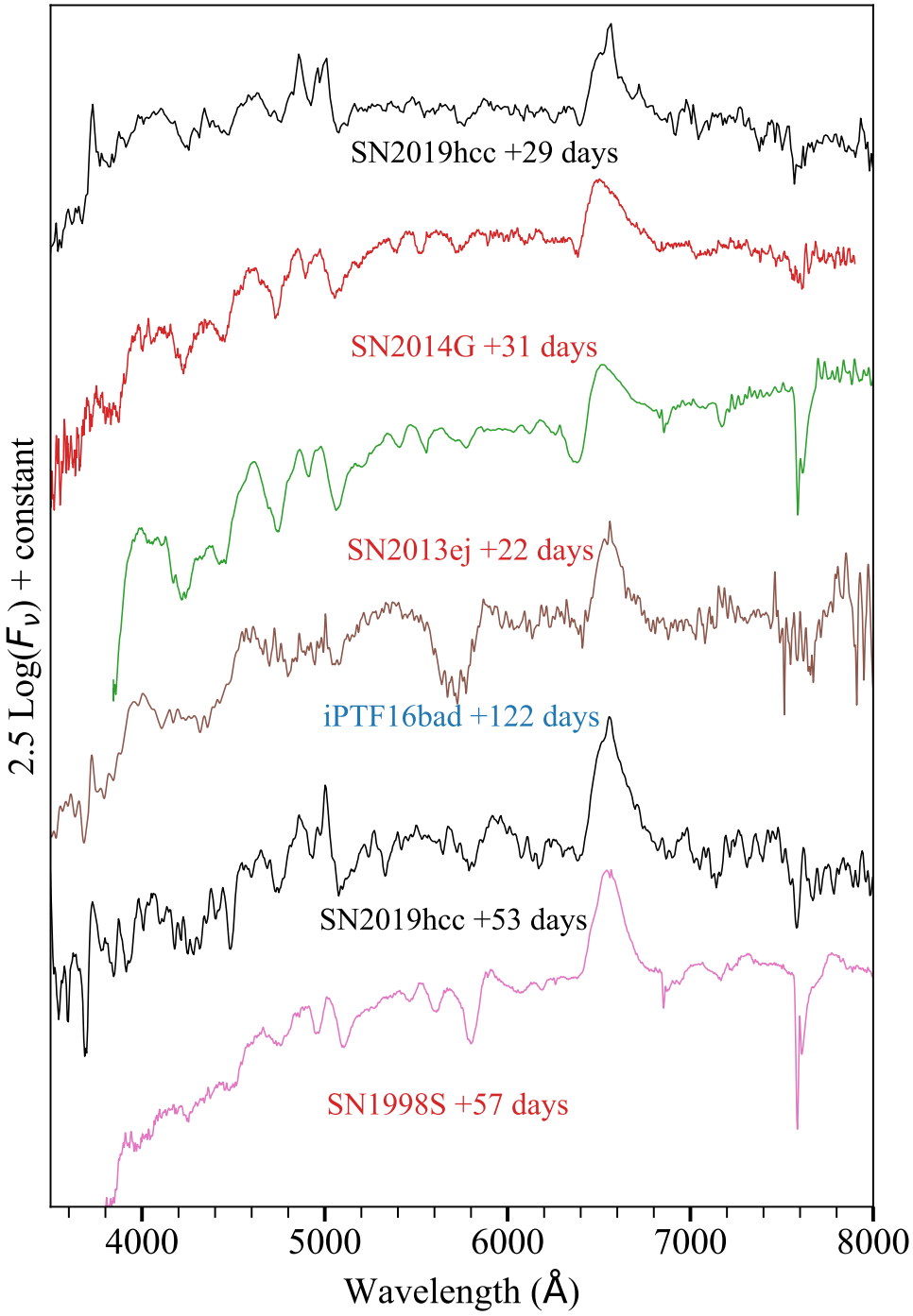

Figure 3.11. SN 2019hcc at +29 days post peak is compared to moderately luminous Type II SN 2014G and SN 2013ej, and SLSN I iPTF16bad which displays Hα at late time (at +100 days post peak) in its spectra. SN 2019hcc at +53 days past peak is also compared to SN 1998S. The wavelength is in the rest frame. Text in red refers to Type II, while in blue to the only SLSN I.

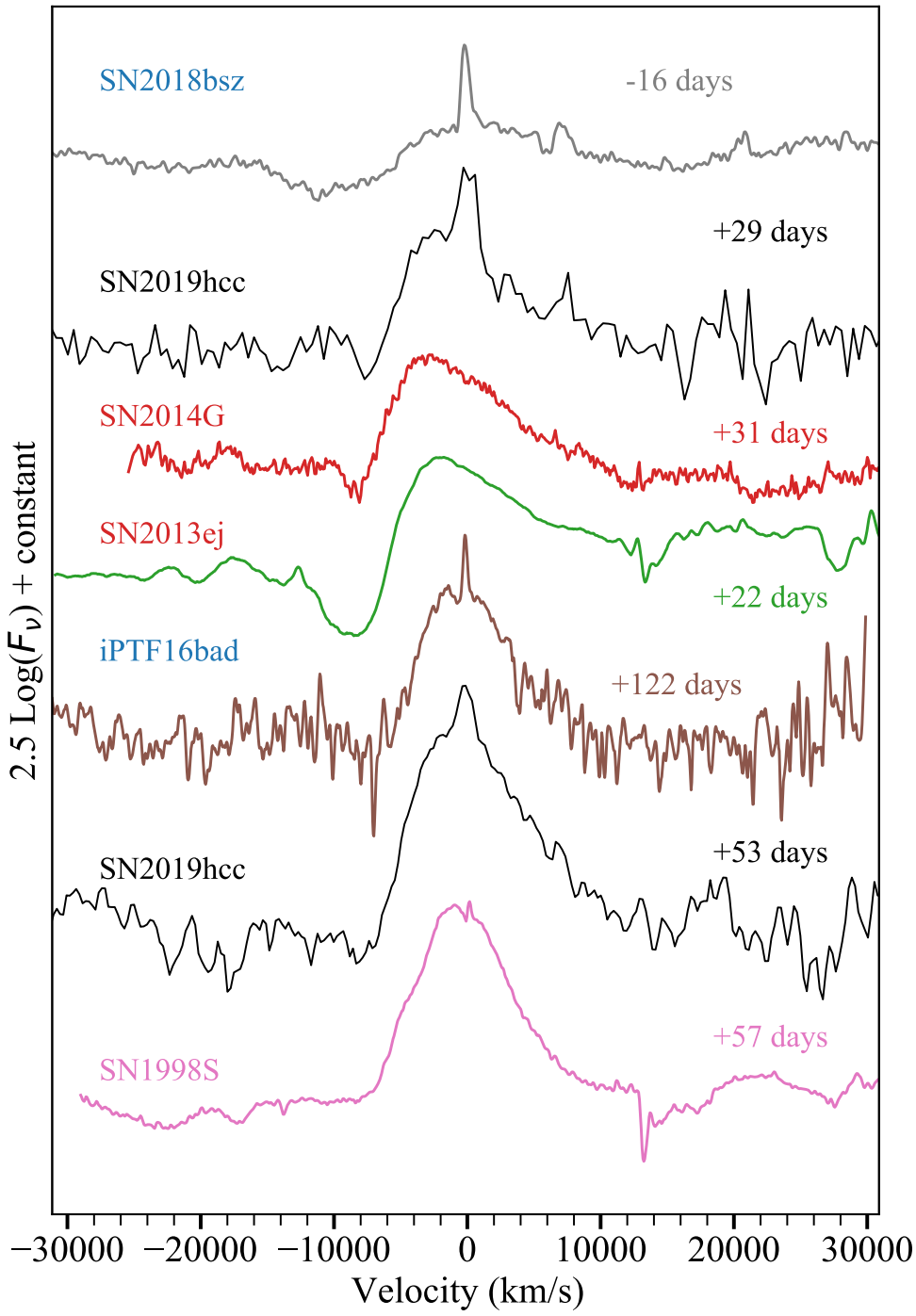

Figure 3.12. A comparison of the Hα profiles for a variety of moderately luminous SNe II and SLSNe I. The wavelength is in the rest frame. Text in red refers to Type II, while in blue to SLSNe I. The velocity is with respect to Hα.

3.6.2 Investigating Signs of Interaction in the Photospheric Spectra

A multi-component Hα profile which does not completely hide the absorption component hints to a degree of interaction. Here the narrow component would belong to the unshocked wind, whilst the medium component to the shocked wind/ejecta. Another sign of interaction between the ejecta and the CSM could be a high velocity (HV) component in the Balmer lines (e.g. Inserra et al., 2013a; Gutiérrez et al., 2017a). The normal velocity originates from the receding photosphere, whilst the high velocity is generated further out where the CSM interaction may excite the Hydrogen to cause a second, high-velocity absorption feature (e.g. Arcavi, 2017). The size and shape of this feature could be related to the progenitor wind density (Chugai et al., 2007). A small absorption bluer than the Hα P-Cygni has been observed in several SNe II but its nature is not always linked to Hα (Gutiérrez et al., 2017a). Such a feature, named 'Cachito', has previously been attributed to HV features of Hydrogen, or Si II λ6533. These features were identified in Inserra et al. (2013a) for some moderately luminous SNe II. Gutiérrez et al. (2017a) also found the 'Cachito' feature is consistent with Si II at early phases, and with Hydrogen at later phases.

High Velocity features

In the top panel of Figure 3.13, an absorption blue-ward of Hα can be seen in SN 2019hcc at +19 days and +29 days at around 6250 Å, however after this epoch it becomes less clear. An absorption feature can also be seen in SN 2013ej, and arguably SN 2014G, as seen in Figure 3.12. The presence of a potential HV Hβ additional to the Hα at a similar velocity would strengthen the latter's status as a HV feature of Hydrogen (e.g. Chugai et al., 2007; Gutiérrez et al., 2017a; Singh et al., 2019). The lower panel on Figure 3.13 shows the Hβ profile for SN 2019hcc at the epochs where it is visible, and an absorption blueward of the P-Cygni could be identified. Gutiérrez et al. (2017a) found that 63% of their sample of SNe II with HV Hα in the plateau phase showed a HV Hβ at the same velocity. Gutiérrez et al. (2017a) also reported that if the absorption is produced by Si II its velocity should be similar to those presented by other metal lines, such as Fe II $\lambda 5169$, a good estimator for the photospheric velocity (Hamuy et al., 2001).

The velocity of this possible Hα HV absorption feature in SN 2019hcc was measured at +19 days and +29 days, with respect to Hα and Si II at $\lambda 6355$. The Fe II lines were also measured for comparison. Figure 3.14 displays the measured velocities in SN 2019hcc for various lines at different epochs in its evolution. The velocity was found by fitting a Gaussian to the absorption features and finding the minimum - after +29 days, this fitting was not successful, therefore there are only two points available. With reference to Figure 3.14 it can be seen that the measured Si II velocity is close to the Fe II velocity at both epochs, suggesting that it is near the photospheric velocity. This would lend support to the feature being more likely associated with Si II. For the HV component, it

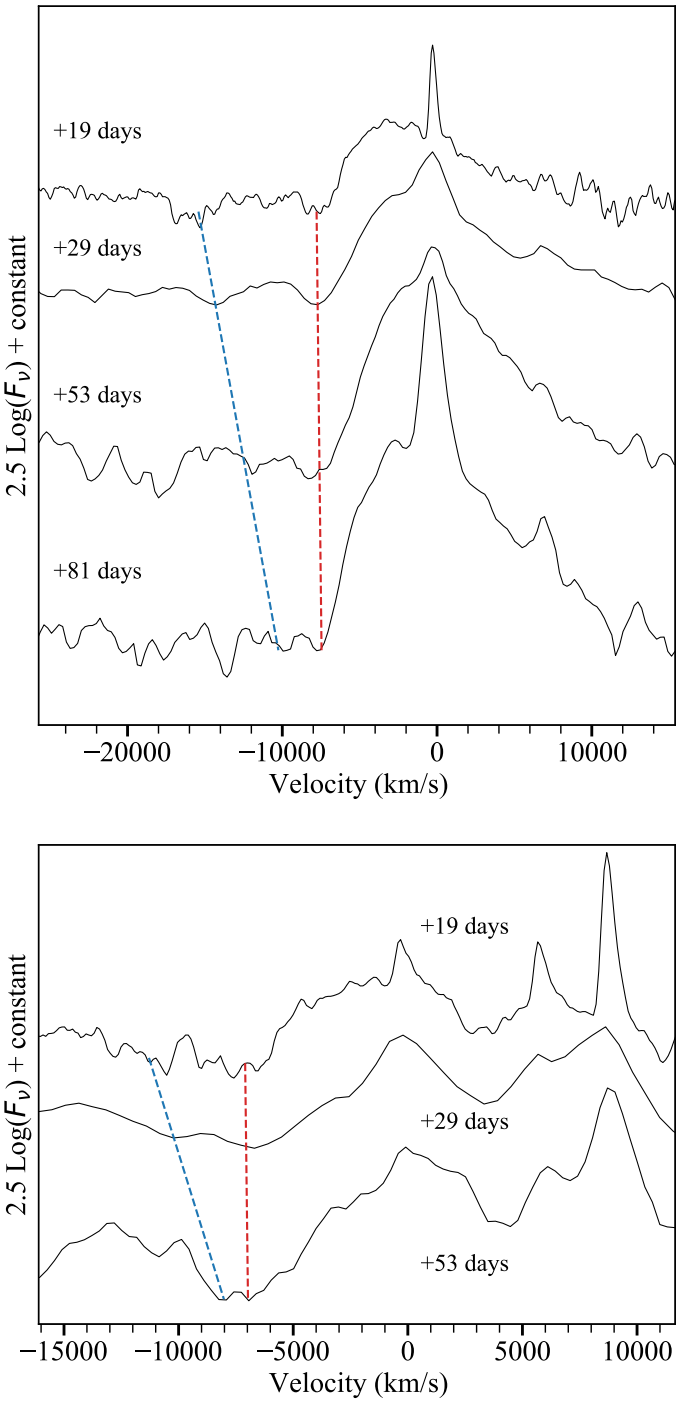

Figure 3.13. Top panel: the Hα profile evolution of SN 2019hcc, the spectra have been smoothed using a moving average. The velocity is with respect to Hα. All spectra show a small feature blue-ward of Hα after smoothing, which could be a HV component indicating early CSM-ejecta interaction. The red dashed line tracks the Hα absorption, and the blue dashed line the possible HV component. Bottom panel: the same as the above panel but with respect to Hβ. The velocity is with respect to Hβ.

would be expected the velocity of the HV Hβ to match that of the HV Hα, and this is not what is found by our velocity analysis. Considering this information, the velocity measurements support that this feature is most likely associated with Si II, and the apparent HV Hβ feature can be interpreted as Fe II.

Velocities were also measured for the lines of Hα, Hβ, and Fe II in SN 2014G and SN 1998S as shown in Figure 3.14, and the Fe II velocities are similar to those of SN 2019hcc - although due to the scarcity of points for SN 2019hcc a meaningful comparison of the velocity evolution is difficult. Additionally the average velocities of these lines as measured by Gutiérrez et al. (2017a) for a sample of 122 SNe II are included in the plot, and show the velocities measured for SN 2014G, SN 2019hcc and SN 1998S are roughly as expected for SNe II.

Photospheric Hα profile

Another sign of interaction in the spectra would be a multi-component Hα profile with additional components to a simple P-Cygni profile. To investigate the possible presence of multi-components, the profile of SN 2019hcc taken from its highest resolution spectrum at +19 days was decomposed by means of Gaussian profiles. Spectral lines can be approximated as Gaussian which are produced due to Doppler broadening where material moving in all directions produces shifts in where the line appears, creating a spread around the central wavelength. In a non-perturbed SN ejecta, the expected components would be both an absorption and an emission from the P-Cygni, as well as emission from the host galaxy. Any additional component could therefore suggest an ongoing ejecta-CSM interaction.

In Figure 3.15 we display a composite Gaussian function. The Hα profile at +19 days was chosen as it is the highest resolution spectrum of SN 2019hcc, with a resolution of 6.0 Å. As can be seen, the multi-component function provides a good fit. The fit contains an absorption and emission component to reproduce the ejecta P-Cygni profile and a narrow emission component for the host galaxy. An additional broad Gaussian component could be due to CSM interaction, however no additional component is required for the fit. The emission component was initially fitted with both a Gaussian and a Lorentzian fit, retrieving similar χ^2 values (0.451 for Gaussian vs. 0.468 for Lorentzian). A Lorentzian profile is typically associated with scattering of photons in an optically thick CSM, and this requires a dense scattering medium (e.g. Reynolds et al., 2020). A better fit with a Lorentzian function indicates that broadening is due to electron scattering rather than expansion (e.g. Chatzopoulos et al., 2011; Taddia et al., 2013; Nicholl et al., 2020). However, as a Lorentzian is not a significantly better fit, this scenario is not supported.

P-Cygni theory predicts emission of Hydrogen to peak at zero rest velocity λ6563.3, however observations reveal that emission peaks are often blue-shifted (Anderson et al., 2014a). Anderson et al. (2014a) found that significant blue-shifted velocities of Hα emission peaks are common and

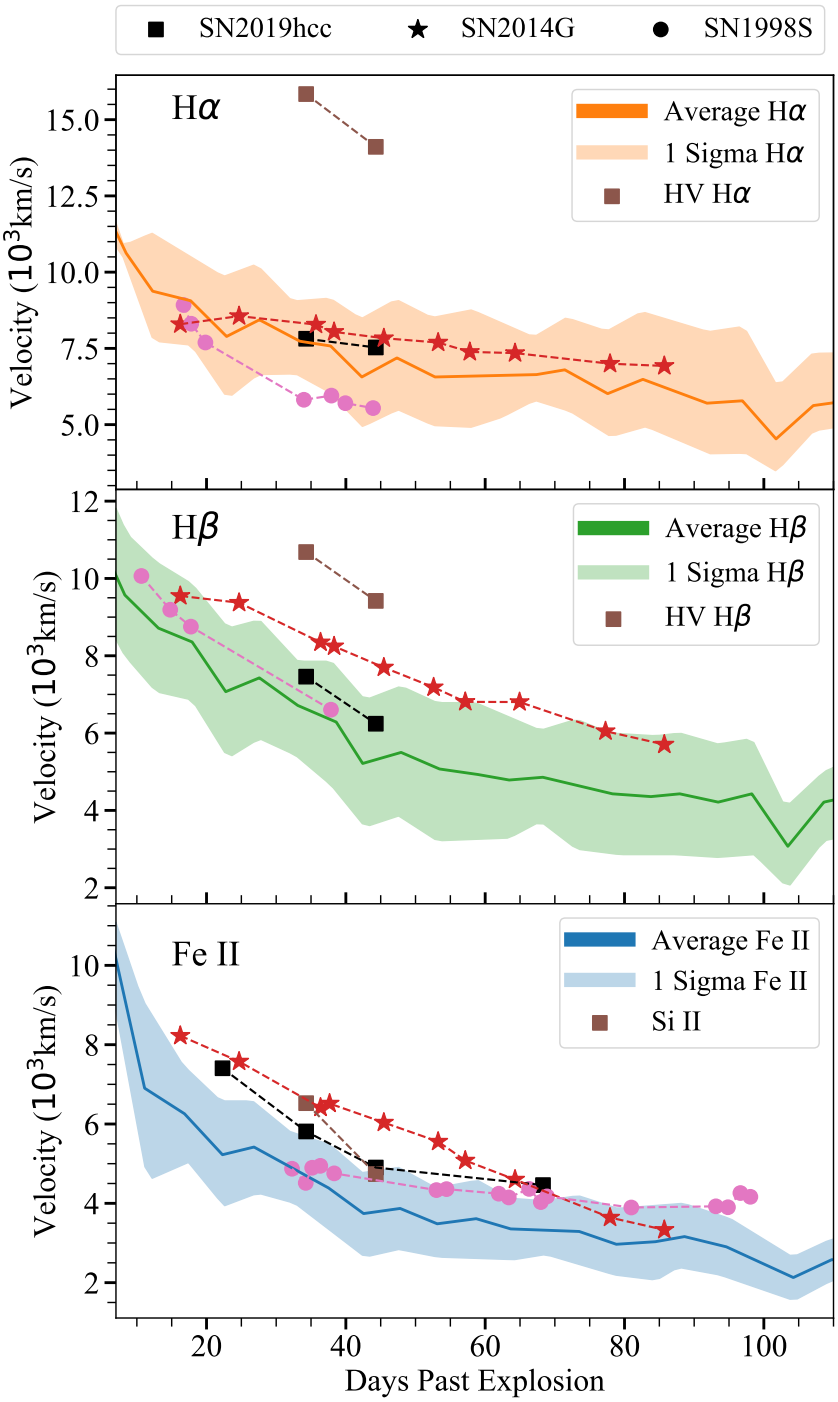

Figure 3.14. The velocity comparisons of different lines for SN 2019hcc, over three different epochs, alongside the velocities of SN 2014G for Fe II, Hα and Hβ. Velocities of SN 1998S from Anupama et al. (2001) and Terreran et al. (2016), SN 2014G from Terreran et al. (2016). The average velocities are found from 122 Type II SNe (Gutiérrez et al., 2017a), the figure reproduced from Dastidar et al. (2021) and reference therein, shown with a 1-sigma error.

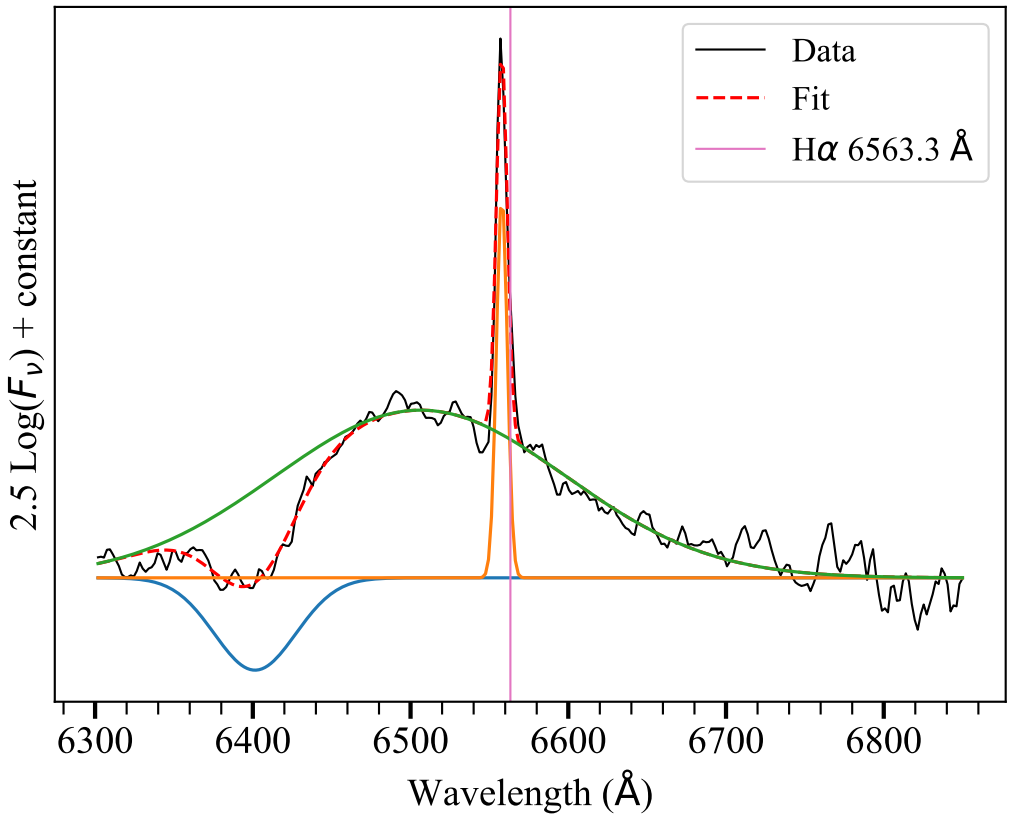

Figure 3.15. The Hα profile for SN 2019hcc at +19 days past maximum with model profiles composed by several Gaussian profiles: a blue-shifted Hα absorption (blue), the galaxy line (orange), a blue-shifted Hα (green).

concluded that they are a fundamental feature of SNe spectra. This has been suggested to be due to the blocking of redshifted emission from the far side of the ejecta by an optically thick photosphere, due to a steep density profile within the ejecta (e.g. Reynolds et al., 2020). The fit allows for a blue-shifted broad emission line as well as host galaxy emission at the rest wavelength. The Doppler shift from Hα in Figure 3.15 is 2610$\pm$140 km/s. Anderson et al. (2014a) found blue-shifted emission velocities on the order of 2000 km/s, therefore this result is consistent. Overall, the above analysis shows that a multi-component profile is not necessary to reproduce the observed Hα profile and hence the spectra do not show any evidence of an ejecta-CSM interaction.

3.7 The early 'w' shaped feature: elements contribution and their nature

One of the most interesting features displayed by SN 2019hcc is its early 'w' shaped feature resembling that of SLSNe. Understanding its nature, composition and the possibility that it is not a trademark of SLSNe I will have important consequences during the Vera C. Rubin and the Legacy Survey for Space and Time (LSST) era. LSST will deliver hundreds of SLSNe (Inserra et al., 2021)

and thousands of CC-SNe for which we might not have the luxury of multiple epoch spectroscopy.

Figure 3.16 shows the O II features in the early spectrum for SN 2019hcc, together with the Type II SNe used for previous comparison, and the previous sample of SLSNe I. The approximate location of peaks and troughs of the SN 2019hcc O II lines are marked by dashed vertical lines for comparison. iPTF16bad (Yan et al., 2017b) was chosen due to the late Hα emission, and SN 2010kd (Kumar et al., 2020) for the carbon emission which resembles Hα. PTF12dam (Nicholl et al., 2013) was chosen for being a well-sampled SLSN I, and LSQ14mo (Chen et al., 2017b) for its similarity to SN 2019hcc with respect to the O II feature at a similar epoch. SN 2014G, amongst the SNe II, appears to have the strongest resemblance to SN 2019hcc, showing a similar pattern in the wavelength region around 4000 Å. A point to note is that SN 2019hcc does not entirely match the O II feature in the SLSNe I - the redder absorption is blue-shifted in comparison.

The features usually associated with O II are formed by many tens of overlapping lines (Anderson et al., 2018c; Gal-Yam, 2019b), and can be contaminated by carbon and metal lines, and also by the presence of well-developed Balmer lines, all of which mean the features cannot be uniquely identified as O II. Therefore, whilst SN 2019hcc, SN 2014G, and SN 1998S could be valid candidates to show O II features as the Balmer lines are less prominent, SN 2013ej is less likely as it shows a strong Hα profile suggesting the spectrum is dominated by Hβ at λ4861 and Hγ at λ4340.

Gal-Yam (2019a) tackled the challenge of line identification with comparison of absorption lines to lists of transitions drawn from the National Institute of Standards and Technology (NIST) database. He found that O II emission lines appear in the gaps between O II absorption, which corresponds to the two peaks - see Figure 3.16 2$^{\rm nd}$ and 4$^{\rm th}$ dashed lines from the left. Anderson et al. (2018c) suggested that a change in the morphology of the spectrum in this wavelength region (between SNe) may be produced through differences in ejecta density profiles or caused by overlapping lines such as Fe III.

Oxygen lines appear when Oxygen is ionised by sufficiently high temperatures, 12000-15000 K (e.g. Inserra, 2019). However, the presence of O II lines around 4000-4400 Å might be a consequence of non-thermal excitation (Mazzali et al., 2016). This requires a power source in the CO core of massive stars (Mazzali et al., 2016). A lack of O II lines would be be the product of rapid cooling or lack of non-thermal sources of excitation (Quimby et al., 2018).

A non-thermal excitation could be in the form of strong X-ray flux from a magnetar, such as the injection of X-rays from an interaction between the SN ejecta and a magnetar wind (Maeda et al., 2007). Vurm & Metzger (2021) modelled SLSNe powered by a relativistic wind from a central engine, such as a millisecond pulsar or magnetar, which inflates a nebula of relativistic electron/positron pairs and radiation behind the expanding supernova ejecta shell. These quickly radiate their energy via synchrotron and inverse Compton (IC) processes in a broad spectrum spanning the X-ray/gamma-ray band, a portion of which heats the ejecta and powers the supernova emission. This process will be most efficient at early times after the explosion, when the column density through the ejecta is at its

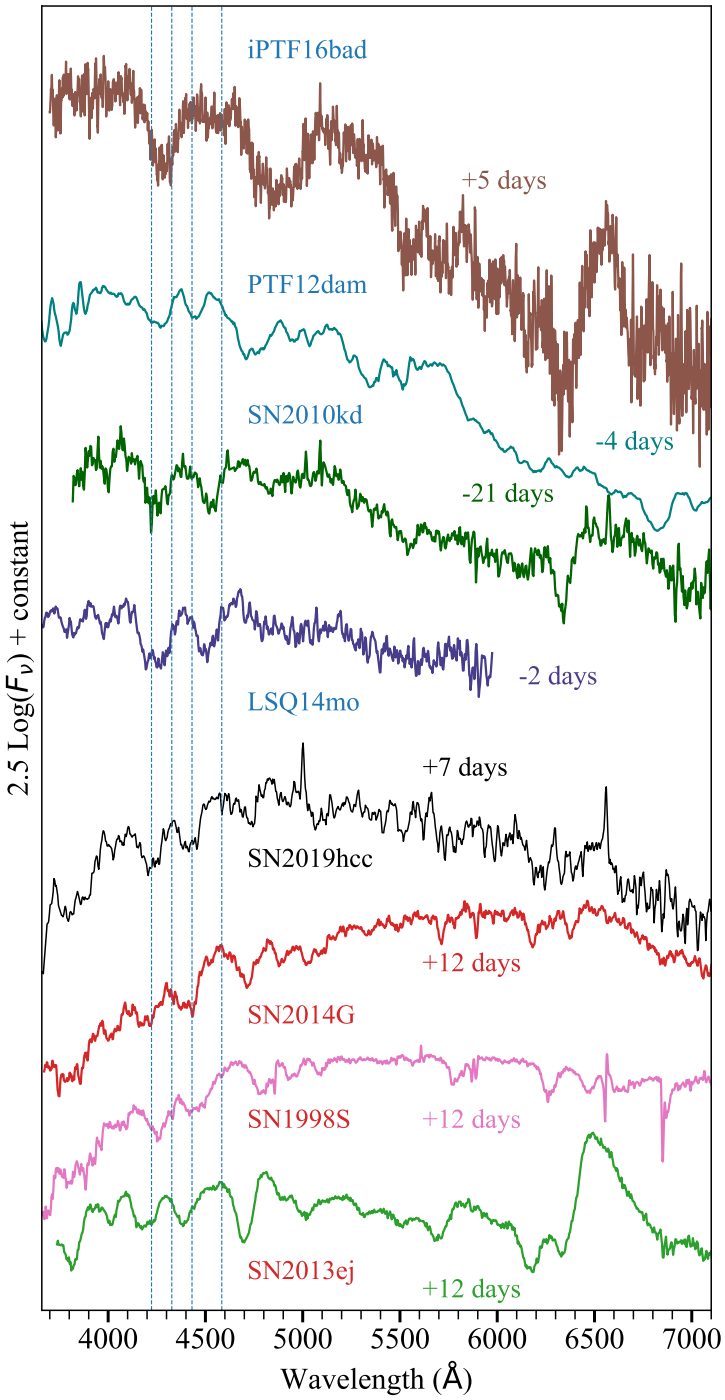

Figure 3.16. SN 2019hcc +7 days post peak is compared to moderately luminous SNe II and SLSNe I. These spectra are displayed in terms of F(ν) to emphasise the absorption features, and the wavelength is in the rest frame. SN 2014G also appears to show a 'w' shaped profile at 4000-4400 Å. The dashed lines correspond to the peaks and troughs of the O II line region in SN 2019hcc. Text in red represents Type II, text in blue SLSN.

highest. Non-thermal excitation could also be due to high energy electrons produced by γ-rays from the radioactive decay of ^{56}Ni (Li et al., 2012), however such a process would more likely be relevant at later times. It could also be produced by ejecta-CSM interaction (Nymark et al., 2006), with a CSM rich in Oxygen producing the associated spectral features (Chatzopoulos & Wheeler, 2012). No SLSN I to date has shown narrow lines in its spectra (Nicholl et al., 2014; Inserra, 2019), and interaction models are yet to reproduce the observed spectra. Nevertheless, the interaction model is still favoured to reproduce the light curve evolution of some SLSNe I (e.g. Chatzopoulos et al., 2013).

Though supposed to be typical to SLSNe I (Branch & Wheeler, 2017), O II lines have already been seen in other SNe, such as SN Ibn OGLE-2012-SN-006 (Pastorello et al., 2015) and SN Ib SN 2008D (Soderberg et al., 2008). SN 2008D was a normal core-collapse SN with an associated X-Ray flash (e.g Li, 2008), whereas OGLE-2012-SN-006 was interpreted as a core-collapse event powered by ejecta-CSM interaction (Pastorello et al., 2015). The presence of O II spectroscopic features here support the argument that ejecta-CSM interaction may be an important factor in maintaining the high levels of energy required to ionize Oxygen (Pastorello et al., 2015).

3.7.1 Ejecta-CSM interaction scenario

The presence of O II lines could be the consequence of ejecta-CSM interaction (e.g. Pastorello et al., 2015). Mazzali et al. (2016) suggested that X-rays would be required for the non-thermal excitation of O II lines, and these X-rays could originate from interaction (Nymark et al., 2006). However, Chevalier & Fransson (1994) suggested that in ejecta-CSM interaction with a SN density profile consistent with that of an RSG progenitor, as with the majority of Type II, the photons produced would be primarily in the UV-range, thus not providing sufficient non-thermal excitation to ionise the Oxygen.

There are no distinctive narrow emission lines in the spectrum of SN 2019hcc, nor is there any unusual behaviour in the light curve such as multiple peaks or undulations which would suggest collision with a shell (e.g. Nicholl et al., 2016; Inserra et al., 2017). A possible HV component of Hα blue-ward of the main emission could be indicative of early weak/moderate CSM-ejecta interaction - as this interaction may excite the Hydrogen to cause a second, high-velocity absorption feature (e.g. Arcavi, 2017). However, our results on the HV Hα analysis reported in Section 3.6.2 suggest that the presence of a HV Hα is unlikely with the absorption blue-ward than Hα plausibly associated with Si II. The overall Hα profile was also analysed and decomposed in multiple components investigating the nature of the profile. However, it was found that no additional components are required to reproduce the shape aside from the expected ejecta P-Cygni and the narrow Hα line from the host galaxy. Therefore, CSM-ejecta interaction is not a viable source for generating high-energy photons capable of non-thermally excited the O II lines in SN 2019hcc.

3.7.2 Magnetar scenario

A magnetar is a type of neutron star with an extremely powerful magnetic field produced as a result of a very short spin period, and is a potential consequence of the core collapse process. Magnetars are thought to form by fast rotation in the collapsing Iron core (Duncan & Thompson, 1992).

A magnetar could produce the non-thermal excitation required to ionize Oxygen and produce the O II features (e.g. Mazzali et al., 2016). Dessart et al. (2012) suggested the magnetar's extra energy heats material and thermally excites the gas. Alternatively, Gilkis et al. (2016) and Soker & Gilkis (2017) suggested that magnetar-driven SLSNe are powered not by the neutrino-driven mechanism but a jet feedback mechanism from jets launched at magnetar birth. These high energy jets could potentially provide the energy to drive O II excitation at early times, and have been used to link magnetars to Gamma Rays Bursts (GRBs) (Wheeler et al., 2000). The generation of a non-relativistic jet during the early supernova phase is a consequence in both the core-collapse and magnetar models of GRBs (Burrows et al., 2007).

Kasen & Bildsten (2010) suggested that a magnetar birth is likely to happen in a few percent of all core-collapse supernovae, and may naturally explain some of the brightest events seen. Orellana et al. (2018) found that magnetar-powered models can actually generate a diversity of Hydrogen-rich SNe, both ordinary and brighter ones. Through their modelling, it was found that the observational appearance of SNe II powered by magnetars can be extremely varied and can also mimic those of normal SNe IIP. It is suggested that magnetars are preferentially formed in the most massive stars collapsing to a neutron star - with a progenitor mass in excess of $40M_{\odot}$ (Davies et al., 2009). However, it has also been suggested that magnetars do not require massive progenitors to form - alternatives could be a 'fossil-field' model, where a seed B-field is inherited from the natal molecular cloud (Davies et al., 2009) or an interacting binary system which causes spin-up in the collapsing CO-core (Cantiello et al., 2007).

Chen et al. (2017a) found an apparent correlation between magnetar spin-down period and host metallicity from a sample of 19 SLSNe I, indicating that faster-rotating magnetars reside in more metal-poor environments.

Such a correlation could be a consequence of several factors - Martayan et al. (2007) found that massive stars rotate more rapidly at lower metallicity (0.2 $Z/Z_{\odot}$) than solar, whilst Mokiem et al. (2007) found in low metallicity environments mass loss of rotating stars is reduced. However, the spin periods of low metallicity stars and neutron stars would also very likely be affected by other parameters. Generally, the greater the spin period, the greater the peak luminosity (Kasen & Bildsten, 2010; Inserra et al., 2013b), therefore a high metallicity host environment could be correlated with low luminosity explosions powered or affected by a magnetar.

From the equations in Kasen & Bildsten (2010), a grid of B14 ($B/10^{14}$ G) and Pms (the spin

period in ms) of a magnetar as a function of the peak luminosity and rise time was produced, using the code presented in Inserra et al. (2013b). Multiple grids were created by varying the ejecta mass in the model, in order to investigate its effect. Figure 3.17 shows an ejecta mass of 2 $M_{\odot}$ vs. 5 $M_{\odot}$. These ejecta masses were chosen based on the bolometric light curve fitting of SN 2019hcc (using the code of Inserra et al., 2013b) and that of SN 2014G which is one of the other potential Type II showing the 'w'-shaped feature. We retrieved an ejecta mass of approx. 2.3 $M_{\odot}$ and 5.0 $M_{\odot}$, respectively. The fitting was focused on matching the rise time and peak magnitude rather than attempting to accurately reproduce the entire shape of the light curve including the tail, as this is also affected by other factors such as ^{56}Ni or CSM interaction. The range of values in the grid are based on physical motivations. Neutron stars cannot spin faster than a centrifugal breakup limit of <1ms - though actual spin periods have been observed to cut off around 1.6ms, with the suggestion that gravitational radiation losses can limit spinning up beyond this (Chakrabarty et al., 2003). Spin periods of approximately <30 ms are required through modelling for a magnetar energy which produces a significant contribution to the peak luminosity/thermal evolution, as can be seen in the grid in Figure 3.17 - spins below 30ms for a 2 Mej ejecta mass would result in peak luminosities fainter even than SN 2019hcc. The B values are those retrieved from galactic magnetars $\approx 10^{14} - 10^{15}$ G (Woods & Thompson, 2006). This figure shows that increasing the ejecta mass, but preserving B14 and Pms, would result in a longer rise time with the luminosity not as significantly affected. SN 2019hcc's location in this parameter space (see Figure 3.17) shows that a lower luminosity supernova (i.e. not a SLSN) could be produced by a high magnetic field and a relatively lower spin. The blue dashed line represents the core-collapse limit for peak luminosity vs. rise time (Inserra, 2019). Sukhbold & Thompson (2017) also presented a proof-of-concept model of a magnetar mechanism producing Type IIP light curve properties for a range of initial spin periods and equivalent dipole magnetic field strengths, and found for a SNe of peak bolometric luminosity of ∼42.5 log(erg s^{-1}), approximately that of SN 2019hcc, one would expect a Pms of 2ms and a B14 of 100 - this agrees very well with the 5 $M_{\odot}$ model in Figure 3.17.

This modelling suggests it is possible to have a magnetar formed as a remnant without injecting further substantial energy to the supernova event leading to superluminous brightness. This could provide sufficient non-thermal contribution to excite the O II lines which appear in the early spectra. The sub-solar metallicity found in Section 3.2 would not provide support for the tentative hypothesis of a correlation between host environment metallicity and magnetar luminosity, as the metallicity is similar to that of the typical low metallicity environments of SLSNe I, whilst the luminosity is typically lower than that of SLSNe I.

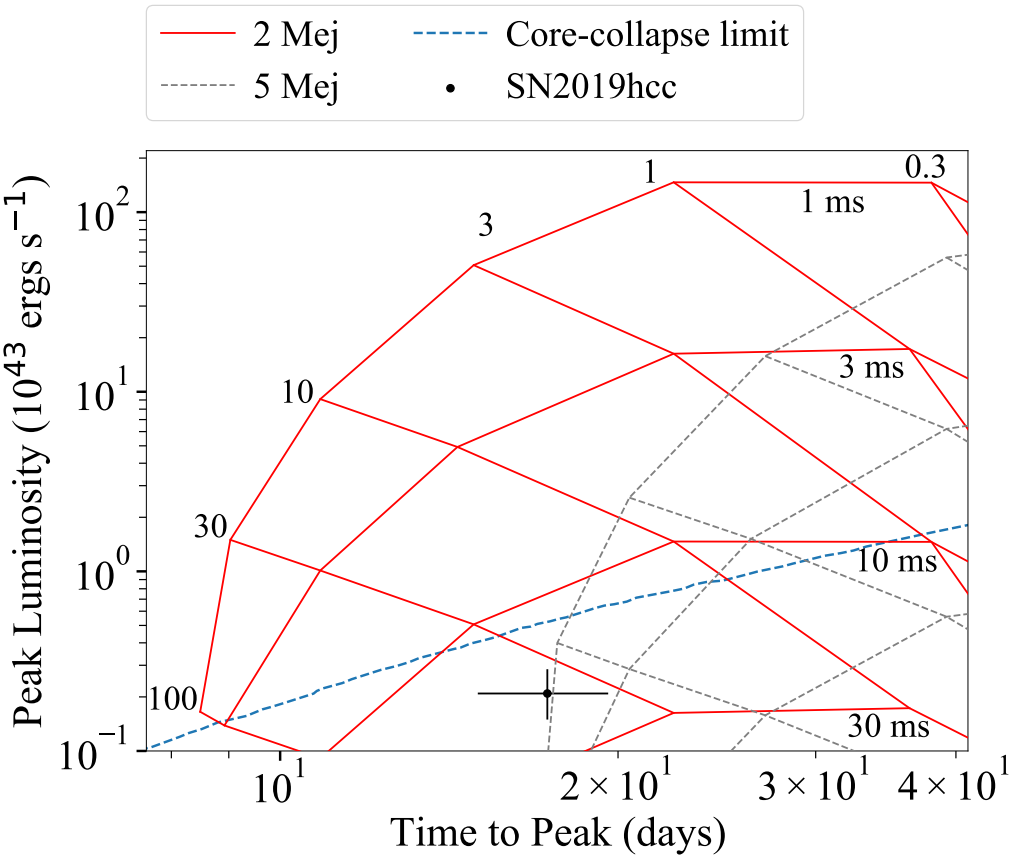

Figure 3.17. The effect of ejecta mass on a magnetar model grid (see text for further information about the grid limits and model used) - with an opacity of 0.34 g cm^{-3} suited for a H-rich ejecta. The grid markers are for Pms in ms and B14 in $B/10^{14}$ G.

3.7.3 Summary

The first spectrum of SN 2019hcc appears relatively featureless aside from a 'w' feature around 4000 Å, characteristic of O II lines typical of SLSNe I. The redder absorption appears to be relatively blue-shifted with respect to SLSNe I. The spectra show a clear Hα profile from +19 days, as well as spectral similarity to various literature SNe II, and the bolometric light curve evolution is that of a SNe IIL. The host metallicity was sub-solar, a value lower than the typical Type II SNe (Gutiérrez et al., 2018). The temperature and colour evolution were typical of a Type II.

Such a 'w'-shaped feature (usually and historically) attributed to O II has never been identified and analysed in SNe II as such and only recognised in SN 2014G thanks to the analysis reported here.

In SLSNe I these lines have been suggested as excited by X-rays produced by a magnetar, or alternatively CSM-ejecta interaction. As there is a lack of any sign of interaction both in the light curve and spectra, aside from a tentative HV component, and potential interaction at late epochs, the CSM-ejecta interaction at early time is disfavoured. We built a model grid, following the work of Kasen & Bildsten (2010) and using the code by Inserra et al. (2013b), and found that a magnetar could be formed as a remnant in a Type II. This would require that the magnetar does not provide enough additional energy to the supernova event to power up the light curve to superluminous luminosities. The magnetar remnant could therefore non-thermally excite the Oxygen whilst not having a significant contribution to the light curve evolution.

The object here presented could then bridge the gap between SLSNe I and normal luminosity core collapse supernovae, as well as reveal more about magnetar formation requirements and mechanisms. Our analysis also shows that a magnetar is a viable remnant of a Type II supernova explosion, the effects on which could be observed in the form of an early 'w'-shaped profile around 4000–4400 Å. This would suggest that such lines are not exclusive to SLSNe I and cannot be used as a sole feature to classify those extreme transients.

Chapter 4

Modelling SN Spectra with TARDIS

4.1 Introduction

This chapter explores TARDIS, a radiative transfer code for modelling SN spectra (see Section 1.3 in Chapter 1 for further details on TARDIS). TARDIS is applied to attempt to model the 'w'-shape in SN 2019hcc. Though this is a brief chapter, TARDIS will also be applied in the next chapter on further modelling the 'w'-shape in SLSNe I.

4.2 SN 2019hcc

Reproducing the 'w' shape of the first spectrum of SN 2019hcc, which is characteristic of SLSNe I rather than SNe II which SN 2019hcc has been identified as, with spectral modelling could cast light on the conditions required to produce it. If the feature is reproduced by modelling Oxygen at a higher temperature than the spectra that display this feature, it would suggest that non-thermal excitation is necessary to produce this feature.

We used TARDIS to model SN 2019hcc's first spectrum. TARDIS was originally designed for Type Ia SNe and recently improved to be used for Type II spectra (Vogl et al., 2019), although the time-varying profile of Hα remains difficult to reproduce. SN 2019hcc was modelled as having a uniform ejecta composition and the results are presented in Figure 4.1. Model spectra were created with various abundances and temperatures and then normalised for comparison with SN 2019hcc. The temperatures were chosen to be around 8100 K (near the measured temperature of SN 2019hcc) or around 14000 K (closer to the SLSNe I used for comparison, see Figure 3.7 in Chapter 3). Higher temperatures up to around 20000 K were also considered to investigate the effect of the temperature on the resulting spectra. The velocity was kept constant for all spectra, at 8000 km/s (start 6000 km/s, stop 8000 km/s), similar to the photospheric velocity measured by Fe II (see Figure 3.14).

SN name	Type	EW (blue/red)	FWHM (blue/red)
SN 2019hcc	SN IIL	1.11±0.05	1.06±0.03
SN 2014G	SN IIL	0.77±0.03	1.03±0.05
SN 1998S	SN IIn	0.94±0.06	0.77±0.04
SN 2010kd	SLSN I	1.39±0.07	1.24±0.02
LSQ14mo	SLSN I	1.61±0.06	1.29±0.04

Table 4.1. Equivalent widths (EW) and full with at half maximum (FWHM) of the absorption of the blue line profile over the red of the 'w' feature.

Elements were investigated individually - with abundances of up to 100% for one element. Starting from the approximate epoch and luminosity of SN 2019hcc, the spectra at approximately 8100 K were modelled by adjusting the input parameters until matching the temperature to that measured from the +7 days spectrum for SN 2019hcc after Cardelli correction, as marked in the figure. The high temperature spectra around 15000 K were found by increasing the luminosity and decreasing the time since explosion in the model.

Modelling revealed that at the lower temperature of 8100 K, Carbon, Oxygen, and Helium are not sufficiently excited to show any lines, therefore they have been omitted from the figure. However, metal (Fe, Mg, Ti) and Balmer lines do show line profiles in this region which could have the potential to reproduce the absorption lines seen for SN 2019hcc. Hydrogen does not have largely significant absorption in this region compared to these metals. Also shown in Figure 4.1 are elements at a higher temperature which is typical of SLSNe I at a similar phase to SN 2019hcc's first spectrum (again see Figure 3.7). These do not match well the overall spectrum of SN 2019hcc but it can be noted that Carbon, Oxygen and Nitrogen produce lines in the region of interest.

The bottom model spectrum of Figure 4.1 shows that at approximately 19000 K a 'w' feature can be produced with a CNO composition (with an even split of abundances). Note that Nitrogen has a relatively small effect in comparison to Carbon and Oxygen in producing this shape. The 'w' feature for SN 2019hcc is slightly shifted compared to the SLSNe I used for previous comparison - such a shift is evident in the red absorption but not the blue. A possible explanation for SN 2019hcc 'w' profile could be a combination of metals at a lower temperature (8100 K) and a non-thermally excited CNO layer. Considering that the temperatures of LSQ14mo and SN 2010kd are around 13000 K (at this temperature CNO does not show a 'w' feature), this could suggest that these SLSNe I require non-thermal excitation to produce this feature.

The feature of SN 1998S looks different to SN 2019hcc - both lines of the 'w'-feature have a different shape. The 'w' feature in SN 1998S is likely caused by Titanium and a combination of other metals like Barium (Faran et al., 2014), which is also seen at redder wavelengths in SN 1998S but not in SN 2019hcc. Titanium does not look responsible for SN 2014G or SN 2019hcc as the ratios and shapes of the two profiles are different. The contribution from the combination of metals including Iron can be seen clearly in SN 2019hcc at 5169 Å, however Iron lines cannot account for

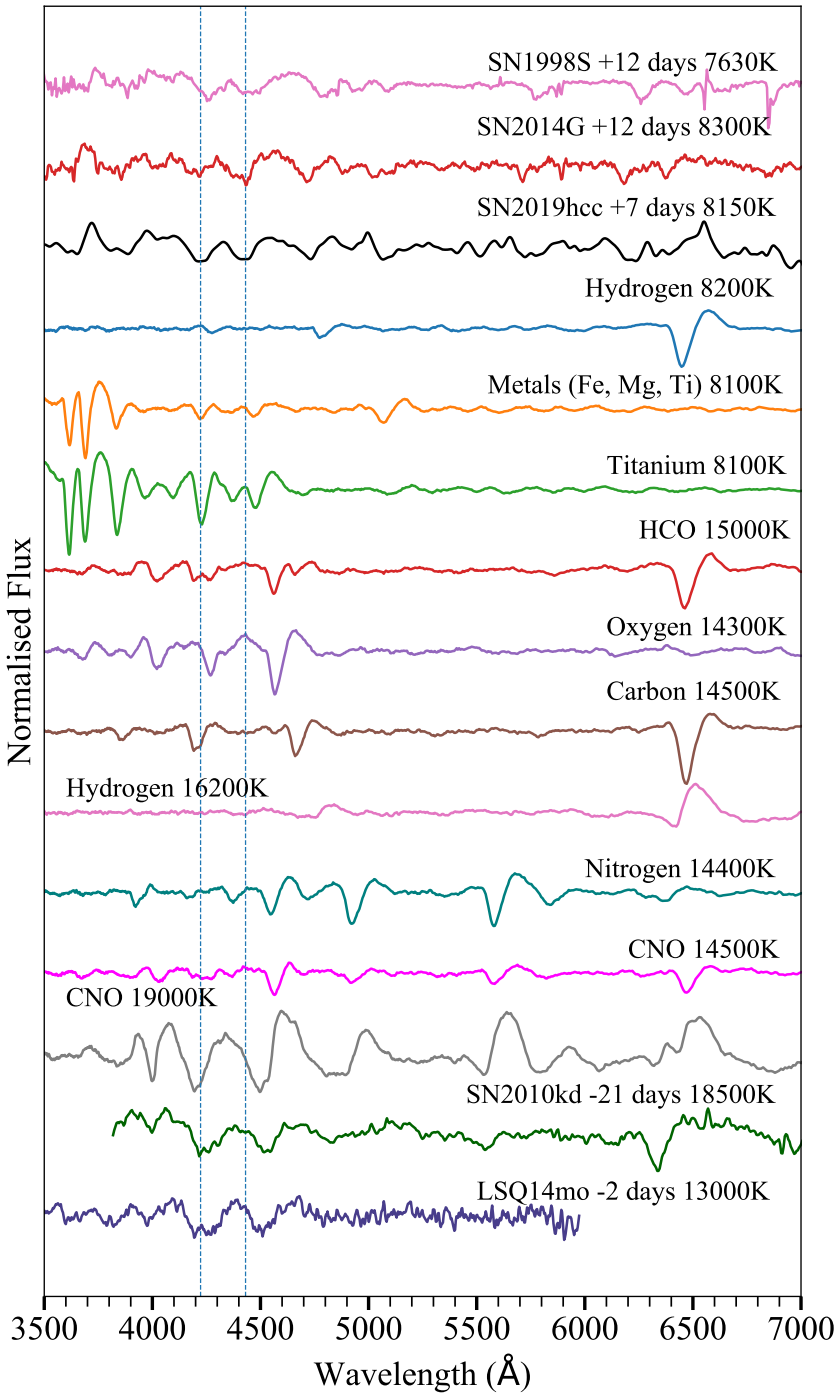

Figure 4.1. The output of the Tardis modelling - spectra with various abundances and temperature. The vertical dashed lines mark the absorption lines for the SN 2019hcc 'w' feature.

the strong absorption in the 'w' feature region. Reproducing the strength of lines would appear to require CNO abundances at higher temperatures - for example Oxygen and Carbon at approximately 14000 K could account for the broader red wing of SN 2019hcc. A combination of CNO at higher temperatures than SN 2019hcc spectrum (i.e. 8100K) and metals at 8100K could be causing the final feature. However, with the tested models it seems impossible to completely reproduce the 'w' feature. Nevertheless, it appears models at T > 14000 K are required to reproduce the strength of the absorption, suggesting a non-thermal excitation responsible for the CNO elements SN 2019hcc at +7 days.

4.2.1 Equivalent Width (EW) and Full Width at Half Maximum (FWHM)

The EW is used to define the strength of a line with respect to the continuum, in order to quantify spectral properties. It is the 'equivalent width' of the line if, rather than a Gaussian, it was a rectangle of the same area and height. This is also a helpful way to compare line strengths. On the other hand, the FWHM is the width of a Gaussian at half its maximum height, and can be an indicator of the velocity distribution. There will be more detail on using and making these measurements in Chapter 5.

EW ratios are measured in order to provide a more quantitative analysis of the feature. The ratio is compared here to give a single value to quantify both absorption profiles of the 'w'-shape. These are reported in Table 4.1 in the form of the EW of the blue line over the red one, as well as the same ratio for FWHM. Of the SNe II, only SN 2019hcc has an EW over 1. The SLSNe I in this table also have a ratio over 1 and are larger with respect to that of SN 2019hcc. In both cases the SLSNe I have a slightly higher FWHM than the SNe II although this is not statistically conclusive due to the small size of the sample. These ratios cannot offer anything conclusive as it suggests all these 'w' features are of a slightly different nature, and could possibly be affected by temperatures, abundances, non-thermal excitation, or the presence of other lines such as metal lines. Possibly SN 2014G could also be non-thermally excited, or have different metal contributions, though its nature looks different to the other SNe as it is the only spectrum with a significantly stronger red line than blue.

4.2.2 Summary

In summary, at temperatures of approximately 19000 K CNO could reproduce the 'w' feature in SN 2019hcc. Some absorption in this region at a temperature of 8100 K could be caused by metal lines e.g. Titanium, however this cannot entirely account for the 'w' feature in SN 2019hcc spectrum. Metals would also produce stronger lines at bluer wavelengths (3500-4000 Å) which are not seen in SN 2019hcc, though these could be obscured by yet more lines in this region. For

thermally exciting CNO much higher temperatures are needed than that observed for SN 2019hcc, therefore non-thermal excitation may be required to produce such features in SN 2019hcc. This appears to also be the case for LSQ14mo and SN2010kd, which show the feature despite LSQ14mo being almost 6000 K short of the required excitation temperature.

He I can also be non-thermally excited, however this excitation usually comes from CSM interaction at the outer boundary of the ejecta (e.g. Chevalier & Fransson, 1994), whereas for the non-thermal excitation of O II in this scenario the exciting X-ray photons would originate from the central engine. The ejecta Helium region would be further away than the Oxygen region for these central high-energy photons which, in our proposed scenario, would explain the absence of He I in the first spectrum of SN 2019hcc. Additionally, though the abundance of Oxygen in the progenitor is relatively low compared to other elements such as Hydrogen, the first spectrum is relatively featureless so O II is not competing with other lines in this region.

Combined with the analysis in Chapter 3, we suggest that the 'w' feature seen in SN 2019hcc's first spectrum could be due to a combination of both non-thermally and thermally excited metal lines, with the non-thermal excitation possibly produced by a magnetar. The following chapter will look further at this 'w'-shape in SLSNe I, including further applications of modelling using TARDIS.

Chapter 5

On the Nature of O II lines in Type I Superluminous Supernovae

5.1 Introduction

The early spectra of Type I superluminous supernovae (SLSNe I) show a distinctive 'w'−shape in the 4000−4600 Å region, commonly attributed to ionized Oxygen (O II). These lines are often the defining characteristic used to identify this SN type.

The aim of this Chapter is to explore the varying nature of this 'w'−shape, in SLSNe I with respect to the SN characteristics such as temperature, phase, or subclass (Fast or Slow). This in turn could shed light on the mechanisms which produce the w-shape, and the chemical compositions of SLSNe I ejecta.

Here we examine a sample of 30 SLSNe I (16 SLSNe I-Fast, 14 SLSNe I-Slow) and measure the pseudo-Equivalent Width (pEW), and Full Width at Half Maximum (FWHM) of each component of the 'w'−shape, together with the blackbody fit to the photometry. We then look for a relationship between these measurements, and their ratios. To explore the nature/composition of such lines we also use TARDIS to create spectral models for Oxygen, Carbon, and Iron group elements. The pEW/FWHM measurements of these spectral models are compared to the observed spectra to look for constituents of the 'w'−shape.

5.2 SLSN I Sample

The SNe spectra in the sample (see Table 5.1) were selected based on the presence of the 'w'−shaped feature at 4200−4400 Å, in the form of a clear double absorption in the relevant region, and with an evolutionary phase $\phi < 10$d from maximum light, when the contribution of single

Table 5.1. The SLSNe I used in the sample. Reference papers from which the spectra are sourced are: the Palomar Transient Factory (PTF, Quimby et al., 2018), the Zwicky Transient Facility (ZTF, Lunnan et al., 2020), the Pan-STARRS1 Medium Deep Survey (PANSTARRS, Lunnan et al., 2018b), the Dark Energy Survey (DES, Angus et al., 2019), the Public ESO Spectroscopic Survey of Transient Objects programme (ePESSTO+, Smartt et al., 2015), and source otherwise stated.

Name	Type	MJD	Redshift	Reference
SN 2005ap	Fast	53436	0.283	Quimby et al. (2007)
SN 2006oz	Slow	54061	0.396	Leloudas et al. (2012)
SN 2009jh	Fast	55068	0.35	PTF
SN 2013dg	Fast	56453	0.265	PTF
SN 2016aj	Fast	57403	0.485	Wang et al. (2019)
SN 2019enz	Fast	58616, 58627	0.22	ePESSTO+
SN 2019nhs	Fast	58722	0.19	ePESSTO+
SN 2020xga	Slow	59159, 59169, 59170	0.44	ePESSTO+
SN 2021bnw	Slow	59249	0.098	ePESSTO+
SN 2022npq	Slow	59811	0.26	ePESSTO+
PTF09cnd	Fast	55059, 55068, 55089	0.259	PTF
SN 2018bgv	Slow	58255	0.08	ZTF
SN 2010gx	Fast	55273, 55276	0.23	PTF, Pastorello et al. (2010)
SN 2011kg	Fast	55922, 55926	0.192	PTF
SN 2015bn	Slow	57070, 57071, 57078, 57092, 57093, 57099, 57108	0.1136	Nicholl et al. (2016)
SN 2016eay	Fast	57528, 57532, 57539, 57545, 57552	0.102	Kangas et al. (2017); Yan et al. (2017a)
SN 2017gci	Slow	57982, 57984, 57987	0.0873	Fiore et al. (2021)
SN 2018bym	Slow	58269, 58281, 58286	0.28	ZTF, Hosseinzadeh et al. (2022)
SN 2018hti	Slow	58428, 58429, 58430, 58433, 58437, 58440, 58446, 58458, 58460	0.0614	Fiore et al. (2022)
DES14X3taz	Slow	56683, 56694	0.608	DES
DES15S2nr	Fast	57283, 57306	0.22	DES
iPTF13ajg	Fast	56390, 56391, 56399	0.7403	Vreeswijk et al. (2014)
LSQ14bdq	Slow	56781, 56783, 56784	0.345	Nicholl et al. (2015b)
LSQ14mo	Fast	56688, 56688, 56694, 56694	0.256	Leloudas et al. (2015b); Chen et al. (2017c)
PTF09atu	Fast	55034, 55068	0.501	PTF
PTF10aagc	Slow	55504, 55505, 55507	0.2067	PTF
PTF12mxx	Fast	56279	0.3274	PTF
PS1-11ap	Slow	55585, 55598, 55612	0.524	PANSTARRS
SN 2016ard	Fast	57449	0.2025	Blanchard et al. (2018)
PTF12dam	Slow	56067, 56068, 56069, 56071, 56092, 56096	0.108	Nicholl et al. (2013); Chen et al. (2015) Vreeswijk et al. (2017), PTF

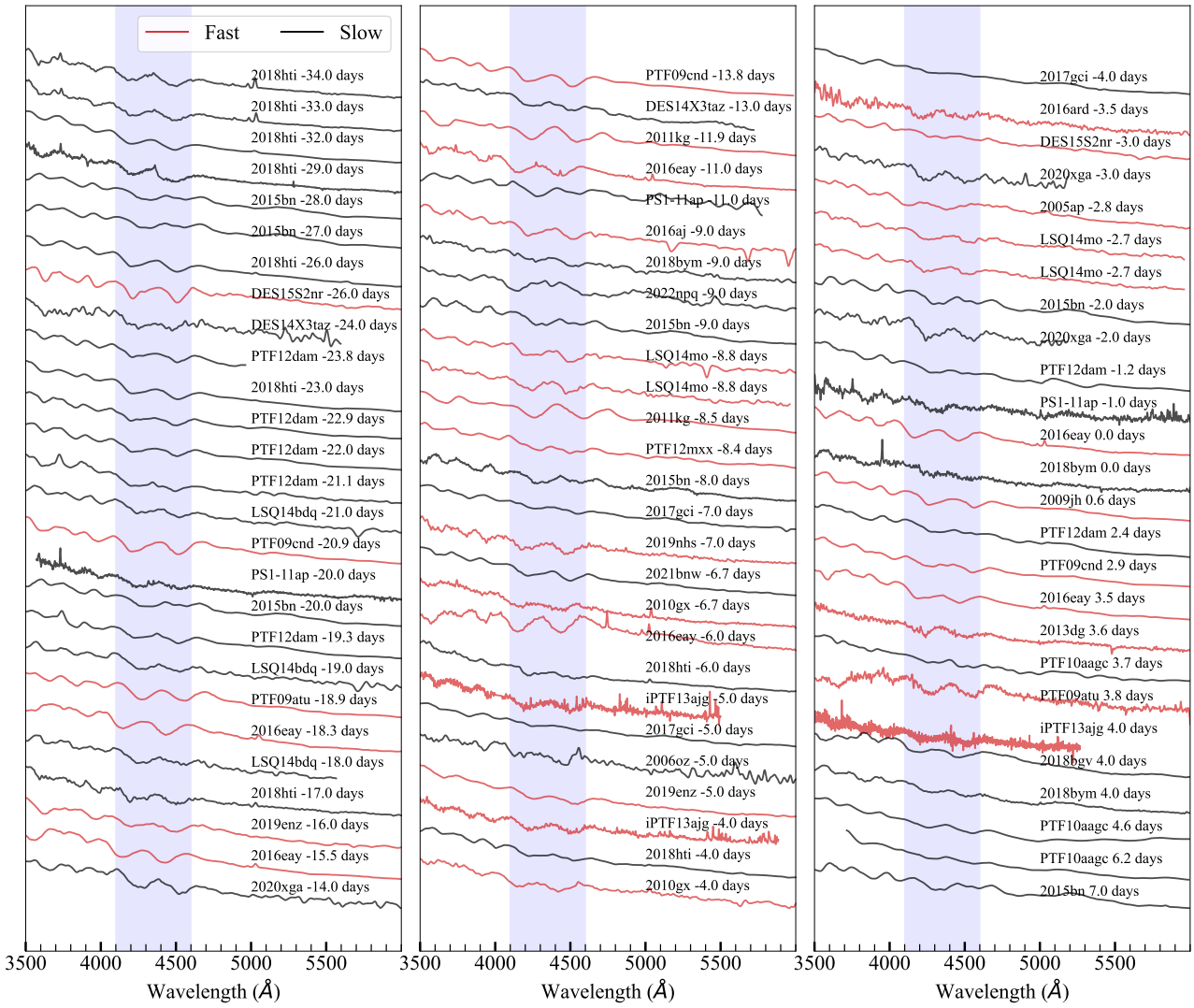

Figure 5.1. The full spectral sample, doppler shifted and smoothed with a 5-sigma gaussian filter, ordered by phase. The red spectra correspond to the 'Fast' class of SLSNe I, and the black to the 'Slow', and the shaded region defines the 'w'-shape region. The wavelength is in the rest frame.

ionised and neutral metals is not predominant. A clear absorption means a 3σ intensity of absorption w.r.t. the background in the 4100 – 4600Å region (shown as the shaded region in Figure 5.1). The majority of SLSNe I show this feature in pre-peak spectra. SLSNe I which were excluded did not have spectra in the correct phase or the signal-to-noise (S/N) was less than 5 in the above region. SLSNe I with a S/N < 5 would need heavy rebinning which would alter the line analysis. Excluded spectra are not included in Table 5.1. Based on these criteria, the sample considered in this Chapter consists of SLSNe I from the Palomar Transient Factory (PTF; Quimby et al., 2018), the Dark Energy Survey (DES; Angus et al., 2019), the Zwicky Transient Facility (ZTF; Lunnan et al., 2020), and the Pan-STARRS1 Medium Deep Survey (Lunnan et al., 2018b), with the addition of other single object studies which meet the criteria. See Table 5.1 for the full sample of SLSNe and their sources. The phases with respect to maximum light were sourced from the same papers as the samples. Hitherto unpublished or classification spectra taken under the advanced Public ESO Spectroscopic Survey of Transient Objects programme (ePESSTO+; Smartt et al., 2015) were also included, and the phases w.r.t. maximum light were calculated from a fit to the Asteroid Terrestrial-impact Last Alert System (ATLAS; Tonry et al., 2018a; Smith et al., 2020) light curves with the phenomenological equation from Bazin et al. (2009), for this chapter. The unpublished spectra were all sourced from ePESSTO+ as can be found in Table 5.1, and there was a total of 8 unpublished new spectra from ePESSTO+. The other 72 spectra were sourced from literature.

Figure 5.1 displays the full spectral sample, doppler shifted according to the redshift found in the literature and de-reddened according to the Cardelli extinction law (Cardelli et al., 1989). The Milky Way extinction was taken from the all-sky Galactic dust-extinction survey (Schlafly & Finkbeiner, 2011), with Rv = 3.1. The Galactic reddening values for each SN were found on the NASA/IPAC Extragalactic Database*. There are 80 spectra, 33 SLSNe I-Fast and 47 SLSNe I-Slow. Only the spectra used in the measurements are plotted in Figure 5.1 and listed in Table 5.1. The Fast and Slow subclasses of SLSNe I are defined based on the speed of decline of the light curve (e.g. Inserra et al., 2018; Quimby et al., 2018; Gal-Yam, 2019a) (See also Chapter 1 Section 1.8.1). Note that this division is contested, and e.g. De Cia et al. (2018) found no clear evidence for such a clear division of subclasses. The spectra are ordered by phase and colour-coded according to whether they are fast or slow, and smoothed by a 5σ Gaussian filter from scipy.ndimage (Virtanen et al., 2020). A Gaussian filter performs a weighted average of surrounding data points based on a Gaussian distribution, with σ defining the amount of smoothing, and is similar to a moving average. This is for plotting purposes only, all later measurements were done on unsmoothed spectra. The 5σ value is the standard deviation of the Gaussian kernel used in smoothing. It was chosen by varying the sigma until the desired level of smoothing was seen, namely reducing noise in higher S/N spectra whilst preserving features in lower S/N spectra. These spectra all display the 'w'−feature usually associated

*The NASA/IPAC Extragalactic Database (NED) is funded by the National Aeronautics and Space Administration and operated by the California Institute of Technology. Found at http://ned.ipac.caltech.edu

with O II[†]. The 'w'-shape is seen in all SLSNe I in this timeframe, excluding rare exceptions such as SN 2020wnt (Gutiérrez et al., 2022).

We first retrieved the spectral energy distribution (SED), from photometry, at the same MJD as the spectra. This was done by interpolating existing photometry data with Gaussian Processes, and where possible the magnitudes at same MJD as the spectra were then measured from the interpolated photometry. The photometric magnitudes were converted to flux for each band and the temperature was then measured from a blackbody fit to the SED for the same night as the spectrum was taken.

For measurements of temperatures where $z > 0.35$ (i.e. iPTF13ajg, LSQ14bdq, DES14X3taz, PS1-11ap), there was an additional 10% uncertainty added due to high redshifts - this error is based on the analysis in Inserra & Smartt (2014) where k-corrections were calculated for a sample of SLSNe at a range of redshifts. At lower redshift there is not a significant difference between the photometry with or without k-correction.

Photometry in at least 4 bands for the epoch of the spectrum in question was not found for SNe 2009jh, 2013dg, 2021bnw, 2005ap, 2006oz, 2016ard, 2016aj, PTF10aagc, and PTF09cnd. Additionally there were not sufficient bands for the ePESSTO+ spectra: SN 2019enz, SN 2019nhs, SN 2020xga, SN 2021bnw, and SN 2022npq. Alongside this, PTF12mxx was excluded as one of the bands had too few points to interpolate for the phase being considered.

For cases where photometry was not available, the blackbody was fit to the spectral continuum in the full wavelength range available minus 100 Å on either end to take into account the quantum efficiency of the grism, which has a below average response at the edges, and where the association between pixel and wavelength is more uncertain leading to less precise wavelength calibration. Spectra were excluded if the blackbody fit to the spectra was giving an unphysical temperature e.g. greater than $\sim$25000$-$30000K or lower than $\sim$8000K (out of range of temperatures measured for SLSNe I in literature), or if they were significantly different from literature measurements for the same SNe. For spectra with photometry available, the temperature from the blackbody fit to the spectra was compared to the temperature measured from the photometry, with an average temperature difference of 2600$\pm$1700 K (where the error is the average propagated error from the spectral fitting and the photometry in quadrature). Of this sample, 8 spectra (of which 5 belonged to PTF12dam) of 61 total had an unphysical blackbody fit to the spectra (though for these spectra the photometry temperature measurement was available and these were taken instead), and none from the group with no photometry available, which was a notably smaller sample. Unphysical fits to the continuum of the spectra were largely due to the spectra not covering the wavelength where the blackbody curve had its characteristic peak. Differences between blackbody curves at various temperatures are smaller the further you are from the peak wavelengths, and therefore there is greater uncertainty in fitting in these wavelength ranges.

[†]These spectra were taken from the Weizmann Interactive Supernova Data Repository (WISeREP) (WISeREP Yaron & Gal-Yam, 2012).

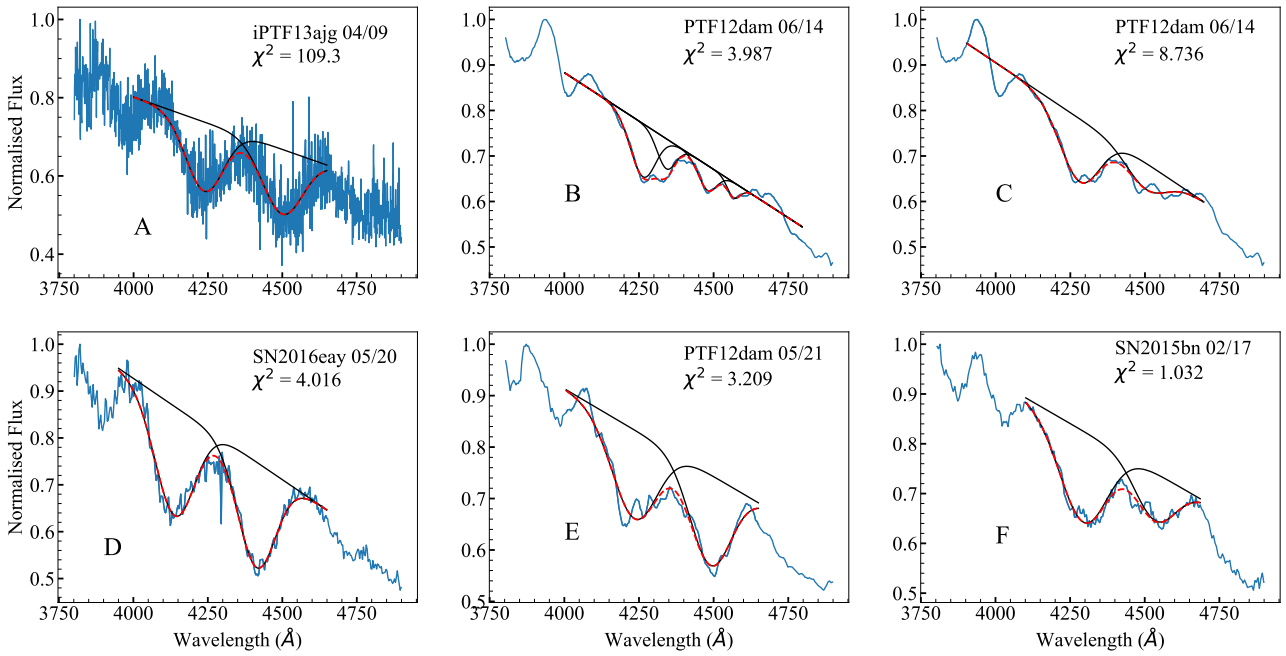

Figure 5.2. Gaussian fits to the 'w'-shape feature in various SLSNe with different profiles and S/N. The original spectrum is shown in blue, the final composite fit in dashed red, and the individual Gaussian components of the final fit in black. Shown above are Panel A, demonstrating a fit with low S/N. Panel B shows an example of a case where four Gaussians provided a slightly better fit than two (Panel C). However, Panels E and F show cases where, though the line profiles do not show a perfect Gaussian, the 2 Gaussian approximation provided appears acceptable. Panel D shows a case with both line profiles displaying a Gaussian. The wavelength is in the rest frame, and the experimental χ^2 test statistic is used to measure the goodness of fit.

5.3 Investigating the Evolution of FWHM and pEW Ratios

SLSNe I vary from each other in physical quantities such as explosion energy, or the density profile of the ejecta, as well as in elemental abundances. From an observational point of view, they can be further divided into two subclasses: Fast and Slow (refer to Chapter 1 Section 1.8.1 for further detail). Slowly-declining events have decline rates which initially resemble the ^{56}Co decay, and the post-peak spectroscopic evolution changes slowly (e.g. Inserra et al., 2017) - such as PTF12dam or SN 2015bn (Nicholl et al., 2015a) in our sample. The others are significantly faster-declining events such as SN 2005ap (Quimby et al., 2007) or LSQ14mo (Leloudas et al., 2015b; Chen et al., 2017c) in our sample. Henceforward these shall be referred to as Slow and Fast SLSNe I respectively (e.g. Inserra et al., 2018; Quimby et al., 2018; Gal-Yam, 2019a). For the sample in this paper, SN 2016eay (an intermediate event) has been classed as a Fast SLSN I following its sub-classification in Inserra et al. (2018) and Quimby et al. (2018). The sub-classification of the SNe in the sample come either from the relevant literature or, where not available, following the criteria set out in Inserra (2019).

The shape/nature of the classic 'w'-shape, attributed to a blended forest of lines from O II (Gal-Yam, 2019a), varies throughout the SN evolution, and between SNe, and a measure of these changes would be useful to quantify the evolution with phase and temperature. The EW is used to define the strength of a line with respect to the continuum, in order to quantify spectral properties. Many regions in a spectrum may be formed of a number of blended lines, and the true underlying continuum level is difficult to identify. Therefore the adopted reference continuum when measuring the EW does not represent the true continuum. Hence, this measurement is referred to as a 'pseudo' EW (pEW, e.g. Folatelli, 2004; Garavini et al., 2007; Nordin et al., 2011a,b; Gutiérrez et al., 2017a). The Full Width at Half Maximum (FWHM) can also be considered when attempting to quantify spectral properties, as FWHM is an indicator of the velocity distribution of the element/ion analysed. However, Gal-Yam (2019a) suggested apparent absorption feature widths for the 'w'-shape are dominated by line density and not by doppler broadening. Measuring the FWHM might be an oversimplification considering the 'w'-shape is a blend of individual lines, however, it is a first approach measurement of the system and its feature and diagnostic of line shape (e.g. Chomiuk et al., 2011; Quimby et al., 2018).

We measured the pEW and the FWHM, in an attempt to encompass the characteristic of these lines. The 'w'-shape has two absorption components, one bluer and one redder, and these shall henceforward be referred to as the line profiles. These two lines were chosen as they are the best sampled lines with the highest intensity. The pEW and FWHM measurement was made for both line profiles. The ratio of the blue over the red line profile was taken alongside individual measurements for each profile, for an additional comparison between different SNe. A single value makes it easier to track behaviour and correlations with temperature or phase, providing a further layer of information.

5.4 TARDIS Modelling

There exists a significant body of modelling work in the literature of previous modelling of this 'w'-shape in SLSNe I, with the features attributed to ions at different temperatures and velocities across works (e.g. Quimby et al., 2007; Dessart et al., 2012; Mazzali et al., 2016; Quimby et al., 2018; Könyves-Tóth et al., 2020). As there are no single unblended features in these spectra, spectral synthesis code is required to determine the chemical composition.

TARDIS (Kerzendorf & Sim, 2014, and see Chapter 4) was used to create model spectra for individual elements/ions such as Oxygen to explore their behaviour, and to model the Slow SLSN I SN 2015bn (Nicholl et al., 2016) and the Fast LSQ14mo (Leloudas et al., 2015b; Chen et al., 2017c), chosen as prototypical SNe of their subclasses due to the richness of their spectroscopic database showing the 'w'-shape. To identify the contributions in this region, models with the following elements were produced at various temperatures: Oxygen, Carbon, Nitrogen, Iron, Silicon, and Titanium, all of which produce absorptions/emissions in the $3000-5000$ Å region.

The velocities needed for the models were retrieved from the literature when available (see Table 5.1), or measured following the same methodology used for the FWHM. Velocities reported for SN 2015bn were approx 6500 km/s and 8500 km/s for Fe II λ4924 and O I λ7774 respectively (Nicholl et al., 2016), and 11000 km/s measured directly from the spectra for O II lines. In the case of LSQ14mo, 10000 km/s for both O I and Fe II λ5169 were reported (Chen et al., 2017a). Adjusting the input velocity for the TARDIS model from 8000 km/s (approx. velocity of SN 2015bn) to 10000 km/s (approx. velocity of LSQ14mo) does not have a significant effect on the features, apart from a small shift in features of 10s of Angstroms. We then used an input velocity with a gradient from 9000 km/s to 10000 km/s, and a density profile starting at $\rho = 1e10^{-12}$, with a power law exponent of of -2, assuming a steady wind (see Sorokina et al., 2016).

Alternatively Mazzali et al. (2016) used a density exponent of -7 for a steeper density profile as they noted a steady state regime with an exponent of -2 cannot explain some of the observables of SNe. Notably, the spectra of many SLSNe are seen to become redder with time as the luminosity evolves, which would not be expected from a steady state regime. A change in the density profile or in the distribution of mass could also have an effect on the velocity distribution, which otherwise cannot be changed in TARDIS as the assumption of homologous expansion means the velocity is calculated based on position. Therefore, a density exponent of -7, and -4 as intermediate between the two suggested profiles, were also investigated to consider the effect on the model spectra. It was found that increasing the steepness of the density exponent to -4 and -7 decreased the pEW of the lines, with no clear effect on the FWHM and hence the velocity, whilst the overall evolution of the pEW and FWHM remained the same. As a result, it can be assumed that varying the density exponent would not have a significant effect on the conclusions drawn from these model spectra.

Models consisting only of Oxygen were produced with TARDIS at temperatures 11000-18000 K. It was found that the contribution from Oxygen begins to diminish around 14000 K and disappears by $\sim$11000 K (see Figure 5.3), with the blue profile disappearing first.

5.4.1 Spectra measurements

The pEW/FWHM (strength/velocity) values were measured using iraf. Measurements were made by fitting a double Gaussian to the flux spectra whilst varying the continuum across five independent measurements The measurements were changed with different start/end wavelengths chosen for the fitting, and varying the level of flux in the continuum, in order to produce different fits. The final values were taken as the mean, or mean of the ratios, for each measurement, and the errors were taken as the standard deviation across these results. Spectra were flux-corrected as described in Section 5.2. For a few SNe (e.g. SN 2015bn and PTF12dam) a clear double component in each line profile of the 'w'-shape was identified. In such cases, a fit comprising of four Gaussians, with the pEWs and FWHMs for each line profile added together, was attempted. The resulting ratios were

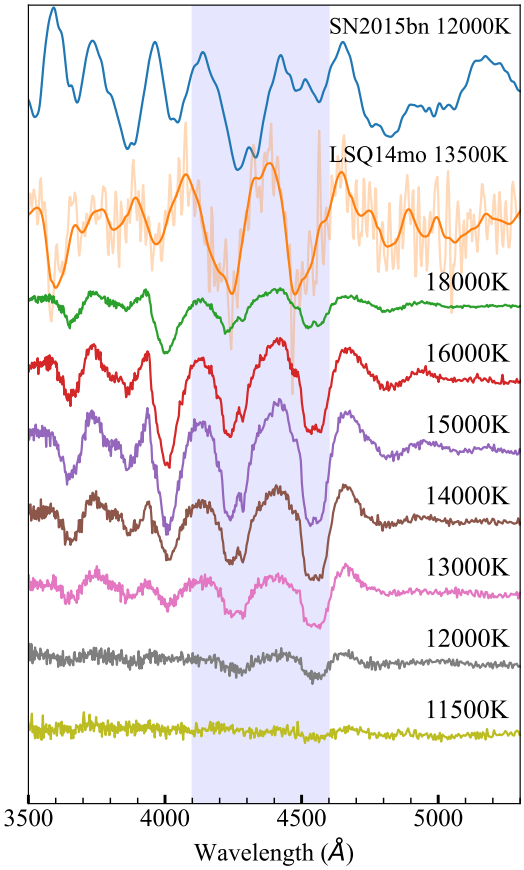

Figure 5.3. Oxygen models produced with TARDIS (at a range of temperatures, and an expansion velocity of 10000 km/s), and a spectrum for LSQ14mo and SN 2015bn. The spectra for LSQ14mo and SN 2015bn have been smoothed by a Gaussian filter of 5σ for ease of comparison, however as LSQ14mo has a lower S/N spectrum, the original has also been plotted behind the smoothed spectrum, for reference. LSQ14mo to Oxygen can approximately reproduce the features of LSQ14mo but not the double absorption in each line profile of SN 2015bn. The wavelength is in the rest frame.

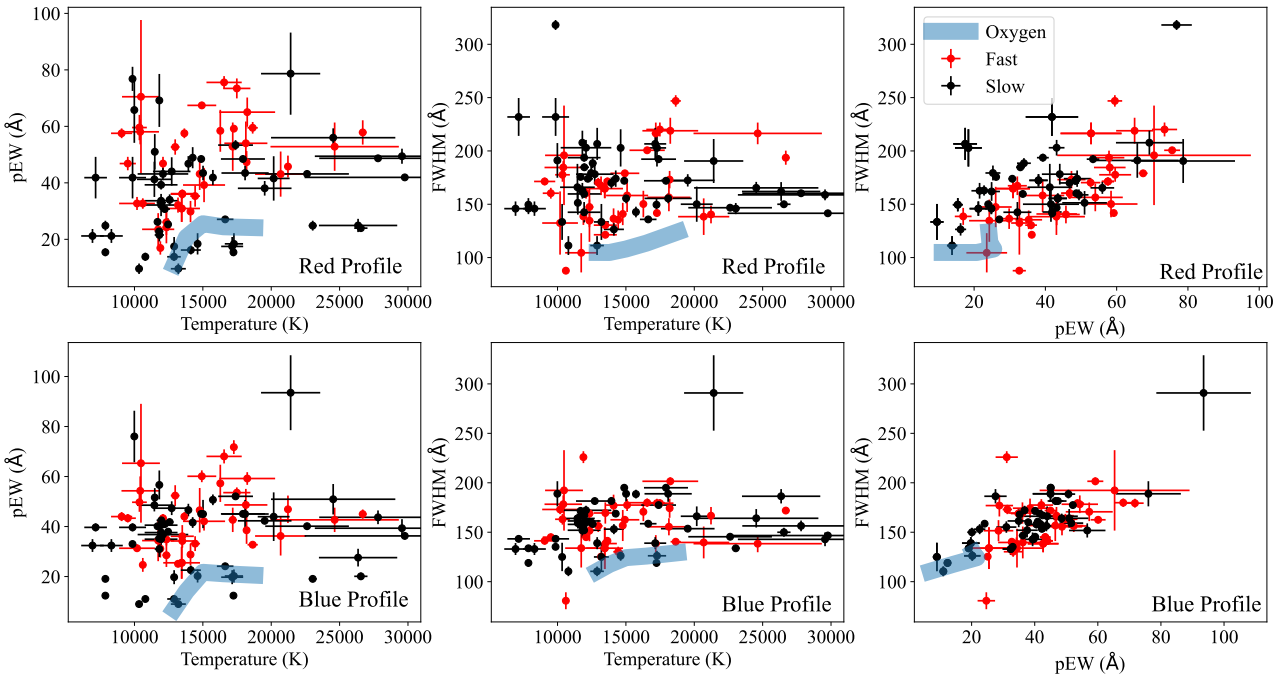

Figure 5.4. Measurements of pEW and FWHM, plotted against each other and against the temperature, for both the blue and red profile of the 'w'-shape for the SLSNe I sample. Red points represent the Fast SLSNe I whilst black are the Slow. The strongest correlation by eye is between pEW and FWHM in each profile, with less obvious correlation of both measurements with temperature in each profile. Also included are the measurements from the model Oxygen spectra created with TARDIS, which are shown in blue. The EW and FWHM of both line profiles for the real spectra are overall greater than the TARDIS Oxygen models, and the trends measured from these models are not entirely reproduced by the real spectra.

compared to the results from the 'standard' two Gaussian fits. The difference in the FWHM and pEW ratios between the two methods were within the uncertainties of both methods. Therefore, two Gaussians were used for all spectra.

Figure 5.2 shows a small sample of spectra encompassing line profiles with different S/N levels and the double-Gaussian fitting to the 'w'−feature for such cases. This sample includes a spectrum with high S/N (Panel A), spectra with some small additional variation in each line profile (Panels D, E and F), and a later spectrum for PTF12dam where four Gaussians were fitted to better match the shape seen (Panel B – $\chi^2 = 3.987$). The latter can be compared with the two Gaussian model at the same epoch (Panel C – $\chi^2 = 8.736$). As displayed and previously mentioned, this approach provides a good fit of the features. It is worth interrogating the double absorption in each profile as seen in SN 2015bn and PTF12dam, as both two and four Gaussians can provide a good fit. For the SN 2015bn spectrum, the wavelength difference between the center of the double absorption of each profile is approximately 60 Å and 80 Å for the blue and red profiles, respectively. The average resolution for the spectrum is 13 Å (Nicholl et al., 2015a), which would suggest this is a real feature.

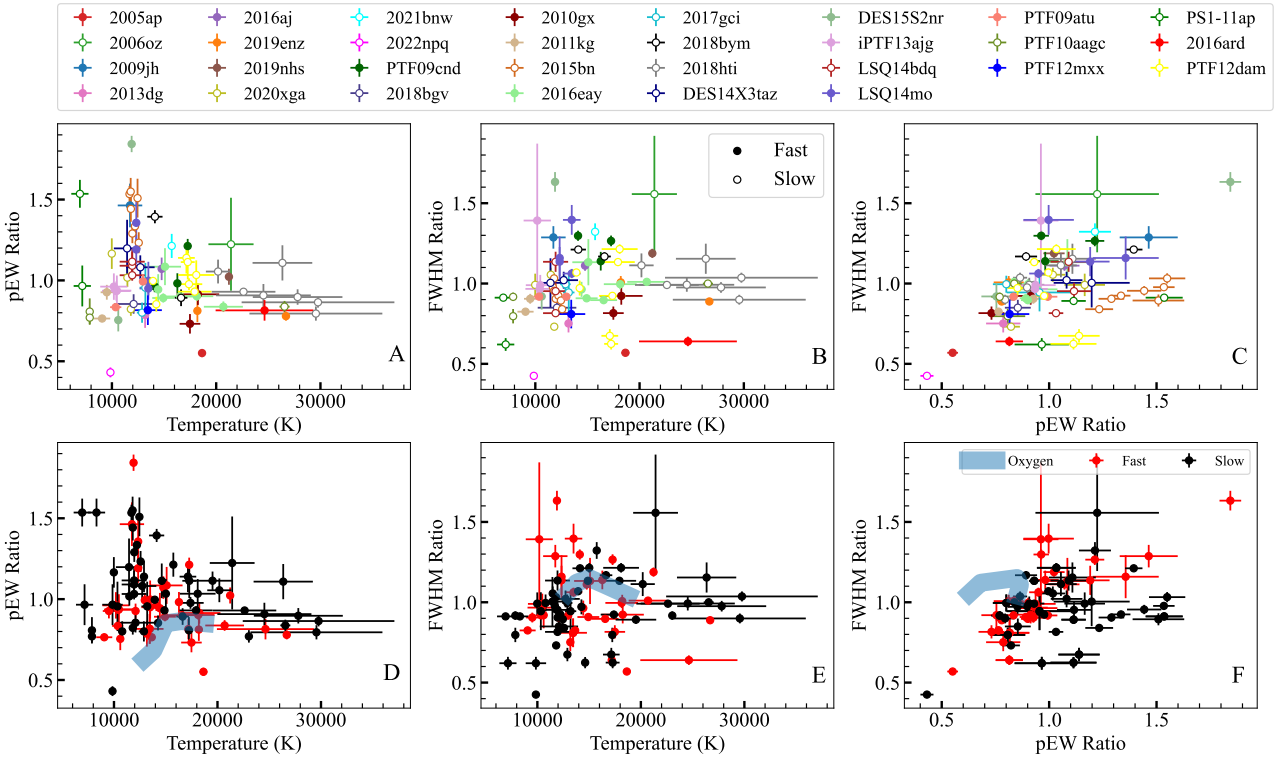

Figure 5.5. Measurements for pEW and FWHM ratios (blue profile over red) as opposed to individual profile measurements. Panels A-C show measurements for the spectral sample highlighting individual SNe, with full circles for the Fast subclass, and open for the Slow. Panel A: pEW vs. Temperature, with a Spearman correlation coefficient of -0.24. Panel B: FWHM vs. Temperature - the correlation is weaker than for pEW, with a correlation coefficient of 0.09. Panel C: pEW vs. FWHM - there is a significant positive correlation of 0.79 for Fast SNe, while only 0.22 for Slow SNe, with an overall coefficient of 0.48. Panels D-F show the same variables, but data are split into Fast (red) and Slow (black) to highlight their different behaviour. Also included are the measurements of pEW and FWHM from the TARDIS model spectra for Oxygen only shown in blue.

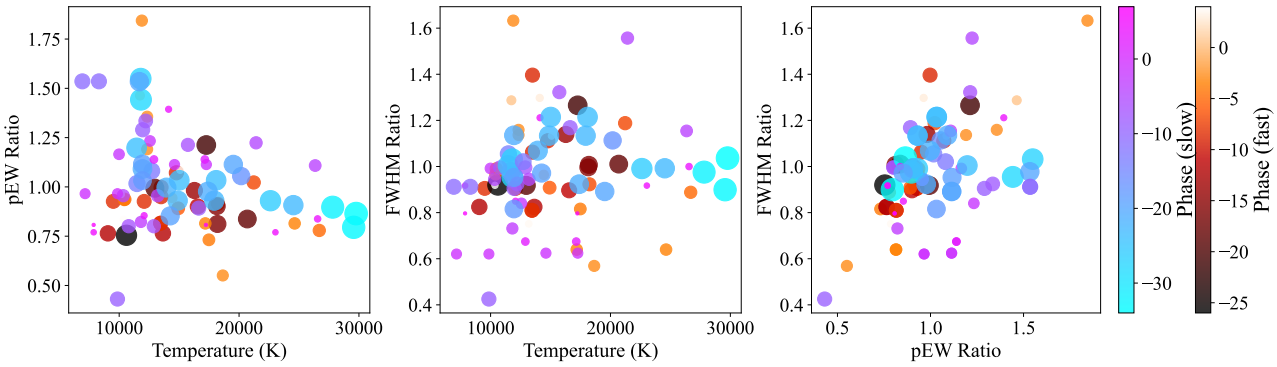

Figure 5.6. The evolution with temperature of the SLSN sample ratio measurements split into Fast and Slow subclasses, with the phase (days past maximum) represented in the colourbars. The size of the points are also scaled to the phase, with smaller points representing later phases.

Figure 5.4 shows the blue and red profile individual measurements (pEW and FWHM) for the full sample of 30 SLSNe, as a function of each other and as a function of temperature. The sample is split into red (Fast) and black (Slow). The strongest correlations appear to be FWHM against pEW for both profiles (see 5.4.2), with less clear correlation in both profiles for pEW/FWHM with temperature.

Figure 5.5 shows these same correlation panels, except with the ratio (blue over red profile pEW and FWHM). Panels A-C show the individual SNe, with open circles representing the Slow SLSNe whilst the filled circles represent the Fast. Panels D-F show the same data but with the sub-classification in Fast and Slow (red and black respectively) to highlight the split between the two SN types. A further visual correlation of such measurements with the SN phase (which is directly linked to the temperature) is reported in Figure 5.6.

The blue 'Oxygen' label refers to the evolution of the TARDIS model presented in Section 5.4. The pEW[‡] and FWHM of the absorption at approximately 4200 Å and 4500 Å were measured for the model spectra of Oxygen - again using iraf, fitting a double Gaussian five times and taking the mean of the ratio of blue over red, as well as the individual measurements, and the standard deviation of these values as the error. These are reported in Figures 5.4 and 5.5 as blue regions.

From Figure 5.5 it can be noted that SN 2015bn, considered as prototypical of the Slow subclass (Nicholl et al., 2015a; Inserra, 2019), is actually one of a minority of Slow SLSNe which fall outside the region of most spectra, see Panels C and F, alongside PS1-11ap, and a subset of spectra for PTF12dam. These SNe follow the same trend with a slight shift to lower FWHM ratios and higher pEW ratios. Otherwise, the majority of the Slow subclass fall into the same region as Fast when considering pEW vs. FWHM ratios.

[‡]We note that in this case, this is a true EW, as this measurement is coming from a model spectrum with a well-defined continuum. However, for the sake of consistency and notation across the Chapter, we will keep referring to it as pEW also in the case of model spectra.

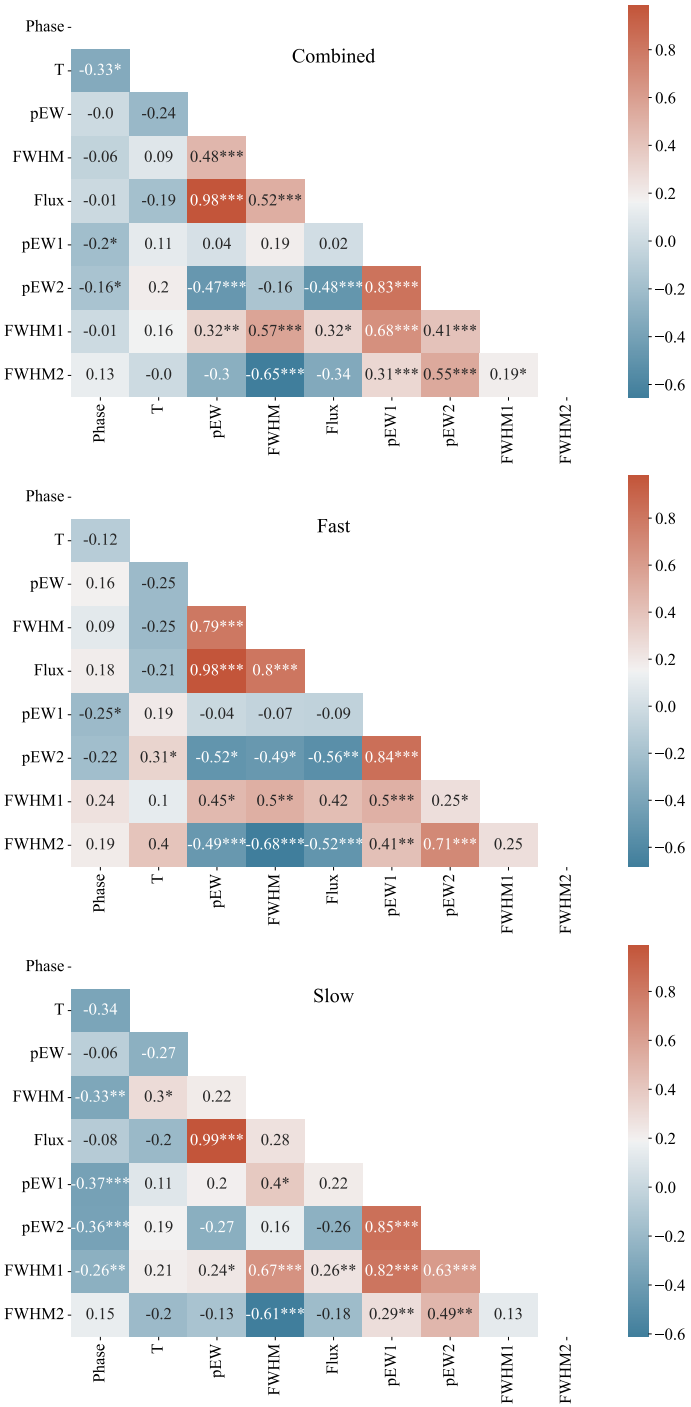

Figure 5.7. Triangular correlation matrices of the Spearman Correlation Coefficient for measurements of the 'w'-shape for the spectra. These measurements include the ratios of blue profile over red for pEW, FWHM, and Flux - these are simply labelled pEW, FWHM and Flux on the above panels. Also included are the pEW and FWHM of each profile, i.e. the blue (pEW1, FWHM1) and red (pEW2, FWHM2). The SN phase from maximum light was taken from literature (Phase, measured in days), and the spectral temperature (T, measured in K) is from the blackbody fit to the continuum. The correlation matrices are split into correlations for the full sample in the top panel, then split into Fast or Slow SLSNe in the lower two panels.Asterisks denote statistical significance: * for p-values less than 0.05, ** for less than 0.01 and *** for less than 0.001.

5.4.2 Correlations

To provide a more quantifiable approach for the trends observed in Figures 5.4 and 5.5, Spearman correlation coefficients were calculated for all pairs of variables and presented via a correlation matrix in Figure 5.7. P-values denoting statistical significance are represented as asterisks: * for p-values less than 0.05, ** for less than 0.01 and *** for less than 0.001. A smaller p-value gives greater confidence in the correlations, and a p-value of 0.05 or 5% is typically the conventional cut-off for statistical significance. A p-value of less than 0.01 is viewed as highly statistically significant, and the values 0.01 and 0.001 were chosen as increasing levels of confidence. However, it has been suggested that this cut-off of less than 0.05 should not be used to confidently conclude the significance of the result, and p-values should be considered a continuum where simply the lower the p-value the greater the confidence (Andrade, 2019). Therefore, correlations in Figure 5.7 should not necessarily be ruled out if not marked with an asterisk. The full set of p-values are reported in Appendix Tables A.7 - A.9. The majority of correlations with temperature do not appear statistically significant.

Individual Profile Correlations

Correlation coefficients are given in Figure 5.7, however using bootstrapping can give confidence intervals and therefore bootstrapped values will also be given for comparison where correlation is low or not statistically significant. Bootstrapping repeatedly resamples values from the original sample and calculates the statistic of each resample.

The individual profile measurements (labelled pEW1 and FWHM1 for blue, pEW2 and FWHM2 for red) of the combined Fast and Slow sample have the strongest correlations between pEW1 and pEW2 (0.83) and pEW1 and FWHM1 (0.68). However, for the Fast subclass the correlation between pEW2 and FWHM2 is greater (0.71) than for pEW1 and FWHM1 (0.5). The Slow subclass shows the opposite trend and pEW1/FWHM1 is 0.82 whereas pEW2/FWHM2 is 0.49.

Correlations between FWHM1 and FWHM2, and correlations of FWHM and pEW for each profile with temperature, do not appear to be statistically significant, with low correlation coefficients.

In summary between pEW and FWHM measurements for each profile some correlations are stronger and some weaker between Fast and Slow, therefore it is difficult to clearly differentiate between the subclasses.

Ratio Correlations

Where line ratios were considered (labelled pEW and FWHM), the strongest correlations are between FWHM and pEW ratios (0.48 for Fast and Slow spectra together), and also for pEW ratio and line flux ratio (also measured using iraf), which is to be expected as pEW is an analogue for the latter. Aside from these, overall there is a low negative correlation between pEW ratio and temperature (-0.24,

or -0.201 ± 0.155 with bootstrapping), and no statistically significant correlation between FWHM ratio and temperature (or 0.183 ± 0.115 with bootstrapping). There appears to be a low correlation between FWHM and temperature for Slow SLSNe I (0.3, or 0.334 ± 0.117 with bootstrapping), which is not statistically significant for Fast SLSNe I (-0.142 ± 0.168 with bootstrapping). The correlation matrices suggest overall that the lower the temperature, the stronger the blue compared to the red line profile in terms of pEW, though this is not a strong correlation. It should also be noted this is only statistically significant for both Fast and Slow subclasses combined, and it appears individually there is not enough to infer a statistically significant correlation. Therefore, when attempting to model this 'w'−feature, the models should try to look for an explanation for this temperature-dependent correlation. When the correlation matrix is split into Fast and Slow, some further differences in trends are observed. The correlation between pEW and FWHM is not statistically significant for Slow SNe whereas there is a strong positive correlation for Fast SNe (0.79). The correlation between pEW and Flux appears to be similar for both, however the correlation between Flux and FWHM is significantly weaker for Slow SNe (0.28, or 0.173 ± 0.126 with bootstrapping) for Slow as opposed to 0.8 for Fast).

5.4.3 pEW and FWHM of Oxygen

The pEW and FWHM evolution behaviour of the TARDIS Oxygen models is examined in Figures 5.4 and 5.5, compared to the observed spectra. The measurements from the models do not entirely match the evolution displayed by the sample of spectra. The model pEW ratios, as well as the blue and red profiles, show a slow steady decrease with decreasing temperature from around 16000 K and hence is no longer consistent with the observations which instead show an increase with lower temperature. This would at least suggest that other ions become predominant in the feature structure at such temperatures (i.e. T < 16000 K). The red profile displays a similar pEW trend to the blue, except the drop below 16000 K is more rapid.

The model FWHM ratio increases with decreasing temperature down to around 16000 K, where there is an inflexion point and the behaviour changes to a decrease with decreasing temperature. The FWHM evolution is similar for the blue and red profiles and close to a linear decrease with decreasing temperature. At first glance, the model pEW vs FWHM ratio behaviour does not appear to match the observations, and for the individual profiles the model pEW and FWHM are much lower than the values measured from the observed spectra, therefore a comparison is difficult. This would also suggest that there are more contributions than Oxygen only to the 'w'-shape as the single element model does not explain the observed pEW and FWHM evolution. However, the slope inclination and then flattening for the pEW vs. FWHM ratios (the increasing slope from low to high pEW and FWHM) is the same displayed by the Fast subgroup but with a factor of 2 difference in their intensity.

Looking further by examining the behaviour for the individual profiles, it appears that the pEW

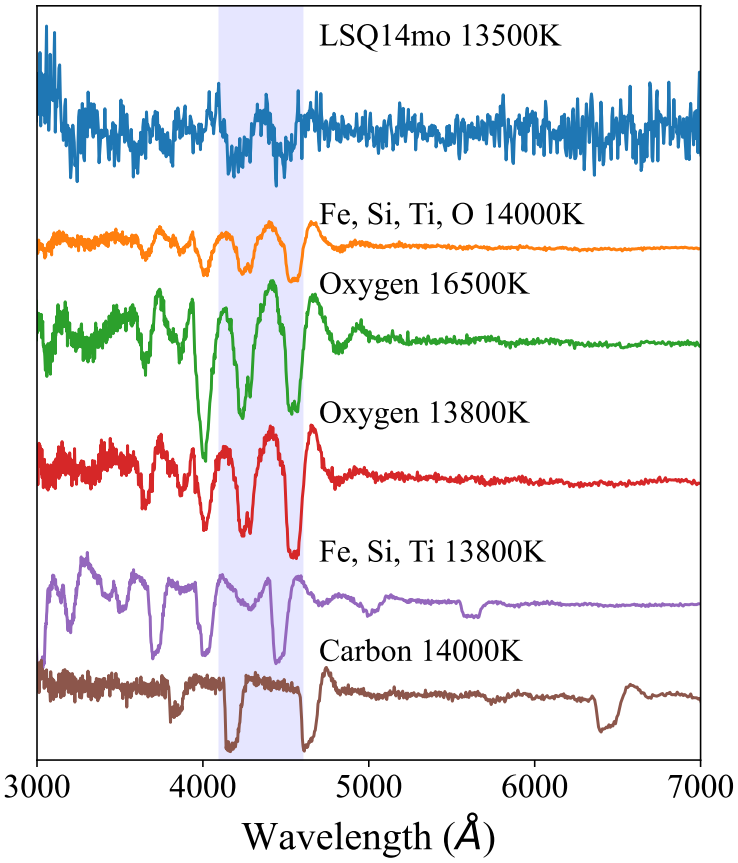

Figure 5.8. The spectrum of LSQ14mo at -8.8 days from maximum light, compared to models with Carbon, Oxygen, and metals at the approximate temperature of the spectrum. Also for comparison is a metal and Oxygen mixture model as for SN 2015bn, including Fe, Si, Ti, and Oxygen. The models have a velocity of 10000 km/s. The wavelength is in the rest frame.

measurements deviate the most from the TARDIS models in their evolution w.r.t. temperature. The steep decrease with decreasing temperature at approximately 16000 K in the TARDIS models could be argued to be seen for some but not all spectra/data points. The pEW vs. FWHM for the blue profile shows a linear increase in TARDIS which is well matched by the spectra sample, however the red profile does not show this linear relationship in the TARDIS models.

It should be noted that other factors aside from temperature could also potentially influence the line profiles. An increased velocity distribution could be expected to increase the FWHM - though this was not replicated by TARDIS. As discussed above, this is likely due to the limitations of the model in changing how the velocity varies with position in a way which differs from the homologous expansion assumption. Additionally, the pEW is a strong function of how much oxygen is excited into the appropriate states that lead to the observed absorption features, and adding more oxygen into these excited states could increase the pEW. However, again, investigating this scenario is limited by the current capabilities of TARDIS

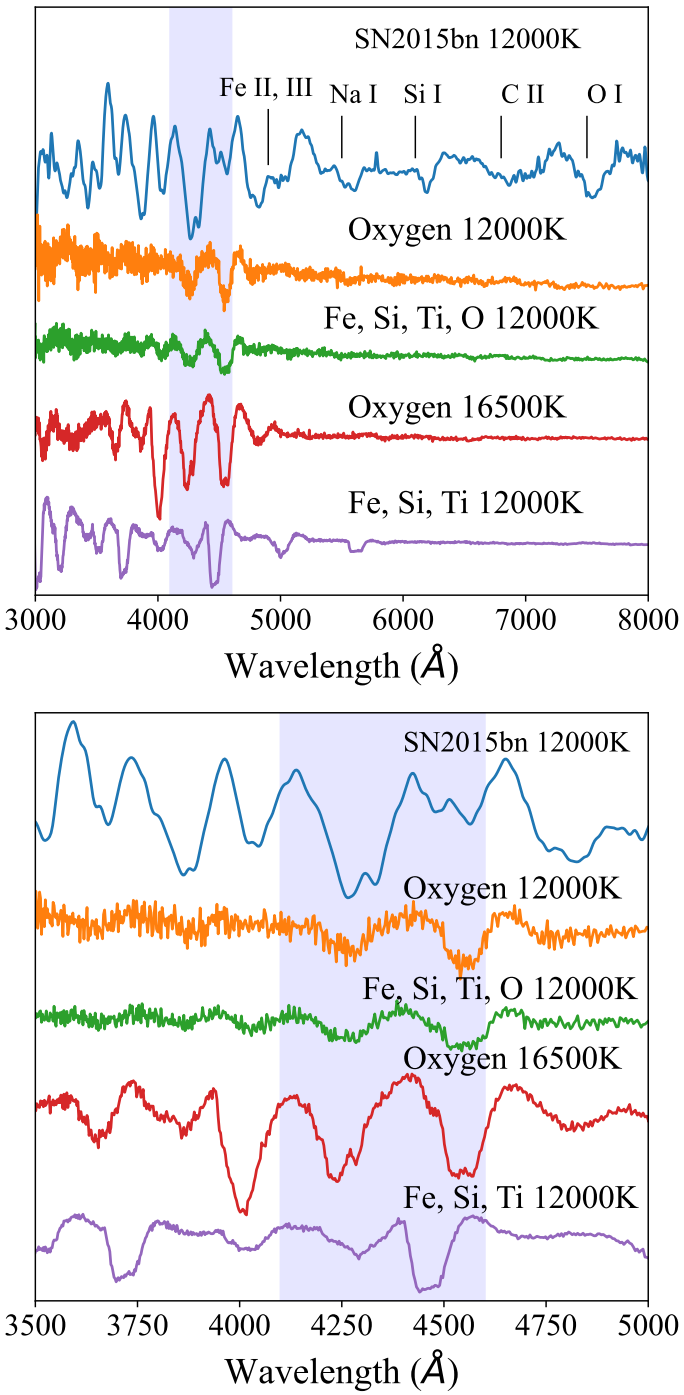

Figure 5.9. Top Panel: The spectrum of SN 2015bn 8 days post maximum light, compared to models with Fe, Si and Ti at the temperature of the spectrum, and Oxygen at 16500 K as a consequence of a non-thermal excitation (see text for further detail). Ions attributed to features redder than 5000 Å by Nicholl et al. (2015a) have been indicated. Bottom Panel: A zoom of the above for the region around the 'w'-shape. All models have a velocity of 8000 km/s. As can be seen, a combination of Oxygen and metals (black line) can reproduce many spectrum features.

5.4.4 LSQ14mo

TARDIS was used to try to reproduce the spectrum of LSQ14mo at -8.8 days - this spectrum has been smoothed by a Gaussian filter of 5σ for ease of comparison with models. This spectrum of LSQ14mo is measured, from a blackbody fit to the photometry, to be at a temperature of approximately 13500 K, at which Carbon and Oxygen produce significant contributions to line formation, therefore these ions are considered in our models shown in Figure 5.8. Metals such as Iron, Silicon and Titanium are also included, with relative abundances (to the total composition) based on those reported in Mazzali et al. (2016): $5e^{-4}$, $2e^{-3}$, and $2e^{-5}$ respectively (considering the total chemical abundances as 1). A combined model with Oxygen, with a relative abundance of 0.475, and such metals is also provided. The ratios between elements are normalized to 1 when a combined TARDIS model is run. However, the absorption features of Carbon, or Iron and Silicon, do not appear necessary to reproduce the features in LSQ14mo, as the Oxygen model seems to match the locations of the peaks and troughs well.

Fiore et al. (2021) considered TARDIS models for Carbon and Oxygen to reproduce the 'w'-shape feature in SN 2017gci and found that the Oxygen spectrum reproduces the shape best, with Carbon also producing a 'w'-shape absorption in a similar region, as can also be seen in Figure 5.8.

The wavelength range of Figure 5.8 is shown from 3000-7000 Å to analyse lines produced by the considered ions at other wavelengths. However, LSQ14mo is relatively featureless at this phase with a high S/N as can also be seen Chen et al. (2017c). Moreover, at early phases, SLSNe do not show line profiles redder than 5000 Å (see Inserra, 2019, for a review). Higher temperatures have higher ionisation states of light elements and therefore absorption is usually in UV regime. However, it can be seen that the Oxygen TARDIS model does not match all features of LSQ14mo blue of 4000 Å such as the absorption at approx. 3500 Å.

In conclusion for LSQ14mo, an Oxygen only model and therefore O II could potentially account for the majority of the features, with perhaps smaller contributions from other ions which could explain the fact that the Oxygen models do not explain the observed pEW/FWHM evolution (see Section 5.4.1).

5.4.5 SN 2015bn

The spectra for SN 2015bn display a double absorption in each line profile of the 'w'-shape (see Figure 5.1). This double feature can also be identified in some other SNe, such as the early spectra of PTF12dam, also a slow subclass SLSN. Figure 5.9 shows the spectrum of SN 2015bn at +7 days from maximum at around 12000 K, a temperature that should not show any significant contribution of Oxygen (see Section 5.4.3), and also marks the ions suggested to be responsible for the line features redwards of 5000 Å by Nicholl et al. (2015a). This temperature is at odds with the

lower temperature of the SN 2015bn spectrum and hence non-thermal excitation should be invoked, allowing this increased excitation level to be reached at an overall lower temperature for the ejected material. Figure 5.9 also shows the model Oxygen spectra at 12000 K and an excited 16500 K, as well as Fe, Si, Ti, with and without the addition of Oxygen, with relative abundances following the prescription of Mazzali et al. (2016). This figure demonstrates the fact that the 12000 K Oxygen model alone does not explain all the features of the SN 2015bn spectrum, requiring non-thermal excitation. As can be seen, the blue line profile of SN 2015bn shows a much stronger absorption than the red, which is not consistent with the Oxygen model. Non-thermally excited Oxygen could possibly explain the double feature in the blue profile, with a combination of metal lines responsible for suppressing the red profile and producing its double absorption. A comparison of the Oxygen only at 12000K and Oxygen with the additional metals shows a slight flattening of the red profile when metals are included. Quimby et al. (2018), similarly to Gal-Yam (2019a), considered the 'w'-shape as a blend of O II lines and compared the locations of absorption lines to the NIST atomic transitions. It was identified that O II transitions alone could produce double features in each profile, but these individual lines could only be distinguished when there was a very narrow velocity distribution, and therefore the lines did not blend together. However, this alone would not explain the significant flux suppression of the redder profile. Additionally, the double absorption in the red profile does not match the ratio of the expected strength of these individual lines accord to the NIST transitions, unlike in the blue profile, suggesting additional contribution is needed to explain the features.

These models do not provide enough information for a firm conclusion. Nicholl et al. (2016) suggested that Fe III is the main contributor to the stronger blue line profile, which is supported by the strong absorption in the Iron model seen at $\sim$4400 Å. However, according to Mazzali et al. (2016), Silicon is present in greater abundances and would produce a stronger absorption than Iron in the red profile. Könyves-Tóth & Vinkó (2021) suggested that the whole 'w'-shape in SN 2015bn is not the same feature observed in the majority of SLSNe I and that there is no contribution from O II. However, our models suggest O II can be used to reproduce the 'w'-shape.

The lower panel of Figure 5.9 shows a zoom of the spectra around the 'w'-shape region, and the upper panel has a range of 3000-8000 Å. Ions from Fe, Si and Ti produce absorption lines at other wavelengths which can also indicate their presence. As can be seen, the absorption in the SN 2015bn spectrum at approximately 5000 Å and 5700 Å, can be explained by the Fe, Si, Ti model while cannot from the Oxygen models. Moreover, the lines blue of 4000 Å require additional contribution beyond Oxygen to fully explain them. Considering absorption lines observed at these wavelengths support the need for contribution from metal lines to explain the SN 2015bn spectrum.

Investigating the metal lines evolution as a function of temperature with TARDIS shows that Titanium, Silicon and Iron are roughly produced in the same regions up to around approximately 16000 K, at which point there is significantly decreasing strength for the Iron lines (see Figure 5.10 for a visual evolution). If the Iron is the main contributor alongside Oxygen for the double absorption

in the blue profile the Iron contribution would diminish at higher temperature, but if Oxygen is the only contributor the shape of the feature would not become less pronounced with increasing temperature. If the double absorption in the red profile is due to Oxygen and Silicon we would also see a less pronounced feature with increasing temperature, although to a lesser extent.

This approach would suggest that the contribution from Iron in the blue line profile disappears first whilst the red line profile continues to show a double absorption from Silicon - see Figure 5.10, showing the evolution of Iron, Titanium and Silicon. This is not seen in the spectra of SN 2015bn and PTF12dam. However, around 19000 K absorption from Titanium (see bottom panel in Figure 5.10), in the same region as Iron showed at lower temperatures, begins to appear, which would therefore continue to contribute to the double absorption in the blue. It should be noted however that SN 2015bn and PTF12dam do not have a steady decrease of temperature with phase and this may complicate trying to look for a pattern in their spectra correlating with temperature.

It is possible that the differences between fast and slow SLSNe I could be in part due to a stronger contribution of iron-group elements as observed in SN 2015bn. However, there is no clear universal trend, and further analysis would be needed with a larger high-quality sample. Iron group elements also produce strong absorption in the UV, and a difference in the strength of the contribution from Iron lines between SLSNe I subclasses could be verified when a sufficient dataset of spectra from both Fast and Slow events in the UV is reached. However this is currently not present in the literature.

There is also an alternative explanation for the double absorption seen in a subset of the SLSN I sample. Detached shells or regions containing Oxygen at separate velocities would produce absorption at different wavelengths and could be responsible for the shape seen. This would also require different abundances in the separate shells as the double components in each line profile have relatively different strengths between them. This a scenario which cannot be modelled with TARDIS within its assumptions, however it should nevertheless be considered as a possibility. As Quimby et al. (2018) suggested a double absorption appears with narrow velocity distributions, for the double absorption to be only due to detached shells would require a wider velocity distribution.

5.5 On the origin of the 'w'−shape profile in SLSNe

As reported in Section 5.4, we considered Oxygen-only TARDIS models and show how well these explain the appearance of the 'w'-shape via modelling, as well as the evolution of the FWHM and pEW with temperature. As non-thermal excitation is thought to cause this feature, a correlation with temperature is not necessarily to be expected, however as can be seen in Figure 5.5 the pEW ratio is never greater than $\sim$1 at any temperature for the model spectra. Therefore, regardless of the level of excitation, ratios above this are not expected to be observed, like the higher ratios seen below 15000 K for many of the Slow and some of the Fast subclasses.

Below we present a discussion of the physical motivation for the behaviour of the pEW and

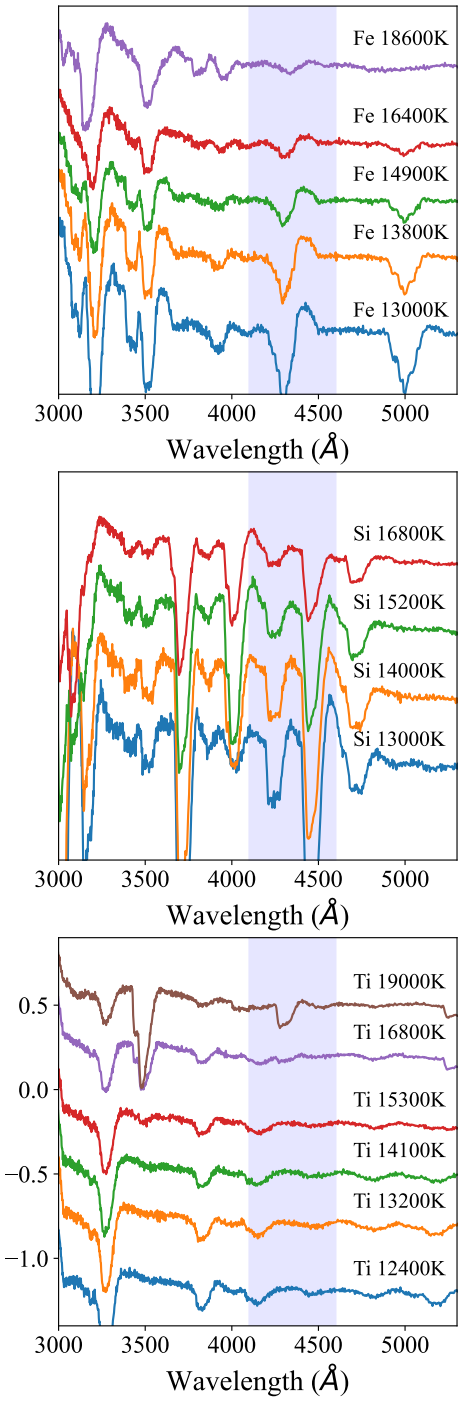

Figure 5.10. Temperature evolution of (from top to bottom) Iron, Silicon, and Titanium models produced by TARDIS. Vertical blue lines represent the locations of the absorption of the two line profiles of the 'w'-shape.

FWHM of our SLSN sample. Spectral properties such as the equivalent widths or velocities of particular features can be correlated with photometric parameters such as peak luminosity, rise time, and luminosity fading rates (Quimby et al., 2018)

A positive correlation between pEW and FWHM could be caused by the correlation of both with explosion energy and/or overall energy budget at those epochs. However this is a general global correlation that will not necessarily follow the evolution of individual SNe. The TARDIS modelling in Section 5.4 suggested that the 'w'-shape in SN 2015bn could possibly be explained by a combination of Oxygen, possibly non-thermally excited, and metals such as Fe, Si and Ti, which also produce absorptions in this region at the relevant temperatures. LSQ14mo's 'w'-shape could also be reproduced with a similar combination, although a simpler model with only Oxygen can also reproduce the observed features without the need to add any metal. It can also be noted that the temperature of LSQ14mo is sufficient to produce the 'w'-shape with Oxygen without the need to invoke non-thermal excitation.

Mazzali et al. (2016) noted for the 'w'-shape in SLSNe I that line width is not easy to relate to a velocity spread, as most lines are actually blends. This was also supported by Gal-Yam (2019a) who suggested line width is rather related to line density, and that the FWHM measure is less useful to consider. Nevertheless, one of the clearest correlations is between FWHM and pEW in each profile, and also for the ratios of each profile. This would at least imply that line density is not the sole possibility as in that case the pEW should increase of the same increment of the FWHM, which is not observed. Concerning the 'w'-shape itself, they conclude that if lines are from O II, they are from very highly excited lower levels. One would expect that excitation of O II levels is not in thermal equilibrium with the local radiation field. This also would suggest that any correlation of pEW and FWHM with temperature would more significantly be due to the presence of other ions rather than non-thermally excited Oxygen. They reproduce the 'w'-shape considering non-thermal excitation in a parameterised way. The strength of the O II lines is influenced by the levels of ionisation, and cannot be increased in strength by increasing Oxygen abundance, supporting our earlier TARDIS approach with the element abundances. After maximum light, the O II lines are no longer very strong, and lines of lower ionisation species are visible which is in line with what we find in our analysis in Section 5.4.

Figure 5.11 reproduces the findings from Hatano et al. (1999), and shows the line optical depths (with the Sobolev method, Sobolev, 1960; Castor, 1970; Jeffery & Branch, 1990b) of neutral, single and double ionised Carbon, Nitrogen and Oxygen, alongside Fe, over a range of temperatures for a C/O rich composition. The horizontal line marks the electron-scattering optical depth $\tau_{\rm es} = 1$, where these ions would produce identifiable spectral features. Hatano et al. (1999) evaluated all line optical depths at the layer in the supernova where the electron-scattering optical depth reaches unity. When electron scattering is the dominant opacity source, this layer can be thought of as roughly the bottom of the line-forming layer (although thermalization of the continuum will take place at a deeper layer) and only transitions that achieve optical depths on the order of unity or greater at will

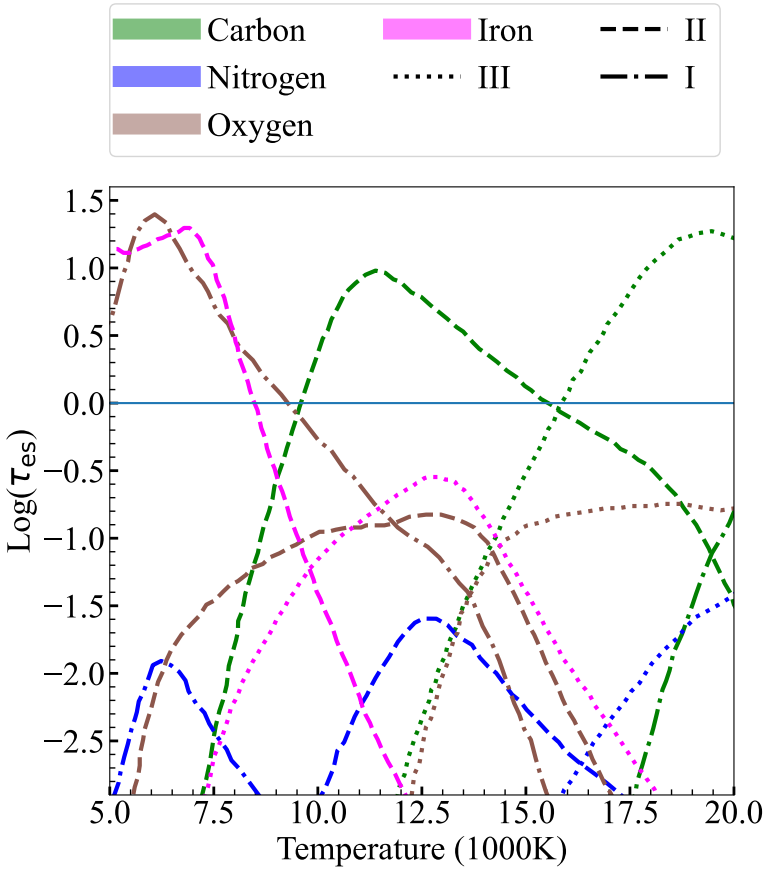

Figure 5.11. Figure reproduced from Hatano et al. (1999), showing the line optical depth (via Sobolev) of neutral, ionised, and doubly ionised Carbon, Nitrogen, Oxygen, and Iron (marked in legend as I, II, III) as a function of temperature. The horizontal line represents where the electron-scattering optical depth $\tau_{\rm es} = 1$, and can be roughly thought of as the bottom of the line-forming layer. Transitions with $\tau_{\rm es} \geq 1$ will always form conspicuous features in the spectrum. This figure makes no allowance for non-thermal excitation and ionization.

be able to form conspicuous features in the spectrum. There are cases where the electron-scattering opacity is smaller than the combined opacity of numerous lines and here, effectively, the bottom of the line-forming layer will be at a shallower layer in the supernova and only lines that have optical depths more than unity will be able to produce identifiable spectral features.

Figure 5.11 can be used to interpret which ions can be considered candidates for line identifications as a function of the temperature, and therefore what ions would be the most major contributors at the temperatures where the 'w'-shape is observed in our sample. In the case of $\tau_{\rm es} < 1$, at each wavelength where a line profile occurs, the major contributor to the profile in that region will be the ions with the highest optical depth. However, if an ion has $\tau_{\rm es} \geq 1$ it means that a line profile will be observed at the transition wavelengths regardless of other ion species which would also produce lines at those wavelengths. This figure would suggest the dominant ions in the temperature range 5000−20000 K, which is the approximate range considered for the SLSNe I in our sample, are C II/C III at intermediate/higher temperatures, and O I/Fe II at lower temperatures, when they are present. It should be noted that the line optical depths for O II and Fe III are very similar and therefore neither would clearly dominate if both are present, therefore distinguishing between them may be difficult.

Könyves-Tóth et al. (2020) performed modelling of spectra for individual ions in an attempt to also reproduce the 'w'-shape seen in SLSNe I. They found that a combination of O II and C II, or O III and C III fit equally well to reproduce the 'w'-shape feature. They noted that these pairs of ions have similar line optical depths at 15000 K, as seen in Figure 5.11, which is the temperature of their model. This would suggest the 'w'-shape is not uniquely produced by O II and other ions with similar optical depth could also contribute or explain this feature.

The TARDIS Oxygen models, and therefore the pure O II hypothesis, match reasonably well with the 'w'-shape of LSQ14mo. Indeed, multiple works have suggested O II can fully reproduce the 'w'-shape feature seen (e.g. Quimby et al., 2007; Dessart et al., 2012; Quimby et al., 2018). However, the feature of SN 2015bn clearly has a different nature, and the pure Oxygen models cannot explain the significant different depth of absorption of each line profile, which is best reproduced by the combination of Oxygen and metals, as suggested in Nicholl et al. (2016). Also previous works on spectra modelling cast a doubt on whether O II is the sole contributor to this region suggesting that other ions such as belonging to Carbon or Silicon are needed to reproduce the 'w'-shape (Chen et al., 2017c; Anderson et al., 2018c; Könyves-Tóth et al., 2020). Additionally, pure Oxygen models produced by TARDIS do not match the pEW and FWHM evolution seen by the spectra sample.

The findings from the TARDIS modelling can be linked back to explaining the behaviour of the pEW evolution via the addition of Iron to the Oxygen model. As seen in Figure 5.10, as the temperature decreases the absorption corresponding with the blue line profile of the 'w'-shape increases in strength which is the opposite behaviour of the Oxygen models (see Figure 5.3). Hence, as the blue/red ratio increases for the sample with decreasing temperature one would expect the

blue line profile to become stronger.

Mazzali et al. (2016) suggested very low metal abundances and hence weak metal lines in SLSNe I such as iPTF13ajg, with a metallicity at 1/4 solar. This was based on the weakness of metal lines and the very blue spectra - which could suggest that the abundances of metals used to create the model of SN 2015bn might have been too high. Nevertheless, based on the R23 approach (Zaritsky et al., 1994), Nicholl et al. (2015a) reported a value of 12+log(O/H) = 8.05 for SN 2015bn - as there were no lines to break the degeneracy between branches, the lower metallicity branch was taken as they are generally favoured for SLSNe I where the degeneracy cannot be resolved. Chen et al. (2017c) reported 12+log(O/H) = 8.2 for LSQ14mo. Converting the 1/4 solar metallicity of iPTF13ajg to the 12+log(O/H) metric would give approximately 12+log(O/H) = 8.09, which is between SN 2015bn and LSQ14mo. These are similarly low metallicity hosts, however these metallicities are global measurements and hence may not be a true reflection of the actual metal abundances of the SNe.

To summarise, the evidence against O II as the sole contributor has been further reinforced both by the TARDIS modelling in this Chapter, and the pEW and FWHM measurements from the spectra combined with the same measurements from the model Oxygen spectra. These weaker correlations could be due to the Slow subclass being more heavily influenced by interaction (Inserra et al., 2017). This could affect emission and absorption lines, leading to a different elemental composition, or a different contribution to the non-thermal ionisation of Oxygen. This difference would be due to the observed spectrum showing contribution from the CSM rather than the SN ejecta alone, and driven by CSM and collisional effects for the line formation and broadness of lines, rather than doppler broadening or line density. It should be noted however that where individual profile measurements are concerned, it appears more difficult to differentiate the Fast and Slow subclasses.

5.6 Summary

In this chapter, a sample of SLSNe I were examined, and their 'w'−shapes round 4200 Å and 4400 Å were quantified by measurements of the pEW and FWHM of the blue and red profile as well as their ratio, and the correlation of these measurements with temperature and phase were considered. The goal was to have a quantitative comparison of the line profile with respect to the temperature of the SN at the time of the spectrum as well as measurements of the line profiles themselves. We found no statistically significant correlation between pEW and FWHM ratios for Slow SLSNe I as opposed to a strong postive correlation for Fast (0.79). This could be due to the Slow subclass being more heavily influenced by interaction (Inserra et al., 2017, 2018), which could influence emission and absorption lines. It was also found that these evolutions with temperature are not entirely consistent with measurements of a pure Oxygen model spectrum, produced with TARDIS, suggesting that Oxygen alone is not responsible for the correlations seen. When considering

individual profile measurements, the most significant deviation between the trends of pEW with temperature for models compared to observed spectra began below approximately 15000 K, which is also the approximate temperature when Iron contribution begins to grow stronger in the blue profile region, and Silicon in the red (see Figure 5.10) - though this deviation from models is not necessarily followed by all SLSNe I.

With the addition of further TARDIS modelling, the conclusion drawn is that the 'w'-shape, attributed to O II lines are likely not caused by Oxygen alone, but requires a contribution of metals such as Titanium, Silicon or Iron. A model with Oxygen and a mixture of such metals can reproduce the double absorption in the 'w'-shape seen in some SLSNe I such as PTF12dam or SN 2015bn. However, the 'w'-shape of SLSNe I such as LSQ14mo can be sufficiently reproduced by O II models as also previously shown by e.g. Dessart et al. (2012) and Könyves-Tóth et al. (2020).

An improved understanding of this 'w'-shape profile has the potential to, with further work, identify a Fast or Slow SLSN I from a very early spectrum (or perhaps correlate the overall yields with those producing a circumstellar material) without needing to determine the classification observationally from the light curve. Additionally, further study of this 'w'-shape could provide further insight into the process causing the additional luminosity and it might provide a means to distinguish between different progenitor scenarios.

Chapter 6

Machine Learning to Predict Supernova Spectra

6.1 Introduction

SNe are observed primarily in terms of photometry and spectroscopy. Spectroscopy provides information on the composition, density, temperature, and velocity of SN ejecta. Advances in telescopes and systematic surveys monitoring large portions of the sky have resulted in an unprecedented large number of SN candidates. The usefulness of this data is dependent on our ability to process them (Ishida, 2019). Being able to augment available spectroscopy to a full spectral evolution could have significant benefit during the Legacy Survey for Space and Time (LSST) era at the Vera C. Rubin Observatory (LSST Science Collaboration et al., 2009). LSST is forecast to discover three to four million more SNe during its ten-year survey*, spanning a very broad range of distances, for which we will not have the luxury of multiple epoch spectroscopy, and in most cases no spectra at all. In many other cases, it may be that there is only one spectrum available per SN to infer the full evolution from. On the Transient Name Server (TNS)† at the moment of writing, there are 11,372 public classified SNe reported since Jan 1, 2016, of which 1,661 are SNe II, and 7,518 are SNe Ia. Therefore, SNe II are currently discovered at a rate of 14% of classified SNe. LSST would be expected to discover approximately 300,000 SNe II, making it impossible to provide a spectroscopic dataset for all SNe II. SNe II evolve depending on many characteristics of the progenitor and its environment, such as the mass and metallicity, and without a full evolution this progenitor information cannot be accurately inferred.

The aim of this work is to predict core-collapse Type II SN spectra (considering also 1987A-like and SNe IIL, but not subtypes with drastically different physics e.g. SNe IIn which are heavily influenced by interaction), in order to augment existing data with incomplete spectroscopic coverage, which will be especially useful in the LSST era, which will produce an unprecedented number of SN

*https://www.lsst.org/science/transient-optical-sky/supernovae
†https://www.wis-tns.org/

candidates[†] with limited resources for multi-epoch spectroscopy. This augmented data could allow the creation of spectral template libraries, unlock detailed population studies, and provide further information on the evolution of observables linked to the progenitor system. Population studies of SNe can track their evolution, and that of their progenitor stars, in different environments throughout the history of the universe. Tracking these populations over time can provide information on progenitor populations at different redshifts and hence different cosmic times, or different environments with respect to host galaxies, e.g. star formation rate or metallicity. However, population studies require comparisons of SNe at the same epoch, as each stage of the SN is determined by different physical regimes. Datasets are largely incomplete in covering every stage of a SN, as observation time and resources are limited. A machine learning tool connecting late and early time physics and allowing a more complete dataset to be inferred, can in turn allow for population studies with a statistically meaningful sample. This work could also generate additional spectroscopic data which could be used for cosmic distance calibration, such as measurement of Fe II λ5169 velocities during the plateau phase for the Standard Candle Method (Hamuy & Pinto, 2002). Whilst this work focuses on Type II SNe, in the future, this approach could be applied to other SN types as well.

This chapter is organised as follows: Section 6.2 details the sample of SNe II which is used as a training set, and the pre-processing involved in preparing the data for machine learning. It also discusses the process of measuring parameters (e.g. line intensity and velocity, spectra temperature) from the spectra to be used in the training set. Section 6.3.1 displays the prediction of spectra from such measured parameters, as well as predicting the parameters for missing evolutionary phases. Section 6.3.2 looks at predicting a complete spectral evolution from a single spectrum. Sections 6.4 and 6.5 are the discussion and conclusion, respectively.

6.2 SN II Sample

In order to make machine learning predictions, it is necessary to build up a large training set - and generally the larger the training set, the better the predictions as there is more information for the model to learn from/validate on. Previous works dealing with Machine learning and SN spectra have used synthetic model spectra as the training set (e.g. Vogl et al., 2020; Wasserman et al., 2021), though some works have also used real spectra (e.g. Peters et al., 2021; Fremling et al., 2021). Here, observed spectra were used in order to best represent the observed data. This has the advantage over models in that models are time-consuming to create and incomplete in terms of physical properties, therefore not completely representative and may be missing features that the machine learning algorithm could learn from. However, it should be noted that using observed data over models also comes with its own challenges and disadvantages, as there are many associated uncertainties, errors, and noise in the observations, as well as a lower number of available spectra, as with models many more can be produced.

The aim is to be able to predict a spectral evolution with as few spectra taken from a SN as possible, and for the predictions to be refined if more spectra are taken. The goal is to have a tool able to reproduce Type II SN spectra at any time with a resolution equal to that of the input spectra, and reproduce key features e.g. spectral lines and their strength/width/velocity within an error of similar order which would be expected from the spectral resolution.

The sample of SNe II would include SNe IIP, IIL, and 1987-A like objects, but not IIn or IIb. The SNe would need to be well observed with many high quality spectra at a range of epochs from explosion. The sample of training SNe II should have well-calibrated spectra with a S/N $\geq$ 5 (the lowest S/N measured in the sample where the lines can comfortably be distinguished) and characteristics to use for training machine learning code, such as meta-data (e.g. redshift, peak absolute magnitude, host properties etc.) and accurate spectral measurements, for example line velocities and Equivalent Widths (EWs). Therefore a good place to start is published spectra and corresponding additional measurements, such as Hα velocities, Fe $\lambda\lambda$5169, 5018 velocities, and EW, and in fewer cases other lines as well such as Na I, Sc II λ5527 and Ba λ6142, depending on which lines are relevant for the publications/the original analysis of the datasets.

The initial training sample was gathered from the following sources: Gutiérrez et al. (2017a,b), the Berkeley sample from de Jaeger et al. (2019), SNe II at low-luminosity hosts from Gutiérrez et al. (2018) and also additional SNe in the database of the Padova-Asiago SN group [‡] (references in Table 6.5), including Type II SN 1987A-like objects. This was a total of 633 spectra for a total of 138 SNe, spanning a range in phase from 4 to 320 days past explosion, with an average redshift of $z = 0.014 \pm 0.012$ (hereafter the golden sample, see Appendix). Exactly which measurements were available varied for each sample, however most had at least the Hα velocity. The subclasses (such as distinction of SN 1987A-like, IIP, IIL) are not fed into the code and all SNe are treated as a single family of Type II.

The S/N was tested for the Gutiérrez spectra as a representative sample. The S/N was measured both using iraf and the specutils package in Python, at various ranges in the continuum to avoid absorption and emission features. These S/N were averaged and compared for both methods. It was found that 98.8% had an average S/N $\geq$ 5, and if adding one standard deviation to the average S/N, 88.4% had an S/N $\geq$ 5. Therefore it can be concluded these spectra have an acceptable level of S/N with respect to the suggested threshold, where spectral lines can still be comfortably distinguished.

Nebular spectra were excluded from the sample as there is no photosphere and no blackbody assumption that holds, and the physics and physical conditions are different. Given both the relatively smaller number of nebular spectra in the initial sample and a different physical regime, good results in predicting nebular spectra would not be expected, hence their exclusion. However, identifying nebular spectra are difficult as there is no clear cut-off epoch, and some are pseudo-nebular spectra (i.e. when the forbidden lines start to appear but do not dominate the spectrum). Based on both an

[‡]https://sngroup.oapd.inaf.it/highlights.html

Sample	No. SNe	No. Spectra	Parameters Measured?	Augmented Data No.	Method
Golden	138	633	Yes	1568 Spectra	Parameter Method
Silver	159	1151	No	25700 Pairings	Spectra Method

Table 6.1. A summary of the Spectra and Parameter Method training samples. Measured parameters are blackbody temperature, Fe II λ5169 velocity, and Hα velocity. There is overlap between the SNe in the two samples as the silver sample contains all spectra from the golden sample, as well as additional spectra.

average epoch from explosion for the end of the photospheric phase of 100 days (Valenti et al., 2016), and the distribution of epochs in the sample, a cut-off of 150 days was chosen to safely exclude all nebular spectra. Some nebular spectra may still slip through but their small number should not have a significant impact on the algorithm for predicting non-nebular spectra.

6.2.1 Additional WISeREP Spectra

In order to increase the quantity and diversity of our sample, an additional 413 unpublished spectra belonging to 40 SNe were sourced from WISeREP (Yaron & Gal-Yam, 2012, WISeREP). Of these, 13 SNe[§] (75 spectra) were sourced via the advanced Public ESO Spectroscopic Survey of Transient Objects programme (ePESSTO+; Smartt et al., 2015). These spectra were all chosen as having more than one spectrum taken, ideally with a range of epochs starting 10-20 days post explosion range, where the SN is relatively hot and as such the spectrum appears as almost featureless and blue. Early spectra (<20 days post explosion) are the most underrepresented spectrum type in the published sample, therefore the aim was to find a number of spectra within this epoch range to fill this gap. The training sample is therefore being expanded by lowering the criteria and sacrificing having parameter measurements in order to have more spectra. This set only includes reduced spectra, it does not include spectral measurements. These were used to create a second sample which can be combined with the spectra from the published sample, for training a model based only on spectra. The combined total number is 1151 spectra for 159 SNe (hereafter the silver sample). Table 6.1 shows a breakdown of both samples, the golden sample with accompanying parameters, and the silver sample. Additional information about these samples can be found in Appendix A.3 - which includes a summary of all SNe used, the number of spectra taken from each SN, and the sub-type where available.

6.2.2 Pre-Processing

The spectra in both samples require consistency to be used as input to a machine learning algorithm - this would involve normalising the spectra in wavelength and flux. The spectra were

[§]SN 2014dq, SN 2015ch (PS15cwo), SN 2018fus, SN 2019unb, SN 2020abtf, SN 2020voh, SN 2020znl, SN 2021afaz, SN 2021afdx, SN 2021qqu, SN 2021tyw, SN 2022sa.

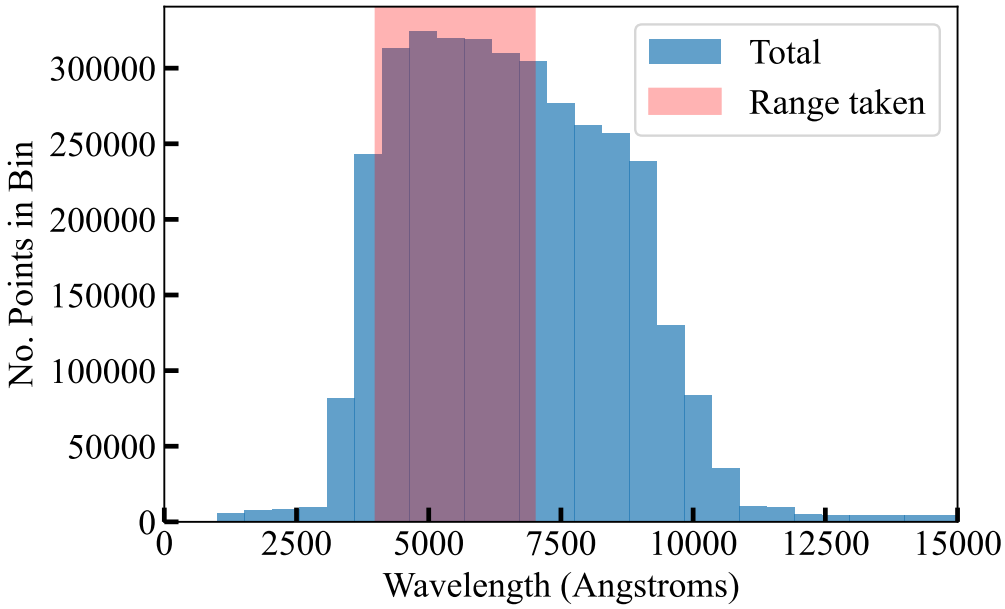

Figure 6.1. Histogram of wavelengths for the golden sample (all wavelength values were gathered together), along with the wavelength range taken marked in pink - few spectra cover wavelengths bluer than 4000Å, while an upper limit of 7000Å keeps 75% of the original spectra set.

limited to a region of 4000-7000 Å in the rest-frame - this range was chosen as it includes relevant features (Hα, Hβ, Hγ, Fe $\lambda\lambda$5018,5169, Na I) whilst keeping as many of the spectra in the sample as possible, as many spectra had a limited wavelength range. Wavelength was standardised by interpolating all spectra to this range with the same intervals between points.

The resolution of the output predictions inherits the resolution of the training sample. Due to the size of the sample, the diversity of spectrographs which was used to take them and, at times, the lack of reported instrument configuration, it was not possible to track the resolution of all input spectra. Hence, an average of 13-18 Å is assumed based on general, published SN spectroscopy. This provides motivation for the chosen interpolation interval of 15 Å, giving 200 points over the 3000 Å range. This interpolation was done using the flux-conserving interpolation in specutils, which also acted as a means of smoothing. This 15 Å interval for interpolation can be assumed to be the minimum resolution of the predictions. Any application of this method with a different training set could, in principle, have a better resolution but the training set needs to be at least at the same resolution as the desired output.

Figure 6.1 shows the histograms of the wavelength coverage of each spectrum in the golden sample. It would be ideal to have as few spectra removed because of restrictions on wavelength range as possible. Our chosen range of 4000-7000 Å includes 75% of the spectra, while a range of 4000-9000 Å would include only 57% of spectra.

Redshift and reddening (following the prescription of Cardelli et al., 1989) corrections were also

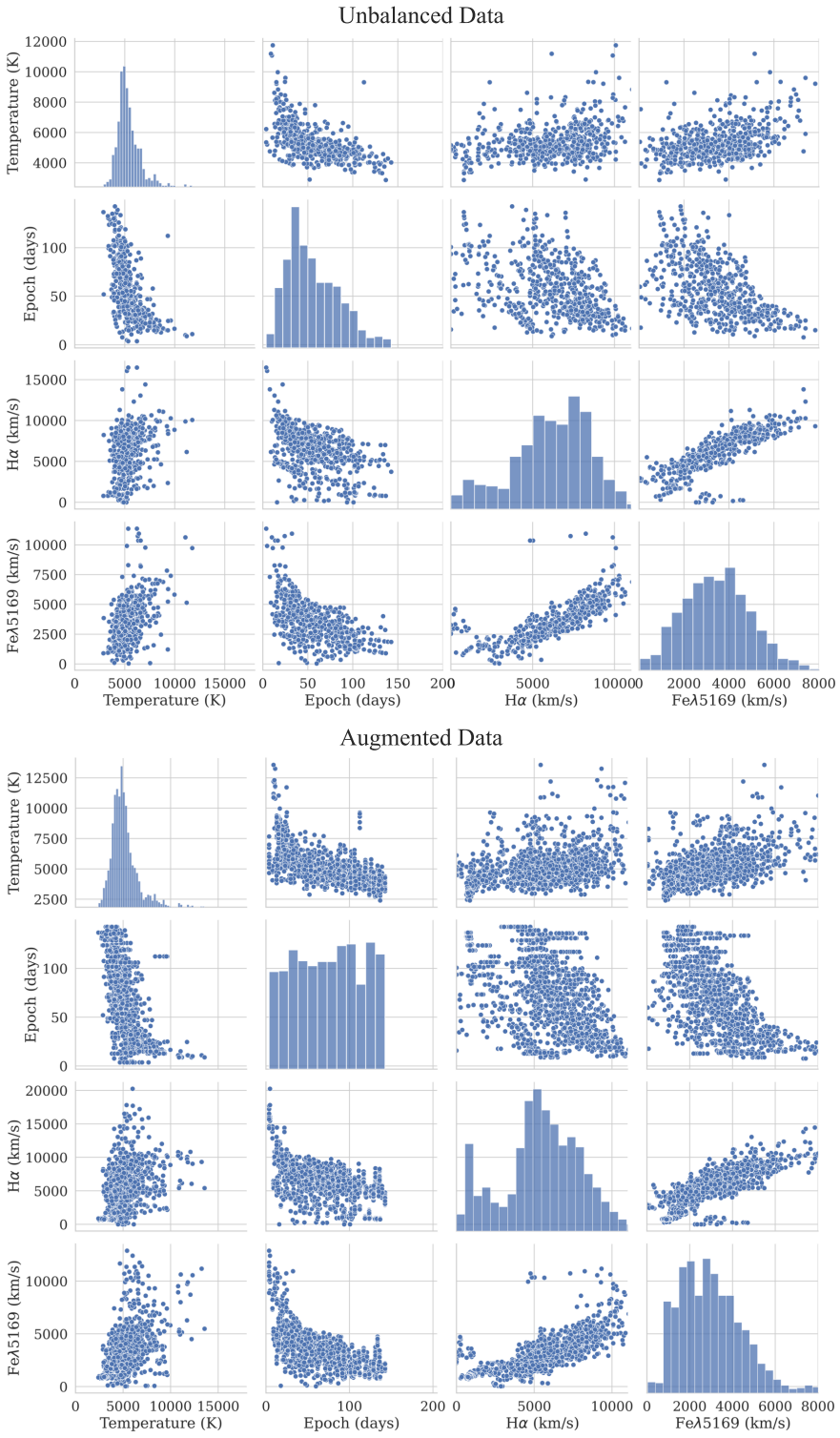

Figure 6.2. Top: the correlation grid for parameters from the training sample: used here are Temperature (T), Epoch (ep), Hα velocity, Fe II λ5169 velocity. Right: same as left but after balancing, using a 'balanced' pairplot with augmented data. This correlation grid has been limited in the x-axis and shows up to approximately 4σ of the distribution. The epoch bins in the bottom panel match the bins in the top, however when binned according to the bins chosen for balancing the distribution would be flat.

performed, with only the reddening from the Milky Way considered. The contextual information (galactic extinction and explosion epoch) was gathered from the relevant papers, or from the Open Supernova Catalogue ¶ when this information was not available from other sources. The phase of the objects throughout the chapter is measured from the explosion date.

The explosion dates for the Gutiérrez, Berkeley and Padova-Asiago samples were determined, where non-detections were available, by the midpoint between non-detection and the first detection. However in the case where this was not available or the cadence of observations was low the explosion date was determined using spectral template matching softwares SNID (Blondin & Tonry, 2007) and GELATO (Harutyunyan et al., 2008). For the remaining unpublished ePESSTO+ spectra and other WISeREP spectra where the explosion epoch was not available from published sources the light curves and non-detections from the Asteroid Terrestrial-impact Last Alert System (ATLAS Tonry et al., 2018b; Smith et al., 2020) were used to determine the explosion epoch, which was the case for 12 SNe. The epoch was chosen as days from explosion rather than days from maximum light primarily due to this being the epoch measurement available in the Gutiérrez, Berkeley, and Padova-Asiago samples, and the additional SNe in the silver sample were measured to be consistent with these. Gutiérrez et al. (2017a) found the explosion epoch determined by SNID and by non-detections were in good agreement, with a mean absolute error between them of 3.9 days for a sample of SNe II. Section 6.4 will examine the influence an uncertainty in the explosion epoch of this order will have on predictions.

For the Gutiérrez sample the redshift information came from the heliocentric recession velocity of each host galaxy as published in the NASA/IPAC extragalactic Database (NED), with the same for the Berkeley sample. Where these were not available the redshift was measured from spectral lines from the H II region. Therefore for the rest of the spectra in the silver and gold sample where redshift was not published with the sample, if the SN was in the Virgo Infall (<20 Mpc) the heliocentric recession velocity was taken, otherwise the redshift from the spectral lines from the H II region (found on WISeREP) was taken. For the unpublished spectra in the Virgo Infall, the redshift from the heliocentric velocities and from the spectral lines from the H II region were compared, with a mean absolute error of 0.0013.

6.2.3 Measuring Parameters

A machine learning algorithm will only be able to learn if the training data contains enough relevant features, therefore it is important to pick parameters which are sufficient to represent the state of the ejecta in each stage of the evolution. Parameters which could easily be measured from the spectra are, for example, properties of the spectral lines such as line velocities and strengths, and

¶https://sne.space/ The Open Supernova Catalogue is no longer operational however the data is still available on the relevant GitHub page: https://github.com/astrocatalogs.

the blackbody fit to the continuum. Other factors to consider could be what lines are present, or global parameters related to the SN itself such as redshift or peak absolute magnitude. Velocities, Equivalent Widths (EWs), phase, and temperature are physically motivated parameters. Temperature and velocity are related to the energy and progenitor's configuration at explosion, whereas EWs are a measure of the strength of spectral lines and are determined by, among other factors, atomic density and chemical yields. The phase provides the time evolution of the SN ejecta.

The temperatures of the spectra were measured by fitting a blackbody to the continuum using scipy.curvefit in Python, unlike the EW and velocity measurements which were taken directly from literature. The blackbody was fit on the full available wavelength range of the spectrum before any wavelength cuts were done, to make use of all the data possible. It should be noted for blackbody fitting to the spectral continuum that there are considerable associated uncertainties (and also would perform better for early spectra) therefore this can only serve as an approximate diagnostic parameter.

The velocities and EWs measured in the golden sample were done using iraf. These measurements were not done for the unpublished spectra in the silver sample as this sample is used for the Spectra Method only, see Table 6.1. For the velocities, the usual method of measurement is for the minimum of the absorption component to be identified using a Gaussian fitting alongside the Doppler relativistic equation and the rest wavelength of each line. The measuring process was repeated many times (changing the pseudo-continuum), and the mean of the measurements was taken. On the other hand, the temperature measurements were done for both samples as these were generally not included in the published papers.

In order to confirm the integrity of the data, the measured velocities were checked with iraf for a small sample of SNe from each set of the golden sample (10 spectra in total). The average error between the existing data and our own checks were 316 km s^{-1} for Fe II λ5169 and 594 km s^{-1} for Hα. For context, the average error in Fe II λ5169 velocity is 763 km s^{-1} for the Gutiérrez sample, 179 km s^{-1} for the Berkeley Sample, and 126 km s^{-1} for the Padova-Asiago sample where errors are reported. For Hα the errors were 665 km s^{-1} for the Gutiérrez sample, 574 km s^{-1} for the Berkeley Sample, and 256 km s^{-1} for the Padova-Asiago sample. The overall average errors are 528$\pm$279 km s^{-1} for Hα and 631$\pm$325 km s^{-1} for Fe II λ5169. The average error between our own checks and the golden sample are both of a similar magnitude to the errors found above, therefore it can be concluded that the dataset is consistent.

An initial algorithm to investigate the dataset was a Random Forest which predicts the 200-point spectrum from features measured in the golden sample. A Random Forest is a number of decision trees where the best results are taken, where a decision tree is an algorithm where the values of the features used for training create different 'branches' that lead to different predictions. Decision trees and therefore Random Forests can be used both for classification tasks and regression (predicting a number rather than a class). This algorithm was used both as a starting point and also a means of evaluating the importance of features, as Random Forests allow ease of calculation of importance

due to the feature-based branching nature of the algorithm. This was done using a Random Forest Regressor from sklearn. There were 200 trees in the forest and for the other parameters (e.g. maximum depth, split conditions) the sklearn pre-coded defaults were used. Only the Gutiérrez set of 383 spectra were used, as these had the most parameters measured in the literature. The features tested were as below:

- Temperature (from the blackbody fit to the continuum)
- Epoch - days from explosion
- Noise - the standard deviation divided by the mean
- The maximum absolute magnitude
- The velocity of Hα
- The EW of the absorption of Hα
- The amplitude of the Hα emission peak
- Fe II λ5169 velocity
- Fe II λ5169 EW

Table 6.2 shows these spectra parameters, alongside the maximum absolute magnitude of the light curves, and the importance of each one as used by the Random Forest Regressor. The feature importance given is a permutation feature importance, which is defined to be the decrease in a model score when a single feature value is randomly shuffled. This procedure breaks the relationship between the feature and the target, thus the drop in the model score is indicative of how much the model depends on the feature. Also included amongst the feature importance scores is a random parameter which also gives comparison to a feature which has no usefulness in predicting spectra - it is found as expected that every feature performs better than the random number.

The final parameters to be chosen are considered as a balance of the following factors: quality of parameter in predicting spectra, ease of interpolating/extrapolating the parameter, and availability of the parameters for the sample spectra. From a look at Table 6.2, temperature and noise are the top predictors - noise is a good prediction parameter as it will have a big impact on the appearance of the spectrum, and it is also possible there are biases of noisier spectra at certain epochs. However this is more specific to each spectrum and when trying interpolate/extrapolate to predict spectra at other epochs is less useful. Despite the inaccuracies in the blackbody fitting for the temperature it still proves to be a useful parameter. The peak magnitude and epoch are less significant for prediction. Epoch will still be included as it is required as a 'training label' to predict spectra at the desired phase. However, its contribution to the properties of any individual spectrum is found

Parameter	Feature Importance Score
Standard Deviation/Mean (Noise)	0.451
Temperature (K)	0.191
Fe II λ5169 Velocity	0.124
Hα Amplitude	0.112
Hα Velocity	0.077
Hα absorption EW	0.042
Epoch (days)	0.021
Fe II λ5169 EW	0.020
Maximum Absolute Magnitude	0.010
Random	0.000

Table 6.2. The random forest scores for different parameters, in order of importance. These importance scores suggest temperature, noise and velocities are the most important. These values have been rounded to 3 significant figures. Also included is a random number between 0 and 1 as a baseline.

to be of relatively low significance, most probably as SNe evolve on different timescales based on their properties and therefore epoch is not a sufficient indicator of the appearance of the spectrum and the stage of evolution of that individual SN. This Random Forest importance indicates which parameters should be selected to go forward with for the full sample and final algorithm. Based on the above considerations, it will be temperature, epoch, and the Hα and Fe II λ5169 velocities, as these are easy to measure (or are generally available) for the full set and have reasonable relatively higher importance.

The left panel in Figure 6.2 shows the correlation of a number of these parameters for the samples, which also shows the histogram of each of the parameters and therefore the distributions of these values and the ranges involved. The parameters shown here are the lines velocities Hα, Fe II λ5169, and the blackbody temperature. Though Hα and Fe II λ5169 are moderately correlated, both parameters showed benefit in terms of importance and therefore both parameters are taken.

6.2.4 Balancing the dataset

Figure 6.2 shows the correlations of the final selected parameters - the left Panel shows the original unbalanced data - as can be seen, there is a strong imbalance towards certain epochs - around 50 days. The dataset can be augmented by resampling spectra of underrepresented categories such as phases, for example those with phases roughly less than 30 days or more than 100 days from explosion. This is where, assuming the epochs are binned into regular intervals, spectra from a certain epoch bin can be randomly selected and duplicated in the sample to attempt to balance out the no. spectra per epoch bin. This newly created sample was added to the training set, proportional to the number spectra at its phase in the dataset. In this way we increase the number of spectra to

train from 633 (including Fe velocity) to 1568, and decrease the training error. See Figure 6.2 left and right panels to see the effect of the augmentation on the distribution of phases. This technique, known as oversampling, can come with an issue of overfitting the spectra at these heavily resampled phases because there is much less variety in the spectra it sees. Overfitting is where the algorithm has very high performance for the training dataset but does not apply well to other similar data.

Oversampling is generally used for algorithms requiring multiple classes, but where some classes have much less data than others. In this case the minority class is resampled and added to the dataset. Data augmentation is a similar case where the resampled data is adjusted slightly e.g. a small amount of noise added. In this case the balancing was done by phase - as this is the parameter by which we request what output we want, it is the most important to make sure it is balanced for phase. The dataset was split into bins based on what epoch the spectra were - bins were in multiples of 10, from 0 to maximum phase present in the original sample. However, the 0-10 days bin had only three spectra. Considering the largest bin 30-40 days had 112 spectra, the 0-10 day bin was combined with the adjacent bin of 10-20 days.

Once these new bins were produced, additional spectra and their associated parameters were sampled from these bins, with an added Gaussian noise up 10% of the parameters (as not all parameters from the samples had errors to utilise) added on to avoid giving the algorithm many copies of exactly the same data. Each bin was sampled up to the size of the largest bin (30-40 days) to 112 spectra. See Figure 6.2 for the effect of balancing.

6.2.5 Including Fe II λ5169 Velocity as a Training Parameter

The Fe II λ5169 velocity is a useful parameter to include alongside Hα velocity as it correlates better with the photospheric velocity. No measurable spectral feature is directly connected to the photosphere as spectra are formed in the outer, more optically thin layer. However, Dessart & Hillier (2005) suggested that the Fe II λ5169 velocity could represent the true photospheric velocity within 5 – 10% accuracy.

In the literature, Fe II λ5169 measurements are not always reported, but other lines can be used as photospheric tracers and then linked to Fe II λ5169. The Pearson Correlation Coefficients were calculated for the following lines: 0.97 for Sc II λ5527, 0.82 for Ba II λ6142, and 0.87 for Hα, which were frequently measured lines where Fe II λ5169 was not reported. Note that measuring Ba II λ6142 can be difficulty as it can blend with other lines. Additionally this line appears after approx. 50 days and would not be useful for earlier times. Fe II λ5018 was also frequently reported however if Fe II λ5018 was measured, almost exclusively Fe II λ5169 was measured as well, and so this is not useful as a substitute. Considering this and the correlations, only Sc II λ5527 (when measured instead of Fe) was used to replace Fe II λ5169 measurements. Requiring Fe II λ5169 or Sc II λ5527 means that the sample size is inevitably reduced from the original, however this step

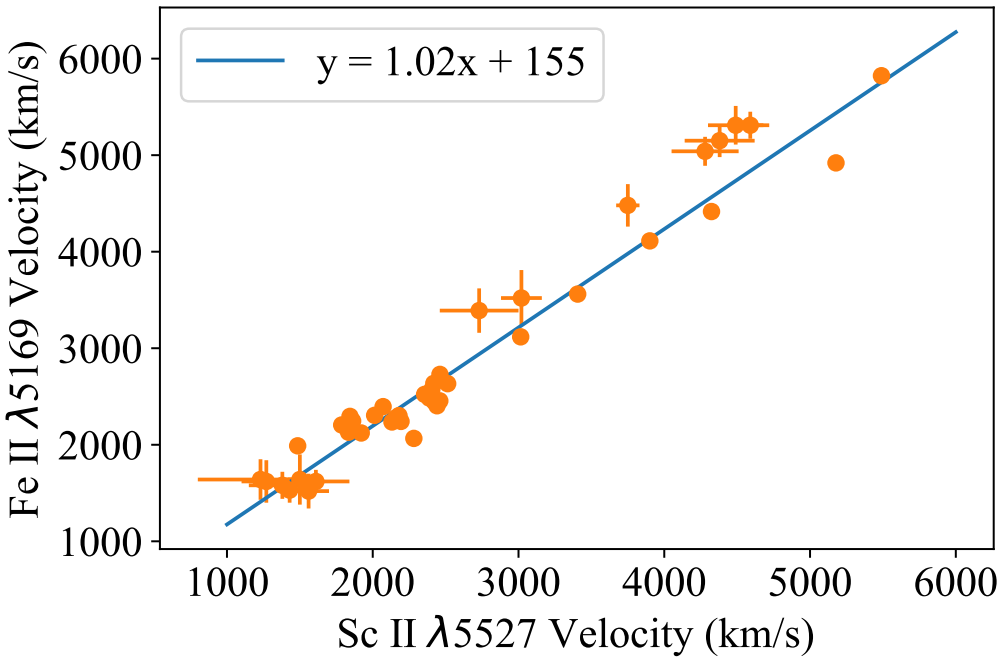

Figure 6.3. Correlation of Fe II λ5169 with Sc II λ5527, with a weighted fit from Python package linmix Some error bars were missing in the data, hence a sub-optimal fit.

allowed an additional 37 spectra to be used which had a Sc II λ5527 but not a Fe II λ5169 velocity measurement. The final spectra numbers previously reported are after this step.

6.3 Predicting Spectra

There will be two algorithms for predicting the spectra in this chapter which will henceforward be referred to as the 'Parameter Method' and the 'Spectra Method'. The Parameter Method relies entirely on describing spectra in terms of the aforementioned parameters such as velocity and temperature, and therefore the interpolation/extrapolation of these parameters can be used to create spectra for 'filling in the gaps' between spectra. It works by predicting these spectra using the measured parameters temperature, Hα velocity, Fe II λ5169 , and phase (days from explosion). Alternatively, the Spectra Method attempts to make predictions from a single spectrum, which may often be all that is available for a given SN in the era of LSST.

6.3.1 Parameter Method

The full training sample for the Parameter Method is the augmented set of 1568 spectra from the published spectra training set. There was a training/test split of 10% and a validation split of 20%. Several algorithms were investigated, including a Gaussian Process Regressor, a Random Forest Regressor and a Neural Network using keras and tensorflow (Abadi et al., 2015), both with and

Model	Autoencoder	Mean Absolute Error
Random Forest	Yes	0.225±0.065
Random Forest	No	0.156±0.063
Gaussian Processes	Yes	0.126±0.055
Gaussian Processes	No	0.120±0.053
Neural Network	Yes	0.046±0.033
Neural Network	No	0.061±0.045

Table 6.3. The Mean Absolute Error for random 10% of the augmented training sample, with or without autoencoder from Section 6.3.2. There is a similar performance between Random Forest and Gaussian Processes, with minor differences from the autoencoder, and slight improvement using a Neural Network. This was performed for the Golden sample only.

without a dimensionality reduction. This dimensionality reduction was done using an autoencoder (see Section 6.3.2). These methods were all similar in terms of performance and training time, and a NN with no dimensionality reduction was ultimately chosen as this had amongst the lowest Mean Absolute Error (MAE - the mean of the difference between prediction and original at every point in the spectrum) - see Table 6.3. Though a NN with an autoencoder had a slightly better MAE reported, it was within errors of not using one and the exclusion of an autoencoder for this stage allowed for a simpler pipeline. It should be noted these MAEs are for reproducing a spectrum/parameter value for the same phase as the observed spectrum, when comparing to later results.

A NN consists of an input, an output, and a number of hidden layers which learn the relationships between the two through a training and validation set. They are designed to mimic neurons in the human brain, with hidden layers carrying information forwards and backwards. As the input data is passed through the model, the output is compared to the target, respectively training loss and validation loss are generated for the training and validation sets. This training loss is used to update the weights and biases of neurons through backpropagation. To avoid overfitting, stagnation of the validation loss means the end of training. NN have been used previously in astrophysical contexts, such as a Recurrent Neural Network (RNN) in Burhanudin et al. (2021) for classifying light curves or light curve anomaly detection (Villar et al., 2021). They have also been used to classify spectra (e.g. SNe Ia spectra in Fremling et al., 2021). The NN presented for the Parameter Method uses three dense hidden layers and a Leaky ReLU activation function, with an Adam optimizer (Kingma & Ba, 2014). Rectified Linear Units, or ReLUs, are a type of activation function that are linear in the positive dimension, but zero in the negative dimension. Leaky ReLU is a type of activation function based on a ReLU, but it has a small slope for negative values instead of a flat slope. Adam is the mostly commonly used optimizer, and is an optimization algorithm that can be used instead of the classical stochastic gradient descent procedure, with better performance

The NN uses 100 epochs with a batch size of 8, and is created using Python packages keras and tensorflow. The loss function is the mean square error. The NN hyperparameters here and

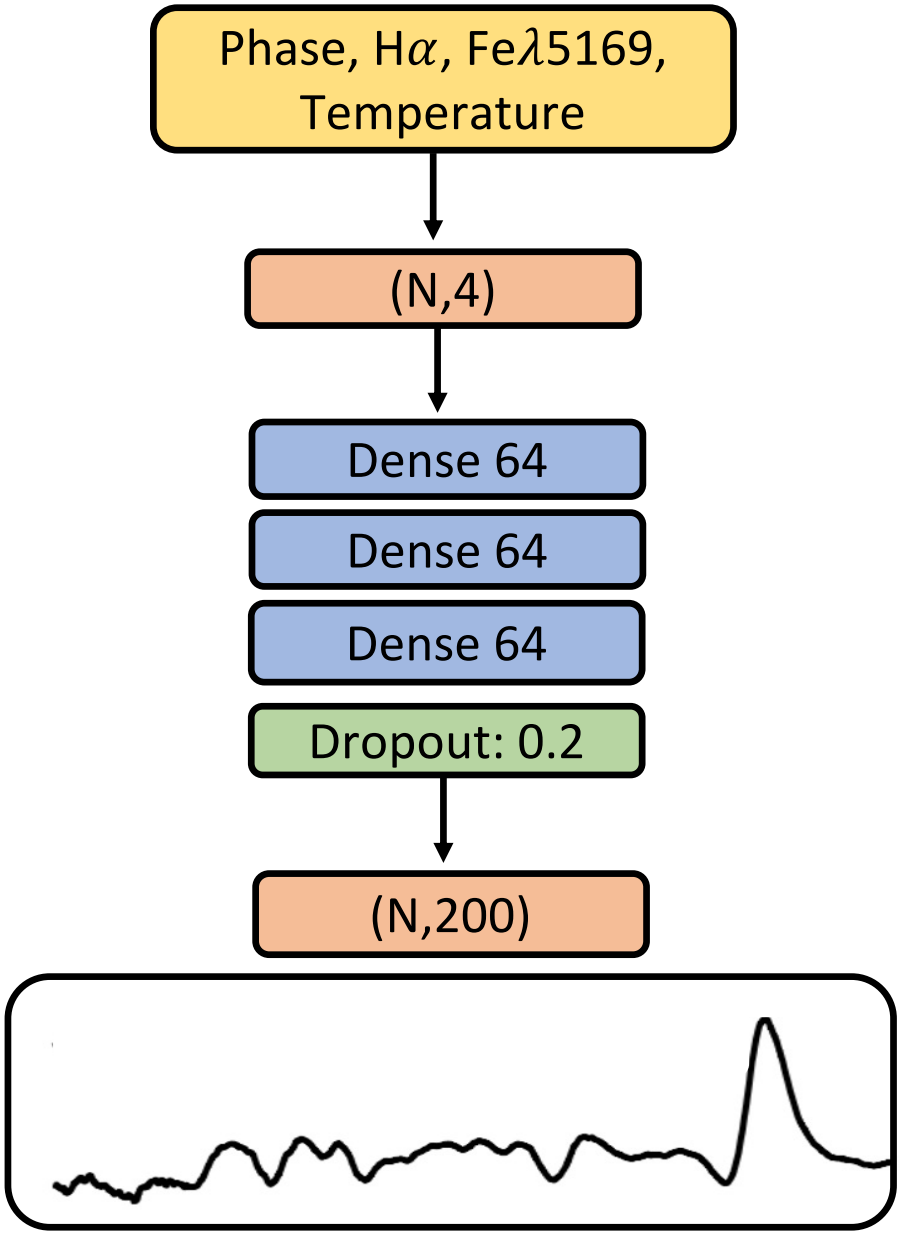

Figure 6.4. Architecture for Parameter Method: input was the measured parameters from the spectra, the output being the 200-point spectrum. For the Dense layer 64 represents the no. nodes (therefore the size of the network), and for Dropout 0.2 is 20%, meaning every epoch (iteration of the NN) a random 20% of this fractions of neurons is switched off in the model to prevent overfitting.

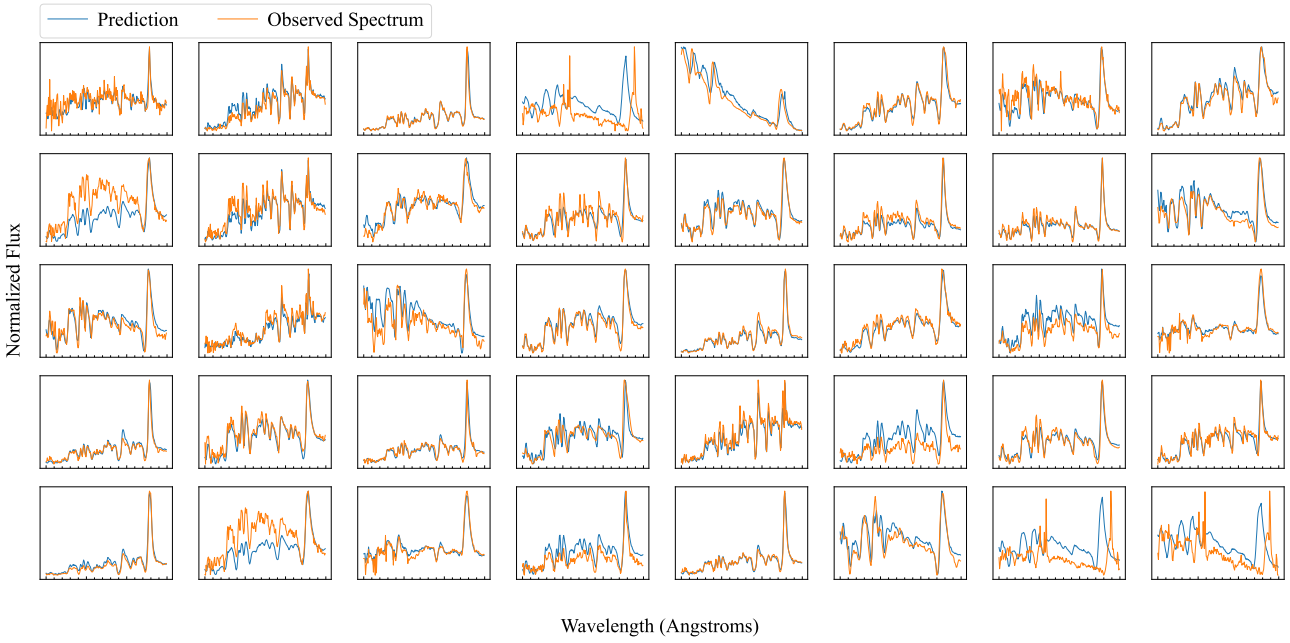

Figure 6.5. A range of test cases to consider the performance of the NN for predicting spectra. Observed spectra from the training sample test set are shown, alongside the predictions made by the NN from the parameters measured for said observed spectra (the epoch, temperature, and velocities). The predictions reproduce the continuum and location of features well (with a MAE of 0.061, or approximately 6% as spectra are normalised between 0 and 1), with some variation in the strength of lines. The x axis is Wavelength from 4000 to 7000 Å. There are a number of cases where the continuum of the prediction is under or over the original spectrum, this largely appears to be due to the strength of lines not being reproduced correctly, and the scaling between 0 and 1 responsible for a shift.

throughout were based on investigation by varying them manually to find the best results. See Figure 6.4 for a detailed view of the architecture. Figure 6.5 shows a subset of the predictions compared to the original spectra from the test sample. The NN can deal with a noisy spectrum and can reproduce the overall shape, the number of features, the continuum, and the most prominent features.

An issue with the code is with respect to the phases distribution of the training sample - early phases are rarer, especially as velocity is difficult to measure in more featureless spectra with a less defined P-Cygni profile. Despite balancing for phase, there is still less variety in the early spectra, and repeating each early spectrum a very large number of times would decrease the integrity of the dataset, as duplicates passed in training would bias the predictions. Overall, this means it could be expected that predictions for especially early and late phases would have worse performance.

Interpolating Parameters

In order to predict spectra for unobserved phases these parameters need to be interpolated to the epochs at which the artificial spectra are requested. The evolution of these parameters would need

to be inferred using the training sample, however the issue with the evolution of these parameters is that they do not cover the same range and timesteps, which makes learning from this data more complicated. Each SN has spectra taken at different epochs with varying timesteps, and some SNe such as SN 1999em are far better sampled with many times more spectra than other SNe in the training sample with as little as one spectrum.

A method which was tried was to interpolate all existing observed data with Gaussian Processes and average those curves which overlapped with the points we were trying to predict for. However sometimes there were quite few timesteps and the interpolation was not very smooth, often with large error regions, therefore an alternative approach was searched for. Fitting a function rather than a generic interpolation could help fix this issue.

There exists a body of work on trying to fit a functional form to temperature and velocity evolution (e.g. Takáts & Vinkó, 2012; Faran et al., 2018), and this is a complex problem. For temperature, an exponential is a purely phenomenological and generic approximation. Up to the plateau phase at approximately 40/50 days the exponential approximation for temperature empirically describes the majority of the data well, however recombination and other more complicated physical effects occur at later phases, which are beyond the scope of this work. The temperature was fit using the general exponential function below:

$$v = Ae^{Bt+C} + D \tag{6.1}$$

Here A,B,C and D are free parameters. Alternatively for the velocities, Nugent et al. (2006) proposed the following relationship for the evolution of Fe II λ5169 velocity:

$$v_{Fe}(t)/v_{Fe}(50d) = (t/50)^c \tag{6.2}$$

Where c is a constant and t is the days past explosion. An updated relationship with a similar form has been suggested by Faran et al. (2014) however this follows the same structure and has the same free parameters ($v_{Fe}(50d)$ is left as a free parameter when fitting this equation). Both Fe II λ5169 and Hα velocity were fit with a function following the form of Equation 6.2. The fitting of these functions to observed temperature and velocity was done using the Metropolis Hastings algorithm, a Monte-Carlo Markov Chain (MCMC). The MCMC algorithm takes starting parameters for the function being fit which are varied randomly and the quality of the fit checked until they converge on a minimum. The starting values are important because if they are too far from the optimal fit it may never converge, or they may get stuck in a local minimum. The starting parameters were based on the average for the fits to the training sample with scipy curvefit, where there were at least 4 points available for fitting. A flat prior was used with no bounds set for the parameters, and a χ^2 likelihood was used. There were 10,000 epochs, and one walker. Step sizes were set based on the size of each parameter and varied by experimenting on the best results/convergence.

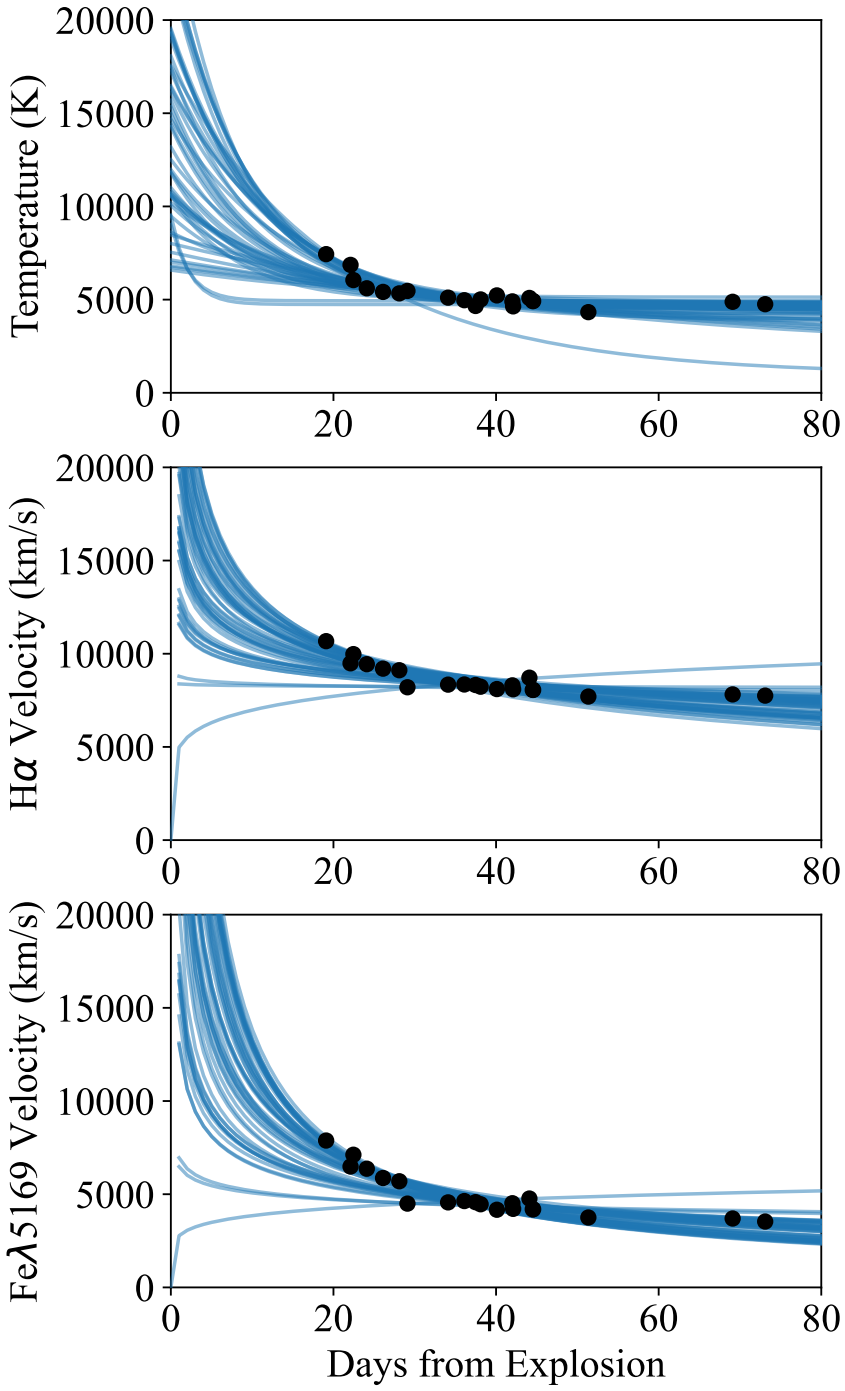

Figure 6.6. MCMC predictions for Temperature, Hα velocity, and Feλ velocity, made 50 times for four random spectra from the full set of 30 spectra in the silver sample. Where the four random spectra are very close together, this can result in very poor fits (see the outlier in the bottom two panels).

Figure 6.6 shows the fitted functions of Equations 6.1 and 6.2 to the measured velocity and temperature from the observed spectra of our test SN, SN 2013ej [‖] (Valenti et al., 2014). The fit is made for 4 randomly sampled epochs from the full set, 50 times. As can be seen the functions chosen provide good fits to the data in the phase range shown. See Table 6.4 for the mean χ^2 values for the 50 fits with different numbers of spectra sampled, for comparison. As the sampled number of epochs decreases to three, the approach can still provide a good fit. However, if the points are too clustered together or there's too much scatter in the data the fitting becomes unreliable (i.e. increase in the χ^2 value). The greater the number of points the better the fit - see Figures A.2-A.9 in Appendix A.4 for 2, 3, 8 and 12 epochs sample. Above 4 points, scipy curvefit could also be a good choice for fitting and this may have more consistent results than the MCMC, however this requires a minimum of 4 and would not work for 2 or 3.

Figure 6.7 shows the predicted evolution of SN 2013ej, which was excluded from the training sample for the NN for the purposes of testing. SN 2013ej was chosen as a well-observed standard luminosity SN II which could be considered representative of this class. The predictions were made every three days, and shows overlapping 50 prediction spectra, with each one from a different random 4-spectrum sample. It is found that the observed spectra (in black) can be generally reproduced well from the parameters, however a bad fit (e.g. an outlier output) to temperature or velocity can produce incorrect or unphysical spectra. Additionally, a large variation in fits to temperature at early times appears to manifest as greater uncertainty in the continuum of predicted spectra at early times, and under-predicted Fe II λ5169 velocity (which can also correspond to what is seen with the functional fits).

The fitting algorithm, using Metropolis-Hastings with a flat prior, does not provide constraints on the fits which can lead to poor/unphysical fits as can be seen in Figure 6.6. Therefore, an alternative MCMC algorithm was also investigated, using the Python package emcee (Foreman-Mackey et al., 2013). There were 32 walkers used with 1000 epochs, and upper and lower bounds were set on the parameters based on the average scipy fits to well-sampled (greater than 4 epochs) SNe in the training sample. A Gaussian Prior was used, where parameters were sampled from a Gaussian distribution centered on the mean values and standard deviation of the parameters based on the training sample fits. Figure A.10 in Appendix A.4 shows the emcee fits compared to the algorithm used in elsewhere in this Chapter (Metropolis-Hastings), and it can be seen that the fits are much improved. Figure A.11 shows a comparison of the spectra predictions, and there is less variation in the predicted spectra. However, in Figure A.12, the average velocity predictions compared to observations are not significantly different from those of Metropolis-Hastings, except with slightly smaller standard deviation (error bars) for emcee.

[‖] The velocities have been measured by fitting a Gaussian to the P-Cygni rather than taking the parameters from the golden sample as all available spectra for SN 2013ej were used, including those in the silver sample which did not have velocity measurements, so they were measured together for consistency.

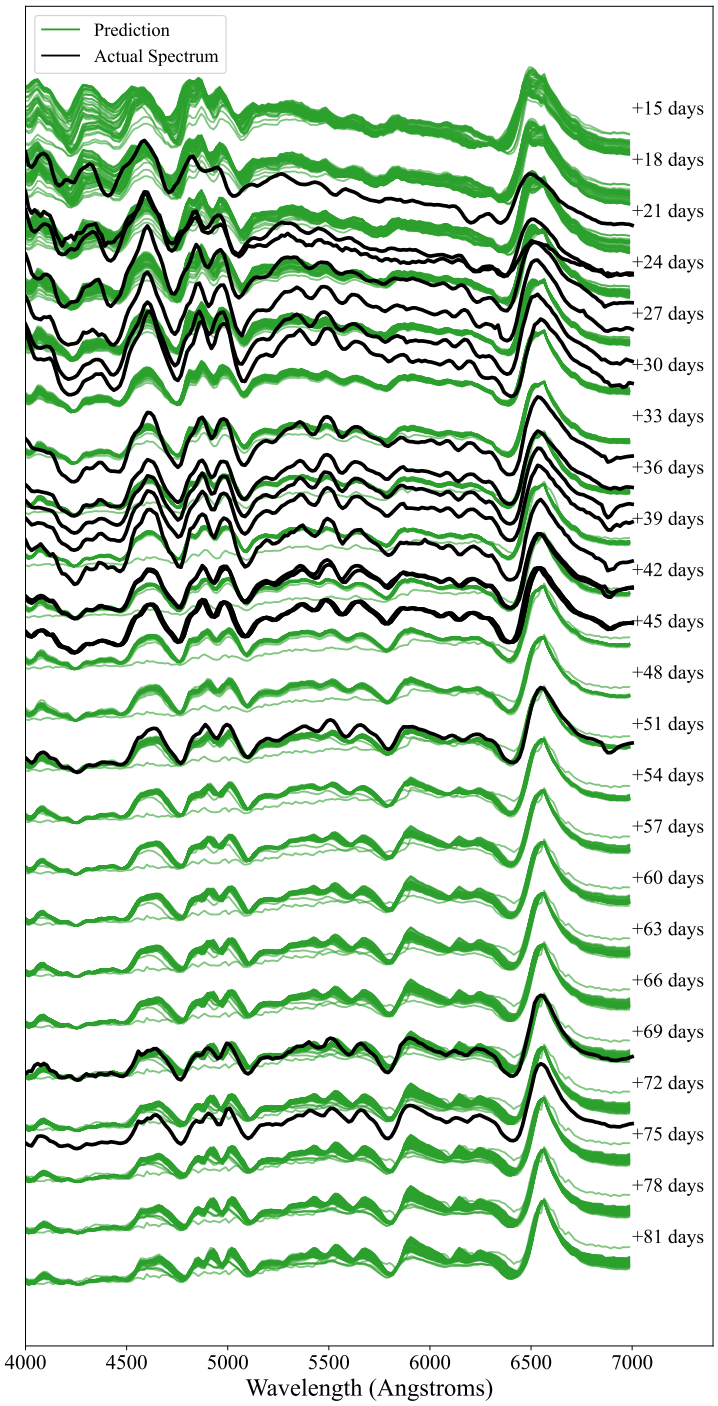

Figure 6.7. Predictions from 50 sets of four random spectra for SN 2013ej. The predictions (in green) were made for every three days, and spectra in black are the observed spectra. The last two spectra appear slightly shifted with respect to predictions. When the functional fitting is poor and results in unphysical interpolated parameters, this can result in very poor predicted spectra with similarly unphysical characteristics (see red of 6500 Å after approx. 50 days, and temperature predictions past 50 days in Figure 6.6). Here the spectra are normalised between 0 and 1 as before and the y-axis offsets each spectrum for display purposes, with increments of 3 days in phase from explosion.

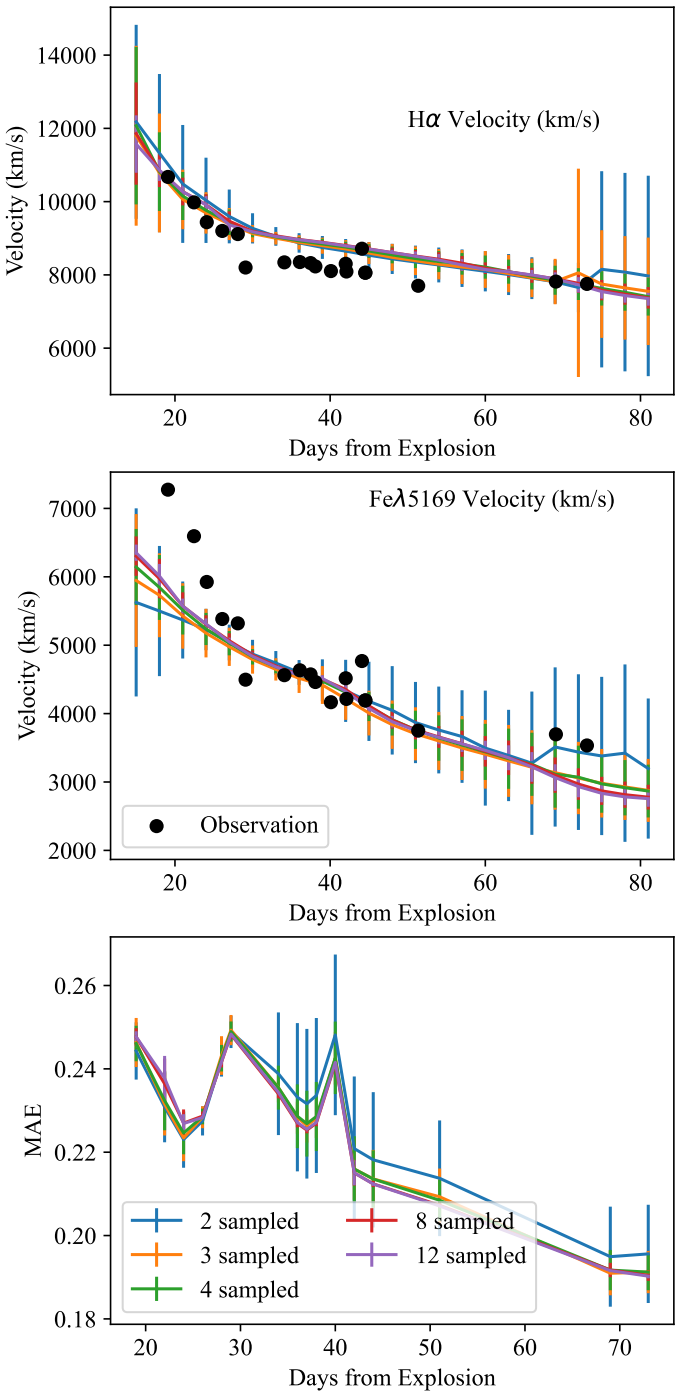

Figure 6.8. Top Panel: Velocity predictions for Hα together with observations. Middle Panel: Velocity Predictions for Fe II λ5169. Bottom Panel: MAE for predictions of spectra for a given epoch from explosion. This is repeated for a variety of numbers of spectra sampled before interpolation together with the prediction. Shown are the average MAEs for the 50 samples, and 1 σ standard deviation error. The fast decline of Fe II λ5169 before approximately 30 days is not reproduced, which is quite a stark difference to the observations and suggests an issue with making earlier epoch predictions.

Testing

Testing the accuracy of predictions is split into two parts - the first is a general measure of how well the spectra match the predictions, measured by the MAE. The MAE is calculated by the mean of the absolute difference between the predicted and observed spectrum, at each wavelength point. As the spectra are normalised between 0 and 1, this can also roughly be thought of as a percentage error. The other means of testing the quality of the predictions is to measure the Fe II λ5169 and Hα velocities directly from the predicted spectra and compare to the observations.

The bottom panel of Figure 6.8 shows the MAE vs. days from explosion for 2, 3, 4, and 8 sampled epochs (i.e. 2 to 8 spectra). The average MAE for the 50 predictions is similar from the 8 down to 2 epochs sampled. However, the standard deviation increases with decreasing numbers of epochs - as could be expected, the more epochs sampled, the less the deviation in predictions. Figure 6.8 also shows the mean and standard deviation of the Fe II λ5169 and Hα velocities measured for SN 2013ej both from the predictions (line plots) and the observed spectra (black points), in the top two panels. The velocities are calculated by a Gaussian fit to the absorption component of the P-Cygni profile. For Fe II λ5169 a small number of outliers were excluded for 2 epochs (4.3%) and 4 epochs (1.0%) where the velocity measured was clearly unphysical (on the order of 12,000 km s^{-1}), likely from the incorrect line being automatically selected by the fitting code. These were excluded to prevent skewing of the mean and standard deviation. Note that due to the random selection of epochs for fitting, predictions, and therefore the number of outliers, vary every time the code is run. In Figure 6.8 a similar issue is seen with outliers for Hα at approximately 55 days for 3 samples.

Figure 6.9 shows a bar chart of the mean difference between predicted and observed (interpolated) velocities, compared to the velocities measured by the same method for the observed spectra. They are split out over a number of bins of days from explosion. The greatest errors appear due to a poor functional fit to the parameters, and the further the fit is from the actual values for the SN the worse the predicted spectrum. Unphysical predicted values for temperature result in unphysical spectra. For example a single very poor fit to temperature appears as a spectrum with a very flat continuum from 40 days onwards in Figure 6.7. Figures 6.8 and 6.9 show largely similar velocity error distributions regardless of the number of samples, and so it can be concluded that the main source of error is the accuracy of the parameter values and therefore the greatest weakness in this method is fitting functions to interpolate/extrapolate the existing measurements.

As can be observed from Figure 6.7 and the supplementary Figures A.2-A.9 in Appendix A.4, there is large error in the Fe II λ5169 velocity at early times, a problem which persists even to 8/12 sampled epochs.

Figure 6.10 shows the same bar chart as Figure 6.9 of the error in Fe II λ5169 and Hα velocity for a sample of nine SNe. Here four epochs were sampled for all, and the SNe were chosen among those with at 7 or 8 available, of which four were sampled 50 times - though the fit is slightly different

each time as a stochastic MCMC is used - and also where the spectra were sufficiently distributed across epochs (range examined was the 20-80 days as for SN 2013ej). The Parameter Method has a tendency to overpredict Hα velocities, and underpredict Fe II λ5169 velocities.

Though specifically the velocities have been compared between the measurements from observed and predicted spectra, the ultimate goal of this method is to reproduce not just the specific Fe II λ5169 and Hα velocities but the whole spectrum, and the velocity measurements here are used alongside MAE as a diagnostic of how well the spectra are reproduced rather than the final goal.

Further Applications of the Parameter Method

Linking key parameters to spectra could be very useful in shortcuts for modelling and simulations, as modelling is very resource and computationally-expensive (e.g Vogl et al., 2020; Kerzendorf et al., 2021). Being able to generate quick spectra linked to the properties of the progenitor, such as mass and explosion energy, could be beneficial in simplifying this process. The parameters chosen for this method were picked for the ease of measurement for all the spectra throughout the evolution, i.e. measuring from the continuum and significant visible lines. However, parameters could feasibly be any information available for the training spectra. This could be worth exploring in further work.

6.3.2 Spectra Method

An alternative means of prediction was investigated, which bypasses measuring and predicting parameters to construct the spectra. The issue with Parameter Method was the need to predict the parameters in a two-part algorithm, as the weakness with this method lay in interpolating the parameters when there were fewer than at least four existing spectra, which would be the likely case for LSST, or if the evolution of velocity and temperature was not well-described by the form of Equations 6.1 and 6.2. The sample used by this method is the silver sample which included the WISeREP and ePESSTO+ spectra. This method will deal with many more features than the previous Parameter Method (as spectra are both inputs and outputs) and therefore a dimensionality reduction is more important.

Variational Autoencoder

The dimensionality of the spectra can be reduced using a variational autoencoder (e.g. Ollivier, 2014). A variational autoencoder can create a latent space (also known as the encoding space) which can also be used in a generative manner to create new spectra, by choosing a random point in the encoding or latent space. The variational aspect stems from the fact that the autoencoder is probabilistic in nature with the latent space resembling a Gaussian distribution, which makes it suitable for generating a new instance which is most likely to resemble the features of real spectra.

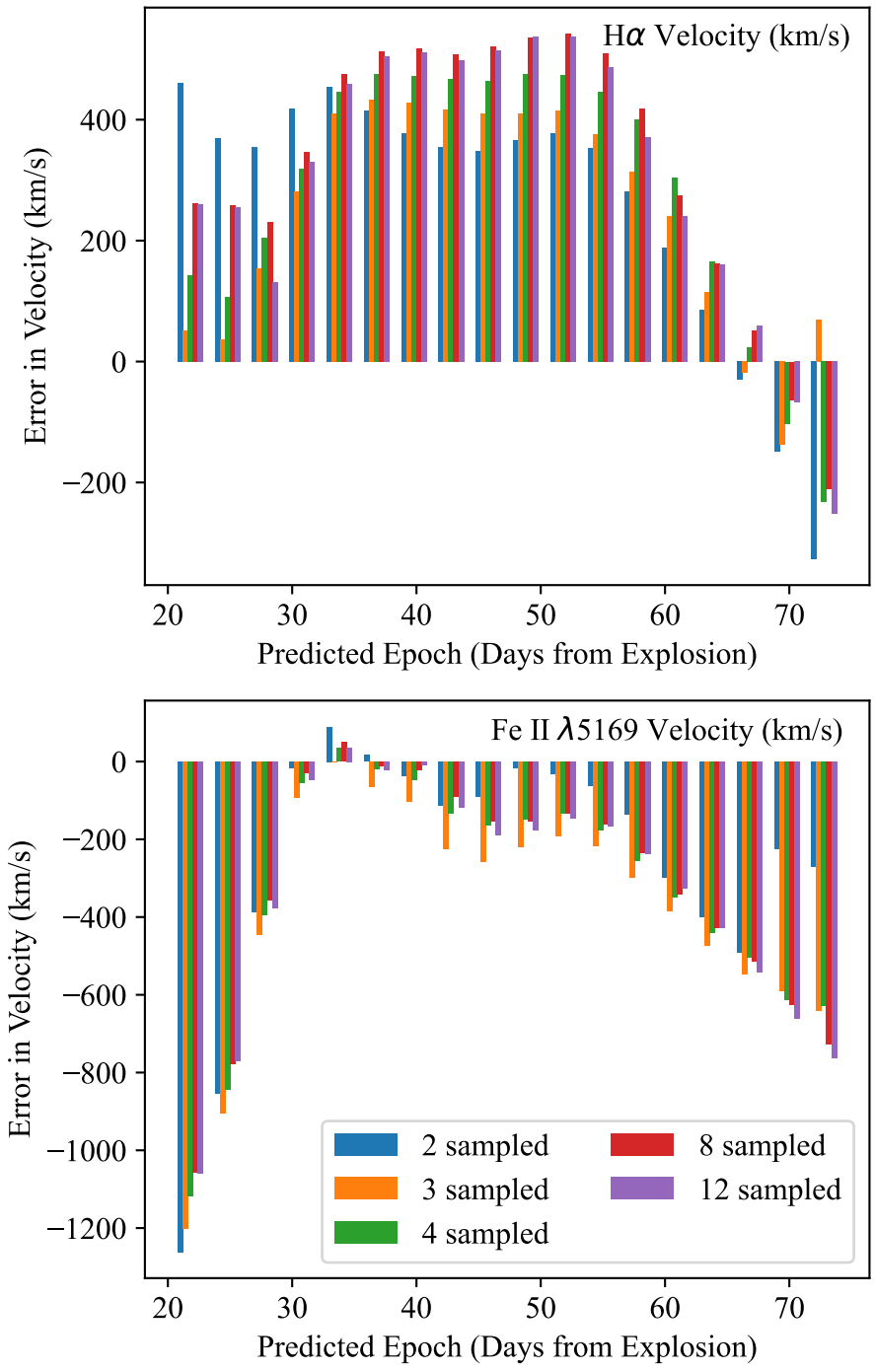

Figure 6.9. Bar chart for the mean difference in observed and predicted velocity per epoch bin for SN 2013ej against the predicted epoch. The top panel shows Hα velocity and the bottom Fe II λ5169.

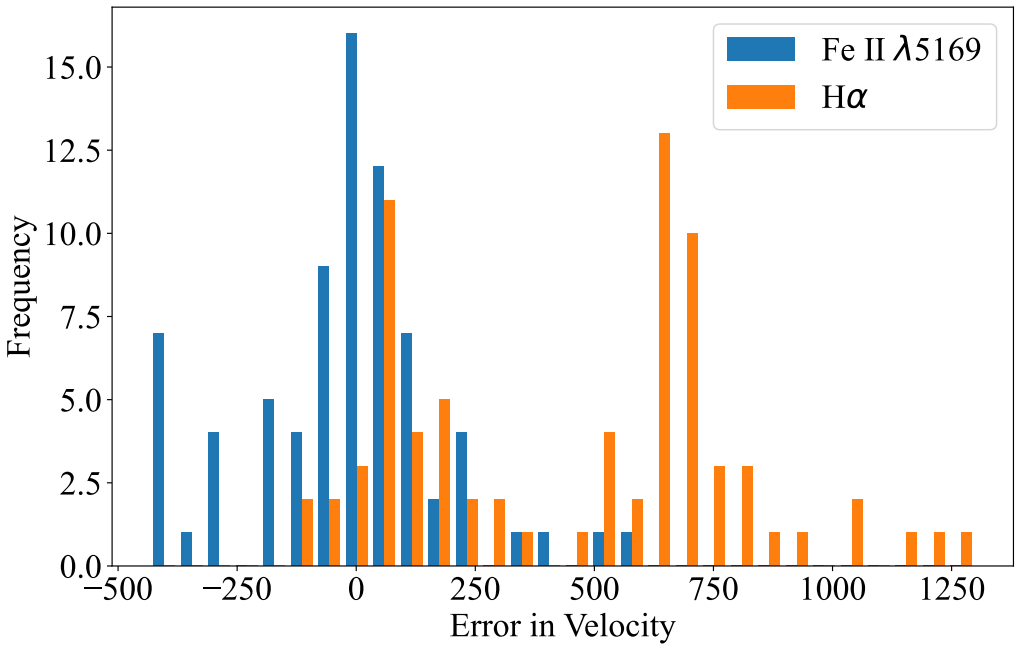

Figure 6.10. Histogram of positive and negative errors for the velocity predictions of a small sample of SNe with 7 or 8 spectra in the golden sample: SN 1986L, SN 2002gw, SN 2002hx, SN 2004fc, SN 2006ai, SN 2006ee, SN 2007oc, SN 2007X, and SN 2009N, with the Parameter Method and four epochs sampled. Hα tends most to be overpredicted and Fe II λ5169 underpredicted.

A variational autoencoder was chosen over other dimensionality reduction, as this advantage in generating new spectra is important because spectra are encoded when input and output into the NN. See Figure A.1 for the latent space trained on the silver sample of Type II SNe, where the 200 data points of the original spectra have been reduced to two dimensions with the autoencoder. The encoded dimensions have no corresponding physical meaning. This latent space could be used to generate new spectra, with the aim of covering the full range of SN II spectra in the phase range considered. Dimensionality reduction assists in reducing computational costs and possibly in removing some random variation in the spectra which would not contribute to learning. The reduced-dimension spectra can be used in training another NN, with the autoencoder trained beforehand separately. The spectra were originally interpolated to 200 data points so reducing this whilst preserving much of the information could be a great benefit in helping the NN recognise more fundamental features, finding patterns in a handful of dimensions rather than 200.

Predicting Spectra

For the Spectra Method, the input is the spectrum used to make predictions (the predictor spectrum). The output is the predicted spectrum at the requested epoch (the predicted/target spectrum at the target epoch). By making multiple predictions, a series of associated spectra from the input

to a range of target phases can be produced, hence a full spectral evolution. To create a training set, every SN had all of its associated spectra paired up with the input one, in combinations of two spectra. Each of these pairs alongside the target epoch were added as a row to the training set. This way the training set builds up a large number of examples of pairs of spectra at a range of epochs (for each SN).

The spectra were encoded to ten dimensions using the variational autoencoder. The NN then took as the input a concatenation of the first spectrum (encoded to 10 dimensions), and also the epoch of the first spectrum and the target epoch for prediction. The output is then the 10 dimensional encoding of the target spectrum. All pairs were taken which includes the reverse of each pairing (predicting the other way). The 10 dimensional encoding was chosen fairly arbitrarily, increasing from the initial 2 to try and capture more of the variance. See Figure 6.11 for the architecture.

In order to balance the data and preventing any bias from over-represented SNe, additional balancing was done. A reduced (or oversampled) number of spectra were taken for each SN (chosen randomly), and then paired with each other. This balancing is done to avoid bias towards certain SNe, e.g. SN 1999em with 58 spectra would take up a very significant portion of the entire training sample. If there were less than 10 total spectra, the set was oversampled to 10 before pairing (90 data points after pairing). If there were between 10 and 20, it was oversampled to 20 (380 after pairing). Otherwise if greater than 20, it was capped at a random sample of 30 (870 after pairing). This is still biased towards better sampled SNe, but these have far better learning potential and cutting down further would be further discarding valuable data.

Figure 6.12 displays the test case of SN 2013ej using the Spectra Method. The variational autoencoder and subsequent NN were trained with the exclusion of this SN. In each Panel, only the blue spectrum was used to predict every other epoch in orange. The black spectra are the other original spectra shown for comparison with our predictions. Generally the predictions reproduce the features and continuum well, however visually the most noticeable error in predictions is reproducing the double absorption for Hα which is the high velocity 'Cachito' feature (e.g. Gutiérrez et al., 2017a,b) at around 6400 Å for early spectra. Also to note in some cases proximity of epochs between the input and output spectra does not lead to improved predictions - see the top left and bottom left panels of Figure 6.12. When the input spectrum is 7 days, the 5500Å region of the 75 day spectra is better reproduced than when the input spectrum is at 75 days. This is not what one would naively expect - and to some extent issues with the autoencoder could be responsible. Nevertheless, this could be a direction for further investigation.

A worse performing case is reported for SN 2005cs (Figure 6.13), a low energy SN IIP which represent a less common sub-variety of Type II (e.g. Takáts & Vinkó, 2012; Kozyreva et al., 2022), where predictions have trouble reproducing the Hα P-Cygni profile. When early spectra are used to make the predictions, the velocity evolution of Hα is significantly shifted in subsequent spectra. This is possibly as a result of the autoencoder not successfully encoding the early spectra and therefore

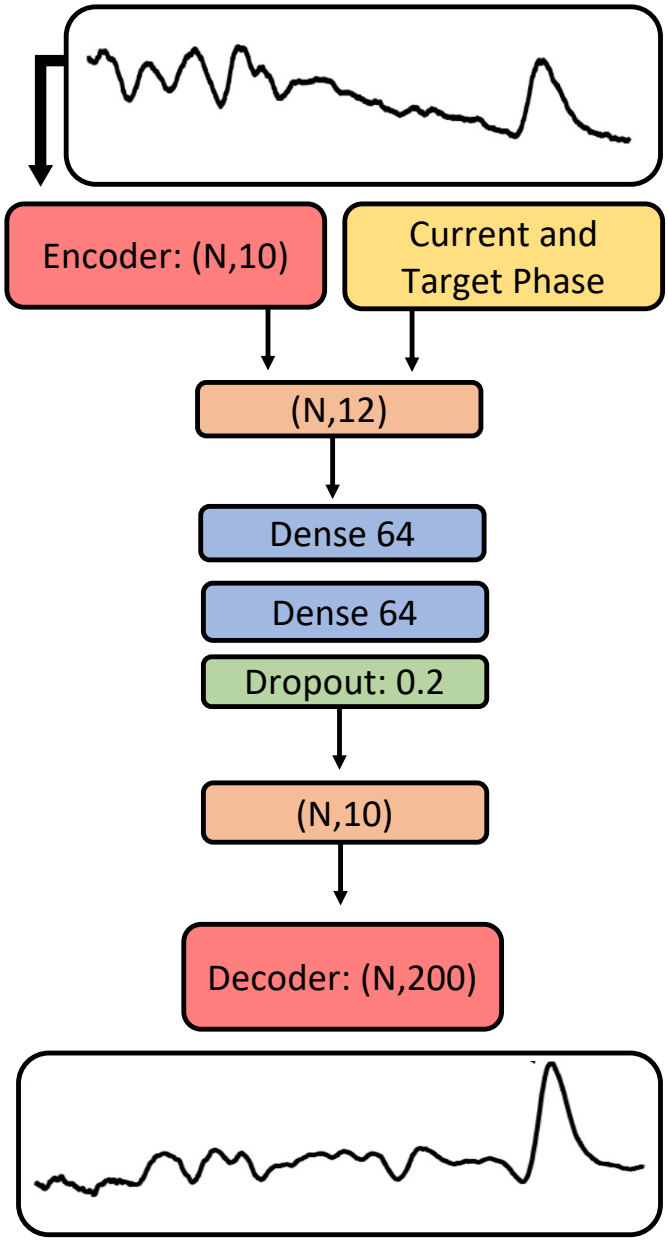

Figure 6.11. Architecture for Spectra Method: input was the original spectrum encoded to 10 dimensions with the VAE, with the addition of the target and original phase, the output being 10 dimensions which are decoded to the predicted spectrum at the target phase.

the whole evolution is shifted, see the predictions for same epoch as the blue spectra for the top panel in Figure 6.13. When later spectra are used to make predictions, the predicted Hα P-Cygni profile is predicted to be an incorrect shape for early spectra. Further test cases (i.e. SN 2004et, SN 2015V and SN 2016X) are reported in Appendix A.4 in Figures A.18 - A.20.

6.4 On the usefulness of predicting spectra/parameters of Type II SNe

The error in predictions is limited by the quality of the autoencoder. Even if the prediction of the spectrum is perfect, this is in a reduced dimensionality form which needs to be decoded to get the full spectrum. Therefore the error in the autoencoder decoding is the lower limit for the error in predictions. For this reason the autoencoder was not included in the Parameter Method, where good results were seen even without it, to avoid further complicating the algorithm. The MAE for the autoencoder was found by comparing the original test spectra vs. the decoded spectrum encoded into 10 dimensions. The mean MAE for 10 percent of training sample (trained only on the augmented golden sample) is 0.026$\pm$0.011, which appears to be approximately the lower limit of the order of errors in the predictions.

Figure A.13, A.14 and A.15 in Appendix A.4 shows the Hα (top panel) and Fe II λ5169 (bottom panel) velocities of the observed spectra against those measured from the predicted spectra in the case of our three test SNe (i.e. SNe SN 2013ej, SN 2005cs and SN 2004et). The test SNe SN 2013ej, SN 2004et and SN 2005cs are chosen as they are well studied objects with a complete dataset, and are representative of the energy distribution of SN II: SN 2013ej is a standard luminosity SN, SN 2004et is a higher luminsoty SN, and SN 2005cs is a low energy and luminosity SN. SN 2005cs and SN 2004et have also been used for distance measurement by Takáts & Vinkó (2012), for which method this work could be applied. The velocities are measured using a Gaussian function to fit the P-Cygni profile. The difference in the absorption minimum from the rest wavelength is used in combination with the Doppler effect to calculate the velocity. In Figure A.14 for SN 2005cs, as the predictions for the first three spectra had significant issues these have been separated out in grey, and the remaining predictions for the velocity have had the mean and standard deviation calculated excluding the above epochs for better clarity. The velocity predictions for Iron are too high for later epochs, and the Hα predictions are also too high.

We then consider the effects of an inaccurate labelling of the epoch (i.e. an error in the measurement of the SN phase) on our method. We added a shift to all the reported phases before making predictions, and the resulting Figures are in Appendix A.4. Figure A.16 has a shift of +10 days, whereas Figure A.17 has a shift of +30 days with respect to the reported epochs of SN 2004et. These shifts were chosen to deliberately be greater than what could realistically be an expected error, with 10 days at the very upper end, and 30 days purely to test how the model performs. The median internight visit gaps of LSST according to Bianco et al. (2022), following two simulated

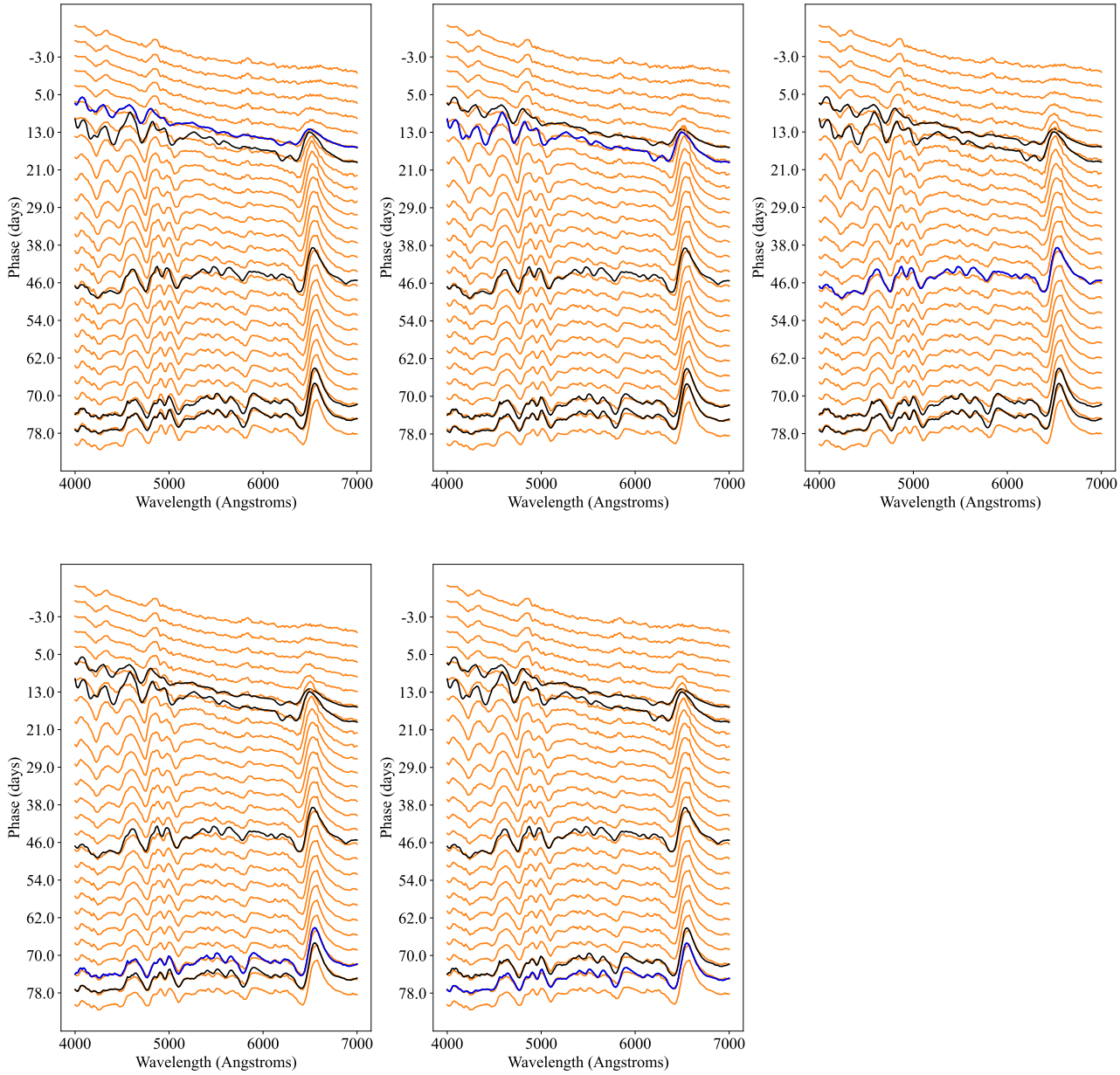

Figure 6.12. Predictions for SN 2013ej using the Spectra Method. The orange spectra are the ouputs of the algorithm, whereas the black are the observed spectra. Each Panel has a different observed spectrum used as the input to make predictions, and this is highlighted in blue to differentiate.

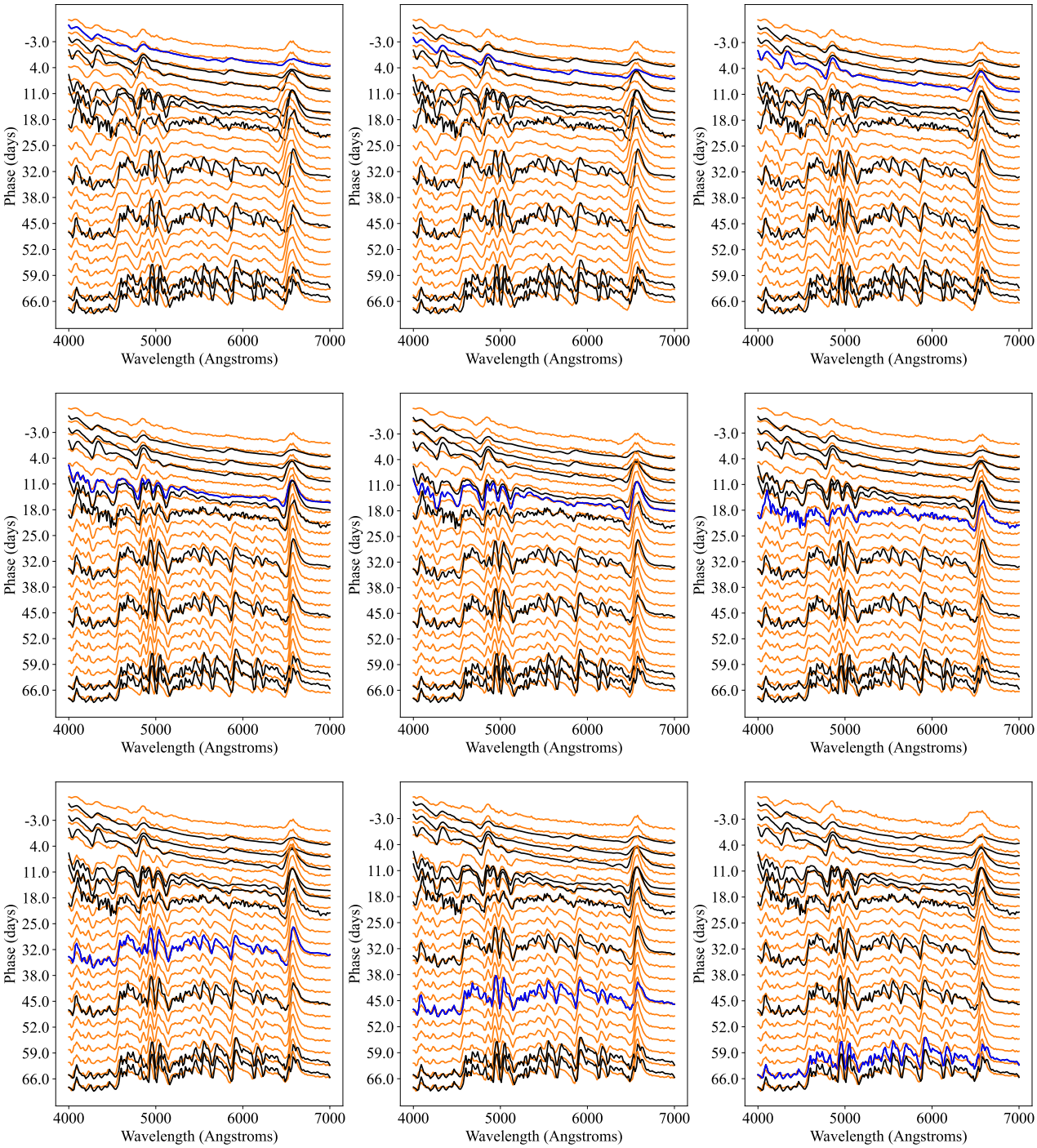

Figure 6.13. Using the Spectra Method to predict SN 2005cs, a low energy SN IIP which deviates significantly from average (Takáts & Vinkó, 2012; Kozyreva et al., 2022). The predictions for this subset of spectra vary in the strength of lines compared to Figure 6.12 however the locations of the absorption lines appear to correspond with the observed spectra, when the spectra used to make the prediction are later than 14 days. Epochs of observed spectra are 4, 5, 8, 14, 17, 22, 34, 44, 61, 62 days from explosion. The P-Cygni Hα profile is not well reproduced, particularly for the earlier spectra.

LSST strategies, is 3 days for observations in any band. Therefore this could be the order of error expected in the explosion epoch, which is comfortably below 10 days.

For a +10 days shift the difference in predictions is small and it is a margin of error that is tolerated well. However, for a +30 days shift the velocity predictions vary much more depending on which spectrum is being used to make predictions, and there is a great spread. Nevertheless, considering the efficiency of spectra classification tools e.g. SNID (Blondin & Tonry, 2007), GELATO (Harutyunyan et al., 2008), and DASH (Muthukrishna et al., 2019), and light-curve information, such large differences will be highly unlikely.

Earlier spectra would be expected to have poorer predictions as they tend to be a blue continuum with few distinguishable features. This also applies to later spectra (e.g. $>$+90 days) as these may no longer be in the photospheric phase and therefore different physics governs their form - for example the blackbody approximation is less appropriate. This means they do not follow the same patterns as the other spectra and given their lower number and variety the algorithm could be expected to perform more poorly. The duration of the photospheric phase ($t_{\rm pt}$) can be measured as the end of the plateau, and e.g. Valenti et al. (2016) found a mean of $t_{\rm pt} = 100$days for SNe II.

In order to have a greater coverage for testing the accuracy of the predictions, a larger set of SNe are tested and the MAE of the predictions reported. Figure 6.14 shows the MAE for 15 test SNe - the bottom panel shows a histogram of the MAEs - the majority of the predicted spectra fall into under 0.1 MAE. The 15 SNe are all the SNe with at least 8 spectra available. This gives a total of 659 pairings of each spectrum with the others, for each SN. Of these 659 pairings, 63.7% were less than 0.1 MAE, 90.1% were within 0.2 MAE, and 98.1% were within 0.3 MAE, which can also be seen on the histogram. In the top panel of Figure 6.14, it can be seen that a minority of spectra have MAEs greater than 0.2. The highest average errors appear to be for predicted spectrum phases later than 90 days when the SN might already be in the pseudo-nebular phase, i.e. after the drop from the plateau.

Figure 6.15 shows histograms of the mean difference between predicted and observed spectral measurements of the Hα and Fe II λ5169 velocity for the test sample - the majority of predictions are within the error measured in the golden sample for line velocities for Fe II λ5169, but not for Hα.

Figure 6.16 shows a bar chart of the mean velocity split by epoch bins. It can be concluded that the majority of Fe II λ5169 velocities are up to around the margin of error measured in the golden sample, however the Hα velocities are often greater - suggesting the algorithm is weaker at correctly predicting the Hα P-Cygni. It should also be noted there is a very large mean error in Hα velocity around the 20 day bin. However, inspecting the other figures this is likely from a minority of the predictions, combined with velocities being more difficult to measure at early times when the spectrum is bluer and featureless. It can however be concluded that when using this tool to make predictions it is better to use and to predict spectra after around 20 days from explosion as performance for these early spectra is poor.

Figure 6.16 also shows that for Hα velocities there appears to be a trend of overpredicting at early times (before 30 days) and underpredicting at late times (100+ days), though between 40 and 100 days there are also variations. For Fe II λ5169 this trend is less clear.

6.4.1 Fe II λ5169 Velocity Prediction

As discussed in Chapter 1 Section 1.5, it is clear that a tool able to predict the Fe II λ5169 could be useful for the Standard Candle Method (SCM) in measuring cosmic distance for SNe II. However, creating better spectral coverage for a SN with machine learning could prove to be beneficial for other distance measure methods as well. Therefore a measure of the performance of the Spectra Method could be the ability to match the Fe II λ5169 velocities.

To test our predictions, we compare the predicted velocity evolution of Fe II λ5169 with the well-sampled case of SN 2004et (Takáts & Vinkó, 2012). Figure A.15 in Appendix A.4 shows the predicted velocity evolution for all SN 2004et spectra in the silver sample, measured with Gaussian fits. For the Spectra Method, the averaged predictions of the Fe II λ5169 velocity for SN 2004et at 50 days past explosion is 3553$\pm$200 km s^{-1}, averaging the results from 32 spectra. The Parameter Method for SN 2004et using four sampled spectra from the set of SN 2004et spectra in the silver sample (excluding all SN 2004et data from the Parameter Method training) gives a Fe II velocity of 2982$\pm$153 km s^{-1} at 50 days, from averaged 50 predictions with four random spectra sampled each time. Increasing the number of sample spectra to eight gives a velocity of 3380$\pm$43 km s^{-1} and hence the mean increases to closer to the Spectra Method while the error decreases.

Takáts & Vinkó (2012) found a velocity of 3740 km s^{-1} at 50 days for SN 2004et based on cross-correlation with SYNOW (Parrent et al., 2010) models to find the photospheric velocity. This is within agreement with the mean measured from predictions, however the standard deviation for the predictions is 5.6% of the mean for the Spectra Method (the largest error of all methods of predictions above) and therefore there is some variation depending on which spectrum is used to make the prediction. Additionally, all methods under-predict the velocity compared to SYNOW. This suggests that the process can be improved further to decrease the uncertainties regardless of the starting spectrum. The mean error in the Fe II λ5169 velocity reported for the Padova-Asiago SN group sample (a subset of the golden sample with the lowest mean error) was 126 km s^{-1}, so the largest error in predictions was approximately 1.5 times greater than the original measurements. The error in Fe II λ5169 velocity associated with a 15 Å resolution would be 870 km s^{-1}, calculated from the Doppler effect assuming a delta of 15 Å and a rest wavelength of 5169 Å, which is relatively quite large and allows for a greater error margin, however generally line centroids can be measured with greater precision than the resolution and cases where the line centroid is displaced by the resolution are very rare, hence this larger error threshold is not appropriate for comparison.

In order to gauge what kind of errors this would result in for distance estimation using the

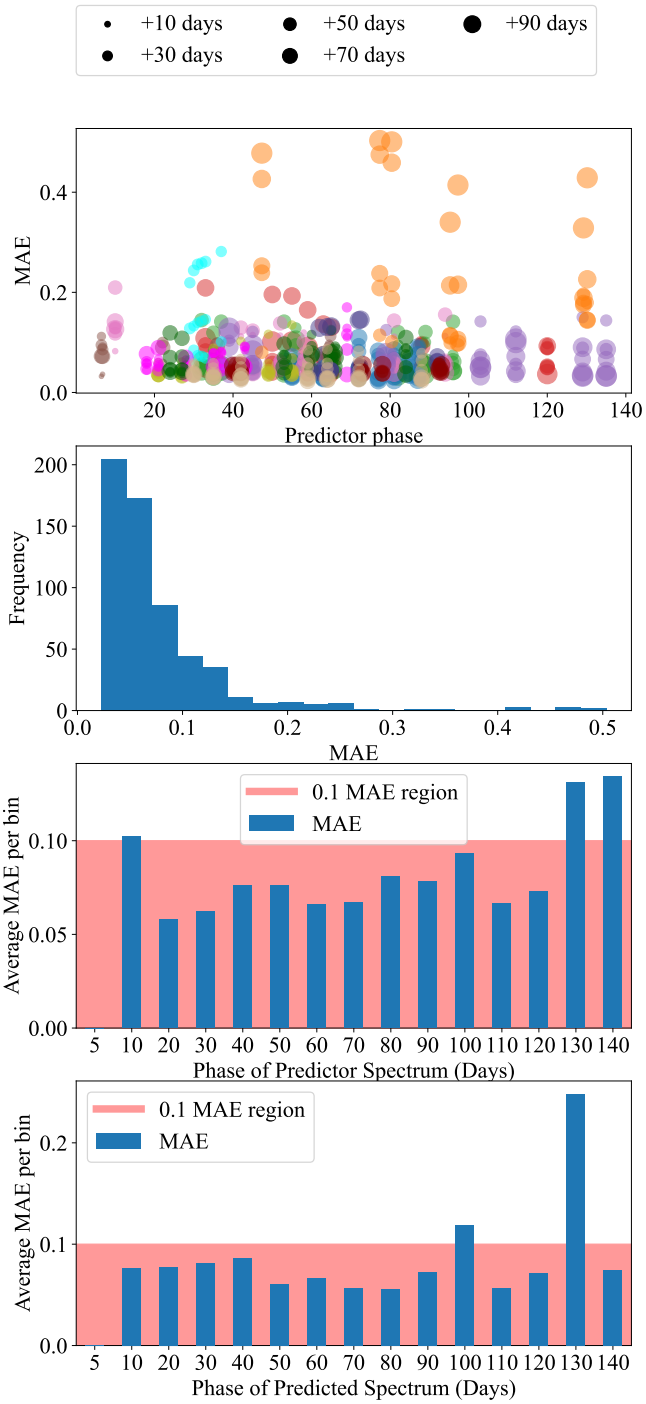

Figure 6.14. Errors for 15 test SNe: SN 1986L, SN 2002gw, SN 2002hx, SN 2003gd, SN 2004ej, SN 2004er, SN 2004fc, SN 2006ai, SN 2006ee, SN 2007oc, SN 2007X, SN 2009js, SN 2009N, SN 2012A, SN 2019unb. These spectra cover a range of epochs from 6 to 135 days from explosion.

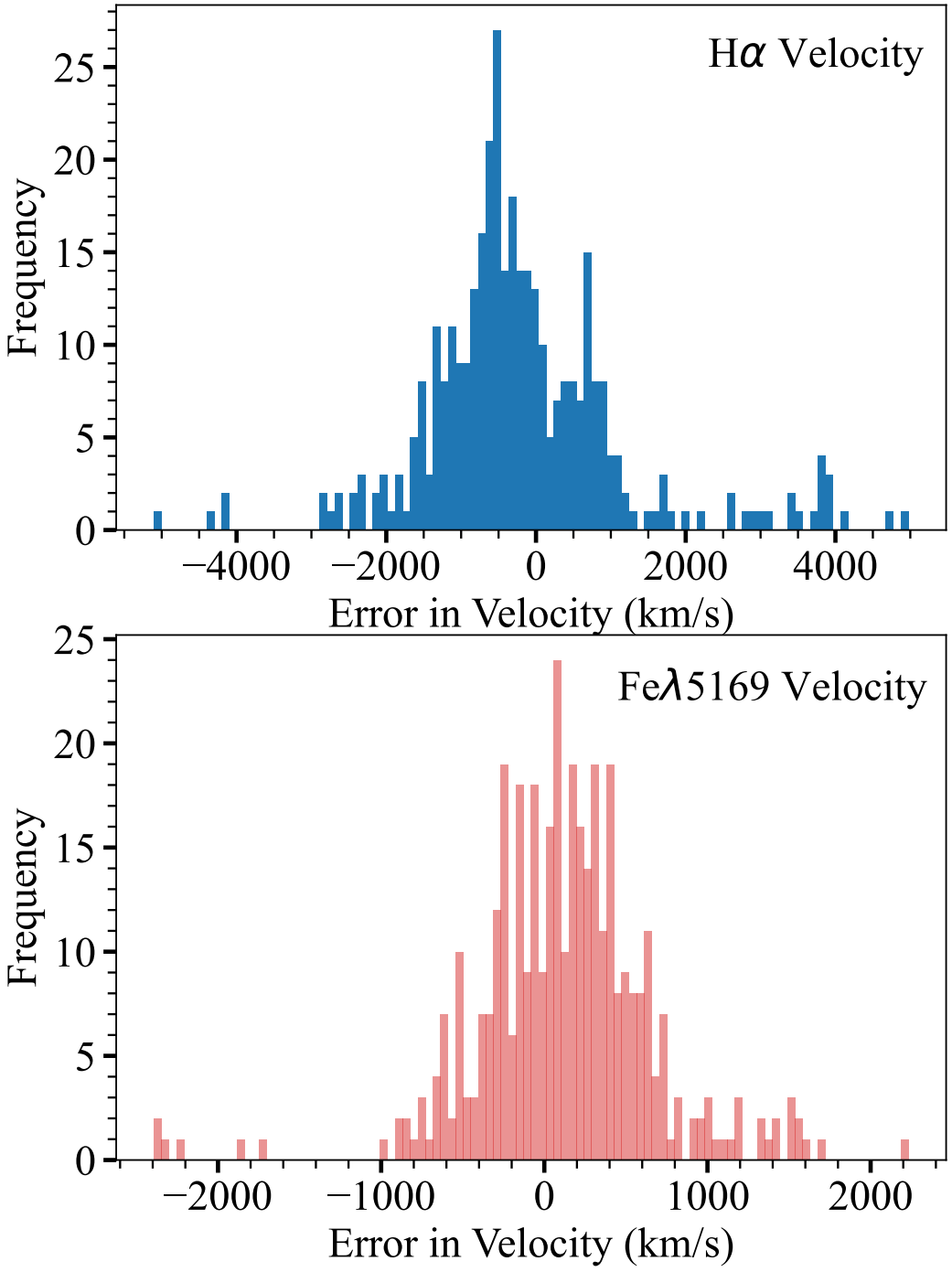

Figure 6.15. Mean velocity difference between predictions and observations for 15 test SNe: SN 1986L, SN 2002gw, SN 2002hx, SN 2003gd, SN 2004ej, SN 2004er, SN 2004fc, SN 2006ai, SN 2006ee, SN 2007oc, SN 2007X, SN 2009js, SN 2009N, SN 2012A, SN 2019unb.

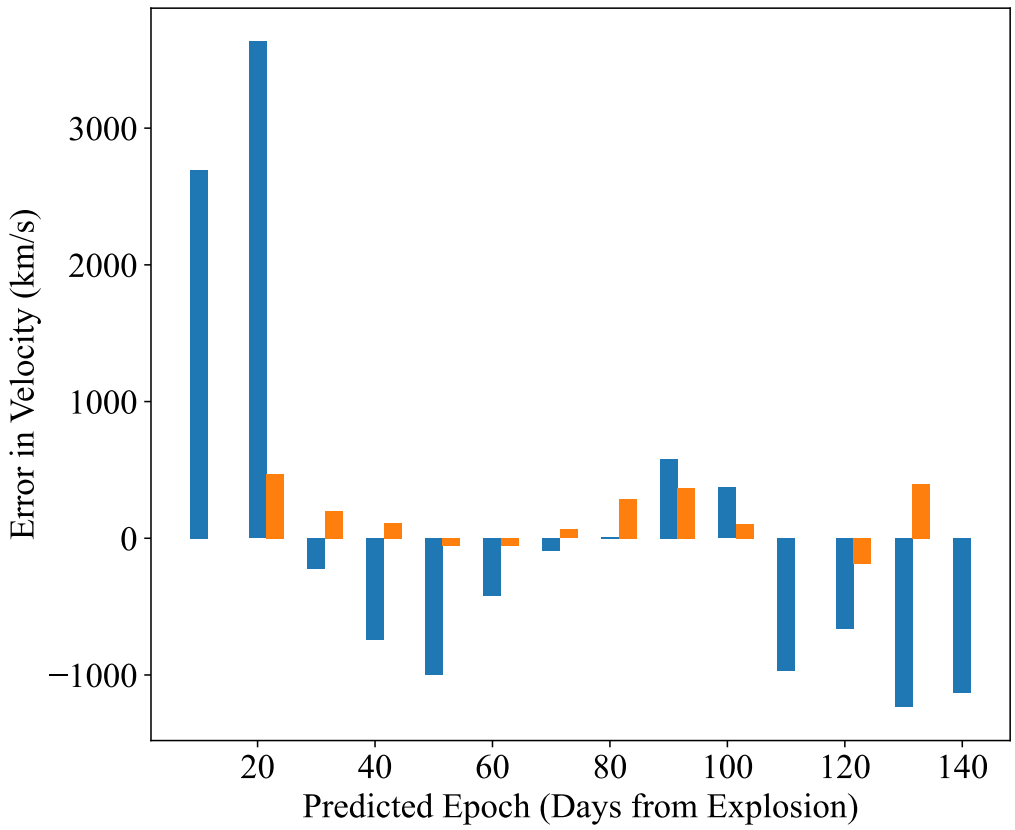

Figure 6.16. Mean velocity difference between observations and predictions for 15 test SNe: SN 1986L, SN 2002gw, SN 2002hx, SN 2003gd, SN 2004ej, SN 2004er, SN 2004fc, SN 2006ai, SN 2006ee, SN 2007oc, SN 2007X, SN 2009js, SN 2009N, SN 2012A, SN 2019unb, split across predicted epoch. The clear trend for Hα appears to be overestimating at early times and underestimating at late times, with no such clear trend for Fe II λ5169.

SCM, the equation and data from Hamuy et al. (2001) was used to calculated distances for SNe SN 1999em, SN 1998br, and SN 1991al, SNe both in Hamuy et al. (2001) and in our silver sample. The magnitude of the plateau at 50 days as well as the reddening and the formula to convert these to recession velocity and hence distance were taken from Hamuy et al. (2001), with a Hubble Constant H_0 of 78 km s^{-1} Mpc^{-1}.

The 50 day spectrum was predicted from each one of the spectra available per SN, and the mean and standard deviation of the distance was taken, and compared to the distance measured from the spectrum nearest to 50 days available for that SN (43 days for SN 1999br, 59 days for SN 1991al, and 51 days for SN 1999em) - this was to keep the velocity measurements consistent. This difference in days from explosion does add extra uncertainty in the distance calculations however the purpose is not for precise distance measurements (as also the Hamuy et al., 2001 relation and values are likely outdated) but to get an idea of the errors involved.

The results are as follows: For SN 1999em the 51 day spectrum directly predicts a distance of 5.94Mpc, whilst the predicted spectra give 7.10+/-1.16Mpc. For SN 1991al the 59 day spectrum predicts 32.67Mpc whilst the predicted spectra give 39.07+/-2.72Mpc. For SN 1999br the 43 day spectrum predicts 13.09Mpc whilst the predicted give 17.03+/-1.84Mpc. All predictions tend to overpredict the distance, with the values from observed spectra generally within a few σ. It should also be noted that the predicted velocities best match for predictor spectra between 30-50 days, so those spectra already close to 50 days, with earlier and later epochs both overpredicting. However with an expanded training set including high resolution spectra, this method could hold potential for use with the SCM method.

6.4.2 The way forward for machine learning techniques applied to SN spectra

In order to apply these machine learning methods to cosmology/spectroscopic analysis in a useful way, the prediction of the continuum or line velocities must decrease the uncertainties on existing methods such as e.g. simple interpolation, or less time consuming and computationally exhaustive than e.g. extensive modelling. This could be improved using an expanded training set as the training sample used was limited in size. The information from the training set could also be used to investigate correlations of parameters in SNe II and give some additional insight into the physics as well. Also worth noting is that the training sample was biased towards SNe in their plateau phase, therefore the methods were poorer at predicting particularly early but also later spectra. Additionally, the training set used was limited in phase to epochs where the Hα and Fe II λ5169 velocities were possible to be measured. Fe II is not visible at temperatures higher than 8000-9000 K (e.g. Hatano et al., 1998) which are approximately the temperatures for a Type II SNe past roughly 10-20 days from explosion - e.g. see Figure 6.6 for SN 2013ej, or Valenti et al. (2016).

The methods outlined in this chapter could provide the starting point for filling in the evolution

of SN II spectra, and could be expanded for other types as well without much difficulty, just requiring an alternative training set and perhaps identifying useful lines to measure velocities. Particularly, the Spectra Method could be used in the era of LSST where multi-epoch spectroscopy will not be available for the majority of targets, where the full velocity evolution, especially the photospheric velocity at plateau, could be extrapolated for a single spectrum allowing the SN to be calibrated for distance (assuming light curve coverage at the plateau phase). For cases lacking light curves, further machine learning could be used. There is work looking at classifying or identifying anomalous light curves (e.g. Vilalta, 2018; Muthukrishna et al., 2021). Further work could look at linking spectral and photometric information, such as Gutiérrez et al. (2017a,b) or Martinez et al. (2022) who looked at connecting SN light curves and optical spectra with the properties of the progenitor, based on a sample of 53 spectra from the Carnegie Supernova Project-I.

6.5 Summary

This chapter presented two methods, namely the Parameter and Spectra Methods, for predicting the evolution of SNe II and generating artificial spectra, or useful parameter values, for epochs not covered by the observation.

The Parameter Method was as follows: parameters of velocity and temperature were measured for a training set of 633 SNe II spectra sourced from a variety of published papers, and the evolution of these parameters for each SN was interpolated. When predicting an unseen spectrum for a SN, existing spectra for the object would have their properties measured and the new parameters would be inferred based on fitting functions to the values obtained from the observed spectra. These parameters then served as an input into a NN which would use them to construct an artificial spectrum for the requested epoch.

A second method was also proposed, the Spectra Method, which paired up all the spectra for each SN in the training sample and used one to predict the other. This training set included additional spectra from WISeREP and ePESSTO/ePESSTO+. This method had the advantage of requiring fewer spectra. This second method however does not make use of every spectrum available for a SN if there is more than one, unless one averages the results.

The advantage of the Spectra Method is that only one spectrum is needed. Nevertheless, the precision of the prediction becomes weaker for unusual SNe which are not well represented in the training sample, an issue shared with the Parameter Method. The method(s) would require more training data to reach its (their) full potential. Of the two methods presented, the Spectra Method provides good velocity predictions as seen for e.g. SN 2004et (i.e. a velocity consistent with that of the real/observed spectrum), which could potentially be used in the Standard Candle Method for distance calibration. The Spectra Method has higher errors in velocity predictions than the Parameter Method, though the majority of Fe II λ5169 velocities fall within the average error in line velocities

Table 6.4. Goodness of fit mean χ^2 values and standard deviation for 50 fits with different number of sampled spectra for SN 2013ej

No. sampled	χ^2 Hα	σ	χ^2 Feλ5169	σ	χ^2 Temperature	σ
2	2752	12640	4471	19732	10551	11831
3	1050	2339	1863	4971	5435	2517
4	666	586	982	852	4280	1657
8	418	147	612	197	3489	1089
12	315	47	486	81	2822	555

measured in the golden sample. Note, however, that the Spectra Method predictions were made with only one spectrum, rather than data from up to 12 as with the Parameter Method.

These methods have the potential to provide a complete spectroscopic coverage for targets with few or only one spectrum taken, which in turn could provide velocity evolution and other information which can be applied to population studies, creating spectral template libraries, or possibly in expanding the available information in order to implement techniques for measuring cosmic distance such as the SCM (Hamuy & Pinto, 2002).

The larger and more diverse the training sample will be, the higher will be the accuracy of the approach here presented. This will in turn allow to maximise the scientific gain of the LSST stream regardless the limited time dedicated to spectroscopic coverage of transients. It should be noted however that in most cases for the LSST there will be no spectra for a SN candidate and further work in linking the photometry to the spectra would be beneficial. Additional further work could explore applying machine learning directly to the prediction of certain line velocities rather than the entire spectrum, for more specialised applications, as the Parameter Method has shown that parameters of the spectrum can be well linked to the spectra themselves.

Table 6.5. References for the SNe in the Padova-Asiago sample.

SN Name	Reference
SN 1999em	Hamuy et al. (2001)
SN 2005cs	Pastorello et al. (2006)
SN 2004et	Sahu et al. (2006)
SN 2002gd	Spiro et al. (2014)
SN 2001dc	Pastorello et al. (2004)
SN 1997D	Pastorello et al. (2004)
SN 1987A	Pun et al. (1995)
SN 2003Z	Spiro et al. (2014)
SN 2009mw	Takáts et al. (2016)
SN 1998A	Pastorello et al. (2005)
SN 1999br	Pastorello et al. (2004)
SN 2006au	Taddia (2012)
SN 2009E	Pastorello et al. (2012)
SN 2004em	Takáts et al. (2016)
SN 2006V	Taddia (2012)
SN 1999eu	Pastorello et al. (2004)
SN 2004ek	Takáts et al. (2016)
SN 1994N	Pastorello et al. (2004)
SN 2005ci	Takáts et al. (2016)

Chapter 7

Conclusion

7.1 Thesis Overview

The main science chapters in this thesis can be split into two parts - the first is modelling and analysis, both for the unusual transitional object SN 2019hcc and for a sample of SLSNe I. The second is a more advanced analysis using machine learning to make predictions of core-collapse SN spectra. Line and spectral analysis is complicated by the many non-unique ways in which line shapes can be produced, with variations in elemental composition, temperature, and density all having an effect. Due to this, it can be difficult to distinguish the state and chemical makeup of a SN ejecta, hence creation and comparison with models is a big aspect of spectral analysis. However, using machine learning could decrease computational cost and labour through learning patterns from training data.

7.2 Key Results

7.2.1 Summary

The findings with relation to the 'w'-shape characteristic of SLSNe I were twofold. First, in line with the theory that these lines require non-thermal excitation which could be in the form of high-energy photons from a magnetar, it could be possible that these lines are produced in an ordinary luminosity core-collapse SN, as a magnetar may power an ordinary SN II light curve whilst non-thermally exciting Oxygen before maximum light. Additionally, modelling and analysis of SLSNe I found further support that the formation of this 'w'-shape feature requires contribution from other ions such as Iron to reproduce its full behaviour and evolution with temperature.

Applying machine learning to SN spectra is an excellent way to process the large amounts of data soon to be available with the upcoming LSST and other future large sky surveys. Additionally,

spectroscopy is a limited resource, and using machine learning to create artificial spectra at epochs where we do not have them could be beneficial towards scientific endeavours such as population studies or spectral template creation. Additionally, artificial spectra could be used to measure line velocities, which could be beneficial for distance calibration methods such as the Standard Candle Method which links the photospheric velocity at 50 days to the luminosity of the plateau in SNe II.

7.2.2 SN 2019hcc

The first spectrum of SN 2019hcc appeared relatively featureless aside from a 'w' feature around 4000 Å, characteristic of O II lines typical of SLSNe I, hence SN 2019hcc was initially classified as a SLSN I. However, the spectra show a clear Hα profile from +19 days, as well as spectral similarity to various literature SNe II. The bolometric light curve evolution, as well as the temperature and colour evolution, were also typical of a Type II. These properties led to a new classification as a SNe II. Such a 'w'-shaped feature (usually and historically) attributed to O II has never been identified and analysed in SNe II.

In SLSNe I these lines have been suggested as excited by X-rays produced by a magnetar, or alternatively CSM-ejecta interaction. As there is a lack of any sign of interaction both in the light curve and spectra, the CSM-ejecta interaction at early time is disfavoured. It was found through modelling that a magnetar could be formed as a remnant in a Type II. This would require that the magnetar does not provide enough additional energy to the supernova event to power up the light curve to superluminous luminosities. The magnetar remnant could therefore non-thermally excite the Oxygen whilst not having a significant contribution to the light curve evolution.

The object here presented could then bridge the gap between SLSNe I and normal luminosity core collapse supernovae, as well as reveal more about magnetar formation requirements and mechanisms. Our analysis also shows that a magnetar is a viable remnant of a Type II supernova explosion, the effects of which could be observed in the form of an early 'w'-shaped profile around 4000–4400 Å. This would suggest that such lines are not exclusive to SLSNe I and cannot be used as a sole feature to classify those extreme transients.

7.2.3 The 'w'-shape characteristic of SLSNe I

To further investigate the 'w'-shape, a sample of SLSNe I were examined, and their 'w'−shapes round 4200 Å and 4400 Å were quantified by measurements of the pEW and FWHM of the blue and red profile as well as their ratio, and the correlation of these measurements with temperature and phase were considered. The goal was to have a quantitative comparison of the line profile with respect to the temperature of the SN at the time of the spectrum as well as measurements of the line profiles themselves.

We found no statistically significant correlation between pEW and FWHM ratios for Slow SLSNe I as opposed to a strong postive correlation for Fast (0.79). This could be due to the Slow subclass being more heavily influenced by interaction (Inserra et al., 2017, 2018), which could influence emission and absorption lines. It was also found that these evolutions with temperature are not entirely consistent with measurements of a pure Oxygen model spectrum, produced with TARDIS, suggesting that Oxygen alone is not responsible for the correlations seen. When considering individual profile measurements, the most significant deviation between the trends of pEW with temperature for models compared to observed spectra began below approximately 15000 K, which is also the approximate temperature when Iron contribution begins to grow stronger in the blue profile region, and Silicon in the red - though this deviation from models is not necessarily followed by all SLSNe I. With the addition of further TARDIS modelling, the conclusion drawn is that the 'w'-shape, attributed to O II lines are likely not caused by Oxygen alone, but requires a contribution of metals such as Titanium, Silicon or Iron.

An improved understanding of this 'w'-shape profile has the potential to, with further work, identify a Fast or Slow SLSN I from a very early spectrum (or perhaps correlate the overall yields with those producing a circumstellar material) without needing to determine the classification observationally from the light curve. Additionally, further study of this 'w'-shape could provide further insight into the process causing the additional luminosity and it might provide a means to distinguish between different progenitor scenarios.

7.2.4 Machine Learning to Predict SN Spectra

This chapter presented two methods, namely the Parameter and Spectra Methods, for predicting the evolution of SNe II and generating artificial spectra, or useful parameter values, for epochs not covered by the observation. The Parameter Method was as follows: parameters of velocity and temperature were measured for a training set and the evolution of these parameters for each SN was interpolated. When predicting an unseen spectrum for a SN, existing spectra for the object would have their properties measured and the new parameters would be inferred based on fitting functions to the values obtained from the observed spectra. These parameters then served as an input into a NN which would use them to construct an artificial spectrum for the requested epoch. A second method was also proposed, the Spectra Method, which paired up all the spectra for each SN in the training sample and used one to predict the other. The advantage of the Spectra Method is that only one spectrum is needed. Nevertheless, the precision of the prediction becomes weaker for unusual SNe which are not well represented in the training sample, an issue shared with the Parameter Method.

The method(s) would require more training data to reach its (their) full potential. Of the two methods presented, the Spectra Method provides good velocity predictions as seen for e.g. SN 2004et

(i.e. a velocity consistent with that of the real/observed spectrum), which could potentially be used in the Standard Candle Method for distance calibration. The Spectra Method has higher errors in velocity predictions than the Parameter Method, though the majority of Fe II λ5169 velocities fall within the average error in line velocities measured in the golden sample. These methods have the potential to provide a complete spectroscopic coverage for targets with few or only one spectrum taken, which in turn could provide velocity evolution and other information which can be applied to population studies, creating spectral template libraries, or possibly in expanding the available information in order to implement techniques for measuring cosmic distance such as the SCM (Hamuy & Pinto, 2002).

The larger and more diverse the training sample will be, the higher will be the accuracy of the approach here presented. This will in turn allow to maximise the scientific gain of the LSST stream regardless the limited time dedicated to spectroscopic coverage of transients.

7.3 Future work

In general, increasing the size of both the SLSNe I sample for analysis of the O II lines and the SNe II sample for training the machine learning algorithm, would be very beneficial. Additionally, a large high-quality sample of UV spectra from both SLSNe I Fast and Slow could help confirm the contribution of other ions to the 'w'-shape, as elements such as Iron produce strong absorption at other wavelengths.

The machine learning algorithm described is a starting point for predicting SN spectra, however, there is much adapting that could be made depending on the specific application. For example, predicting photospheric velocities directly rather than measuring from the spectra could cut unnecessary extra steps for making distance predictions for the Standard Candle Method, or linking spectra to photometric observations, as in many cases no spectra will be available, only photometry.

7.4 Concluding remarks

In conclusion, the field of SNe is a very exciting one and the upcoming LSST at the Vera C. Rubin Observatory could have a massive impact from the sheer number of transients and SNe discovered across its 10-year span. However, having the tools and the understanding to make use of this data is crucial, and the work in this thesis explores some of how we can prepare for this. A better understanding of the mechanisms behind characteristic lines, and being able to fill in missing data with artificially generated spectra, could help interpret and make use of the wealth of information we shall uncover.

Appendix A

Appendix

A.1 SN2019hcc: Data

Table A.1. The measured apparent magnitudes of the host galaxy for SN 2019hcc from LT and LCO images.

Filter	Apparent Magnitude
B	20.70 (0.18)
V	20.05 (0.23)
g	20.68 (0.24)
r	20.67 (0.28)
i	20.37 (0.29)
z	20.56 (0.18)

Table A.2. NIR GROND magnitudes as seen in Figure 3.5

MJD	Phase from maximum (days)	J	H	K
58644	8	18.08 (0.17)	17.87 (0.25)	17.64 (0.50)
58648	12	18.08 (0.17)	17.90 (0.25)	17.80 (0.03)
58661	25	18.23 (0.18)	17.64 (0.23)	17.12 (0.28)
58667	31	18.26 (0.18)	17.91 (0.23)	17.56 (0.32)
58674	38	18.33 (0.17)	18.00 (0.23)	-

Table A.3. Photometry data shown in Figure 3.5.

MJD	Phase from maximum (days)	B	V	g	r	i	z	Telescope
58644	8	-	-	18.84 (0.11)	18.73 (0.09)	18.78 (0.11)	18.69 (0.12)	GROND
58647	11	-	-	19.19 (0.31)	19.01 (0.22)	19.51 (0.26)	19.22 (0.26)	LT
58647	11	-	-	-	-	19.37 (0.29)	-	LCO
58648	12	-	-	19.15 (0.03)	18.87 (0.10)	18.90 (0.12)	18.75 (0.12)	GROND
58651	15	-	-	-	-	19.67 (0.44)	-	LCO
58653	17	-	-	-	-	19.48 (0.40)	19.23 (0.38)	LCO
58653	17	-	-	-	-	19.06 (0.42)	-	LT
58656	20	-	-	19.50 (0.40)	19.23 (0.38)	19.46 (0.32)	19.59 (0.45)	LT
58657	21	20.30 (0.30)	19.46 (0.36)	19.65 (0.36)	19.44 (0.35)	19.78 (0.36)	-	LCO
58659	23	19.48 (0.29)	19.58 (0.37)	19.75 (0.37)	19.43 (0.29)	19.80 (0.36)	-	LCO
58660	24	20.60 (0.31)	19.49 (0.34)	19.96 (0.39)	19.47 (0.27)	19.77 (0.33)	-	LCO
58661	25	-	-	19.72 (0.03)	19.16 (0.17)	19.22 (0.17)	19.14 (0.17)	GROND
58662	26	20.52 (0.25)	19.62 (0.36)	19.86 (0.37)	19.47 (0.29)	-	-	LCO
58662	26	-	-	20.04 (0.42)	19.46 (0.25)	19.84 (0.26)	19.63 (0.29)	LT
58664	28	20.86 (0.34)	19.69 (0.38)	20.17 (0.43)	19.72 (0.31)	-	-	LCO
58665	29	20.70 (0.29)	19.74 (0.39)	20.03 (0.40)	19.51 (0.29)	19.88 (0.36)	-	LCO
58667	31	-	-	19.83 (0.03)	19.34 (0.03)	19.28 (0.14)	19.23 (0.14)	GROND
58670	34	-	-	20.46 (0.51)	19.63 (0.27)	19.79 (0.26)	19.67 (0.32)	LT
58673	37	21.15 (0.38)	19.94 (0.42)	20.37 (0.47)	19.68 (0.31)	-	-	LCO
58674	38	-	-	20.08 (0.03)	19.44 (0.03)	19.42 (0.14)	19.35 (0.14)	GROND
58675	39	-	-	-	19.67 (0.31)	19.86 (0.30)	19.89 (0.37)	LT
58680	44	21.48 (0.73)	20.43 (0.66)	20.95 (0.71)	19.90 (0.45)	19.97 (0.46)	-	LCO
58684	48	-	20.56 (0.62)	21.38 (0.81)	20.05 (0.41)	20.46 (0.50)	-	LCO
58685	49	-	-	-	20.10 (0.46)	20.62 (0.45)	20.42 (0.51)	LT
58690	54	22.31 (0.59)	20.93 (0.66)	22.13 (1.06)	-	-	-	LCO
58694	58	-	-	21.94 (1.00)	20.95 (0.49)	22.04 (0.71)	21.29 (0.65)	LT
58697	61	22.51 (0.60)	-	22.91 (1.50)	21.37 (0.63)	21.55 (0.73)	-	LCO
58704	68	-	-	-	21.57 (0.68)	-	22.41 (1.09)	LT
58713	77	-	-	-	21.28 (0.69)	21.40 (0.71)	-	LT
58716	80	-	-	-	20.91 (0.55)	-	-	LCO
58725	89	23.86 (1.15)	22.07 (1.09)	-	21.52 (0.67)	22.59 (1.16)	-	LCO
58732	96	-	-	-	-	22.71 (1.28)	-	LCO
58767	131	-	-	-	-	-	21.76 (0.80)	LT
58772	136	-	-	23.03 (1.74)	-	-	22.61 (1.17)	LT

Table A.4. *Swift* AB magnitudes as seen in Figure 3.5.

MJD	Phase from maximum (days)	UVM2	UVW1	UVW2	u
58645	9	20.72 (0.14)	20.21 (0.24)	20.71 (0.20)	19.68 (0.21)
58651	15	20.78 (0.31)	>20.39	20.72 (0.31)	>19.72
58658	22	20.80 (0.15)	20.50 (0.20)	21.17 (0.21)	20.54 (0.32)
58660	24	21.30 (0.23)	20.67 (0.24)	21.72 (0.32)	>20.58
58663	27	20.76 (0.16)	20.79 (0.24)	20.95 (0.19)	>20.70
58666	30	21.32 (0.21)	20.67 (0.22)	21.14 (0.21)	>20.71

Table A.5. ATLAS AB magnitudes as reported in Figure 3.5.

MJD	Phase from maximum (days)	cyan	orange
58609	-27	>20.61	-
58609	-27	>20.69	-
58609	-27	>20.43	-
58609	-27	>19.91	-
58611	-25	-	>20.15
58611	-25	-	>20.16
58611	-25	-	>19.81
58617	-19	-	>20.06
58617	-19	-	>20.12
58617	-19	-	>20.20
58617	-19	-	>20.44
58619	-17	-	>19.71
58619	-17	-	>19.65
58619	-17	-	>19.69
58619	-17	-	>19.74
58620	-16	-	>19.01
58620	-16	-	>19.00
58620	-16	-	>19.13
58620	-16	-	>19.22
58620	-16	-	>19.40
58621	-15	-	>19.41
58621	-15	-	>19.51
58621	-15	-	>19.56
58621	-15	-	>19.60
58623	-13	-	>17.86
58623	-13	-	>19.14
58623	-13	-	>18.98
58623	-13	-	>19.20
58631	-5	-	19.25 (0.22)
58631	-5	-	18.97 (0.24)
58631	-5	-	18.55 (0.21)
58633	-3	18.73 (0.11)	-
58633	-3	18.83 (0.11)	-
58633	-3	18.73 (0.11)	-
58633	-3	18.70 (0.16)	-
58637	1	18.57 (0.09)	-
58637	1	18.84 (0.10)	-
58637	1	18.55 (0.08)	-
58637	1	18.54 (0.09)	-

MJD	Phase from maximum (days)	cyan	orange
58643	7	-	18.90 (0.15)
58643	7	-	18.87 (0.15)
58643	7	-	19.11 (0.20)
58643	7	-	18.96 (0.17)
58645	9	-	18.80 (0.13)
58645	9	-	18.69 (0.11)
58645	9	-	19.14 (0.18)
58645	9	-	18.79 (0.17)
58647	11	-	19.16 (0.21)
58647	11	-	19.16 (0.21)
58649	13	-	18.90 (0.31)
58649	13	-	18.81 (0.26)
58659	23	-	19.01 (0.21)
58659	23	-	19.54 (0.33)
58659	23	-	18.96 (0.19)
58659	23	-	19.33 (0.30)
58659	23	-	19.05 (0.23)
58659	23	-	19.53 (0.35)
58665	29	20.07 (0.29)	-
58665	29	19.91 (0.26)	-
58665	29	19.57 (0.21)	-
58667	31	-	19.62 (0.27)
58667	31	-	19.70 (0.27)
58667	31	-	19.17 (0.16)
58667	31	-	19.31 (0.21)
58669	33	19.89 (0.31)	-
58669	33	19.55 (0.24)	-
58669	33	19.17 (0.17)	-
58670	34	19.99 (0.31)	-
58670	34	20.16 (0.34)	-
58671	35	19.92 (0.30)	-
58671	35	20.01 (0.30)	-
58671	35	19.51 (0.24)	-
58674	38	-	19.49 (0.23)
58674	38	-	19.62 (0.23)
58674	38	-	19.69 (0.29)
58685	49	-	18.97 (0.30)
58723	87	-	20.23 (0.33)

A.2 Investigating OII lines: Data

Table A.6. The pEW, FWHM, and Temperature measurements for the full sample. Phase is in days from maximum.

Name	Subclass	Phase	MJD	Blue pEW	±	Red pEW	±	Blue FWHM	±	Red FWHM	±	Temperature (K)	±
SN 2005ap	Fast	-2.8	53436	32.73	0.70	59.50	2.05	140.4	1.59	246.90	5.36	13484	138
SN 2006oz	Slow	-5	54061	93.52	14.98	78.66	14.54	290.84	38.13	190.56	20.62	11342	1396
SN 2009jh	Fast	0.6	55068	34.38	8.23	23.55	5.72	133.92	19.60	104.48	18.41	14230	166
SN 2013dg	Fast	3.6	56453	25.09	0.92	32.12	2.67	125.34	3.60	167.34	8.73	15259	68
SN 2016aj	Fast	-9	57403	46.52	8.90	43.17	5.69	156.8	15.71	140.88	10.47	18027	502
SN 2019enz	Fast	-16	58616	38.52	5.44	47.32	3.94	174.3	9.70	173.10	8.15	15481	277
SN 2019enz	Fast	-5	58627	44.98	1.84	57.85	4.30	171.92	3.18	193.66	6.61	22938	412
SN 2019nhs	Fast	-7	58722	46.90	5.49	45.77	3.88	166.72	8.81	140.42	8.32	15512	156
SN 2020xga	Slow	-14	59159	51.60	3.77	50.99	6.27	159.22	5.39	151.32	11.05	15530	299
SN 2020xga	Slow	-3	59169	56.65	5.77	69.18	9.38	151.8	7.15	207.70	11.28	16397	543
SN 2020xga	Slow	-2	59170	76.02	10.29	65.79	11.62	188.88	12.71	191.10	16.28	12590	273
SN 2021bnw	Slow	-6.7	59249	50.69	2.13	41.88	2.68	188.56	4.40	142.72	4.99	15953	205
SN 2022npq	Slow	-9	59811	33.02	0.52	76.81	4.28	135.24	1.09	318.12	4.66	10994	137
PTF09cnd	Fast	-20.9	55059	71.76	2.77	59.18	0.97	179.38	4.45	141.78	1.70	13328	222
PTF09cnd	Fast	-13.8	55068	57.27	7.44	58.42	7.42	170.66	9.43	150.22	12.41	14967	234
PTF09cnd	Fast	2.9	55089	28.79	4.34	29.83	3.76	176.96	11.02	136.48	9.62	16426	163
SN 2018bgv	Slow	4	58255	36.79	2.09	43.15	2.21	172.16	4.60	203.00	7.32	12082	1851
SN 2010gx	Fast	-6.7	55273	59.21	2.53	65.03	5.18	201.52	3.89	218.92	12.21	18246	2040
SN 2010gx	Fast	-4	55276	53.56	2.08	73.43	3.53	179.36	3.89	220.12	6.53	17484	993
SN 2011kg	Fast	-11.9	55922	43.98	1.80	57.54	1.73	141.32	3.70	171.38	3.60	11737	123
SN 2011kg	Fast	-8.5	55926	43.33	1.67	46.83	2.38	145.02	3.51	160.34	5.05	10708	90
SN 2015bn	Slow	-28	57070	31.01	3.18	21.54	2.29	155.2	5.77	162.64	7.36	11817	340
SN 2015bn	Slow	-27	57071	35.22	1.13	22.79	1.54	168.02	2.18	162.92	4.81	11799	319
SN 2015bn	Slow	-20	57078	40.12	0.79	26.17	0.97	171.6	1.64	175.62	2.84	11686	189
SN 2015bn	Slow	-9	57092	42.48	0.78	32.98	1.19	167.06	1.56	184.68	3.56	11960	343
SN 2015bn	Slow	-8	57093	40.96	0.31	30.72	1.08	160.72	0.74	173.90	2.86	12214	381
SN 2015bn	Slow	-2	57099	41.80	0.24	33.98	1.94	158.28	0.30	188.48	4.76	12572	277
SN 2015bn	Slow	7	57108	37.95	0.68	25.28	2.11	160.14	1.39	179.32	6.98	12457	132
SN 2016eay	Fast	-18.3	57528	36.22	7.81	43.10	7.99	139.66	16.10	138.36	17.15	20689	1870
SN 2016eay	Fast	-15.5	57532	48.64	6.41	54.01	7.71	155.52	8.64	156.44	13.00	18145	1575
SN 2016eay	Fast	-11	57535	68.05	2.81	75.56	2.23	179.86	4.23	200.62	2.92	16553	1289
SN 2016eay	Fast	-6	57539	60.10	2.36	67.43	1.26	162.58	3.54	179.02	1.60	14923	1055
SN 2016eay	Fast	0	57545	33.16	2.97	35.32	3.76	130.28	5.09	135.44	8.72	14435	359
SN 2016eay	Fast	3.5	57552	42.10	3.70	39.23	6.07	177.46	5.99	158.22	15.44	15088	1537
SN 2017gci	Slow	-7	57982	11.03	1.04	13.82	1.44	110.46	4.87	111.26	8.84	10676	72
SN 2017gci	Slow	-5	57984	8.99	1.30	9.58	1.85	125	14.35	133.42	16.85	10380	56
SN 2018bym	Slow	-9	58269	24.12	0.67	27.07	1.04	158.62	1.80	135.80	2.22	16632	607
SN 2018bym	Slow	4	58286	22.56	1.81	16.21	1.56	153.1	5.07	126.44	5.80	14122	732
SN 2018hti	Slow	-34	58428	36.25	1.32	41.93	0.46	146.66	3.67	141.54	1.13	29766	7326
SN 2018hti	Slow	-33	58429	39.33	3.63	49.42	2.67	142.82	6.93	158.80	5.08	29562	6374
SN 2018hti	Slow	-32	58430	43.69	2.74	48.69	0.93	156.4	5.41	160.32	1.79	27809	4298
SN 2018hti	Slow	-26	58437	40.13	1.27	43.16	0.52	145.44	2.63	146.74	1.09	22621	3059
SN 2018hti	Slow	-23	58440	50.92	6.09	55.99	3.31	164.1	9.34	165.36	5.61	24531	4545
SN 2018hti	Slow	-17	58446	43.94	9.72	41.56	7.86	166.16	9.94	150.04	16.48	20180	1167
SN 2018hti	Slow	-4	58460	27.57	3.54	24.91	2.34	186.38	7.24	161.98	8.80	26352	2863
DES14X3taz	Slow	-24	56683	48.54	2.49	41.24	6.24	163.96	4.86	165.94	21.92	11455	1269
DES14X3taz	Slow	-13	56694	47.34	2.75	44.04	5.02	181.54	3.15	178.20	9.72	12722	1373
DES15S2nr	Fast	-26	57283	24.66	2.77	32.68	1.84	80.718	8.57	87.70	3.08	10540	113
DES15S2nr	Fast	-3	57306	31.13	3.53	16.94	2.35	225.92	6.01	138.60	7.97	11835	74
iPTF13ajg	Fast	-5	56390	65.31	23.76	70.49	27.17	192.32	40.66	195.88	46.66	10474	1385
iPTF13ajg	Fast	-4	56391	54.29	5.77	58.07	4.43	178.3	8.95	184.48	5.91	10419	1371
iPTF13ajg	Fast	4	56399	31.32	1.48	32.70	2.31	173.02	4.73	132.40	29.64	10186	1307
LSQ14bdq	Slow	-21	56781	34.93	3.53	32.15	3.93	161.4	6.27	142.50	9.58	11945	1202
LSQ14bdq	Slow	-19	56783	37.59	3.39	33.66	1.06	152.02	7.22	159.66	2.25	11945	1202
LSQ14bdq	Slow	-18	56784	40.55	2.19	39.29	1.66	157.94	4.05	193.68	3.64	11945	1202
LSQ14mo	Fast	-8.8	56688	36.11	4.46	36.18	0.64	169.44	10.74	121.38	1.41	13495	843
LSQ14mo	Fast	-8.8	56688	34.22	2.67	35.98	1.64	138.54	6.19	130.40	3.83	13495	843
LSQ14mo	Fast	-2.7	56694	34.82	2.38	26.06	4.49	168.9	4.45	147.42	18.91	12335	286
LSQ14mo	Fast	-2.7	56694	28.52	4.68	24.26	5.68	151.54	10.68	134.58	19.82	12335	286
PTF09atu	Fast	-18.9	55034	52.38	4.15	52.69	2.72	156.32	6.11	170.28	4.43	12977	321
PTF09atu	Fast	3.8	55068	49.72	3.82	59.58	4.48	163.12	5.44	177.64	6.54	10363	539
PTF10aagc	Slow	3.7	55504	20.09	1.48	23.96	0.90	149.98	4.52	150.00	1.79	15127	138
PTF10aagc	Slow	4.6	55505	19.07	0.45	24.84	1.75	133.76	1.49	145.96	5.23	7872	170
PTF10aagc	Slow	6.2	55507	12.37	0.65	15.42	1.40	118.96	3.93	149.56	6.20	18423	249
PTF12mxx	Fast	-8.4	56279	25.50	6.36	30.92	4.76	133.88	21.09	164.68	8.98	14107	124
PS1-11ap	Slow	-11	55598	32.40	2.56	21.19	2.46	133.02	6.05	145.88	6.75	6929	826
PS1-11ap	Slow	-20	55585	42.29	0.90	38.07	2.58	153.6	1.21	172.40	5.78	20152	2027
PS1-11ap	Slow	-1	55614	39.67	1.60	41.84	7.36	143.3	2.06	231.86	17.76	7157	828
SN 2016ard	Fast	-3.5	57449	42.67	4.87	52.81	8.55	138.42	8.64	216.44	10.16	24638	4693
PTF12dam	Slow	-23.8	56067	45.01	5.65	43.48	2.58	188.88	8.12	155.50	4.60	18089	1727
PTF12dam	Slow	-22.9	56068	45.06	0.89	48.44	0.43	194.98	2.56	172.02	1.48	17931	1610
PTF12dam	Slow	-22	56069	46.59	2.51	46.77	2.69	181.6	4.08	169.98	5.15	14980	165
PTF12dam	Slow	-21.1	56070	52.08	1.12	53.36	1.76	177.46	2.20	192.28	3.68	17392	1273
PTF12dam	Slow	-19.3	56071	41.61	2.16	48.91	3.73	168.78	3.31	174.00	7.68	14548	323
PTF12dam	Slow	-1.2	56092	20.21	2.60	18.40	3.77	126.18	5.00	202.84	17.47	16201	183
PTF12dam	Slow	2.4	56096	19.75	2.80	17.49	3.33	138.94	6.08	206.60	15.03	17144	803

Table A.7. The full set of p-values for the correlation matrix of pEW and FWHM measurements for all spectra, rounded to 3 decimal places.

	Phase	T	pEW	FWHM	Flux	pEW1	pEW2	FWHM1	FWHM2
Phase	0.000	0.003	0.995	0.627	0.916	0.082	0.164	0.955	0.262
T	0.003	0.000	0.038	0.449	0.107	0.337	0.093	0.157	0.990
pEW	0.995	0.038	0.000	0.000	0.000	0.739	0.000	0.005	0.008
FWHM	0.627	0.449	0.000	0.000	0.000	0.108	0.170	0.000	0.000
Flux	0.916	0.107	0.000	0.000	0.000	0.868	0.000	0.005	0.002
pEW1	0.082	0.337	0.739	0.108	0.868	0.000	0.000	0.000	0.007
pEW2	0.164	0.093	0.000	0.170	0.000	0.000	0.000	0.000	0.000
FWHM1	0.955	0.157	0.005	0.000	0.005	0.000	0.000	0.000	0.106
FWHM2	0.262	0.990	0.008	0.000	0.002	0.007	0.000	0.106	0.000

Table A.8. The full set of p-values for the correlation matrix of pEW and FWHM measurements for FAST spectra.

	Phase	T	pEW	FWHM	Flux	pEW1	pEW2	FWHM1	FWHM2
Phase	0.000	0.473	0.346	0.608	0.300	0.136	0.185	0.156	0.267
T	0.473	0.000	0.129	0.135	0.203	0.263	0.062	0.548	0.015
pEW	0.346	0.129	0.000	0.000	0.000	0.821	0.001	0.005	0.002
FWHM	0.608	0.135	0.000	0.000	0.000	0.680	0.002	0.002	0.000
Flux	0.300	0.203	0.000	0.000	0.000	0.616	0.000	0.009	0.001
pEW1	0.136	0.263	0.821	0.680	0.616	0.000	0.000	0.002	0.011
pEW2	0.185	0.062	0.001	0.002	0.000	0.000	0.000	0.137	0.000
FWHM1	0.156	0.548	0.005	0.002	0.009	0.002	0.137	0.000	0.135
FWHM2	0.267	0.015	0.002	0.000	0.001	0.011	0.000	0.135	0.000

Table A.9. The full set of p-values for the correlation matrix of pEW and FWHM measurements for SLOW spectra.

	Phase	T	pEW	FWHM	Flux	pEW1	pEW2	FWHM1	FWHM2
Phase	0.000	0.012	0.690	0.016	0.563	0.007	0.008	0.053	0.267
T	0.012	0.000	0.053	0.027	0.149	0.438	0.175	0.128	0.160
pEW	0.690	0.053	0.000	0.104	0.000	0.141	0.046	0.078	0.331
FWHM	0.016	0.027	0.104	0.000	0.044	0.003	0.257	0.000	0.000
Flux	0.563	0.149	0.000	0.044	0.000	0.109	0.059	0.059	0.184
pEW1	0.007	0.438	0.141	0.003	0.109	0.000	0.000	0.000	0.032
pEW2	0.008	0.175	0.046	0.257	0.059	0.000	0.000	0.000	0.000
FWHM1	0.053	0.128	0.078	0.000	0.059	0.000	0.000	0.000	0.341
FWHM2	0.267	0.160	0.331	0.000	0.184	0.032	0.000	0.341	0.000

A.3 Machine Learning: Data

A.4 Machine Learning: Figures

Table A.10. The SNe II used in the golden training sample. Subtypes, as labelled on WISeREP, are included when available.

SN Name	Gutierrez	Padova-Asiago	Berkeley	Total Spectra	Subtype	SN Name	Gutierrez	Padova-Asiago	Berkeley	Total Spectra	Subtype
SN 1999em	2	25	0	27	IIP	SN 2003bl	3	0	0	3	-
SN 2004et	0	19	0	19	IIP	SN 2003ci	3	0	0	3	-
SN 2002gd	10	8	0	18	IIP	SN 2003fb	3	0	0	3	-
SN 1987A	0	17	0	17	II-pec	SN 2003hd	3	0	0	3	-
SN 2005cs	0	15	0	15	IIP	SN 2003hg	3	0	0	3	-
SN 1999br	6	8	0	14	II-pec	SN 2003hl	3	0	0	3	IIP
SN 2008aw	8	0	4	12	-	SN 2003ho	3	0	0	3	-
SN 1997D	0	10	0	10	II-pec	SN 2003ib	3	0	0	3	IIP
SN 2008ag	10	0	0	10	-	SN 2004ek	0	3	0	3	-
SN 2008if	9	0	1	10	-	SN 2004fb	3	0	0	3	-
SN 2003bn	9	0	0	9	-	SN 2005ci	0	3	0	3	-
SN 2003Z	0	9	0	9	IIP	SN 2006be	3	0	0	3	-
SN 2004fx	9	0	0	9	-	SN 2006V	0	3	0	3	-
SN 2005J	9	0	0	9	-	SN 2007ab	3	0	0	3	-
SN 2006au	0	9	0	9	-	SN 2007av	3	0	0	3	-
SN 2007aa	9	0	0	9	IIP	SN 2007P	3	0	0	3	-
SN 2007il	5	0	4	9	-	SN 2008bh	3	0	0	3	-
SN 2009ao	5	0	4	9	-	SN 2008bm	3	0	0	3	IIn
SN 2002gw	8	0	0	8	-	SN 2008br	3	0	0	3	-
SN 2004fc	8	0	0	8	-	SN 2008gr	3	0	0	3	-
SN 1986L	7	0	0	7	-	SN 2008K	3	0	0	3	-
SN 2002hx	7	0	0	7	IIP	SN 2009au	3	0	0	3	IIn
SN 2004ej	7	0	0	7	-	SN 2009mw	0	3	0	3	-
SN 2004er	7	0	0	7	-	SN 2011cj	0	0	3	3	IIP
SN 2006ai	7	0	0	7	-	SN 2011ef	0	0	3	3	-
SN 2007oc	7	0	0	7	-	SN 2014G	0	0	3	3	IIL
SN 2007X	7	0	0	7	-	SN 2016adg	0	0	3	3	IIP
SN 2009N	6	0	1	7	IIP	SN 2017faf	0	0	3	3	-
SN 1998A	0	6	0	6	II-pec	SN 1993S	2	0	0	2	-
SN 2003B	6	0	0	6	-	SN 2001dc	0	2	0	2	IIP
SN 2005an	6	0	0	6	-	SN 2003ej	2	0	0	2	IIP
SN 2005Z	6	0	0	6	-	SN 2003gd	2	0	0	2	-
SN 2006ee	6	0	0	6	-	SN 2003hk	2	0	0	2	IIP
SN 2007ck	0	0	6	6	IIP	SN 2006iw	2	0	0	2	-
SN 2007od	3	0	3	6	IIP	SN 2006ms	2	0	0	2	-
SN 2008m	6	0	0	6	-	SN 2007U	2	0	0	2	-
SN 2013ab	0	0	6	6	IIP	SN 2008bk	2	0	0	2	IIP
SN 2014cy	0	0	6	6	IIP	SN 2008bx	0	0	2	2	-
SN 2015V	0	0	6	6	-	SN 2009ay	0	0	2	2	-
SN 2016X	0	0	6	6	IIP	SN 2009js	0	0	2	2	IIP
SN 2003ef	5	0	0	5	IIP	SN 2009kr	0	0	2	2	-
SN 2003hn	5	0	0	5	-	SN 2012A	0	0	2	2	IIP
SN 2005dz	5	0	0	5	-	SN 2013am	0	0	2	2	IIP
SN 2006Y	5	0	0	5	-	SN 2015O	0	0	2	2	-
SN 2007W	5	0	0	5	-	SN 2016fqr	0	0	2	2	IIn?
SN 2008gi	4	0	1	5	-	SN 1990E	1	0	0	1	IIP
SN 2008in	4	0	1	5	IIP	SN 1992af	1	0	0	1	-
SN 2008W	5	0	0	5	-	SN 1992ba	1	0	0	1	-
SN 2009aj	5	0	0	5	-	SN 1994N	0	1	0	1	-
SN 2009E	0	5	0	5	IIP	SN 2002ig	1	0	0	1	-
SN 2013ej	0	0	5	5	IIP	SN 2004em	0	1	0	1	-
SN 210	5	0	0	5	-	SN 2006it	1	0	0	1	-
SN 1991al	4	0	0	4	-	SN 2006qr	1	0	0	1	-
SN 2002hj	4	0	0	4	IIP	SN 2007hm	1	0	0	1	-
SN 2003cn	4	0	0	4	IIP	SN 2007ld	1	0	0	1	-
SN 2003cx	4	0	0	4	-	SN 2007sq	1	0	0	1	-
SN 2003eg	4	0	0	4	IIP	SN 2008ex	0	0	1	1	-
SN 2003ip	4	0	0	4	IIP	SN 2008ho	1	0	0	1	-
SN 2003iq	4	0	0	4	IIP	SN 2008il	1	0	0	1	-
SN 2003T	4	0	0	4	-	SN 2009at	0	0	1	1	-
SN 2005dn	4	0	0	4	-	SN 2009bz	1	0	0	1	-
SN 2009bu	4	0	0	4	-	SN 2010id	0	0	1	1	IIP
SN 2011fd	0	0	4	4	IIP	SN 2012ec	0	0	1	1	IIP
SN 2012aw	0	0	4	4	IIP	SN 2013gd	0	0	1	1	IIP
SN 1990K	3	0	0	3	-	SN 2014ce	0	0	1	1	-
SN 1993K	3	0	0	3	-	SN 2015be	0	0	1	1	-
SN 1999cr	3	0	0	3	-	SN 2015C	0	0	1	1	-
SN 1999eu	0	3	0	3	II-pec	SN 2015W	0	0	1	1	-
SN 2002fa	3	0	0	3	-	SN 2016cok	0	0	1	1	IIP

Table A.11. The silver training sample, with subtypes as labelled on WISeREP where available.

SN Name	Gutierrez	Padova-Asiago	Berkeley	WISeREP	Total	Subtype	SN Name	Gutierrez	Padova-Asiago	Berkeley	WISeREP	Total	Subtype
SN 1999em	2	52	0	26	80	IIP	SN 2004em	0	2	0	2	4	-
SN 2002gd	10	18	0	15	43	IIP	SN 2005dn	4	0	0	0	4	-
SN 2013ej	0	0	6	35	41	IIP	SN 2007P	4	0	0	0	4	-
SN 2004et	0	20	0	20	40	IIP	SN 2007U	4	0	0	0	4	-
SN 2012ec	0	0	8	31	39	IIP	SN 2008bx	0	0	4	0	4	-
SN 2013ab	0	0	12	26	38	IIP	SN 2009bu	4	0	0	0	4	-
SN 2005cs	0	24	0	12	36	IIP	SN 2012ck	0	0	4	0	4	-
SN 2012aw	0	0	4	32	36	IIP	SN 2016adg	0	0	4	0	4	IIP
SN 1987A	0	18	0	16	34	II-pec	SN 2018fus	0	0	0	4	4	-
SN 2016X	0	0	8	17	25	IIP	SN 2020voh	0	0	0	4	4	-
SN 2007od	4	0	3	15	22	IIP	SN 2021afdx	0	0	0	4	4	-
SN 2008aw	8	0	4	9	21	-	SN 1990K	3	0	0	0	3	-
SN 2014G	0	0	5	14	19	IIL	SN 1993K	3	0	0	0	3	-
SN 2003Z	0	9	0	9	18	IIP	SN 1999cr	3	0	0	0	3	-
SN 1999br	6	8	0	0	14	II-pec	SN 1999eu	0	3	0	0	3	II-pec
SN 2014cy	0	0	8	6	14	IIP	SN 2002fa	3	0	0	0	3	-
SN 2003hl	3	0	0	8	11	IIP	SN 2003bl	3	0	0	0	3	-
SN 2009ao	5	0	6	0	11	-	SN 2003ci	3	0	0	0	3	-
SN 2011fd	0	0	6	5	11	IIP	SN 2003fb	3	0	0	0	3	-
SN 1997D	0	10	0	0	10	II-pec	SN 2003hd	3	0	0	0	3	-
SN 2007il	5	0	5	0	10	-	SN 2003hg	3	0	0	0	3	-
SN 2008ag	10	0	0	0	10	-	SN 2003ho	3	0	0	0	3	-
SN 2008if	9	0	1	0	10	-	SN 2003ib	3	0	0	0	3	IIP
SN 2009E	0	5	0	5	10	IIP	SN 2004ek	0	3	0	0	3	-
SN 2014dq	0	0	0	10	10	IIP	SN 2004fb	3	0	0	0	3	-
SN 2003bn	9	0	0	0	9	-	SN 2005ci	0	3	0	0	3	-
SN 2004fx	9	0	0	0	9	-	SN 2006V	0	3	0	0	3	-
SN 2005J	9	0	0	0	9	-	SN 2007ab	3	0	0	0	3	-
SN 2006au	0	9	0	0	9	-	SN 2007av	3	0	0	0	3	-
SN 2006be	3	0	0	6	9	-	SN 2008bh	3	0	0	0	3	-
SN 2007aa	9	0	0	0	9	IIP	SN 2008bm	3	0	0	0	3	IIn
SN 2008in	4	0	3	2	9	IIP	SN 2008br	3	0	0	0	3	-
SN 2011cj	0	0	5	4	9	IIP	SN 2008gr	3	0	0	0	3	-
SN 2015V	0	0	9	0	9	-	SN 2008K	3	0	0	0	3	-
SN 2020abtf	0	0	0	9	9	-	SN 2009au	3	0	0	0	3	IIn
SN 2021qqu	0	0	0	9	9	-	SN 2009mw	0	3	0	0	3	-
SN 2002gw	8	0	0	0	8	-	SN 2011ef	0	0	3	0	3	-
SN 2004fc	8	0	0	0	8	-	SN 2016cok	0	0	1	2	3	IIP
SN 1986L	7	0	0	0	7	-	SN 2020znl	0	0	0	3	3	-
SN 2002hx	7	0	0	0	7	IIP	SN 2021tyw	0	0	0	3	3	-
SN 2003gd	2	0	0	5	7	-	SN 1993S	2	0	0	0	2	-
SN 2004ej	7	0	0	0	7	-	SN 2001dc	0	2	0	0	2	IIP
SN 2004er	7	0	0	0	7	-	SN 2003ej	2	0	0	0	2	IIP
SN 2006ai	7	0	0	0	7	-	SN 2003hk	2	0	0	0	2	IIP
SN 2006ee	6	0	1	0	7	-	SN 2006iw	2	0	0	0	2	-
SN 2007oc	7	0	0	0	7	-	SN 2006ms	2	0	0	0	2	-
SN 2007X	7	0	0	0	7	-	SN 2008bk	2	0	0	0	2	IIP
SN 2009js	0	0	3	4	7	IIP	SN 2008ex	0	0	2	0	2	-
SN 2009N	6	0	1	0	7	IIP	SN 2009ay	0	0	2	0	2	-
SN 2012A	0	0	3	4	7	IIP	SN 2013am	0	0	2	0	2	IIP
SN 2016fqr	0	0	7	0	7	IIn?	SN 2013gd	0	0	2	0	2	IIP
SN 2019unb	0	0	0	7	7	-	SN 2015O	0	0	2	0	2	-
SN 1998A	0	6	0	0	6	II-pec	SN 2022sat	0	0	0	2	2	-
SN 2003B	6	0	0	0	6	-	SN 1990E	1	0	0	0	1	IIP
SN 2005an	6	0	0	0	6	-	SN 1992af	1	0	0	0	1	-
SN 2005Z	6	0	0	0	6	-	SN 1992ba	1	0	0	0	1	-
SN 2008gi	4	0	2	0	6	-	SN 1994N	0	1	0	0	1	-
SN 2008m	6	0	0	0	6	-	SN 2002ig	1	0	0	0	1	-
SN 2009kr	0	0	6	0	6	-	SN 2006ek	0	0	1	0	1	-
SN 2015be	0	0	6	0	6	-	SN 2006it	1	0	0	0	1	-
SN 2015ch	0	0	0	6	6	-	SN 2006qr	1	0	0	0	1	-
SN 2017faf	0	0	6	0	6	-	SN 2007hm	1	0	0	0	1	-
SN 2003ef	5	0	0	0	5	IIP	SN 2007ld	1	0	0	0	1	-
SN 2003hn	5	0	0	0	5	-	SN 2007sq	1	0	0	0	1	-
SN 2005dz	5	0	0	0	5	-	SN 2008ho	1	0	0	0	1	-
SN 2006Y	5	0	0	0	5	-	SN 2008il	1	0	0	0	1	-
SN 2007ck	0	0	5	0	5	IIP	SN 2009at	0	0	1	0	1	-
SN 2007W	5	0	0	0	5	-	SN 2009bz	1	0	0	0	1	-
SN 2008W	5	0	0	0	5	-	SN 2010id	0	0	1	0	1	IIP
SN 2009aj	5	0	0	0	5	-	SN 2013bu	0	0	1	0	1	-
SN 2021afaz	0	0	0	5	5	-	SN 2013ft	0	0	1	0	1	IIP
SN 210	5	0	0	0	5	-	SN 2014ce	0	0	1	0	1	-
SN 1991al	4	0	0	0	4	-	SN 2015C	0	0	1	0	1	-
SN 2002hj	4	0	0	0	4	IIP	SN 2015W	0	0	1	0	1	-
SN 2003cn	4	0	0	0	4	IIP	SN 2015X	0	0	1	0	1	-
SN 2003cx	4	0	0	0	4	-	SN 2016cyx	0	0	1	0	1	-
SN 2003eg	4	0	0	0	4	IIP	SN 2017iit	0	0	1	0	1	-
SN 2003ip	4	0	0	0	4	IIP	SN 2017jbj	0	0	1	0	1	-
SN 2003iq	4	0	0	0	4	IIP	SN 2018hde	0	0	1	0	1	IIP
SN 2003T	4	0	0	0	4	-	-	-	-	-	-	-	-

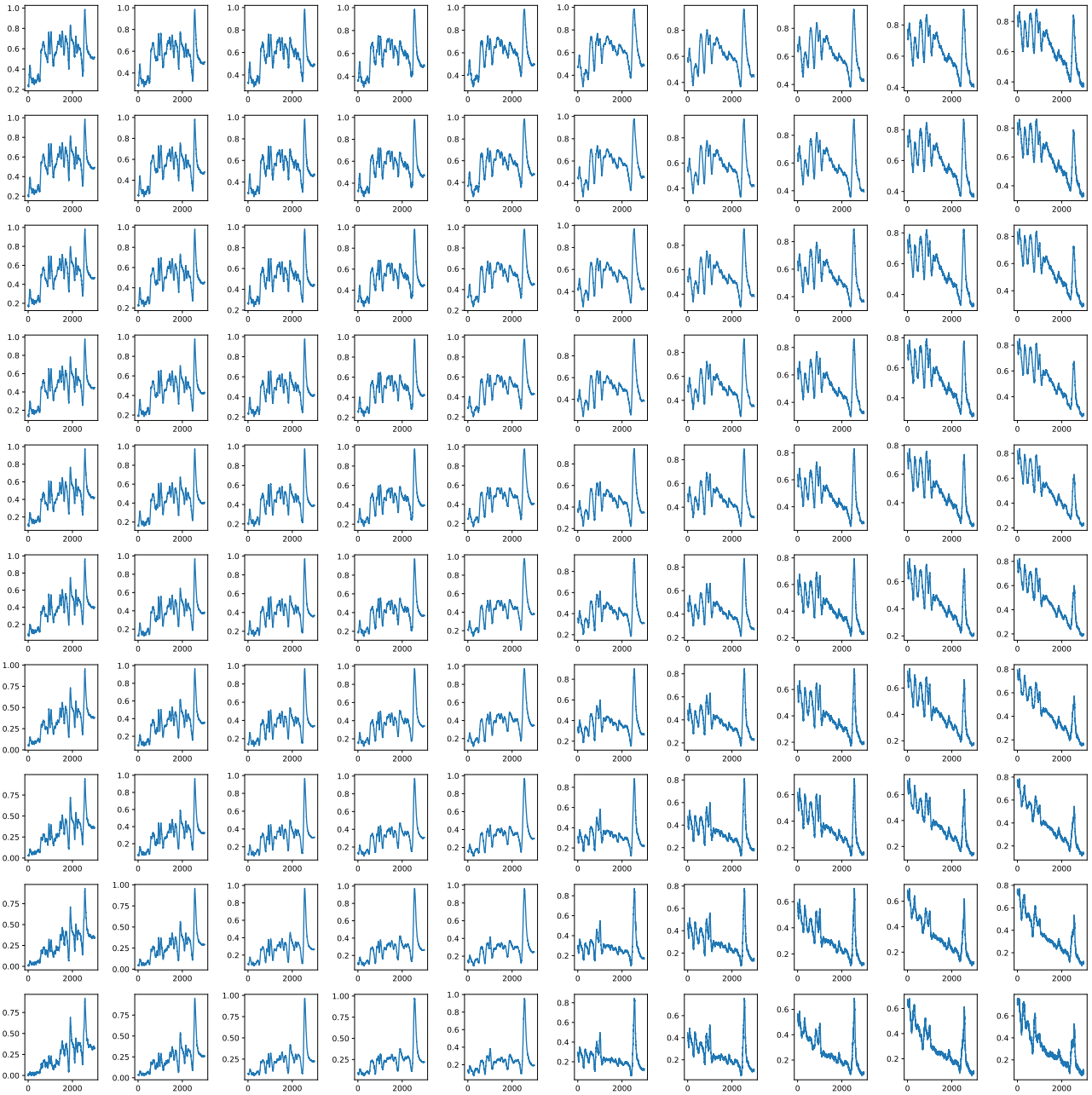

Figure A.1. Latent space for the variational autoencoder. Here the number of encoded dimensions is 2, in order to be able to display in a grid as above. The x and y axes of the grid are encoded dimension, in order to see how changing these two dimensions could in theory encompass the entire variability of spectra. With this latent space one can also produce a range of artificial spectra which encompass both the physically possible and impossible. Note this latent space displayed above does not have the full range as the edge values have been trimmed which describe the most outlying spectra, e.g. very noisy or irregular.

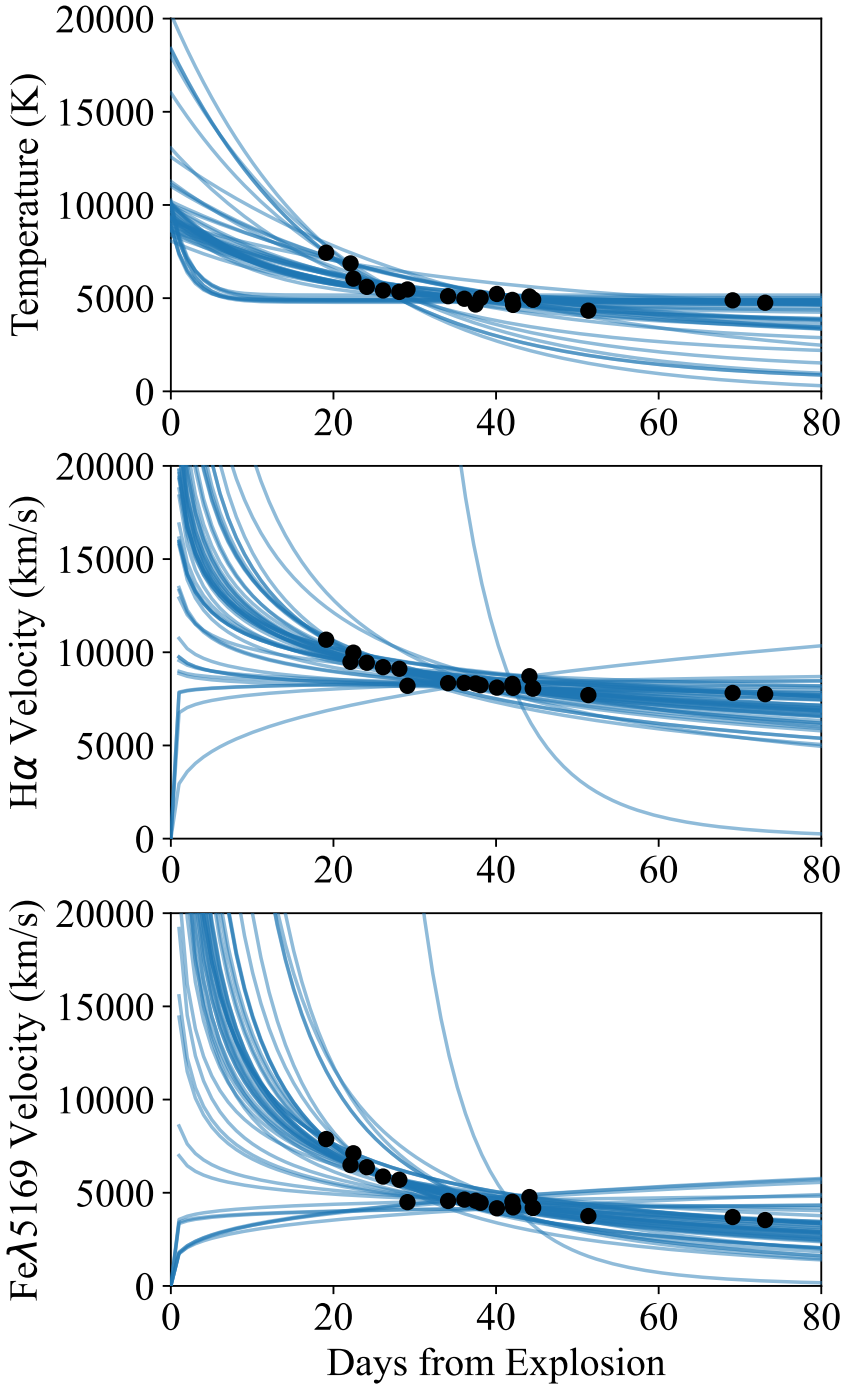

Figure A.2. MCMC predictions for Temperature, Hα velocity, and Feλ5169 velocity, made 50 times for 2 random spectra from the full set of 30.

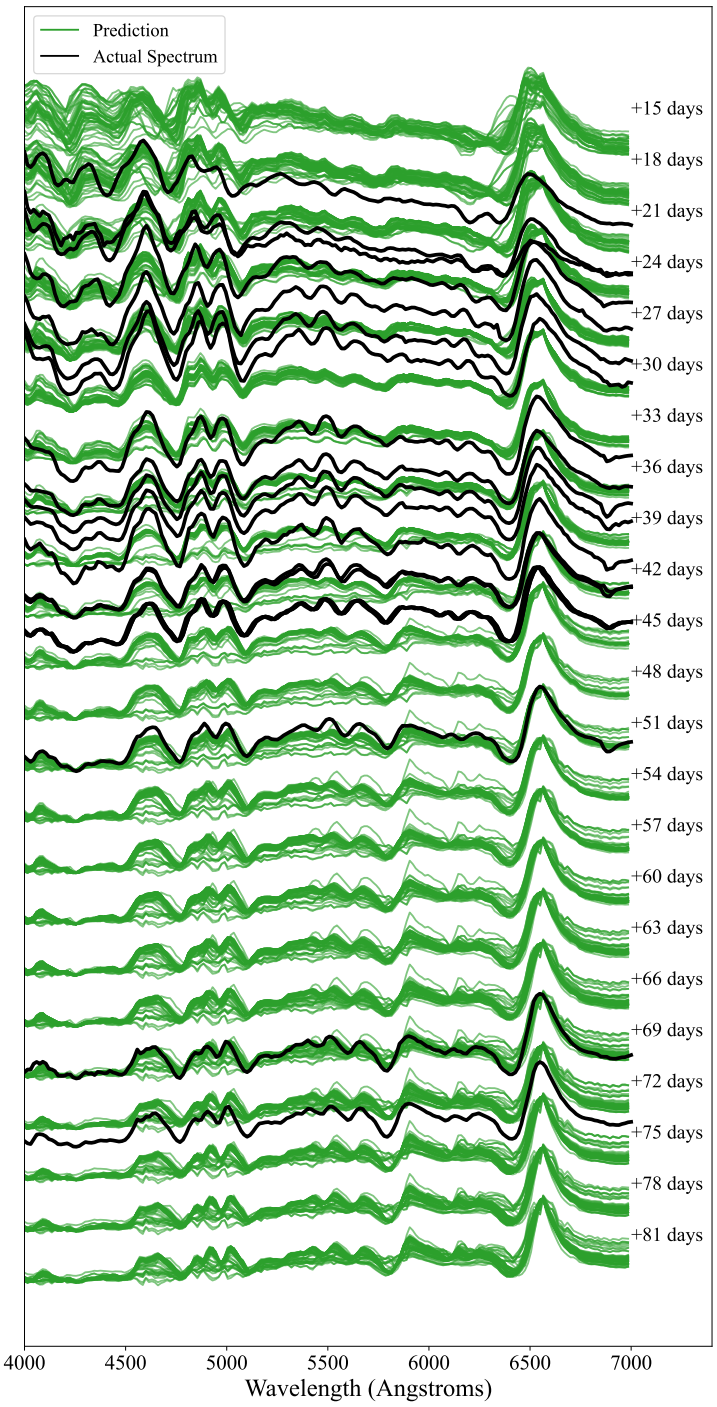

Figure A.3. Predictions from 50 sets of 2 random spectra for SN 2013ej. The predictions (in green) were made for every 3 days, and spectra in black are the observed spectra. The last two spectra appear slightly shifted with respect to predictions.

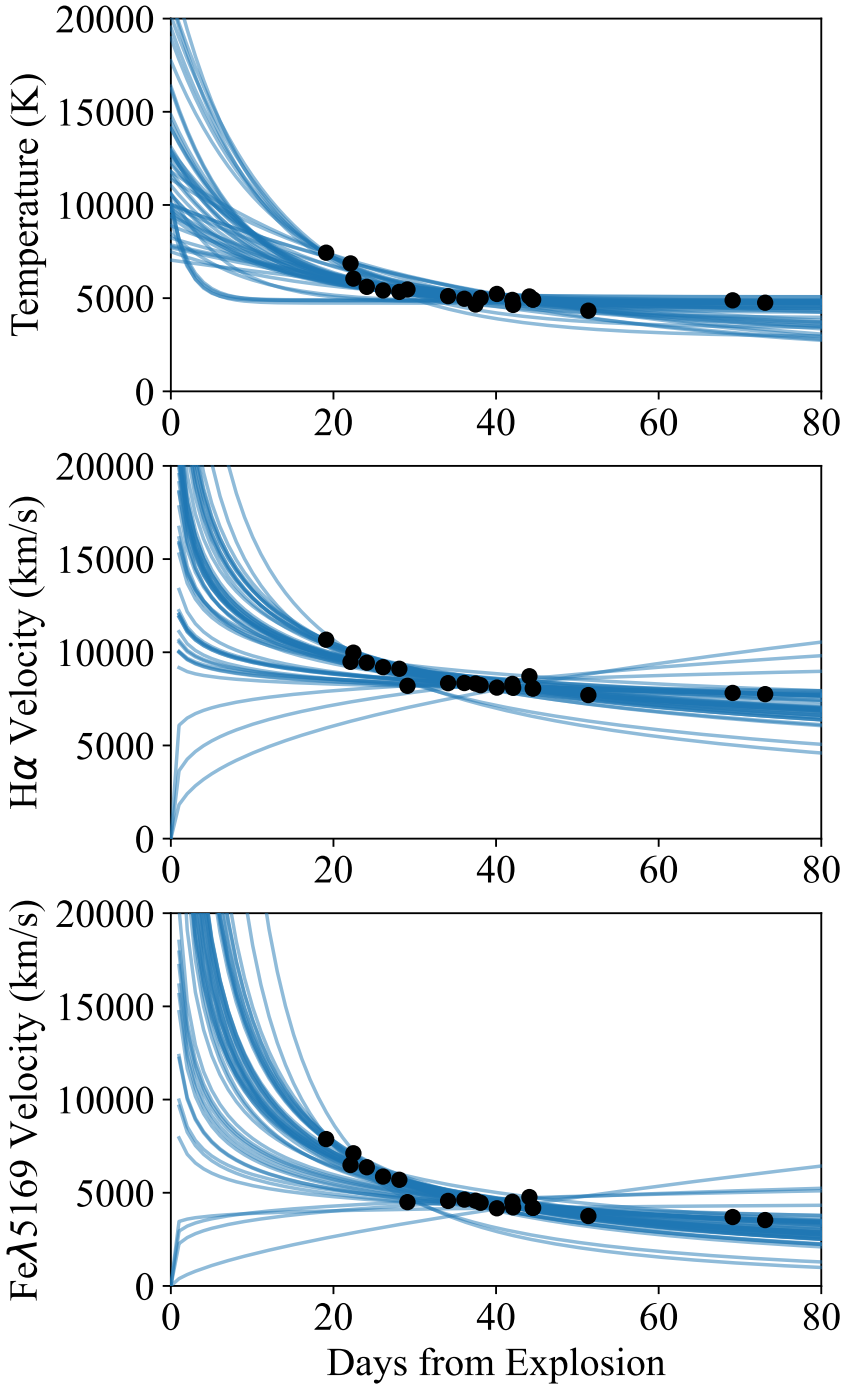

Figure A.4. MCMC predictions for Temperature, Hα velocity, and Feλ5169 velocity, made 50 times for 3 random spectra from the full set of 30.

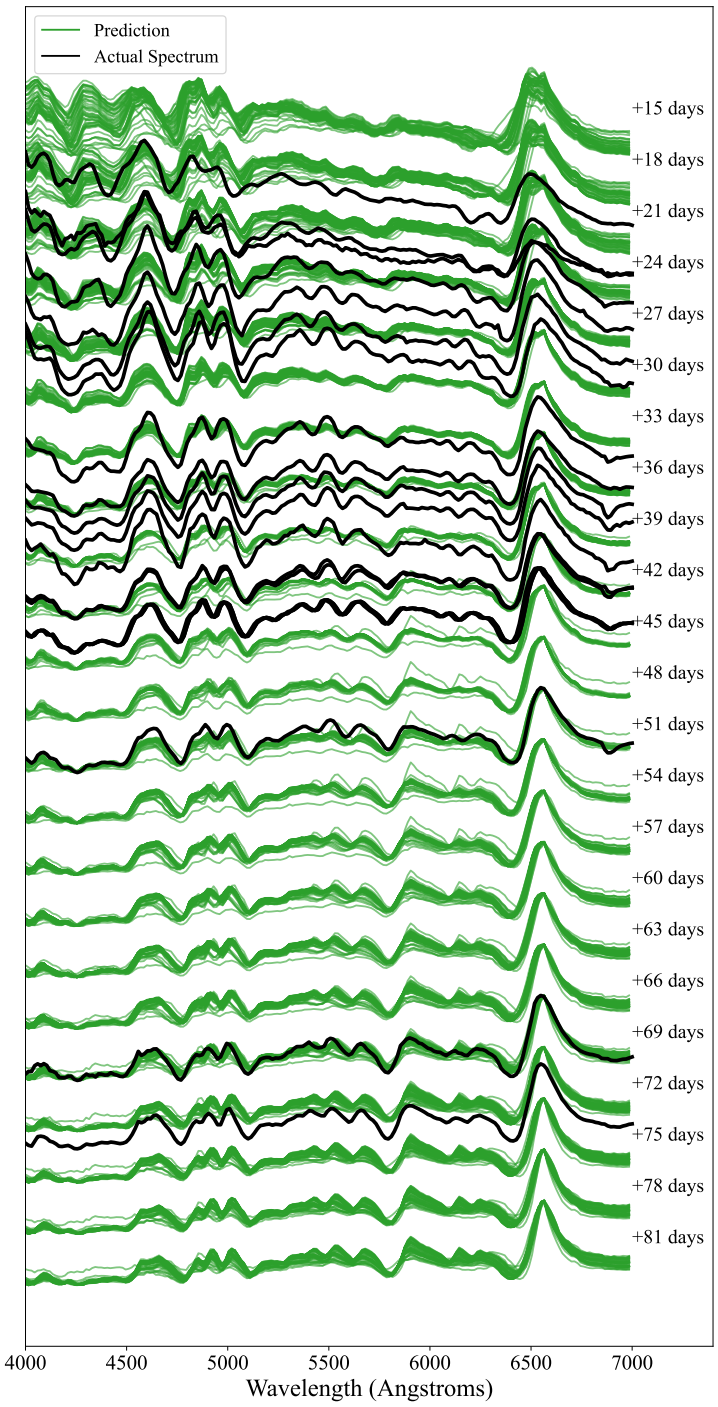

Figure A.5. Predictions from 50 sets of 3 random spectra for SN 2013ej. The predictions (in green) were made for every 3 days, and spectra in black are the observed spectra. The last two spectra appear slightly shifted with respect to predictions.

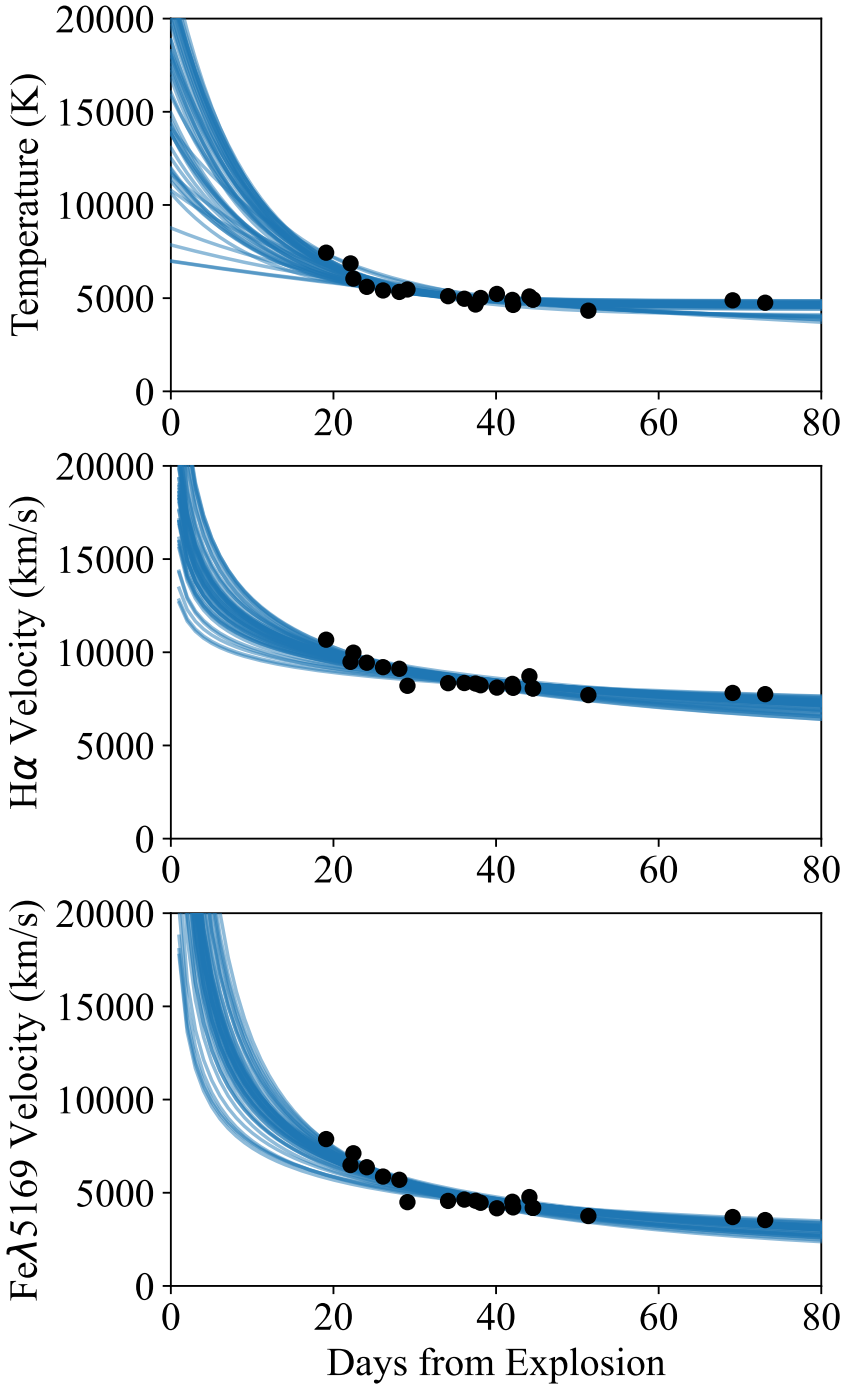

Figure A.6. MCMC predictions for Temperature, Hα velocity, and Feλ5169 velocity, made 50 times for 8 random spectra from the full set of 30.

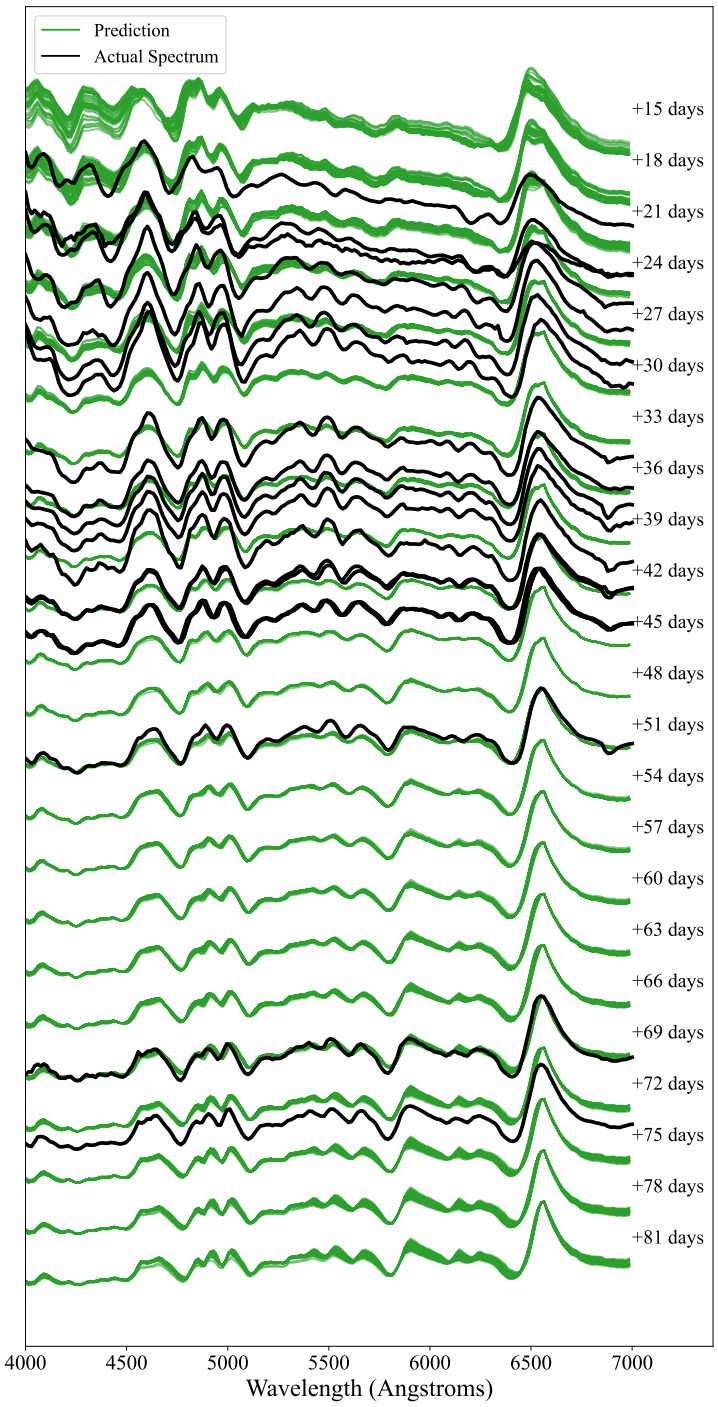

Figure A.7. Predictions from 50 sets of 8 random spectra for SN 2013ej. The predictions (in green) were made for every 3 days, and spectra in black are the observed spectra. The last two spectra appear slightly shifted with respect to predictions.

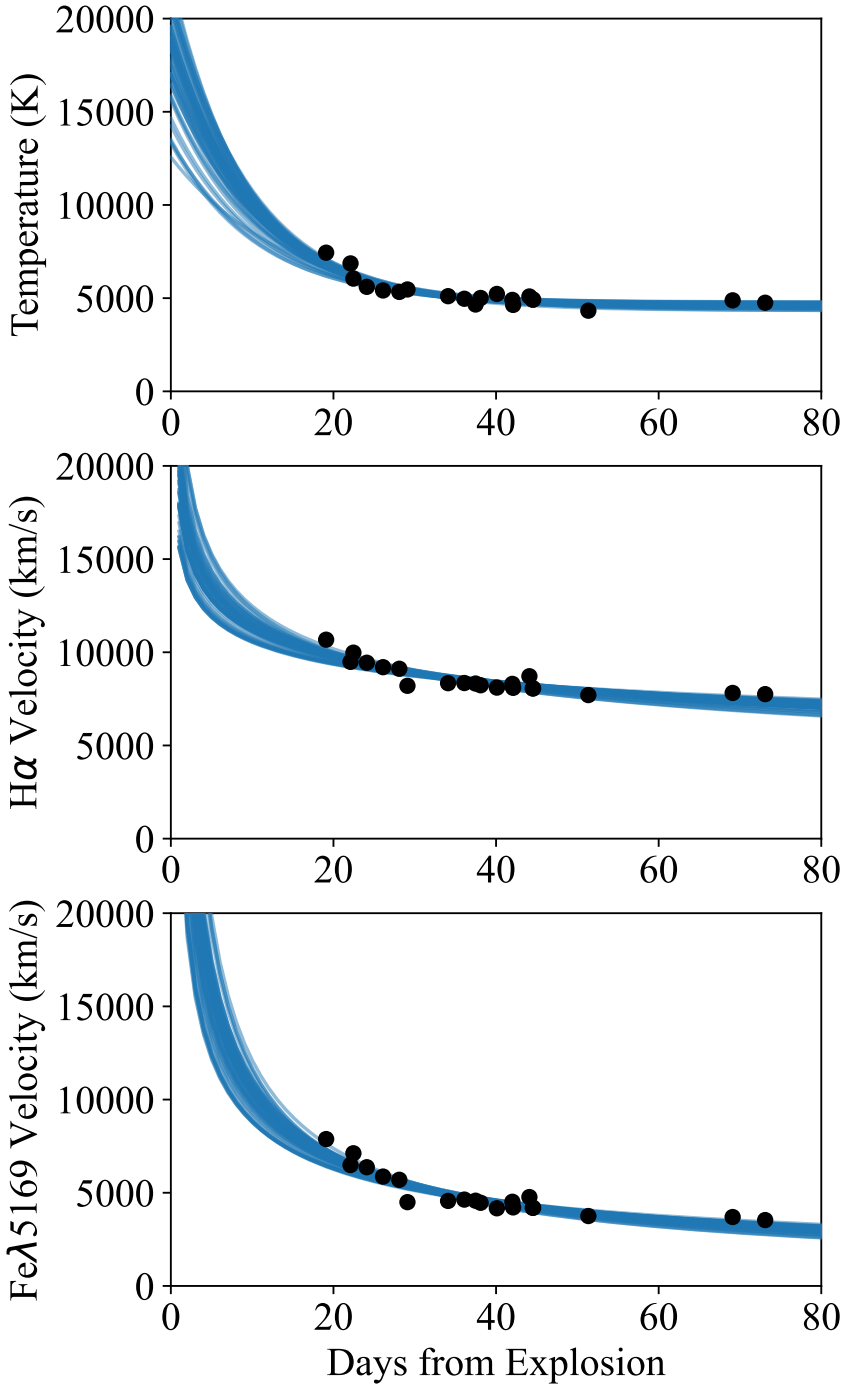

Figure A.8. MCMC predictions for Temperature, Hα velocity, and Feλ5169 velocity, made 50 times for 12 random spectra from the full set of 30.

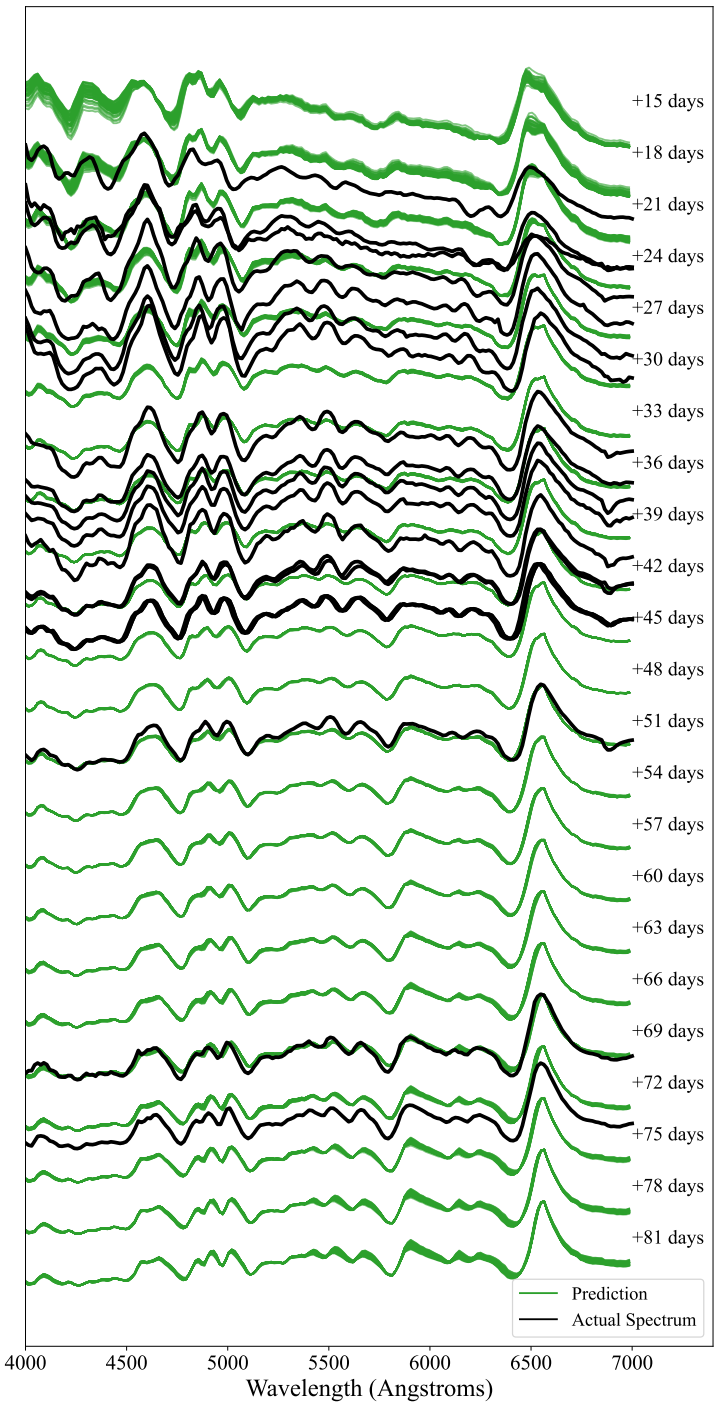

Figure A.9. Predictions from 50 sets of 12 random spectra for SN 2013ej. The predictions (in green) were made for every 3 days, and spectra in black are the observed spectra. The last two spectra appear slightly shifted with respect to predictions.

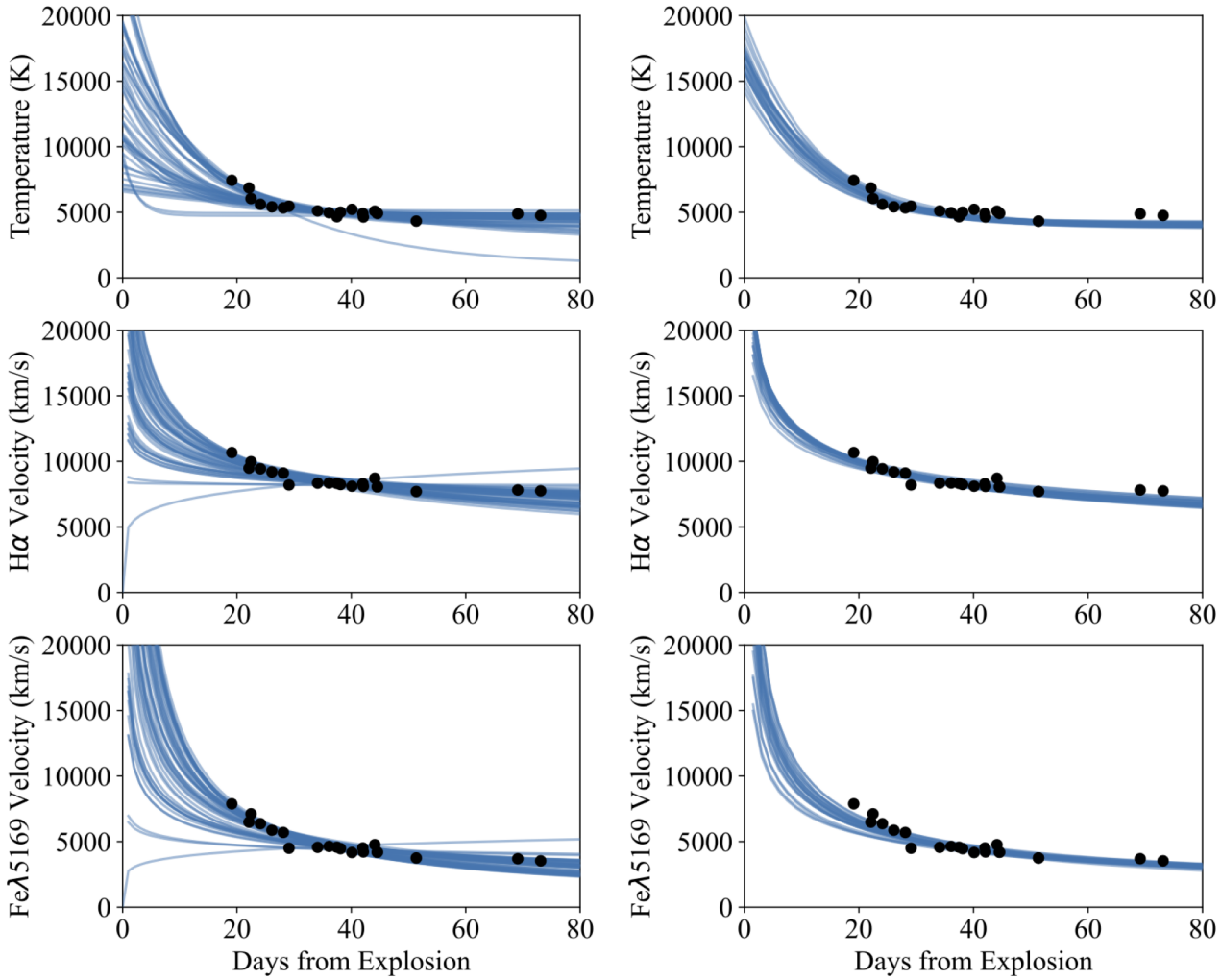

Figure A.10. Left Panel: MCMC predictions for Temperature, Hα velocity, and Feλ5169 velocity, made 50 times for 4 random spectra from SN 2013ej, using the Metropolis-Hasting algorithm as with Figures A.2-A.9. Right Panel: The fitting is done with the package emcee using a Gaussian prior, also for 4 spectra 50 times, for comparison. There is much less variation in the fits when using emcee.

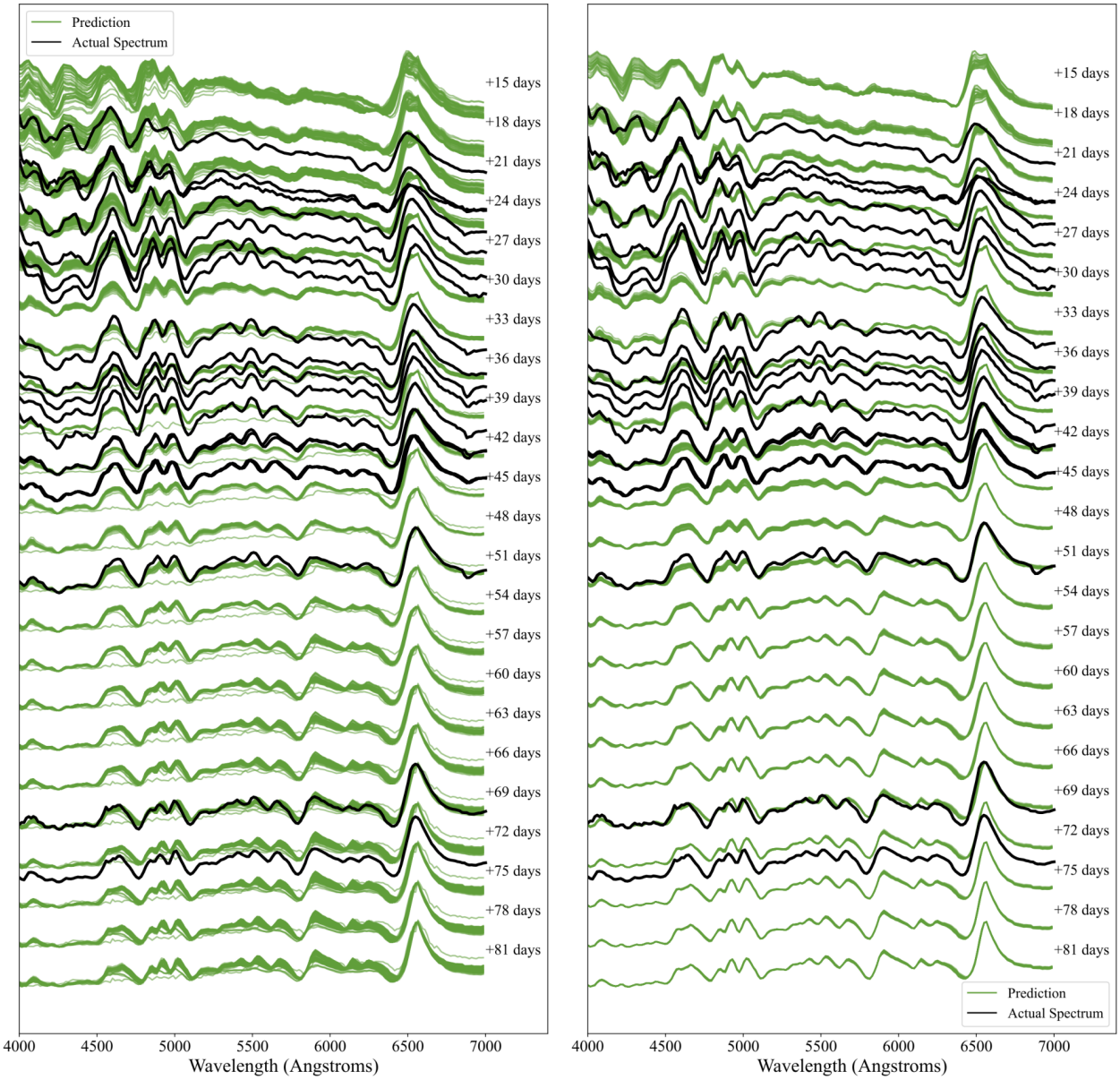

Figure A.11. Left Panel: Predictions from 50 sets of 4 random spectra for SN 2013ej. The predictions (in green) were made for every 3 days, and spectra in black are the observed spectra. The predictions are based on the Metropolis-Hasting algorithm as with Figures A.2-A.9. Right Panel: Spectra predictions based on emcee with a Gaussian prior. This figure accompanies Figure A.10.

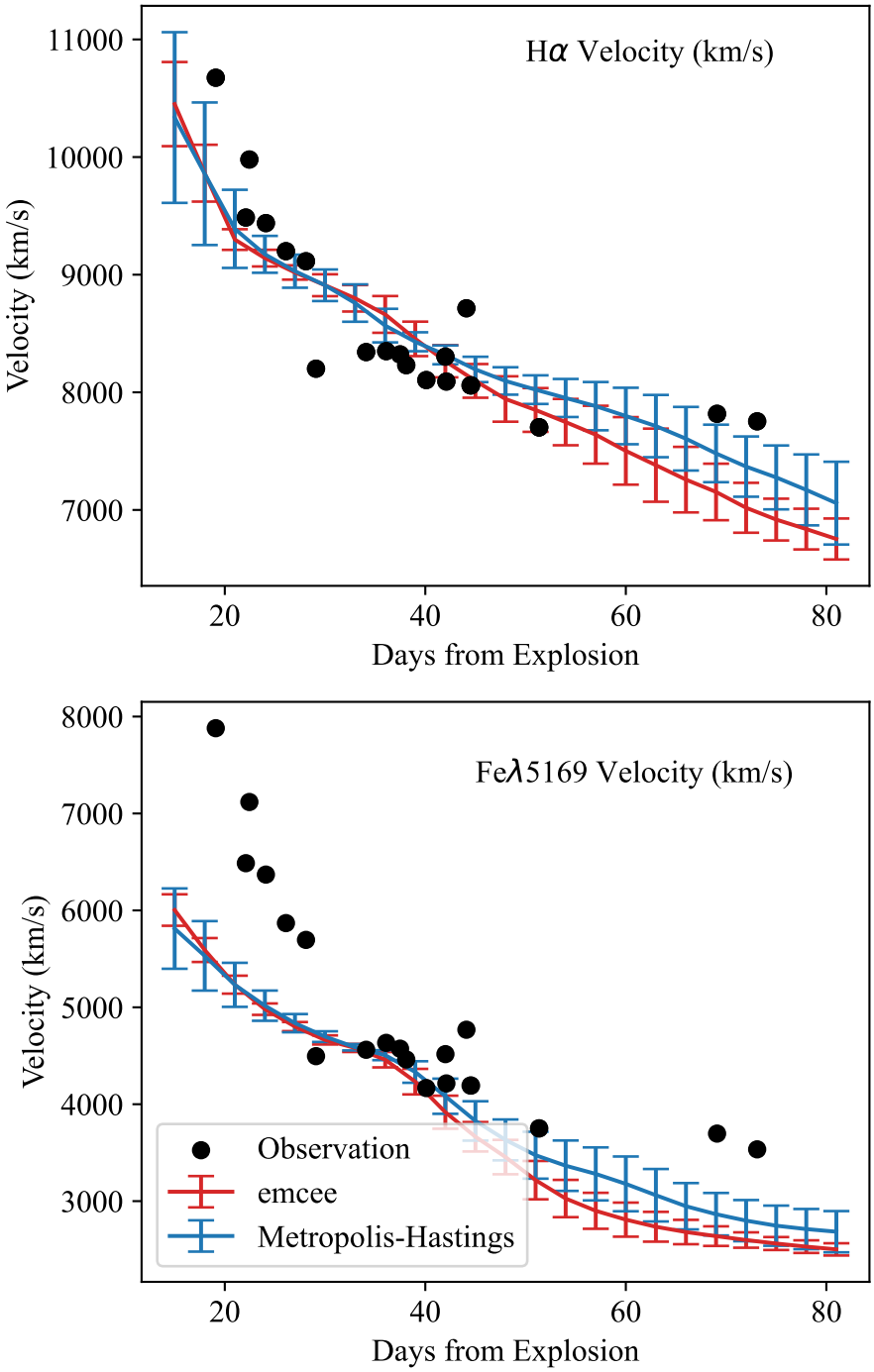

Figure A.12. Comparison of the velocity predictions using the Metropolis-Hastings algorithm (Blue) and emcee with a Gaussian Prior (Red). Despite providing closer fits to the Temperature, Hα velocity, and Feλ5169 velocity (see Figure A.10), the average velocity predictions of the emcee fits does not provide significantly improved predictions, only smaller error bars/less variation in predictions (as can also be observed in the green spectra in Figure A.11).

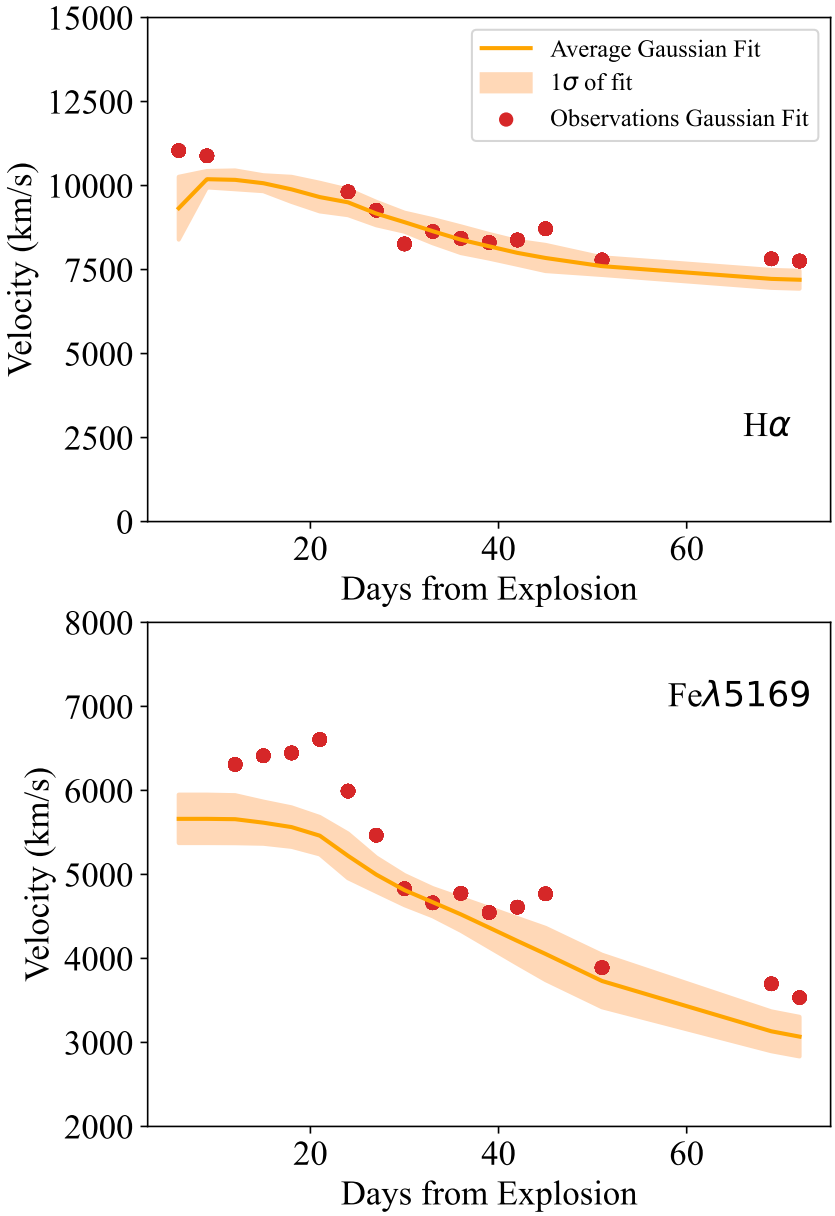

Figure A.13. SN 2013ej Gaussian fit velocity predictions for Hα velocity (Top Panel) vs. Fe II λ5169 velocity (Bottom Panel) for SN 2013ej. The shaded region shows the 1σ range for all predictions (for each spectrum of SN 2013ej). The predictions are poor particularly for Fe II λ5169 before approx. 30 days.

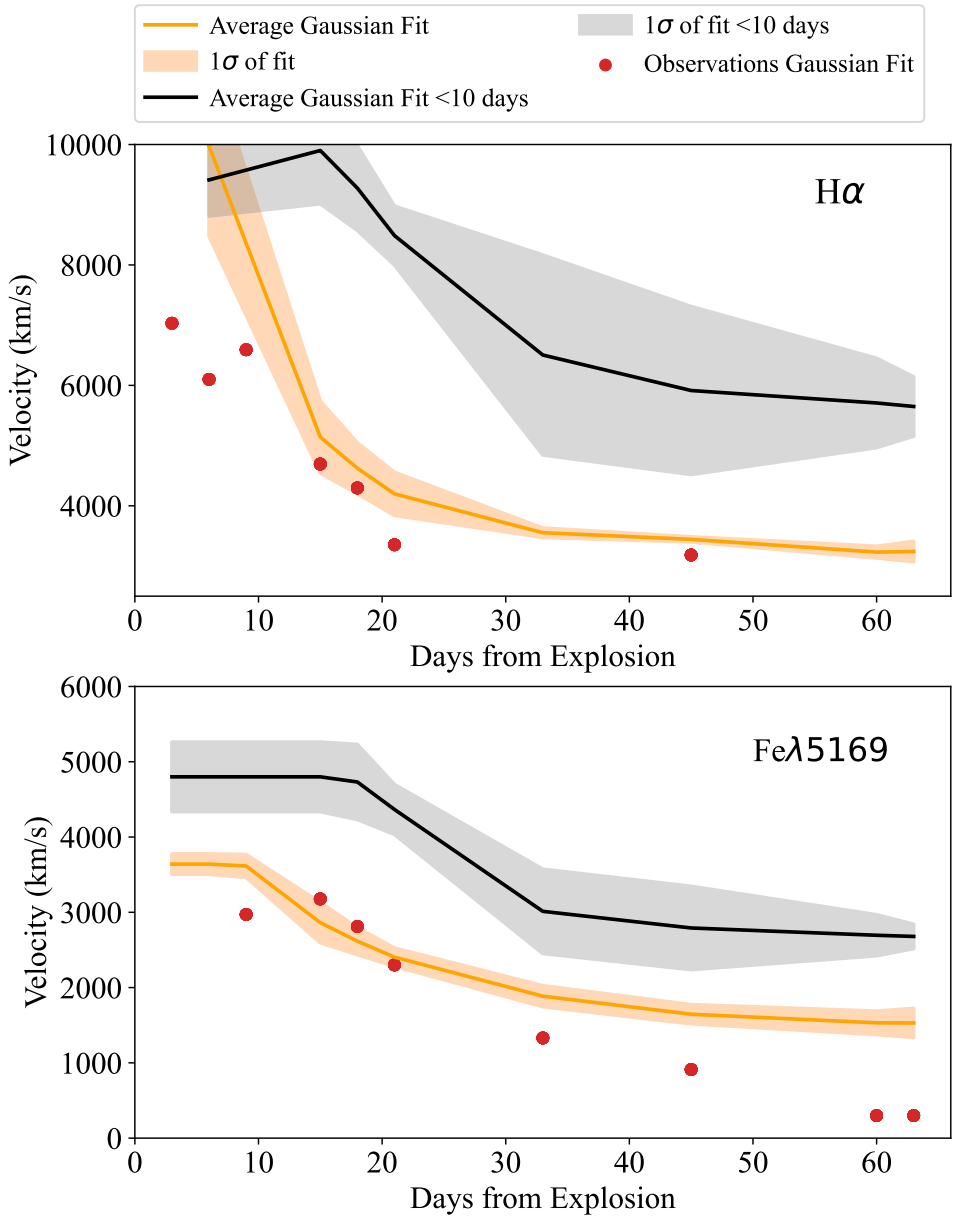

Figure A.14. SN 2005cs Gaussian fit velocity predictions for Hα velocity (Top Panel) vs. Fe II λ5169 velocity (Bottom Panel) for SN 2005cs. The shaded region shows the 1σ range for all predictions (for each spectrum of SN 2005cs, 11 in total.

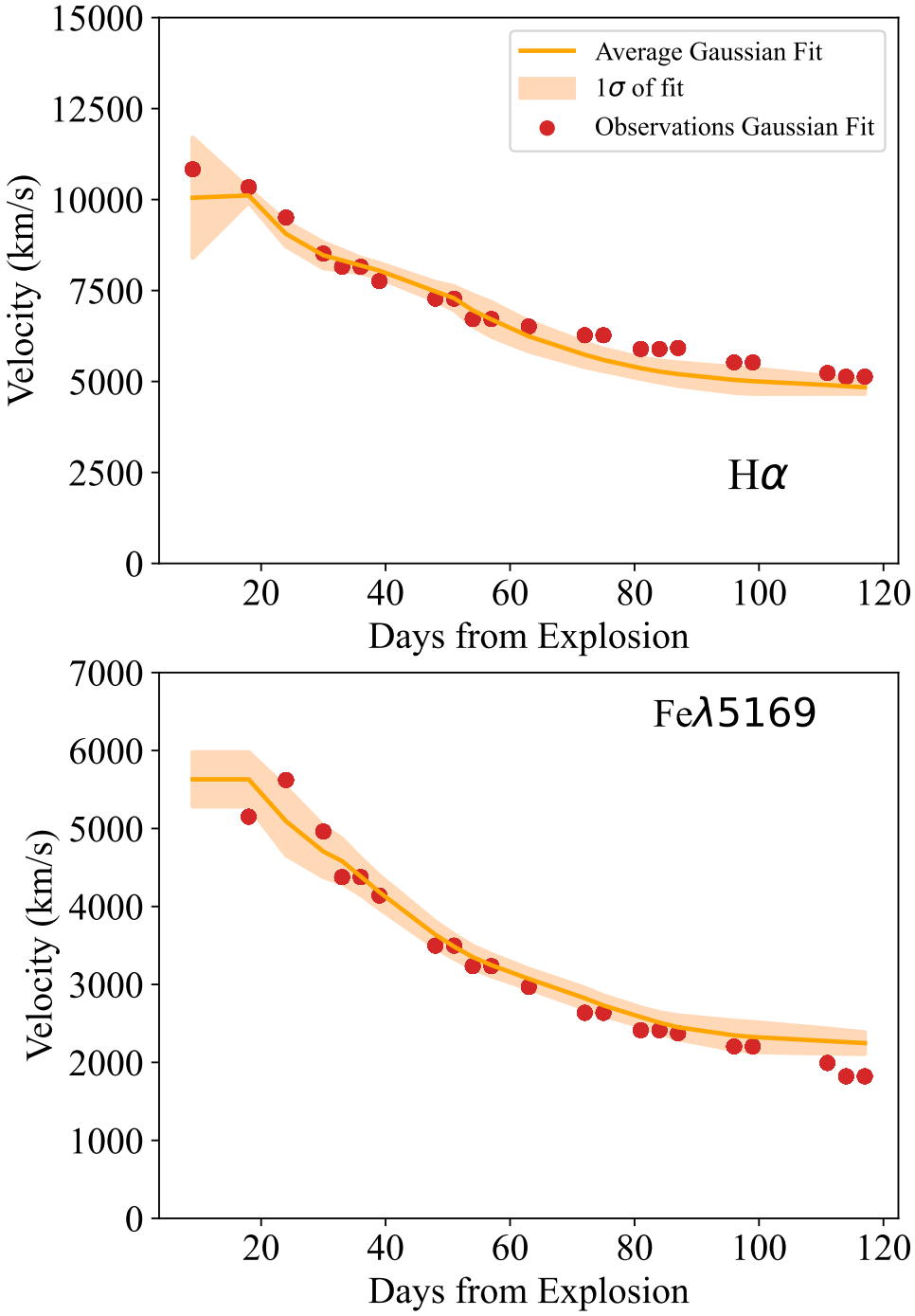

Figure A.15. SN 2004et velocity predictions **(Refer to Figure A.13 for a more detailed caption).**

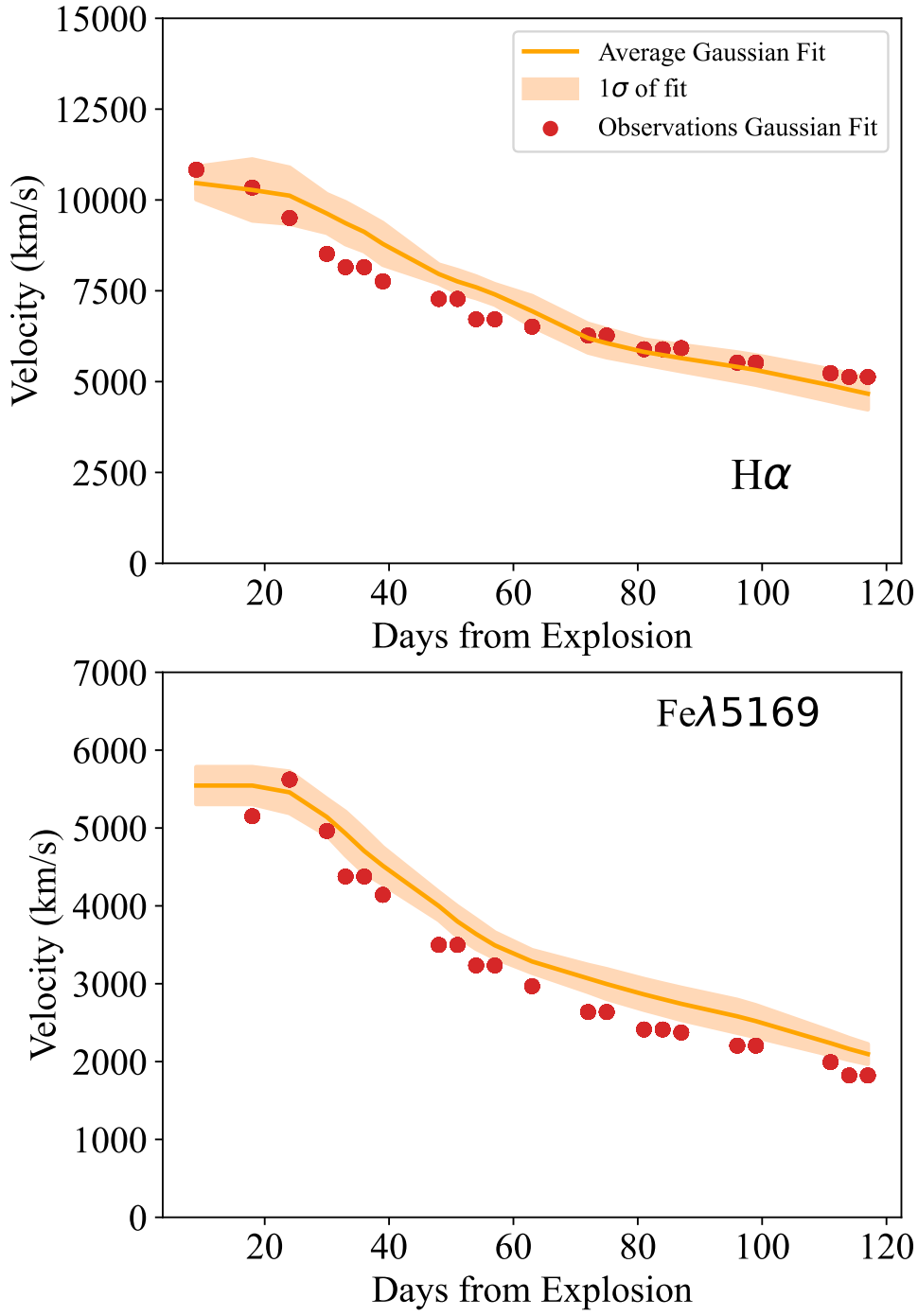

Figure A.16. SN 2004et velocity predictions **(Refer to Figure A.13 for a more detailed caption)** with input phase of observed spectra off by +10 days - there is not a significant difference from the predictions made with unshifted epochs.

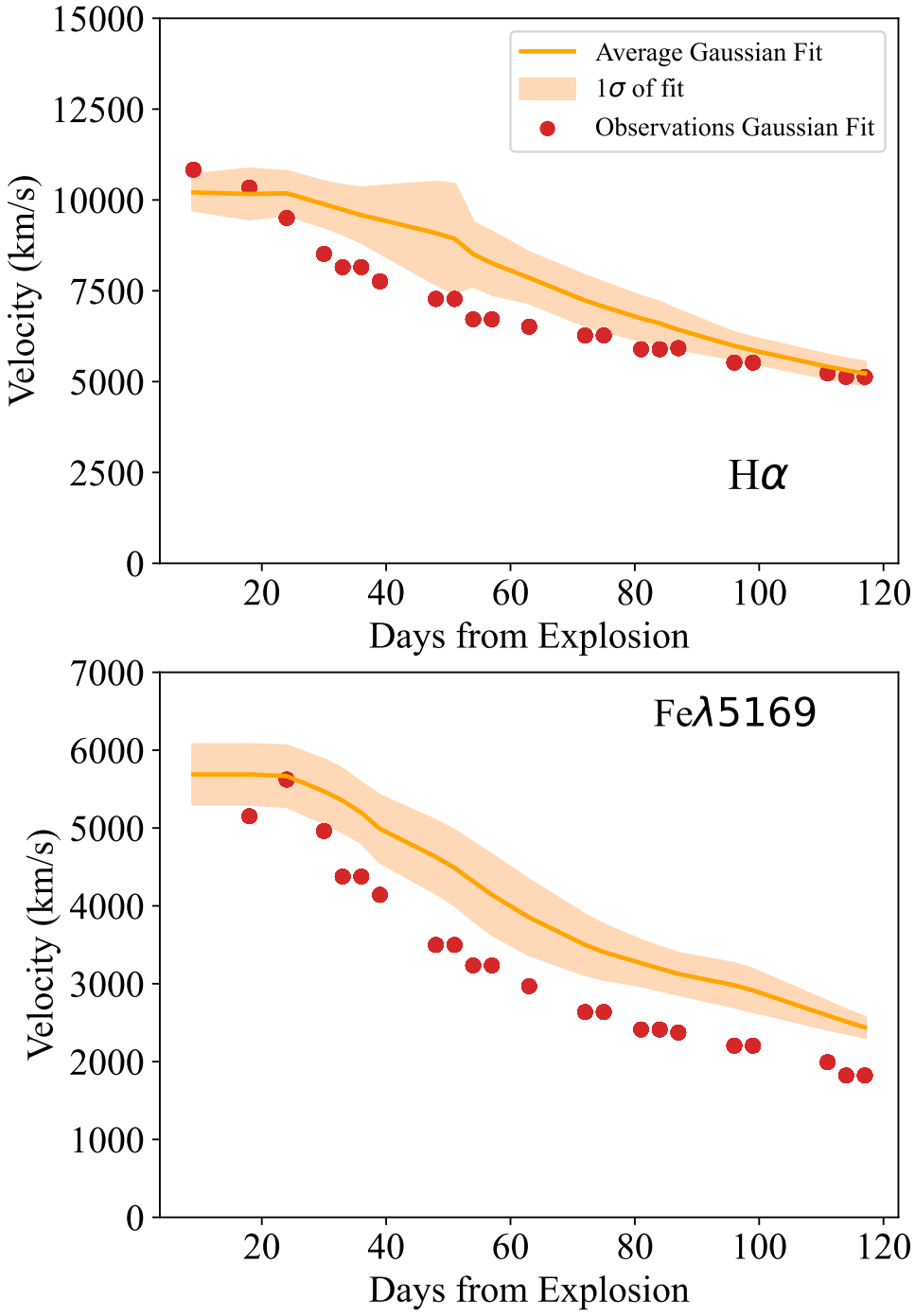

Figure A.17. SN 2004et velocity predictions **(Refer to Figure A.13 for a more detailed caption)** with input phase of observed spectra off by +30 days - the predictions are notably worse than for unshifted epochs.

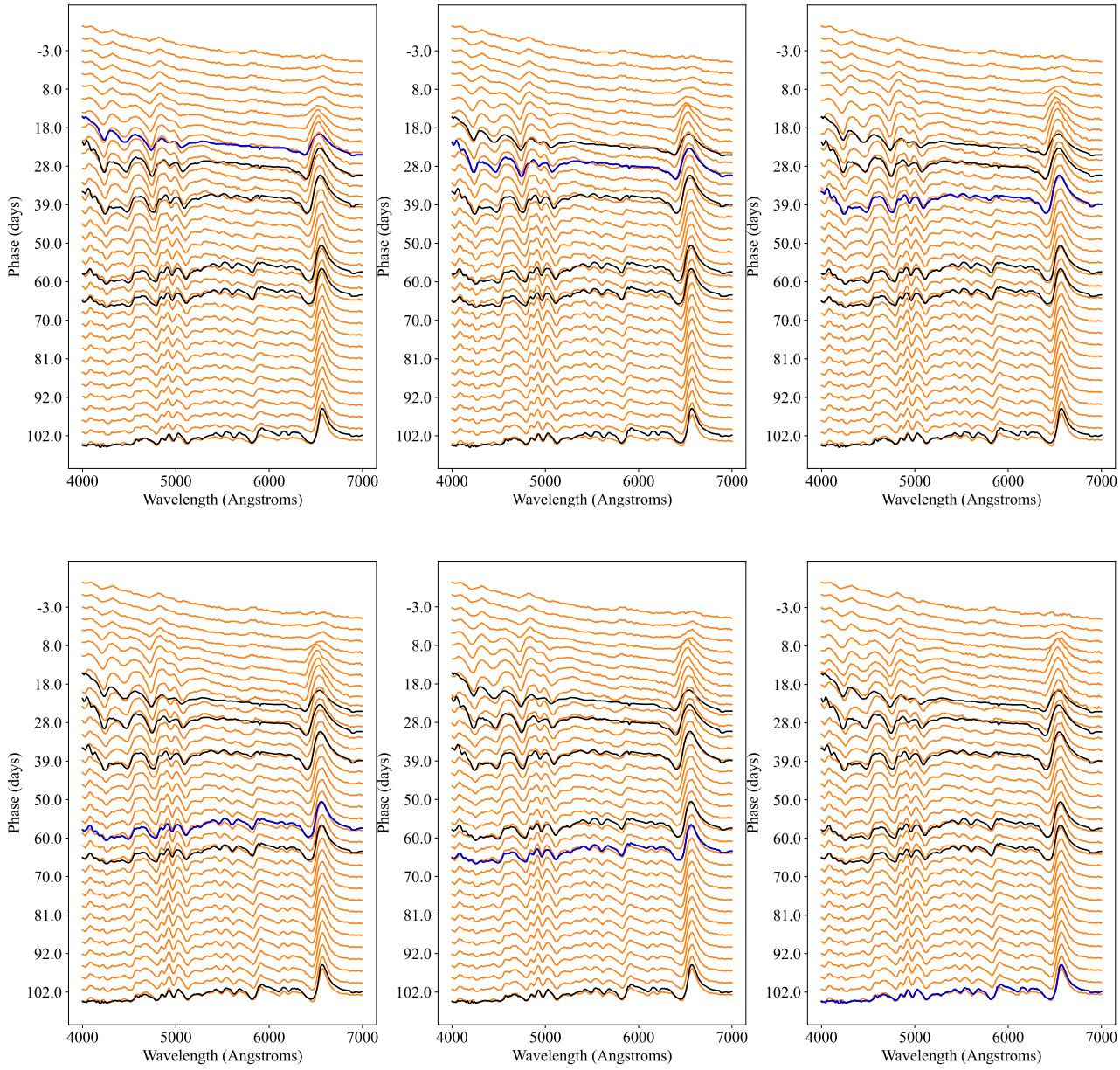

Figure A.18. Predictions for SN 2004et, with 6 spectra chosen at roughly regular intervals up to 100 days **(Refer to Figure 6.12 for a more detailed caption).**

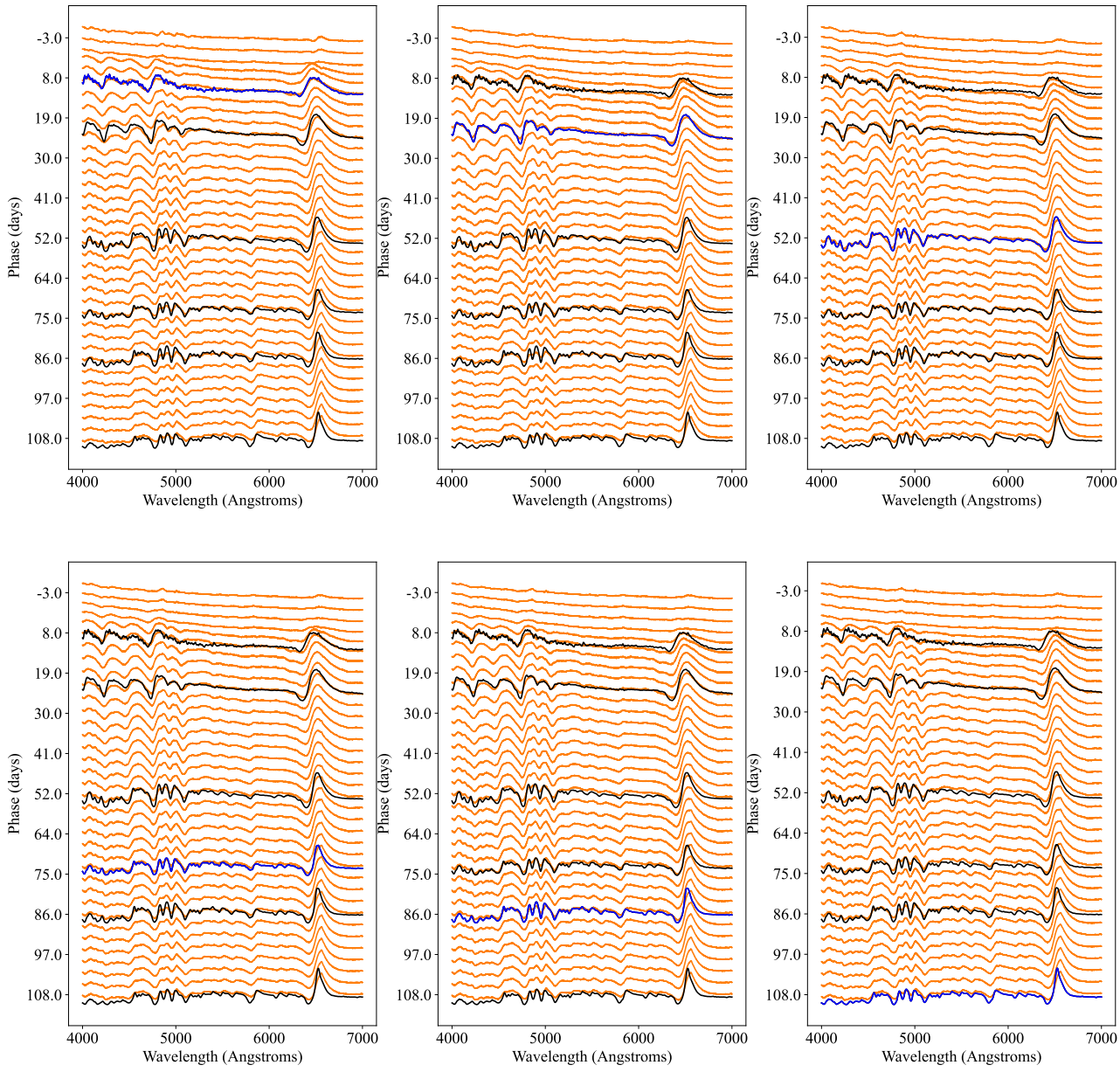

Figure A.19. Predictions for SN 2015V, with 6 chosen spectra at roughly regular intervals. The shape of the P-Cygni profile for Hα is slightly different particularly for predictions after 50 days **(Refer to Figure 6.12 for a more detailed caption).**

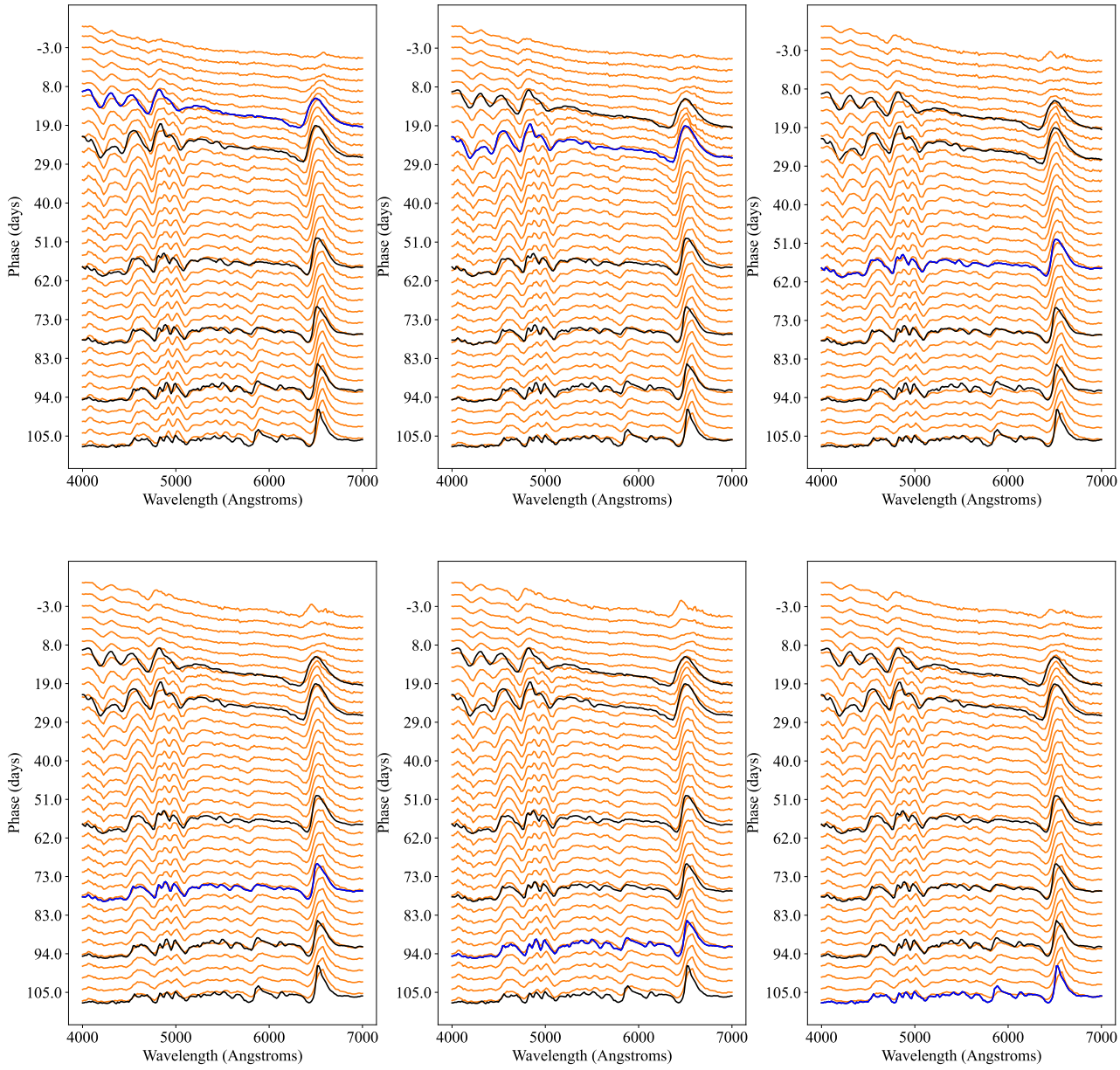

Figure A.20. Predictions for SN 2016X **(Refer to Figure 6.12 for a more detailed caption).**

Bibliography

Abadi M., et al., 2015, TensorFlow: Large-Scale Machine Learning on Heterogeneous Systems, `https://www.tensorflow.org/`

Agnoletto I., et al., 2009, *ApJ*, 691, 1348

Anderson J. P., 2019, *A&A*, 628, A7

Anderson J. P., et al., 2014a, *MNRAS*, 441, 671

Anderson J. P., et al., 2014b, *ApJ*, 786, 67

Anderson J. P., et al., 2016, *A&A*, 589, A110

Anderson J. P., et al., 2018a, Nature Astronomy, 2, 574

Anderson J. P., et al., 2018c, *A&A*, 620, A67

Anderson J. P., et al., 2018b, *A&A*, 620, A67

Andrade C., 2019, Indian Journal of Psychological Medicine, 41, 210

Andrews J. E., et al., 2019, *ApJ*, 885, 43

Angus C. R., et al., 2019, *MNRAS*, 487, 2215

Anupama G. C., Sivarani T., Pandey G., 2001, *A&A*, 367, 506

Arcavi I., 2017, Hydrogen-Rich Core-Collapse Supernovae. Springer International Publishing AG, p. 239, doi:10.1007/978-3-319-21846-5_39

Asplund M., Grevesse N., Sauval A. J., Scott P., 2009, *ARAA*, 47, 481

Barbon R., Ciatti F., Rosino L., 1979, *A&A*, 72, 287

Battisti A. J., Calzetti D., Chary R. R., 2016, *ApJ*, 818, 13

Bazin G., et al., 2009, *A&A*, 499, 653

Benetti S., et al., 2016, *MNRAS*, 456, 3296

Bianco F. B., Modjaz M., Oh S. M., Fierroz D., Liu Y. Q., Kewley L., Graur O., 2016, Astronomy and Computing, 16, 54

Bianco F. B., et al., 2022, *ApJS*, 258, 1

Blanchard P. K., et al., 2018, *ApJ*, 865, 9

Blondin S., Tonry J. L., 2007, *ApJ*, 666, 1024

Boone K., 2019, *AJ*, 158, 257

Bose S., et al., 2015, *ApJ*, 806, 160

Bradley L., et al., 2020, astropy/photutils: 1.0.0, doi:10.5281/zenodo.4044744, `https://doi.org/10.5281/zenodo.4044744`

Branch D., Tammann G. A., 1992, *ARAA*, 30, 359

Branch D., Wheeler J. C., 2017, Supernova Explosions. Springer-Verlag GmbH Germany, doi:10.1007/978-3-662-55054-0

Branch D., Falk S. W., McCall M. L., Rybski P., Uomoto A. K., Wills B. J., 1981, *ApJ*, 244, 780

Brennan S. J., Fraser M., 2022, *A&A*, 667, A62

Brown T. M., et al., 2011, in American Astronomical Society Meeting Abstracts #218. p. 132.02

Burhanudin U. F., et al., 2021, *MNRAS*, 505, 4345

Burrows A., Livne E., Dessart L., Ott C. D., Murphy J., 2006, New A Rev., 50, 487

Burrows A., Dessart L., Livne E., Ott C. D., Murphy J., 2007, *ApJ*, 664, 416

Buzzoni B., et al., 1984, The Messenger, 38, 9

Caffau E., Ludwig H. G., Steffen M., Freytag B., Bonifacio P., 2011, Sol. Phys., 268, 255

Calzetti D., 2001, *PASP*, 113, 1449

Calzetti D., Armus L., Bohlin R. C., Kinney A. L., Koornneef J., Storchi-Bergmann T., 2000, *ApJ*, 533, 682

Cantiello M., Yoon S. C., Langer N., Livio M., 2007, *A&A*, 465, L29

Cardelli J. A., Clayton G. C., Mathis J. S., 1989, *ApJ*, 345, 245

Castor J. I., 1970, *MNRAS*, 149, 111

Chabrier G., 2003, *PASP*, 115, 763

Chakrabarty D., Morgan E. H., Muno M. P., Galloway D. K., Wijnands R., van der Klis M., Markwardt C. B., 2003, *Nature*, 424, 42

Chambers K. C., et al., 2016, arXiv e-prints, p. arXiv:1612.05560

Chatzopoulos E., Wheeler J. C., 2012, *ApJ*, 760, 154

Chatzopoulos E., et al., 2011, *ApJ*, 729, 143

Chatzopoulos E., Wheeler J. C., Vinko J., Horvath Z. L., Nagy A., 2013, *ApJ*, 773, 76

Chen T. W., et al., 2015, *MNRAS*, 452, 1567

Chen T.-W., Smartt S. J., Yates R. M., Nicholl M., Krühler T., Schady P., Dennefeld M., Inserra C., 2017a, *MNRAS*, 470, 3566

Chen T. W., et al., 2017b, *A&A*, 602, A9

Chen T. W., et al., 2017c, *A&A*, 602, A9

Chen T.-W., et al., 2017d, *ApJ*, 849, L4

Chen T. W., et al., 2018, *ApJ*, 867, L31

Chevalier R. A., Fransson C., 1994, *ApJ*, 420, 268

Chevalier R. A., Irwin C. M., 2011, *ApJ*, 729, L6

Chomiuk L., et al., 2011, *ApJ*, 743, 114

Chruslinska M., Nelemans G., 2019, *MNRAS*, 488, 5300

Chugai N. N., Chevalier R. A., Utrobin V. P., 2007, *ApJ*, 662, 1136

Clemens J. C., Crain J. A., Anderson R., 2004, in Moorwood A. F. M., Iye M., eds, Society of Photo-Optical Instrumentation Engineers (SPIE) Conference Series Vol. 5492, Ground-based Instrumentation for Astronomy. pp 331–340, doi:10.1117/12.550069

Clocchiatti A., Wheeler J. C., 1997, *ApJ*, 491, 375

Conroy C., Gunn J. E., White M., 2009, *ApJ*, 699, 486

Cutri R. M., et al., 2013, Explanatory Supplement to the AllWISE Data Release Products, Explanatory Supplement to the AllWISE Data Release Products

Dastidar R., et al., 2021, *MNRAS*, 504, 1009

Davies B., Figer D. F., Kudritzki R.-P., Trombley C., Kouveliotou C., Wachter S., 2009, *ApJ*, 707, 844

Davis S., et al., 2019, *ApJ*, 887, 4

De Cia A., et al., 2018, *ApJ*, 860, 100

Delgado A., Harrison D., Hodgkin S., Leeuwen M. V., Rixon G., Yoldas A., 2019, Transient Name Server Discovery Report, 2019-957, 1

Dessart L., Hillier D. J., 2005, *A&A*, 439, 671

Dessart L., Hillier D. J., 2020, *A&A*, 642, A33

Dessart L., Hillier D. J., Waldman R., Livne E., Blondin S., 2012, *MNRAS*, 426, L76

Dessart L., Hillier D. J., Waldman R., Livne E., 2013, *MNRAS*, 433, 1745

Dessart L., et al., 2014, *MNRAS*, 440, 1856

Duncan R. C., Thompson C., 1992, *ApJ*, 392, L9

Faran T., et al., 2014, *MNRAS*, 445, 554

Faran T., Nakar E., Poznanski D., 2018, *MNRAS*, 473, 513

Fassia A., et al., 2000, *MNRAS*, 318, 1093

Fassia A., et al., 2001, *MNRAS*, 325, 907

Filippenko A. V., 1988, *AJ*, 96, 1941

Filippenko A. V., 1997, *ARAA*, 35, 309

Filippenko A. V., Matheson T., Ho L. C., 1993, *ApJ*, 415, L103

Fiore A., et al., 2021, *MNRAS*, 502, 2120

Fiore A., et al., 2022, *MNRAS*, 512, 4484

Fischer T., et al., 2011, *ApJS*, 194, 39

Folatelli G., 2004, New A Rev., 48, 623

Foley R. J., 2015, *MNRAS*, 452, 2463

Foreman-Mackey D., et al., 2013, emcee: The MCMC Hammer, Astrophysics Source Code Library, record ascl:1303.002 (ascl:1303.002)

Foreman-Mackey D., Sick J., Johnson B., 2014, Python-Fsps: Python Bindings To Fsps (V0.1.1), doi:10.5281/zenodo.12157

Fransson C., Chevalier R. A., 1989, *ApJ*, 343, 323

Freedman W. L., Madore B. F., 2010, *ARAA*, 48, 673

Fremling C., et al., 2021, *ApJ*, 917, L2

Frohmaier C., et al., 2019, Transient Name Server AstroNote, 27, 1

Frohmaier C., et al., 2021, *MNRAS*, 500, 5142

Gaia Collaboration et al., 2016, *A&A*, 595, A1

Gal-Yam A., 2012, Science, 337, 927

Gal-Yam A., 2017, in Alsabti A. W., Murdin P., eds, , Handbook of Supernovae. Springer International Publishing AG, p. 195, doi:10.1007/978-3-319-21846-5_35

Gal-Yam A., 2019a, *ApJ*, 882, 102

Gal-Yam A., 2019b, *ApJ*, 882, 102

Gal-Yam A., et al., 2014, *Nature*, 509, 471

Gal-Yam A., Yaron O., Pastorello A., Taubenberger S., Fraser M., Perley D., 2021, Transient Name Server AstroNote, 76, 1

Galbany L., et al., 2016, *AJ*, 151, 33

Galbany L., et al., 2018, *ApJ*, 855, 107

Gall E. E. E., et al., 2018, *A&A*, 611, A25

Garavini G., et al., 2007, *A&A*, 470, 411

Gilkis A., Soker N., Papish O., 2016, *ApJ*, 826, 178

Gilmozzi R., et al., 1987, *Nature*, 328, 318

González-Gaitán S., et al., 2015, *MNRAS*, 451, 2212

Graur O., Bianco F. B., Modjaz M., Shivvers I., Filippenko A. V., Li W., Smith N., 2017, *ApJ*, 837, 121

Greiner J., et al., 2008, *PASP*, 120, 405

Guillochon J., Parrent J., Kelley L. Z., Margutti R., 2017, *ApJ*, 835, 64

Gutiérrez C. P., et al., 2017a, *ApJ*, 850, 89

Gutiérrez C. P., et al., 2017b, *ApJ*, 850, 90

Gutiérrez C. P., et al., 2018, *MNRAS*, 479, 3232

Gutiérrez C. P., et al., 2020, *MNRAS*, 499, 974

Gutiérrez C. P., et al., 2021, *MNRAS*, 504, 4907

Gutiérrez C. P., et al., 2022, *MNRAS*, 517, 2056

Hamuy M., Pinto P. A., 2002, *ApJ*, 566, L63

Hamuy M., Walker A. R., Suntzeff N. B., Gigoux P., Heathcote S. R., Phillips M. M., 1992, *PASP*, 104, 533

Hamuy M., Suntzeff N. B., Heathcote S. R., Walker A. R., Gigoux P., Phillips M. M., 1994, *PASP*, 106, 566

Hamuy M., et al., 2001, *ApJ*, 558, 615

Harutyunyan A. H., et al., 2008, *A&A*, 488, 383

Hatano K., Branch D., Deaton J., 1998, *ApJ*, 502, 177

Hatano K., Branch D., Fisher A., Millard J., Baron E., 1999, *ApJS*, 121, 233

Heger A., Woosley S. E., 2002, *ApJ*, 567, 532

Hosseinzadeh G., Berger E., Metzger B. D., Gomez S., Nicholl M., Blanchard P., 2022, *ApJ*, 933, 14

Howell D. A., 2001, *ApJ*, 554, L193

Howell D. A., et al., 2006, *Nature*, 443, 308

Hu L., Chen X., Wang L., 2022, *ApJ*, 930, 70

Huang F., et al., 2015, *ApJ*, 807, 59

Inserra C., 2019, Nature Astronomy, 3, 697

Inserra C., Smartt S. J., 2014, *ApJ*, 796, 87

Inserra C., et al., 2013a, *A&A*, 555, A142

Inserra C., et al., 2013b, *ApJ*, 770, 128

Inserra C., et al., 2017, *MNRAS*, 468, 4642

Inserra C., et al., 2018, *MNRAS*, 475, 1046

Inserra C., et al., 2021, *MNRAS*,

Ishida E. E. O., 2019, Nature Astronomy, 3, 680

Ishida E. E. O., et al., 2019, *MNRAS*, 483, 2

Ishida E. E. O., et al., 2021, *A&A*, 650, A195

Janka H.-T., 2012, Annual Review of Nuclear and Particle Science, 62, 407

Janka H. T., Langanke K., Marek A., Martínez-Pinedo G., Müller B., 2007, *Phys. Repts.*, 442, 38

Jeffery D. J., Branch D., 1990a, in Wheeler J. C., Piran T., Weinberg S., eds, Vol. 6, Supernovae, Jerusalem Winter School for Theoretical Physics. p. 149

Jeffery D. J., Branch D., 1990b, in Wheeler J. C., Piran T., Weinberg S., eds, Vol. 6, Supernovae, Jerusalem Winter School for Theoretical Physics. p. 149

Jerkstrand A., Fransson C., Maguire K., Smartt S., Ergon M., Spyromilio J., 2012, *A&A*, 546, A28

Jha S. W., Maguire K., Sullivan M., 2019, Nature Astronomy, 3, 706

Johnson B. D., Leja J. L., Conroy C., Speagle J. S., 2019, Prospector: Stellar population inference from spectra and SEDs (ascl:1905.025)

Kangas T., et al., 2017, *MNRAS*, 469, 1246

Kasen D., Bildsten L., 2010, *ApJ*, 717, 245

Kasen D., Woosley S. E., 2009, *ApJ*, 703, 2205

Kerzendorf W. E., Sim S. A., 2014, *MNRAS*, 440, 387

Kerzendorf W. E., Strampelli G., Shen K. J., Schwab J., Pakmor R., Do T., Buchner J., Rest A., 2018, *MNRAS*, 479, 192

Kerzendorf W. E., Vogl C., Buchner J., Contardo G., Williamson M., van der Smagt P., 2021, *ApJ*, 910, L23

Kessler R., et al., 2019, *PASP*, 131, 094501

Kewley L. J., Ellison S. L., 2008, *ApJ*, 681, 1183

Kingma D. P., Ba J., 2014, arXiv e-prints, p. arXiv:1412.6980

Kirshner R. P., Kwan J., 1974, *ApJ*, 193, 27

Könyves-Tóth R., Vinkó J., 2021, *ApJ*, 909, 24

Könyves-Tóth R., Thomas B. P., Vinkó J., Wheeler J. C., 2020, *ApJ*, 900, 73

Kozma C., Fransson C., 1998, *ApJ*, 497, 431

Kozyreva A., Blinnikov S., 2015, *MNRAS*, 454, 4357

Kozyreva A., Janka H.-T., Kresse D., Taubenberger S., Baklanov P., 2022, *MNRAS*, 514, 4173

Kriek M., Conroy C., 2013, *ApJ*, 775, L16

Krühler T., et al., 2008, *ApJ*, 685, 376

Kumar A., et al., 2020, *ApJ*, 892, 28

LSST Science Collaboration et al., 2009, arXiv e-prints, p. arXiv:0912.0201

Lang D., 2014, *AJ*, 147, 108

Lecun Y., Bengio Y., Hinton G., 2015, *Nature*, 521, 436

Leja J., Johnson B. D., Conroy C., van Dokkum P. G., Byler N., 2017, *ApJ*, 837, 170

Leloudas G., et al., 2012, *A&A*, 541, A129

Leloudas G., et al., 2015a, *MNRAS*, 449, 917

Leloudas G., et al., 2015b, *ApJ*, 815, L10

Li L.-X., 2008, *MNRAS*, 388, 603

Li C., Hillier D. J., Dessart L., 2012, *MNRAS*, 426, 1671

Lu J., et al., 2023, *ApJ*, 948, 27

Lucy L. B., Danziger I. J., Gouiffes C., Bouchet P., 1989, in Tenorio-Tagle G., Moles M., Melnick J., eds, , Vol. 350, IAU Colloq. 120: Structure and Dynamics of the Interstellar Medium. p. 164, doi:10.1007/BFb0114861

Lunnan R., et al., 2014, *ApJ*, 787, 138

Lunnan R., et al., 2018a, Nature Astronomy, 2, 887

Lunnan R., et al., 2018b, *ApJ*, 852, 81

Lunnan R., et al., 2020, *ApJ*, 901, 61

Maeda K., et al., 2007, *ApJ*, 666, 1069

Mainzer A., et al., 2014, *ApJ*, 792, 30

Maiolino R., et al., 2008, in Funes J. G., Corsini E. M., eds, Astronomical Society of the Pacific Conference Series Vol. 396, Formation and Evolution of Galaxy Disks. p. 409

Martayan C., Frémat Y., Hubert A. M., Floquet M., Zorec J., Neiner C., 2007, *A&A*, 462, 683

Martin D. C., et al., 2005, *ApJ*, 619, L1

Martinez L., et al., 2022, *A&A*, 660, A41

Mazzali P. A., Sullivan M., Pian E., Greiner J., Kann D. A., 2016, *MNRAS*, 458, 3455

McCrum M., et al., 2015, *MNRAS*, 448, 1206

McGaugh S. S., 1991, *ApJ*, 380, 140

McMahon R. G., Banerji M., Gonzalez E., Koposov S. E., Bejar V. J., Lodieu N., Rebolo R., VHS Collaboration 2013, The Messenger, 154, 35

Meisner A. M., Lang D., Schlegel D. J., 2017, *AJ*, 153, 38

Menzies J. W., et al., 1987, *MNRAS*, 227, 39P

Milisavljevic D., et al., 2015, *ApJ*, 815, 120

Minkowski R., 1941, *PASP*, 53, 224

Mitchell R. C., Baron E., Branch D., Hauschildt P. H., Nugent P. E., Lundqvist P., Blinnikov S., Pun C. S. J., 2002, *ApJ*, 574, 293

Modjaz M., Gutiérrez C. P., Arcavi I., 2019, Nature Astronomy, 3, 717

Mokiem M. R., et al., 2007, *A&A*, 473, 603

Muthukrishna D., Parkinson D., Tucker B. E., 2019, *ApJ*, 885, 85

Muthukrishna D., Mandel K. S., Lochner M., Webb S., Narayan G., 2021, arXiv e-prints, p. arXiv:2112.08415

Nicholl M., et al., 2013, *Nature*, 502, 346

Nicholl M., et al., 2014, *MNRAS*, 444, 2096

Nicholl M., et al., 2015a, *MNRAS*, 452, 3869

Nicholl M., et al., 2015b, *ApJ*, 807, L18

Nicholl M., et al., 2016, *ApJ*, 826, 39

Nicholl M., et al., 2020, Nature Astronomy, 4, 893

Nordin J., et al., 2011a, *A&A*, 526, A119

Nordin J., et al., 2011b, *ApJ*, 734, 42

Nugent P., et al., 2006, *ApJ*, 645, 841

Nymark T. K., Fransson C., Kozma C., 2006, *A&A*, 449, 171

Ochsenbein F., Bauer P., Marcout J., 2000, A&AS, 143, 23

Ofek E. O., et al., 2007, *ApJ*, 659, L13

Oke J. B., 1990, *AJ*, 99, 1621

Ollivier Y., 2014, arXiv e-prints, p. arXiv:1403.7752

Orellana M., Bersten M. C., Moriya T. J., 2018, *A&A*, 619, A145

Osterbrock D. E., 1989, Astrophysics of gaseous nebulae and active galactic nuclei. University Science Books

Osterbrock D. E., Ferland G. J., 2006, Astrophysics of gaseous nebulae and active galactic nuclei. University Science Books

Ostriker J. P., Gunn J. E., 1971, *ApJ*, 164, L95

Parrag E., et al., 2021, *MNRAS*, 506, 4819

Parrent J., Branch D., Jeffery D., 2010, SYNOW: A Highly Parameterized Spectrum Synthesis Code for Direct Analysis of SN Spectra, Astrophysics Source Code Library, record ascl:1010.055 (ascl:1010.055)

Pastorello A., et al., 2004, *MNRAS*, 347, 74

Pastorello A., et al., 2005, *MNRAS*, 360, 950

Pastorello A., et al., 2006, *MNRAS*, 370, 1752

Pastorello A., et al., 2010, *ApJ*, 724, L16

Pastorello A., et al., 2012, *A&A*, 537, A141

Pastorello A., et al., 2015, *MNRAS*, 449, 1941

Patat F., et al., 2011, *A&A*, 527, A91

Perley D. A., et al., 2020, *ApJ*, 904, 35

Perlmutter S., et al., 1999, *ApJ*, 517, 565

Pessi P. J., et al., 2019, *MNRAS*, 488, 4239

Peters E., et al., 2021, npj Quantum Information, 7, 161

Popov D. V., 1993, *ApJ*, 414, 712

Poznanski D., Prochaska J. X., Bloom J. S., 2012, *MNRAS*, 426, 1465

Pumo M. L., Cosentino S. P., Pastorello A., Benetti S., Cherubini S., Manicò G., Zampieri L., 2023, *MNRAS*, 521, 4801

Pun C. S. J., et al., 1995, *ApJS*, 99, 223

Pursiainen M., et al., 2022, *A&A*, 666, A30

Quimby R. M., Aldering G., Wheeler J. C., Höflich P., Akerlof C. W., Rykoff E. S., 2007, *ApJ*, 668, L99

Quimby R. M., et al., 2011, *Nature*, 474, 487

Quimby R. M., Yuan F., Akerlof C., Wheeler J. C., 2013, *MNRAS*, 431, 912

Quimby R. M., et al., 2018, *ApJ*, 855, 2

Reynolds T. M., et al., 2020, *MNRAS*, 493, 1761

Richmond M. W., 2014, Journal of the American Association of Variable Star Observers (JAAVSO), 42, 333

Riess A. G., et al., 1998, *AJ*, 116, 1009

Roming P. W. A., et al., 2005, Space Sci. Rev., 120, 95

Sahu D. K., Anupama G. C., Srividya S., Muneer S., 2006, *MNRAS*, 372, 1315

Salim S., Narayanan D., 2020, *ARAA*, 58, 529

Sánchez-Sáez P., et al., 2019, *ApJS*, 242, 10

Sanders N. E., et al., 2015, *ApJ*, 799, 208

Scalzo R. A., et al., 2010, *ApJ*, 713, 1073

Schlafly E. F., Finkbeiner D. P., 2011, *ApJ*, 737, 103

Schlegel E. M., 1990, *MNRAS*, 244, 269

Schulze S., et al., 2018, *MNRAS*, 473, 1258

Schulze S., et al., 2021, *ApJS*, 255, 29

Seeger P. A., Fowler W. A., Clayton D. D., 1965, *ApJS*, 11, 121

Shen K. J., et al., 2018, *ApJ*, 865, 15

Silverman J. M., et al., 2013, *ApJS*, 207, 3

Singh A., Kumar B., Moriya T. J., Anupama G. C., Sahu D. K., Brown P. J., Andrews J. E., Smith N., 2019, *ApJ*, 882, 68

Smartt S. J., et al., 2015, *A&A*, 579, A40

Smartt S. J., et al., 2017, *Nature*, 551, 75

Smith N., et al., 2007, *ApJ*, 666, 1116

Smith N., Foley R. J., Filippenko A. V., 2008, *ApJ*, 680, 568

Smith K. W., et al., 2020, *PASP*, 132, 085002

Sobolev V. V., 1960, Moving Envelopes of Stars. Harvard University Press, doi:10.4159/harvard.9780674864658

Soderberg A. M., et al., 2008, *Nature*, 453, 469

Soker N., Gilkis A., 2017, *ApJ*, 851, 95

Sorokina E., Blinnikov S., Nomoto K., Quimby R., Tolstov A., 2016, *ApJ*, 829, 17

Speagle J. S., 2020, *MNRAS*, 493, 3132

Spiro S., et al., 2014, *MNRAS*, 439, 2873

Steele I. A., et al., 2004, in Oschmann Jacobus M. J., ed., Society of Photo-Optical Instrumentation Engineers (SPIE) Conference Series Vol. 5489, Ground-based Telescopes. pp 679–692, doi:10.1117/12.551456

Stephenson F. R., Green D. A., 2002, Historical supernovae and their remnants, 5

Sukhbold T., Thompson T. A., 2017, *MNRAS*, 472, 224

Swann E., Frohmaier C., Nicholl M., Short P., Yaron O., 2019, Transient Name Server Classification Report, 2019-963, 1

Taddia F., 2012, in Roming P., Kawai N., Pian E., eds, Vol. 279, Death of Massive Stars: Supernovae and Gamma-Ray Bursts. pp 403–404, doi:10.1017/S1743921312013555

Taddia F., et al., 2013, *A&A*, 555, A10

Taddia F., et al., 2018, *A&A*, 609, A136

Takáts K., Vinkó J., 2012, *MNRAS*, 419, 2783

Takáts K., et al., 2016, *MNRAS*, 460, 3447

Taubenberger S., 2017, in Alsabti A. W., Murdin P., eds, , Handbook of Supernovae. Springer International Publishing AG, p. 317, doi:10.1007/978-3-319-21846-5_37

Terreran G., et al., 2016, *MNRAS*, 462, 137

Thomas R. C., Nugent P. E., Meza J. C., 2011, *PASP*, 123, 237

Tipping M. E., Bishop C. M., 1999, Journal of the Royal Statistical Society: Series B (Statistical Methodology), 61, 611

Tody D., 1986, in Crawford D. L., ed., Society of Photo-Optical Instrumentation Engineers (SPIE) Conference Series Vol. 627, Instrumentation in astronomy VI. p. 733, doi:10.1117/12.968154

Tonry J. L., et al., 2018a, *PASP*, 130, 064505

Tonry J. L., et al., 2018b, *PASP*, 130, 064505

Tutukov A. V., Yungelson L. R., 1994, *MNRAS*, 268, 871

Utrobin V. P., 2007, *A&A*, 461, 233

Valenti S., et al., 2008, *MNRAS*, 383, 1485

Valenti S., et al., 2014, *MNRAS*, 438, L101

Valenti S., et al., 2016, *MNRAS*, 459, 3939

Vilalta R., 2018, in Journal of Physics Conference Series. p. 052014 (arXiv:1812.10403), doi:10.1088/1742-6596/1085/5/052014

Vilalta R., Dhar Gupta K., Boumber D., Meskhi M. M., 2019, *PASP*, 131, 108008

Villar V. A., Cranmer M., Berger E., Contardo G., Ho S., Hosseinzadeh G., Lin J. Y.-Y., 2021, *ApJS*, 255, 24

Vincenzi M., Sullivan M., Firth R. E., Gutiérrez C. P., Frohmaier C., Smith M., Angus C., Nichol R. C., 2019, *MNRAS*, 489, 5802

Virtanen P., et al., 2020, Nature Methods, 17, 261

Vogl C., Sim S. A., Noebauer U. M., Kerzendorf W. E., Hillebrandt W., 2019, *A&A*, 621, A29

Vogl C., Kerzendorf W. E., Sim S. A., Noebauer U. M., Lietzau S., Hillebrandt W., 2020, *A&A*, 633, A88

Vreeswijk P. M., et al., 2014, *ApJ*, 797, 24

Vreeswijk P. M., et al., 2017, *ApJ*, 835, 58

Vurm I., Metzger B. D., 2021, *ApJ*, 917, 77

Wang S.-Q., et al., 2019, *ApJ*, 877, 20

Wasserman A., Tiwari V., BenZvi S., DESI Collaboration 2021, in American Astronomical Society Meeting Abstracts. p. 554.01

Wheeler J. C., Harkness R. P., Clocchiatti A., Benetti S., Brotherton M. S., Depoy D. L., Elias J., 1994, *ApJ*, 436, L135

Wheeler J. C., Yi I., Höflich P., Wang L., 2000, *ApJ*, 537, 810

Woods P. M., Thompson C., 2006, Soft gamma repeaters and anomalous X-ray pulsars: magnetar candidates. Cambridge University Press, pp 547–586

Woosley S. E., Pinto P. A., Hartmann D., 1989, *ApJ*, 346, 395

Woosley S. E., Blinnikov S., Heger A., 2007, *Nature*, 450, 390

Wright E. L., et al., 2010, *AJ*, 140, 1868

Wright A. H., et al., 2016, *MNRAS*, 460, 765

Yan L., et al., 2015, *ApJ*, 814, 108

Yan L., et al., 2017a, *ApJ*, 840, 57

Yan L., et al., 2017b, *ApJ*, 848, 6

Yaron O., Gal-Yam A., 2012, *PASP*, 124, 668

Yoon S. C., Langer N., 2005, *A&A*, 435, 967

Zaritsky D., Kennicutt Robert C. J., Huchra J. P., 1994, *ApJ*, 420, 87

de Jaeger T., et al., 2018, *MNRAS*, 476, 4592

de Jaeger T., et al., 2019, *MNRAS*, 490, 2799

de Jaeger T., et al., 2020, *MNRAS*, 495, 4860

de Souza R. S., et al., 2023, Astronomy and Computing, 44, 100715

van Dokkum P. G., Bloom J., Tewes M., 2012, L.A.Cosmic: Laplacian Cosmic Ray Identification (ascl:1207.005)